EPFL

Thèse n° 10 340

Diagenetic isotope exchange in biocalcites for paleoclimate reconstruction

Présentée le 26 janvier 2024

Faculté de l'environnement naturel, architectural et construit
Laboratoire de géochimie biologique
Programme doctoral en génie civil et environnement

pour l'obtention du grade de Docteur ès Sciences

par

Deyanira Graciela CISNEROS LAZARO

Acceptée sur proposition du jury

Dr S. Takahama, président du jury
Prof. A. Meibom, directeur de thèse
Prof. D. Jacob, rapporteuse
Prof. E. Gischler, rapporteur
Prof. S. Bernasconi, rapporteur

École polytechnique fédérale de Lausanne

2024

Abstract

The oxygen isotope compositions of fossil biocalcites, such as foraminifera, bivalves, brachiopods, and belemnites have allowed for reconstructions of sea surface and deep ocean temperatures throughout the Phanerozoic and constitute the most important record of paleo-ocean conditions. However, following the death and burial of these marine organisms, their shells and tests encountered porewaters with isotope compositions and temperatures different from the seawater in which they lived. This could have driven post-burial isotope exchange that would significantly alter the original biocalcite O-isotope compositions and hence introduce bias in, e.g., paleo-seawater temperature reconstructions. These processes need to be better understood to improve the accuracy of marine paleo-environment reconstructions, which are essential to contextualize anthropogenic climate change in a geological perspective.

In this thesis, the calcitic tests of three species of modern benthic foraminifera (*Ammonia confertitesta*, *Haynesina germanica,* and *Amphistegina lessonii*) and one fossil benthic foraminifera (*Ammonia beccarii*), as well as the calcitic prismatic layers of two modern bivalve mollusks (*Pinna nobilis* and *Pinctada margaritifera*) were subjected to experiments simulating the effects of fluid-mediated isotope exchange. Tests and shells were incubated in a highly ^{18}O-enriched artificial seawater at 90 °C for 6 days, at chemical equilibrium. The experimentally incubated samples were texturally indistinguishable from pristine specimens but their bulk oxygen isotope compositions indicated rapid and substantial isotope exchange with the artificial seawater. NanoSIMS imaging, combined with scanning electron microscopy, electron backscatter diffraction, and cathodoluminescence was used to visualize and quantify how fluids penetrated and isotopically exchanged with these biocalcites. The analyses revealed that oxygen isotope exchange was closely linked to species-specific differences in shell and test ultrastructures and the distribution of intracrystalline organic matter.

Comparison between the extent of isotope exchange in modern benthic foraminifera tests (*Ammonia confertitesta*) and fossil equivalents (*Ammonia beccarii*) showed that when the intracrystalline organic material is already partially degraded by the natural fossilization process, the rate of diagenetic O-isotope exchange is lower than in the pristine tests, but O-isotope exchange nevertheless remains an effective process. Fossil biocalcites thus remain susceptible to O-isotope exchange millions of years after sedimentation and burial. A conceptual model is presented for how the diagenetic susceptibility of biocalcites changes over time.

The establishment of a strong link between the distribution of organic matter and the rate of O-isotope exchange motivated a more thorough investigation of the former. Correlated NanoSIMS imaging and Photo-induced Force Microscopy mapping of the calcitic prismatic layer of bivalves revealed that the distribution of intracrystalline saccharide-rich organic matter was closely linked to the observed distribution of O-isotope exchange, while intracrystalline proteinaceous material was generally scarce. This suggests that intracrystalline saccharides play a much more prominent role in facilitating diagenetic isotope exchange than intracrystalline proteins. Future studies of intracrystalline saccharide degradation during diagenesis thus gain priority.

By identifying a species-specific susceptibility to diagenesis and elucidating the role of intracrystalline organic matter during O-isotope exchange in foraminifera tests and prismatic bivalve layers, this thesis contributes to our understanding of diagenesis in biocalcites and represents a significant step towards the development of more accurate reconstructions of paleo-ocean conditions.

Keywords: Diagenesis, paleoclimate reconstruction, foraminifera, bivalves, biocalcite, isotopic exchange, biomineralization, NanoSIMS, PiFM

Résumé

La composition élémentaire et isotopique de restes fossilisés d'organismes marins calcifiants constituent l'archive la plus importante des conditions paléo-océaniques. L'étude de la composition isotopique de l'oxygène des biocalcificateurs fossiles tels que les foraminifères, les bivalves, les brachiopodes et les bélemnites a permis de reconstruire le profil des températures de surface et de profondeur des mers et océans pour l'ensemble du Phanérozoïque. De leur vivant, ces organismes accumulent par leur métabolisme de l'oxygène dont la signature isotopique correspond à celle de l'environnement dans lequel ils vivent, à une température spécifique. Cependant, après leur mort et leur enfouissement, leur coquille et leur test sont alors exposés à des eaux interstitielles dont la composition isotopique et la température sont différentes de celles de l'eau de mer à partir de laquelle ils ont été formés. L'échange isotopique entre les eaux interstitielles et la calcite de la coquille lors de la diagenèse après enfouissement peut modifier considérablement leur composition isotopique d'origine et engendrer des erreurs dans les reconstructions des profils de températures du paléoenvironnement marin. La compréhenseion et quantification de ces échanges isotopiques diagénétiques représentent donc l'un des principaux défis à la reconstruction précise des conditions océaniques passées, ce qui est essentiel pour contextualiser le changement climatique anthropique actuel dans une perspective géologique.

Dans cette thèse, les tests calcitiques de trois espèces de foraminifères benthiques modernes (*Ammonia confertitesta, Haynesina germanica* et *Amphistegina lessonii*) et de foraminifères benthiques fossiles (*Ammonia beccarii*), ainsi que les couches prismatiques calcitiques de deux mollusques bivalves modernes (*Pinna nobilis* et *Pinctada margaritifera*) ont été soumis à des expériences simulant les effets de l'échange d'isotopes médié par les fluides. Les échantillons ont été incubés dans de l'eau de mer artificielle fortement enrichie en ^{18}O à 90 °C pendant 6 jours à l'équilibre chimique. Les échantillons incubés expérimentalement n'ont pas révélé de différences sur le plan textural par rapport aux spécimens témoins. Cependant leur composition isotopique totale de l'oxygène ont indiqué un échange rapide et substantiel d'isotopes de l'oxygène avec l'eau de mer artificielle. L'imagerie par NanoSIMS, combinée à des techniques de microscopie électronique à balayage, de diffraction par rétrodiffusion d'électrons et de cathodoluminescence, a permis de visualiser la manière dont les fluides pénètrent dans ces structures biocalcifiées et de quantifier les échanges isotopiques entre les deux milieux. Les analyses ont révélé que l'échange

d'isotopes d'oxygène est étroitement lié aux différences dans l'ultrastructure des coquilles ou tests spécifiques à chaque espèce et à la présence de matière organique intracristalline.

La comparaison des échanges isotopiques dans les tests de *l'Ammonia confertitesta* moderne et dans ceux de l'équivalent fossile, *l'Ammonia beccarii*, a montré que lorsque la matière organique intracristalline est déjà partiellement dégradée en raison des processus naturels de fossilisation, le taux d'échange diagénétique des isotopes de l'oxygène est plus faible que dans les tests modernes, mais reste un processus efficace. Les biocalcites fossiles restent donc sensibles à l'échange d'isotopes d'oxygène des millions d'années après leur sédimentation et leur enfouissement. À la suite de ces résultats, un modèle conceptuel est présenté pour expliquer comment la susceptibilité à la diagenèse des biocalcites évolue au fil du temps.

L'établissement d'un lien étroit entre la distribution de la matière organique dans la coquille et le taux d'échange isotopique en oxygène a motivé une étude de la composition et de la distribution de la matière organique inter- et intra-cristalline. L'imagerie par NanoSIMS et la microscopie à force photo-induite de la couche prismatique calcitique des bivalves ont révélé que la distribution de la matière organique intracristalline riche en saccharides est étroitement liée à la distribution observée de l'échange d'isotopes d'oxygène, tandis que la matière protéique intracristalline est en général rare. Cela suggère que les saccharides intracristallins jouent un rôle beaucoup plus important dans la facilitation des échanges isotopiques diagénétiques que les protéines intracristallines, soulignant la nécessité d'étudier les effets de la préservation (ou de la dégradation) des saccharides intracristallins au cours de la diagenèse des biocalcites.

En identifiant une sensibilité aux effets diagénétiques propre à chaque espèce et en élucidant le rôle de la matière organique intracristalline pendant l'échange isotopique dans les tests de foraminifères et la couche prismatique calcitique chez les bivalves, cette thèse constitue une étape importante vers notre compréhension de la diagenèse dans les biocalcites et donc au développement de reconstructions plus précises des conditions paléo-océaniques.

Mots clefs : Diagenèse, reconstruction paléoclimatique, foraminifères, bivalves, biocalcite, échange isotopique, biominéralisation, NanoSIMS, PiFM

Acknowledgements

I would first and foremost like to thank my supervisor, Anders Meibom. When we first sat down for that coffee almost five years ago, I could never have imagined what a wonderful journey I was embarking on. My deepest gratitude for your guidance, your mentorship, your trust and of course, your incredible turnaround time on corrections! I am especially grateful for the freedoms you accorded me to pursue every avenue of enquiry, wherever that led (turns out it's to the other side of the world!).

Secondly, this thesis would never have been possible without Arthur Adams. Besides being a brilliant experimentalist, who problem solved our way out every challenge this project has thrown at us, you have been a constant support throughout this thesis. I can't thank you enough, particularly for these last few weeks of helpful feedback and encouragement.

To everyone on the ERC team, you really showed me the beauty of collaboration and being part of such a large and diverse research group has been one of the great pleasures of this PhD. To my two closest external collaborators, Laura Otter and Jarek Stolarski, it has been an absolutely joy to have worked with you both. We make a fantastic team and I hope we will continue to work together far into the future. I am enormously grateful to everyone who contributed to the final edits of this thesis, your keen eyes always could spot things I could not.

To the technical staff at EPFL and UNIL, you are the grease that keeps the wheels of science turning. Without you, none of the results in this thesis would have been possible. Thank you to Stephane Escrig for the hundreds of hours of help on the NanoSIMS, those many hours in the NanoSIMS room would never have been the same without our funny and interesting conversations. Thank you to Cristina Martin-Olmos, for all the help with SEM and AFM imaging and for sharing your enthusiasm for all things microscopy. And thank you to Florent Plane, not just for the technical help but also for all the pieces of wood and metal you have cut for my home DIY projects over the years. To everyone at the EMF but particularly to Jean Daraspe, Antonio Mucciolo, and Damien De Bellis , thank you being so fun to be around and for all the times you helped me with my sample prep.

During my PhD I was lucky enough to complete two international research visits. My visits to the LPG-BIAF in Angers, France to learn all about foraminifera and their cultivation was a wonderful experience, thanks to Christine Barras and Inge van Dijk who were patient enough to answer all my questions without complaint. My two-month research visit to ANU in Canberra, Australia was one of the happiest and most productive periods of my life. Thank you so much to Dorrit Jacob and Brett Knowles for facilitating my visit, Jochen Brocks for the fascinating discussions, and Wei (Vivian) Xiao and Yang Wu for all the assistance with PiFM and especially the many, many nitrogen bottle changes. To Michael Förster, your calming presence was always welcome and together with Laura, we had some fantastic lunches amused by the surrounding Australian birdlife. A big thank you to the team at Broken Bay Pearl Farm for a fantastic visit, and especially to Celeste Boonaerts for your time and of course, all the beautiful shells I could come back with.

A big thank you to everyone at LGB, past and present. Although after my office move to Geopolis we didn't see each other as much as I would've liked, whenever I came in to EPFL, I never failed to leave with a smile on my face. Throughout my PhD there were many times when I gate crashed both Torsten's and the SIMS's group lunches, and for that I thank you all for bringing me much needed levity and distraction when I needed it most.

To my previous supervisors Lukas Baumgartner and Jodie Miller, this PhD wouldn't have been possible if all those years ago you hadn't believed in me when I didn't believe in myself. Words can't thank you enough for how you changed the trajectory of my life.

To my friends, thank you for putting up with my rollercoaster of emotions and accepting with grace all the times I cancelled our plans because of work. Finally, I would like to thank my parents and my siblings. Your love and continued support over the years have been invaluable and I thank you from the very bottom of my heart. Last but not least, to my partner Marisa, thank you for your love, your endless patience, and just for the way you've made life so much fun.

Table of Contents

1 Introduction 1

1.1 $\delta^{18}O$ of seawater 3

1.2 The vital effect 5

1.3 Biomineralization in foraminifera 6

1.4 Biomineralization in bivalves 10

1.5 Diagenesis of biocalcites 13

1.5.1 Diagenesis in foraminifera 14

1.5.2 Diagenesis in bivalves 18

1.6 Motivation and aims of the thesis 21

1.7 Approach and organization of the thesis 21

2 Fast and pervasive diagenetic isotope exchange in foraminifera tests is species-dependent 23

2.1 Introduction 25

2.2 Methods 27

2.2.1 Test cleaning and oxygen isotope exchange experiments 27

2.2.2 NanoSIMS preparation and imaging 28

2.2.3 TEM preparation and imaging 29

2.2.4 Calculating cogwheel interface densities and diagenesis resistance ratios 29

2.3 Results 30

2.3.1 Oxygen isotope exchange experiments 30

2.3.2 Ultrastructure of the starting materials 31

2.3.3 Ultrastructure of the experimentally incubated materials 34

2.3.4 Species-specific bulk ^{18}O-enrichments 35

2.3.5 NanoSIMS imaging of ^{18}O-enrichments 36

2.3.6 The difference in reactivity between biogenic and abiotic calcite 39

2.4 Discussion 40

2.4.1 Localized ^{18}O-enrichments 40

2.4.2 Pervasive ^{18}O-enrichments 41

2.4.3 Species-specific susceptibility to isotope exchange 42
2.4.4 Paleo-environmental reconstructions based on biogenic calcites – an outlook 45
2.4.5 Code Availability Statement 47
2.5 Supplementary information 48
3 Fossil biocalcite remains open to isotopic exchange with seawater for tens of millions of years 65
3.1 Introduction 67
3.2 Methods 69
3.2.1 Cleaning procedures and incubation experiments 69
3.2.2 Imaging by SEM, AFM, CL, NanoSIMS and EBSD 70
3.3 Results 72
3.3.1 Comparing the ultrastructures and crystallography of modern and fossil Ammonia 72
3.3.2 NanoSIMS imaging of ^{18}O-enrichments in modern and fossil Ammonia tests exposed to identical diagenetic conditions 78
3.4 Discussion 81
3.4.1 Preservation state of fossil tests used in this study 81
3.4.2 The difference in diagenetic susceptibility between modern and fossil calcite 85
3.4.3 The role of organic matter degradation in fossil calcite diagenesis and the implications for paleo-environmental reconstructions 86
3.5 Supplementary information 89
4 Abundant intracrystalline saccharides within the calcitic prisms of bivalve Pinctada margaritifera: Insights into biomineralization and bioinspired structural materials 97
4.1 Introduction 99
4.2 Methods 102
4.2.1 SEM and EBSD 102
4.2.2 NanoSIMS 102
4.2.3 PiFM 103
4.3 Results 104

4.3.1 The hierarchical structural arrangements of calcitic prisms in Pinctada margaritifera 104
4.3.2 Crystallography and chemistry of the calcitic prismatic shell architecture 104
4.3.3 Nanoscale mapping of organic components with PiFM 111

4.4 Discussion 115
4.4.1 Composition of the organic moiety 115
4.4.2 Morphology of intracrystalline organic moieties 118
4.4.3 Relationship between intracrystalline organic moieties and the crystallography of prisms 120
4.4.4 Conclusions 121

4.5 Supplementary information 122

5 In-situ identification of the biomacromolecules relevant to diagenetic isotope exchange in bivalves 131

5.1 Introduction 133

5.2 Methods 134

5.3 Results 136
5.3.1 Ultrastructures of the prismatic layer in P. nobilis and P. margaritifera 136
5.3.2 Oxygen isotope exchange experiments 138
5.3.3 Distribution of organic components in P. nobilis and P. margaritifera 142

5.4 Discussion 145
5.4.1 Species-specific diagenetic isotope exchange in the prismatic layer of bivalves 145
5.4.2 The role of saccharide-rich organic matter in diagenetic isotope exchange 147

5.5 Conclusions 149

5.6 Supplementary information 150

6 Conclusions 157

6.1 Species-specific diagenetic isotope exchange 157

6.2 Diagenetic isotope exchange in fossil biocalcites 158

6.3 Outlook 159

7 References 161

8 Curriculum Vitae 183

1 Introduction

The elemental and isotopic compositions of the fossilized shells of marine organisms, such as foraminifera, bivalves, brachiopods, and belemnites serve as proxies for past environmental conditions and have allowed for the reconstruction of a wide range of important oceanographic parameters on geologic timescales (Brand *et al.*, 2003; Katz *et al.*, 2010; Mutterlose *et al.*, 2010; Bernasconi *et al.*, 2011; Schöne *et al.*, 2011; Schone and Surge, 2012; Immenhauser *et al.*, 2016). Arguably one of the most well-established and comprehensive of these is the oxygen isotope paleothermometer. Its development by Urey and colleagues in the 1950's was facilitated by two key scientific and technological breakthroughs: The discovery of the temperature-dependent oxygen isotope fractionation between carbonate and water and the development of mass spectrometers sensitive enough to measure the minute differences in the isotopic composition of natural (bio-)minerals (Urey, 1948; Mckinney *et al.*, 1950; Epstein *et al.*, 1951, 1953; Urey *et al.*, 1951). The oxygen isotope paleothermometer is based on the principle that, under near-equilibrium conditions, the $^{18}O/^{16}O$ ratio of calcium carbonate depends only on the temperature and the $^{18}O/^{16}O$ ratio of the ambient seawater from which it precipitates. In the words of Urey himself (Urey, 1948):

> *"It is evident that, if an animal deposits calcium carbonate in equilibrium with water in which it lives, and the shell sinks to the bottom of the sea and is buried securely in the earth and remains unchanged from that time to this, it is only necessary to determine the ratio of the isotopes of oxygen in the shell today in order to know the temperature at which the animal lived".*

Due to the small differences between O-isotopic compositions of terrestrial samples, the measurements of $^{18}O/^{16}O$ isotope ratios of a sample relative to a laboratory standard are reported as $\delta^{18}O$ (in parts-per-thousand) according to the following equation:

$$\delta^{18}\mathrm{O} = \left(\frac{\left(\frac{^{18}O}{^{16}O}\right) sample}{\left(\frac{^{18}O}{^{16}O}\right) standard} - 1 \right) \times 1000 \qquad (1)$$

In the 70+ years since its development, the oxygen isotope paleothermometer has been applied to a wide range of important scientific challenges, such as proving Milankovitch's orbital theory of the ice ages (Emiliani, 1958; Hays *et al.*, 1976), understanding past El Niño events (Metcalfe *et al.*, 2020), explaining the main causes of the mass extinction at the Permian/Triassic transition (Gruszczynski *et al.*, 1989), and reconstructing low latitude (30° S–30° N) sea surface temperatures curves for the global ocean for the entire Phanerozoic (Grossman and Joachimski, 2022) (Fig. 1.1).

Remarkably, from the outset, Urey and colleagues identified several fundamental concerns, or limitations of the O-isotope carbonate paleothermometer, which remain valid today: 1) The oxygen isotope ratio of global ocean seawaters may have changed over time, 2) calcifying organisms may fractionate oxygen isotopes during their calcification, referred to as the 'vital effect' by Urey and colleagues, and 3) not all fossil shells might have preserved their original isotopic signatures due to the effects of diagenesis (Urey *et al.*, 1951).

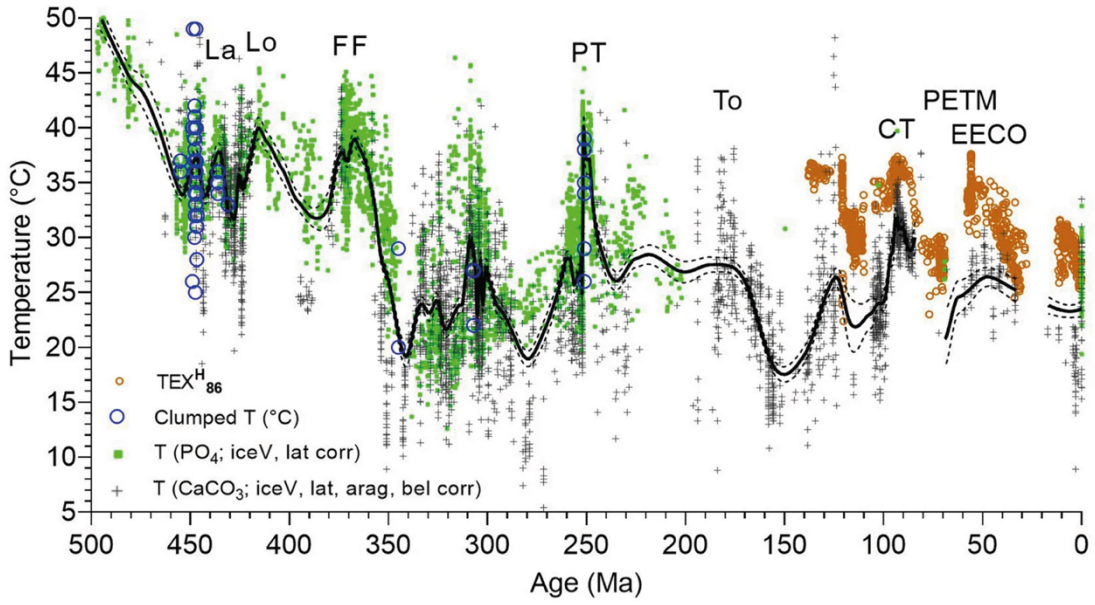

Figure 1.1 A reconstruction of low latitude (30° S–30° N) sea surface temperatures over the past 500 million years based on the $\delta^{18}O$ of phosphate and carbonate fossils, plus other proxies. Modified after Grossman and Joachimski (2022).

1.1 $\delta^{18}O$ of seawater

Urey's research associate, the micropaleontologist Cesare Emiliani, analyzed planktonic foraminifera from piston core-derived marine sediments from the late Pleistocene to modern times and found periodic oscillations in their $^{18}O/^{16}O$ ratios that were initially interpreted as evidence for >6 °C global surface ocean-temperature variations due to cycling between glacial and interglacial phases, offering support to the orbital theory of ice ages (Emiliani, 1955). However, his temperature calculations did not sufficiently take into account the effect that the growth and decline of large volumes of ice sheets would have on global mean O-isotope seawater composition. The growth of ice sheets, which are depleted in ^{18}O due to the combined effects of isotopic fractionation during evaporation and condensation of the seawater from which they are formed, leave the ocean enriched in ^{18}O during glacial periods. The subsequent melting of the ice sheets during interglacial periods returns the global ocean to a lighter O-isotopic composition; this variation is estimated to be significant, around 1.2‰ (Shackleton and Opdyke, 1973). The effect of global ice-sheet volume on ocean O-isotope composition is now well established and accounted for in paleoclimatic reconstructions (Shackleton, 1967; Zachos *et al.*, 2001; Oerlemans, 2004).

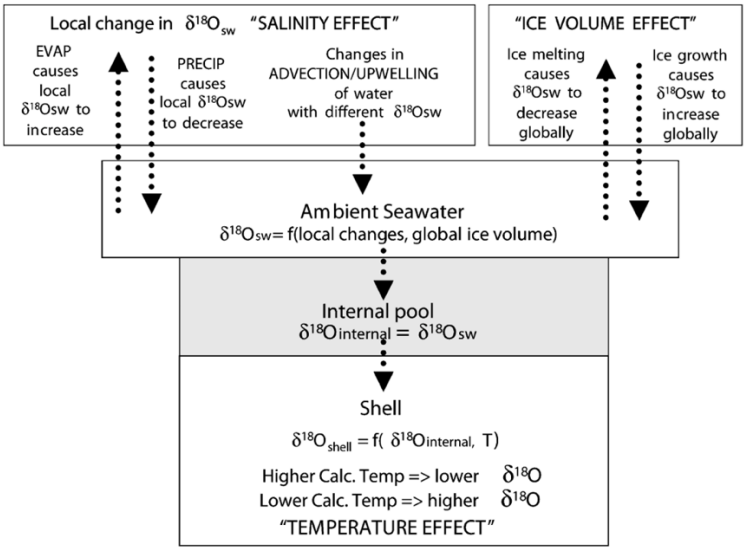

Figure 1.2 Environmental factors affecting the $\delta^{18}O_{SW}$ biocalcites precipitate from. Modified after Ravelo *et al.* (2007).

The O-isotope composition of seawater ($\delta^{18}O_{sw}$; relative to the current standard mean sea seawater standard, VSMOW) depends not only on the global ice volume, but also on local processes, such as the evaporation-precipitation balance, local freshwater input from rivers, iceberg melting, and advection (Ravelo and Hillaire-Marcel, 2007; Grossman, 2012; Pearson, 2012) (Fig. 1.2). Increased evaporation shifts both seawater salinity and $\delta^{18}O_{sw}$ to higher values, while the opposite is true for precipitation. This correlation between $\delta^{18}O$ values and salinity has been termed 'the salinity effect' on $\delta^{18}O_{SW}$. As the $\delta^{18}O$ of precipitation varies with latitude, correction factors for $\delta^{18}O_{SW}$ have been developed for use in global compilations of sea surface temperatures (Zachos *et al.*, 1994). Online tools now exist that allow researchers to correct for the 'salinity effect' on their calcium carbonate $\delta^{18}O$ temperature reconstructions using a range of methods, from modern $\delta^{18}O_{SW}$ at the sample locality and depth, estimates of $\delta^{18}O_{SW}$ based on latitude alone, or $\delta^{18}O_{SW}$ estimated from isotope-enabled climate models (Gaskell and Hull, 2023). Compilations from paleotropical brachiopod and belemnite fossils show $\delta^{18}O$ values increasing by 4–8‰ from the Cambrian to the present, which would imply early to mid-Paleozoic ocean temperatures between 30–60 °C. But, such temperatures are beyond the optimal temperature regime for many biological marine communities (Veizer *et al.*, 1999; Veizer and Prokoph, 2015) (Fig. 1.3). There is lively debate as to whether this long-term increasing $\delta^{18}O$ trend reflects a cooling of the earth's oceans over time, a changing isotopic composition of the seawater, or progressive sample diagenesis with time (Knauth and Epstein, 1976; Land, 1995; Veizer and Prokoph, 2015; Grossman and Joachimski, 2022). Different researchers have attempted to resolve this issue through different means, but most include corrections for ice volume and paleolatitudes (Zachos *et al.*, 1994, 2001; Grossman, 2012; Veizer and Prokoph, 2015; Song *et al.*, 2019; Grossman and Joachimski, 2022).

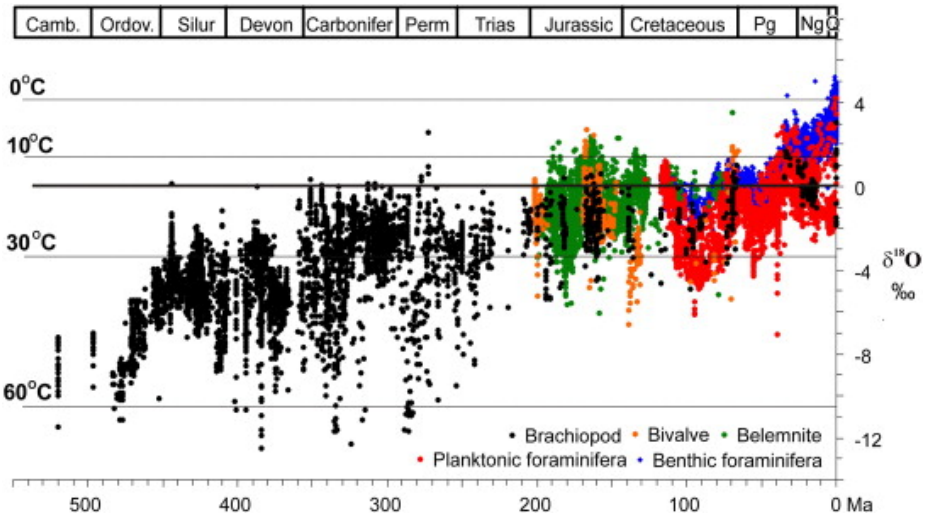

Figure 1.3 Phanerozoic ocean temperature estimates from the $\delta^{18}O$ of low-Mg calcitic fossils using a $\delta^{18}O$ of modern seawater (0‰ relative to the Vienna Standard Mean Ocean Water (VSMOW) standard). Modified after Veizer and Prokoph (2015).

1.2 The vital effect

Urey and colleagues predicted that not all calcifying organisms would grow their shell in isotopic equilibrium with ambient seawater due to biological isotope fractionation, referred to as the vital effect, which – it was suggested – could only be resolved through experiments (Urey *et al.*, 1951). This was soon proven by Duplessy and colleagues (1967), who demonstrated species-specific offsets in the $\delta^{18}O$ composition of two shells of benthic foraminifera taken from the same core depth, which yielded temperatures that did not agree with the measured seawater temperatures in that region. Planktonic foraminifera *N. pachyderma* has been shown to secrete a test — foraminifera shells are called tests — where the intra-test variations in the $\delta^{18}O$ exceed the equilibrium $\delta^{18}O$ value of the specimen's habitat by a factor of three (Kozdon *et al.*, 2009). Although some marine organisms precipitate their shells in isotopic equilibrium with their surrounding fluids, many benthic and planktonic foraminifera, bivalves and brachiopods do not (Carpenter and Lohmann, 1995; Bauch *et al.*, 1997; Steuber, 1999; Curry and Fallick, 2002; Mancuso *et al.*, 2022). Therefore, it has become standard practice to adjust for species-specific vital effects on $\delta^{18}O$ paleoclimate reconstructions (Shackleton *et al.*, 1984; Zachos *et al.*, 1994, 2001; Cramer *et al.*, 2009).

As the vital effect on shell oxygen isotope compositions show, a reasonable level of understanding of the biomineralization strategies of different marine calcifiers is essential for the accurate reconstruction of paleoclimatic conditions based on their mineralized hard parts. What follows is brief overview of the biomineralization mechanisms of the tests of rotaliid foraminifera and the calcitic prismatic layer of bivalves, the two biocalcite-forming organisms principally investigated in this thesis.

1.3 Biomineralization in foraminifera

Foraminifera are single-celled amoeboid protists that first appeared in the Early Cambrian and are now widely distributed across the world's oceans (Pawlowski *et al.*, 2003). They can be differentiated into agglutinated foraminifera that assemble their tests from surrounding particles, and calcifying foraminifera that primarily secrete calcitic, or in some cases, aragonitic tests (Boersma, 1998). Calcifying foraminifera can be divided into imperforate or porcelaneous foraminifera that precipitate high-Mg calcite and perforate or hyaline foraminifera, which precipitate low-Mg calcite (Boersma, 1998; de Nooijer *et al.*, 2014b). It is this latter group that is mostly used for paleoclimatic reconstructions: planktonic hyaline foraminifera that float at various depths in the open ocean are used to reconstruct sea surface temperatures and benthic hyaline foraminifera that live directly on the sea floor are used to reconstruct deeper ocean temperatures (Pearson, 2012).

Element and isotope ratios in foraminifera differ from that of surrounding seawater, and exhibit intra-shell, inter-specimen, and inter-species differences (Bentov and Erez, 2006; Kunioka *et al.*, 2006; Kozdon *et al.*, 2009; de Nooijer *et al.*, 2014a; Paris *et al.*, 2014; Fehrenbacher *et al.*, 2017; Levi *et al.*, 2019; van Dijk *et al.*, 2019). Significant controversy exists over the biological or inorganic processes responsible for this variability, which include mechanisms such as seawater vacuolization (Erez, 2003; Bentov *et al.*, 2009; Evans *et al.*, 2018), active ion exchange/pumping (Bentov and Erez, 2006; Nehrke *et al.*, 2013; Nagai *et al.*, 2018a; Geerken *et al.*, 2022), pH regulation (de Nooijer *et al.*, 2009; Toyofuku *et al.*, 2017), and crystallization via metastable phases such as vaterite or amorphous calcium carbonate (ACC) (Jacob *et al.*, 2017). However, theories for calcification in foraminifera can be broadly divided into two competing schools of thought. The first postulates that foraminifera incorporate seawater vacuoles, extracting and removing the ions

as needed before transporting the vacuoles to the site of calcification (Erez, 2003; Bentov *et al.*, 2009). The second is based on the idea of ion transport over membranes, with a small percentage of ions arriving at the site of calcification via leakage or vacuolization of seawater (Nehrke *et al.*, 2013).

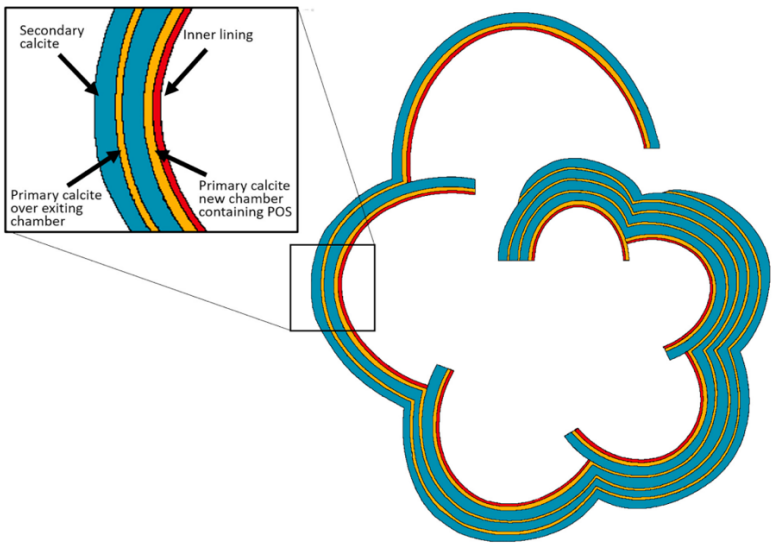

Figure 1.4 Proposed calcification scheme in lamellar hyaline foraminifera. Calcification of each new chamber starts with the delineation of a primary organic sheet (POS). Primary calcite, enriched in trace elements, is precipitated on both sides of the POS followed by thick secondary calcite precipitation that is lower in trace element composition. Modified from Levi *et al.* (2019).

The three species of foraminifera investigated in this thesis are all benthic hyaline radial foraminifera belonging to the order Rotaliida, so the following discussion will focus on calcification in rotaliid foraminifera. Rotaliid foraminifera build their test by sequentially adding chambers, with the growth of each new chamber being associated to thickening of the previous chambers. Calcification starts with the delineation of an organic template, referred to as the primary organic sheet (POS). The POS is 'sandwiched' between two additional organic layers, the outer and inner organic layer (Nagai *et al.*, 2018a, 2018b). Calcification then takes place within this 'delimited' or 'privileged' space, which is isolated from the environment (Erez, 2003; de Nooijer *et al.*, 2014b; Tyszka *et al.*, 2019). The POS and other organic layers, collectively called organic linings, are rich in polysaccharides and proteins (Fhlaithearta *et al.*, 2013). Polysaccharides are thought to provide

structural support, while the proteins offer charged sites for the nucleation of calcite (Towe and Cifelli, 1967; de Nooijer *et al.*, 2014b). With each added chamber, rotaliid foraminifera thicken older parts of the existing test (Nehrke *et al.*, 2013), such that older chambers contain progressively more organic linings (Fig. 1.4). The first calcite precipitated over the POS, called primary calcite, is thought to be rich in magnesium and other trace elements. This is followed by a thicker secondary calcite that has lower concentration of magnesium and other trace elements (Erez, 2003; Levi *et al.*, 2019). Microspatial mapping techniques, such as electron microprobe (EMPA) mapping and NanoSIMS imaging have shown that trace-elemental banding is closely associated with the organic linings, suggesting that element banding is intrinsically linked to chamber formation (van Dijk *et al.*, 2017, 2019; Geerken *et al.*, 2019).

Rotaliid foraminifera tests are composed of approximately spherical calcite nanograins in the size-range between 20–100 nm (Dubicka *et al.*, 2018). These nanograins are organized into sub-units that have the same crystallographic orientation, with the c-axis perpendicular to the shell surface and therefore rotating with the curvature of the test (Towe and Cifelli, 1967; Boersma, 1998). Noting that the surfaces of slightly etched hyaline tests showed irregular suture boundaries, Towe and Cifelli (1967) proposed that the sub-units defined by these suture boundaries are test domains with a single crystallographic orientation. Building on the work of Banner and colleagues (1973), Haynes (1981) postulated that, upon extrusion of the organic template, there is an initial deposition of 'blocky grains' of calcite around tubules, which are now called pores, followed by infilling with 'calcareous' skeleton (Fig. 1.5). The implication here is that the suture patterns seen on the surface of tests are the result of competing crystallization from different centers of calcification, i.e., automorphous mutual boundaries that reflect the relative orientation of neighboring nucleation sites (Debenay *et al.*, 2000). Subsequently it was shown by field-emission transmission electron microscopy (FESEM) and selected area electron diffraction (SAED) that the sub-units bounded by these sutures do indeed represents areas of a single c-axis orientation perpendicular to the shell surface, and that the interfaces between units are characterized by substantial strain (Nakajima *et al.*, 2016). These domains and their interfaces have been termed 'cogwheel structures' and systematic investigation of their distribution across a wide array of benthic and planktonic foraminifera revealed species-specific differences in their distribution and morphology (van Dijk *et al.*, 2020). It has not yet been established if these suture zones are filled with organics, high-Mg calcite, or another carbonate polymorph (van Dijk *et al.*, 2020).

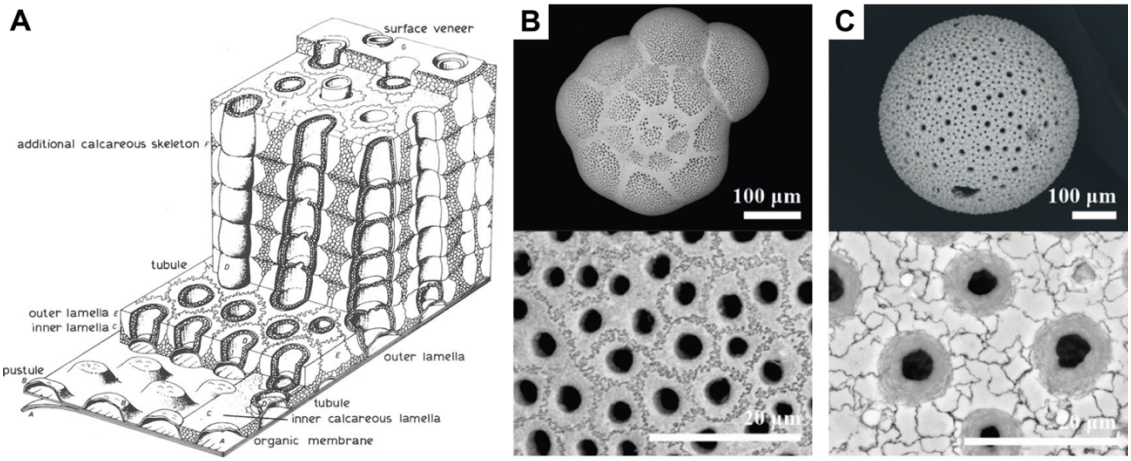

Figure 1.5 Schematic model and representative examples of cogwheel structures in rotaliid foraminifera. (a) Schematic representation of rotaliid calcification that is proposed to initiate around pores, with sutures/cogwheel structures resulting from competing crystallization from different 'centers of calcification'. Modified after Haynes (1981). (b-c) Examples of cogwheel structures seen on the surfaces of partially decalcified benthic *Ammonia* sp. and planktonic *Orbulina universa*. Modified after van Dijk *et al.* (2020).

Subsequently, great progress has been made deciphering the crystallographic organization of rotaliid foraminifera through the use of electron backscatter diffractions (EBSD): both planktonic and benthic tests are composed of strongly interdigitating mesocrystals with the c-axis perpendicular to the surface and extensive 60° twinning of calcite, which is thought to strengthen the walls of the tests (Yin *et al.*, 2021; Lastam *et al.*, 2023b, 2023a). Mesocrystals are defined here as 'crystalline entities over space that consists of numerous smaller subunits on the sub-micrometer to ~1 µm scale, which are mutually slightly misoriented and thus separated by small-angle boundaries' (Yin *et al.*, 2021). Crystallographic continuity is maintained across organic linings, and the biopolymers within the organic linings are thought to be responsible for guiding the alignment of the c-axis (Lastam *et al.*, 2023a).

1.4 Biomineralization in bivalves

Bivalve mollusks are soft-bodied animals that first appeared in the Early Cambrian and are now widely distributed, occupying a broad range of ecological niches in marine and freshwater environments (Vinther, 2015). Bivalves presumably evolved to protect themselves from the environment and predation by secreting a hard exoskeleton made of different forms of calcium carbonate (Currey, 1989; Marin *et al.*, 2012). Their abundant fossil record, cosmopolitan distribution and long-lifespans (>500 years in some cases (Butler *et al.*, 2011)) make them excellent for recording paleo-environmental conditions on yearly, seasonal, and potentially even daily timescales (Schöne and Gillikin, 2013; Warter *et al.*, 2018).

The outer surface of the bivalve shell is covered by an organic layer called the periostracum, which isolates the mineralization compartment, the extrapallial space, from the surrounding seawater, —although to what extent it is truly isolated from the environment is still being debated— and serves as a template for biomineralization (Cuif *et al.*, 2010a; Marin *et al.*, 2012; Suzuki and Nagasawa, 2013). Initial calcification occurs directly on the periostracum at the ventral margin within the extrapallial space, which is supersaturated with respect to calcium carbonate by the mineralizing organ, the mantle epithelium (Nakahara and Beve, 1971; Marin *et al.*, 2012; Suzuki and Nagasawa, 2013) (Fig. 1.6). The mantle is comprised of an inner epithelium that is in contact with the ambient seawater, and an outer epithelium that faces the shell, and is thought to be responsible for the transport of the inorganic ions necessary for calcification from ambient seawater to the site of calcification (Carre *et al.*, 2006; Marin *et al.*, 2012). There is some debate as to whether an amorphous phase first forms in vesicles within specialized cells that are then delivered to the site of calcification, which implies a lesser importance of the extrapallial fluid (Addadi *et al.*, 2006).

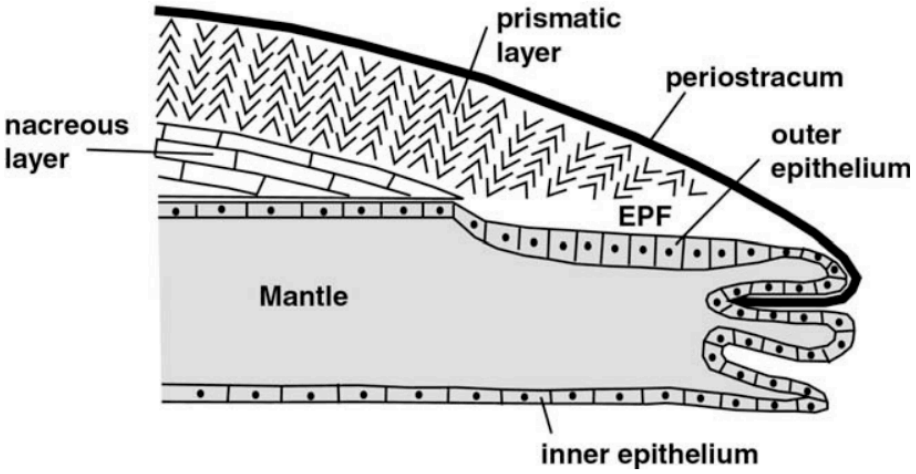

Figure 1.6 Schematic representation of a cross-section of a nacroprismatic bivalve shell. EPF- extrapallial fluid. Modified from Carre *et al.* (2006).

Together with the periostracum, the bivalve shell can be considered to be made up of three layers: the outer periostracum, a middle mineralized layer, and an inner mineralized layer, with the myostracum separating the two mineralized layers. Several microstructural architectures are possible for each mineral layer and include prismatic, nacreous, foliated, composite prismatic etc. (Kobayashi and Samata, 2006). The majority of these microstructural types are aragonitic, whereas calcite mostly occurs as prisms (columnar) or as folios (sheets) (Suzuki and Nagasawa, 2013; Harper and Checa, 2017). Nacroprismatic shell types have an outer calcitic layer and an inner nacreous layer. The outward facing calcitic layer provides protection against chemical or mechanical attacks from predators, while the highly fracture resistant nacreous layer confers the shell with high mechanical strength (Currey, 1989; Marin *et al.*, 2012; Gim *et al.*, 2019; Wan *et al.*, 2019). The calcitic prismatic microstructure consists of prisms with polygonal cross-sections elongated perpendicular to the shell surface, where prisms are separated from one another by interprismatic membranes 0.5–8 μm thick (Dauphin, 2003; Checa *et al.*, 2005, 2016; Cuif *et al.*, 2014; Dauphin *et al.*, 2019; Strag *et al.*, 2019) (Fig. 1.7). EBSD imaging has shown two possible crystallographic orientations of calcitic prisms: the genus Pinnidae, which includes *Atrina rigida* and *Pinna nobilis*, exhibit prisms with a single, uniform crystallographic orientation where the *c*-axis is parallel to the length of the prisms (Checa *et al.*, 2005; Reich *et al.*, 2019). In contrast, the

genus Pinctada produces calcite prisms that are subdivided into regions with different crystallographic orientations that generally have the c-axis perpendicular to prism length (Checa *et al.*, 2013; Dauphin *et al.*, 2019). Organic material in the prismatic layer, which includes both the interprismatic membranes as well as intracrystalline organic matter, is thought to consist primarily of proteins, polysaccharides, and lipids (Dauphin, 2003; Farre and Dauphin, 2009; Furuhashi *et al.*, 2009a; Suzuki and Nagasawa, 2013). The distribution of this organic matter is heterogenous, with proteins primarily found within the interprismatic membranes, and polysaccharides as intra-prismatic organic matter (Dauphin *et al.*, 2003a; Nudelman *et al.*, 2007; Huang *et al.*, 2021).

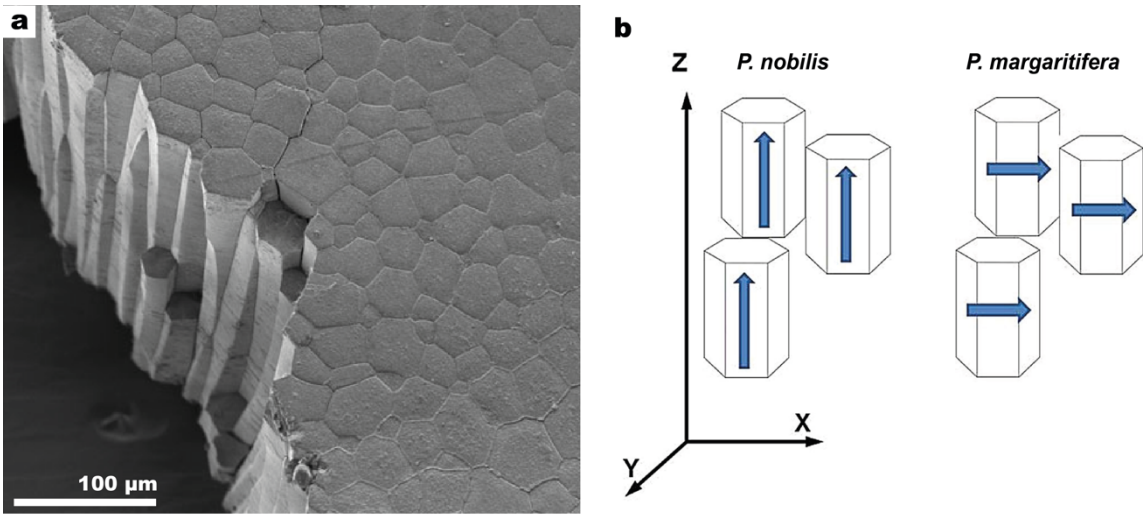

Figure 1.7 The calcitic prismatic microstructure in bivalve shells. (a) SEM image of the surface of the prismatic layer in *Atrina rigida*. Modified from Nudelman *et al.* (2007). (b) Schematic illustrations of the crystallographic orientation of *Pinna nobilis* and *Pinctada margaritifera* prisms. In *P. nobilis* the *c*-axis is parallel to prism length and in *P. margaritifera* it is perpendicular to prism length. Modified from Dauphin *et al.* (2019).

1.5 Diagenesis of biocalcites

The potential for diagenesis to affect the preservation of elemental or isotopic compositions within biogenic carbonates throughout geological time was recognized right at the beginning of paleoclimate research (Urey, 1948). Diagenesis of oceanic carbonates refers to all low temperature (<250 °C) and low pressure processes by which sediments are altered after deposition, i.e., preceding and potentially subsequent to thermal metamorphism (Flügel, 1982; Montañes and Crossey, 2018). Diagenesis can have highly variable effects on biocarbonates buried in oceanic sediments, depending on the time and length scales at which it proceeds, the sediment and pore water compositions, and the sediment accumulation rate (Delaney, 1983).

Although displaying vastly different hierarchical organizations of organic components at different length scales, at their most fundamental level, the majority of biocarbonates are composed of nanograins 10–150 nm in diameter (Cuif *et al.*, 2010a; Wolf *et al.*, 2016). This nanogranular organization coupled with the many inter- and intracrystalline organic-mineral interfaces offers enormous surface areas onto which diagenetic fluids can act and modify the original geochemistry of biocalcites, and thus affect their suitability for paleoclimate reconstruction(s) (Ross *et al.*, 1990; Casella *et al.*, 2017; Lange *et al.*, 2018; Pederson *et al.*, 2019; Forjanes *et al.*, 2022). The following two subsections address the process of diagenesis in foraminiferal tests and in the prismatic layer of bivalves, the two biocalcites to be investigated in this thesis.

1.5.1 Diagenesis in foraminifera

With few exceptions (Mccorkle *et al.*, 1995; Sexton and Wilson, 2009; Edgar *et al.*, 2013; Schneider *et al.*, 2017), most studies on diagenesis in foraminifera have focused on planktonic foraminifera. This is partly because benthic foraminifera, with their more heavily calcified tests formed at water temperatures close to their initial burial temperatures, were thought to be less susceptible to diagenetic overprinting (Edgar *et al.*, 2013). There are three mechanisms by which foraminifera tests are thought to be altered: partial dissolution, overgrowth, and recrystallization. These processes can, in principle, begin to act on the test of a dead foraminifera already within the water column and can continue on the seafloor and within seafloor sediments after burial (Pearson and Burgess, 2008; Edgar *et al.*, 2015).

A large body of literature records the impacts of partial dissolution on the isotopic and elemental ratios of planktonic foraminiferal tests (Lorens *et al.*, 1977; Mccorkle *et al.*, 1995; Rosenthal and Lohmann, 2002; Regenberg *et al.*, 2006; Fehrenbacher and Martin, 2014). Partial dissolution is thought to decrease bulk Mg/Ca ratios and increase oxygen isotopic ratios (due to the preferential loss of relatively Mg-rich and ^{18}O-poor primary calcite), such that their direct interpretation will subsequently yield colder past water temperature estimates (Lohmann, 1995; Lea *et al.*, 2000; Rosenthal *et al.*, 2000; Rosenthal and Lohmann, 2002). The effects of secondary calcite precipitation on foraminiferal bulk-chemistry is manyfold: it can cause strong shifts in δ^{13}C and δ^{18}O (Shieh *et al.*, 2002) and increase bulk Mg/Ca ratios significantly due to the precipitation of high-Mg calcite (Boussetta *et al.*, 2011). Both partial dissolution and secondary precipitation/overgrowth can be recognized by secondary electron microscopy (SEM) and — where more egregious — by optical microscopy: dissolution etches outer test walls (Edgar *et al.*, 2015) and overgrowths are recognized as larger, often equant-sized crystals (Pearson and Burgess, 2008; Kontakiotis *et al.*, 2016). SEM and optical microscopy can also often be used to identify recrystallization, which is the in-situ replacement of the original nanogranular wall structure by large blocky crystals. Recrystallization is driven by the energetic gains from replacing a high-surface area nanogranular texture by larger crystals (Pearson and Burgess, 2008) and can cause substantial alteration of test δ^{18}O values (Pearson *et al.*, 2001; Williams *et al.*, 2005; Sexton *et al.*, 2006b; Pearson and Burgess, 2008).

A ‘structural’ criterion for excluding foraminifera tests from chemical or isotopic analysis for paleo-environment reconstructions has recently found wide acceptance and application: the ‘frosty’ vs ‘glassy’ paradigm. The basic idea is that ‘glassy’ tests, i.e. those that appear transparent under the optical microscope, have undergone minimum alteration (Sexton *et al.*, 2006b) (Fig. 1.8). These tests are often retrieved from clay-rich settings where it is thought that the low porosity and permeability of these sediments ‘seals them off’, preventing the tests from interacting with surrounding pore waters (Pearson *et al.*, 2001; Wilson *et al.*, 2002). In contrast, ‘frosty’ tests, which are typically derived from pelagic settings, are considered extensively altered and therefore are not suitable for paleoceanographic reconstructions (Sexton *et al.*, 2006b). On a historical note, Urey and colleagues specifically cautioned that only translucent biocalcite samples should be used for reconstruction, and they can thus be considered the first implementers of the glassy *vs.* frosty sample screening criterion, which only came into systematic use half a century later (Urey *et al.*, 1951). Several studies have quantified the effects of diagenesis on the same species of foraminifera from different sites using ‘glassy’ foraminifera as the ground truth (Pearson and Burgess, 2008; Edgar *et al.*, 2013, 2015; Pearson *et al.*, 2015; Schneider *et al.*, 2017), with the assumption that ‘glassy’ foraminifera have not significantly changed their compositions post-burial. Such studies led to the resolution of the ‘cool-tropics’ paradox, according to which the $\delta^{18}O$ record of planktonic foraminifera indicated that tropical ocean surface temperatures during the late Cretaceous and Paleogene were well below present-day values, while low-latitude ocean surface temperatures approximated or exceeded present-day values (Zachos *et al.*, 1994; D’Hondt and Arthur, 1996). However, the results from exclusively glassy foraminifera showed mean tropical sea surface temperatures similar to modern day values (approximately 30 $^{\circ}$C) implying that diagenesis lowered temperature estimates by as much as 10 $^{\circ}$C (Pearson *et al.*, 2001, 2007; Wilson and Norris, 2001; Wilson *et al.*, 2002).

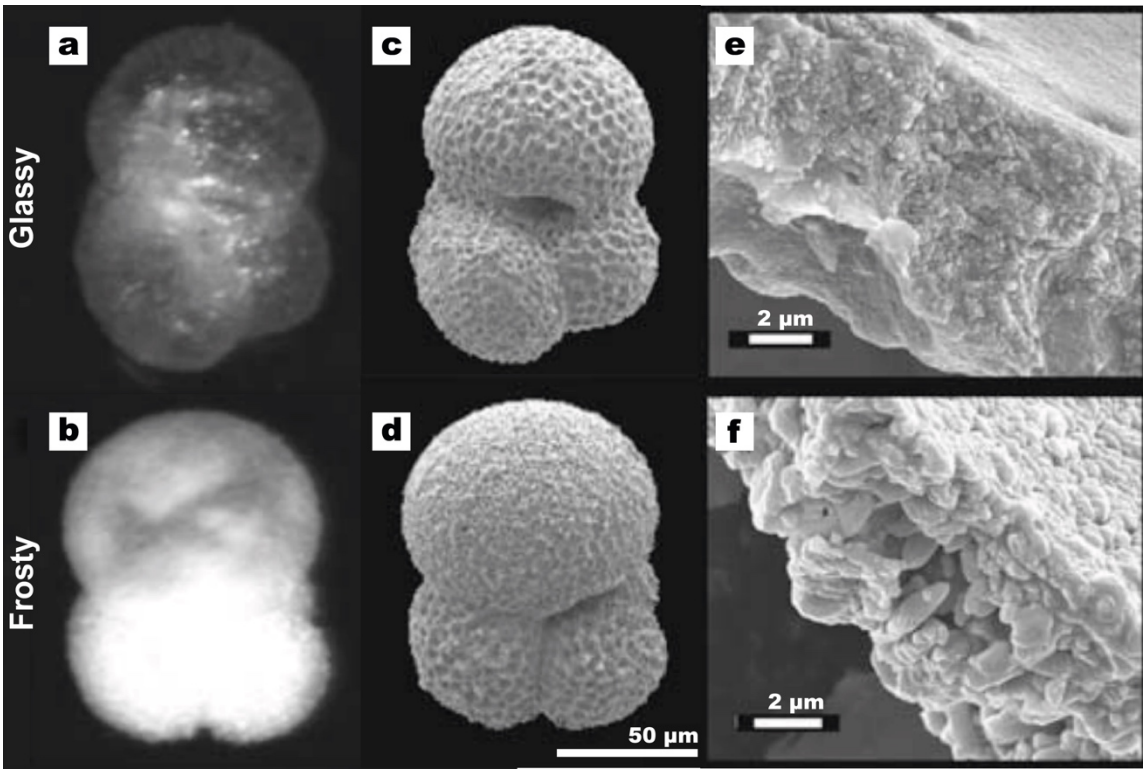

Figure 1.8 Comparison of the microstructures in glassy vs frosty planktonic *Subbotina linperta*. (a-b) Optical images. (c-f) SEM images. Modified from Pearson and Burgess *et al.* (2008).

A few studies have discussed the possibility of recrystallization without any apparent textural changes. Based on electron microprobe, SEM-EDAX, and X-ray diffraction studies of fossil miliolacean foraminifera, Towe and Hemleben (1976) identified an early stage of diagenesis, preceding later textural recrystallization, where Mg was lost from the test calcite *without a visible alteration of the original biogenic crystal habit*. Mitchell and colleagues (1997), based on stable isotopic compositions of variably diagenetically infilled foraminifera and ostracods, concluded that even ostracods that appear pristine when observed by optical/SEM microscopy, had relatively negative isotopic values, implying either the presence of hard-to-see cements, or recrystallization without physical expression. Gorski and Fantle (2017) discussed the phenomenon of minerals exchanging with an aqueous environment without textural changes, and defined the term "stable mineral recrystallization as *a reaction in which a ''stable mineral" extensively exchanges atoms*

with ions in solution under apparent chemical equilibrium conditions with no overt changes in mineral structure, morphology, or grain size.

A recent study by Bernard and colleagues (2017) demonstrated that dramatic changes in bulk isotopic composition of foraminifera tests are indeed possible without observable (by optical microscopy or SEM) morphological/structural changes. These workers subjected planktonic foraminifera tests to elevated temperatures and pressures (300 °C, 200 bar) for 3 months in autoclaves with artificial seawater produced from pure $H_2{}^{18}O$ and compositionally adjusted to be in chemical equilibrium with calcite at these experimental conditions. Subsequent high-resolution SEM and NanoSIMS imaging demonstrated that the calcitic tests exchanged up to 15 vol% of their oxygen with the seawater analogue, without any observable change to their ultrastructures. It was proposed that this exchange could have taken place either through fluid mediated interface-coupled dissolution-precipitation (Putnis, 2014; Ruiz-Agudo *et al.*, 2014) and/or by solid state grain boundary and volume diffusion (Anderson, 1969). Increased temperatures during burial mean that even with a constant porewater composition, isotopic disequilibrium between the tests of benthic foraminifera and surrounding porewaters creates a driving force for diffusion. Numerical modelling of this burial-induced isotopic re-equilibration indicated that diagenesis via diffusion — the slowest possible diagenetic process — can cause overestimations of ocean paleotemperatures on a timescale of about 10 My (Bernard *et al.*, 2017). Chanda and colleagues (2019) similarly found that the calcium isotope composition of foraminifera tests can be substantially reset without visible recrystallization. They used a ^{45}Ca radiotracer to explore stable mineral recrystallization in foraminifera within fluids near calcite saturation at low temperatures (25 $^{\circ}$C). The radiotracer was found to be incorporated into the calcite solids with minimal structural changes apart from some minor widening of pores. This indicated that while some net dissolution occurred, a concomitant precipitation-flux incorporated the tracer. These authors posited that intra-test heterogeneity, in the form of trace-element rich and trace-element poor regions, drove the stable mineral recrystallization of foraminiferal calcite. Together, these two studies call into question the widely accepted notion that 'glassy' foraminifera can be assumed to retain their original elemental and isotopic signatures after burial while hosted within pore fluids (Bernard *et al.*, 2017; Chanda *et al.*, 2019).

1.5.2 Diagenesis in bivalves

Since aragonitic skeletons are less resistant to diagenesis than their calcitic counterparts (Al-Aasm and Veizer, 1986), most studies on diagenesis in nacroprismatic bivalves have focused on the conversion of the aragonite layers into calcite (Hendry *et al.*, 1995; Casella *et al.*, 2017; Lange *et al.*, 2018; Pederson *et al.*, 2019; Forjanes *et al.*, 2022). Although diagenesis of the calcitic prismatic layer of bivalves has been less studied, it is well established that it is not impervious to the effects of diagenesis (Al-Aasm and Veizer, 1986; Woo *et al.*, 1993; Elorza and Garcia-Garcia, 1996; Elorza and Garcia-Garmilla, 1998; Gomez-Alday and Elorza, 2003). The recognition of marine or meteoric diagenetic overprints on initial elemental and isotopic compositions is thus essential for the successful use of bivalve shells as paleoproxies.

Simulated diagenesis experiments on bivalves have demonstrated that during the initial stages of diagenesis, the degradation of the organic interprismatic membranes and intraprismatic organic matter generates porosity within the bivalve shell and provides pathways for facilitated diagenetic fluid penetration (Ross *et al.*, 1990; Casella *et al.*, 2017; Lange *et al.*, 2018; Pederson *et al.*, 2019; Forjanes *et al.*, 2022). In the calcitic prismatic layer, these diagenetic fluids result in microstructural changes, such as the rounding or fusion of prisms, the appearance of etch pits or the precipitation of cement overgrowths on individual prisms (Al-Aasm and Veizer, 1986; Ross *et al.*, 1990; Gomez-Alday and Elorza, 2003), and the resetting of the original shell geochemistry (Casella *et al.*, 2017; Lange *et al.*, 2018; Pederson *et al.*, 2019; Forjanes *et al.*, 2022). However, in some shells there are no microstructural changes, and diagenesis is instead inferred from whole-shell geochemical changes (Elorza and Garcia-Garcia, 1996; Elorza and Garcia-Garmilla, 1998; Gomez-Alday and Elorza, 2003). As the degree of diagenesis increases, bivalve shell $\delta^{18}O$ values tend to decrease accompanied with decreased strontium and sodium concentrations, whereas manganese, silica and iron concentrations tend to increase, although these trends can vary depending on the diagenetic environment (Al-Aasm and Veizer, 1986; Steuber, 1999; Gomez-Alday and Elorza, 2003; de Winter and Claeys, 2016; de Winter *et al.*, 2020). As increased

manganese concentrations are linked to changes in luminescence, cathodoluminescence is used to screen for diagenesis (Elorza and Garcia-Garcia, 1996; Elorza and Garcia-Garmilla, 1998; Ivany and Runnegar, 2010; Briard *et al.*, 2020). The association of elevated manganese and depleted strontium concentrations with increased diagenesis have led to these elements being used as markers to evaluate whether samples have been diagenetically altered (Immenhauser *et al.*, 2005; Korte *et al.*, 2009; Ivany and Runnegar, 2010), although variations in the in vivo incorporation of these elements renders interpretations of the degree of diagenesis based on these elements ambiguous (Ullmann and Korte, 2015). de Winter therefore advocated for a multi-proxy approach for recognizing diagenesis based on a combination of the evaluation of Si, Ca, Mn, Fe and Sr concentrations, $\delta^{18}O$ values, and SEM observations of shell microstructures at the site of analysis (de Winter *et al.*, 2020).

1.6 Motivation and aims of the thesis

To accurately apply the oxygen isotope paleothermometer, the effects of post-burial modification on the oxygen isotope composition of fossil material must be understood and quantified. At their most fundamental level, most of the shells of marine organisms used for paleoclimatic reconstructions are composed of sub-spherical calcite domains 10–150 nm in diameter surrounded by an envelope of organic matter (Cuif *et al.*, 2010a; Wolf *et al.*, 2016). Upon the death of the organism and subsequent burial, their fossilized remains continue to be in contact with sediment porewaters for millions of years. Bernard and colleagues (2017) established that the small sizes of these calcite domains means that on a timescale of >10 My, the effects of solid-state grain boundary and volume diffusion can significantly alter the original oxygen isotope composition of these shells and hence significantly bias paleoclimatic reconstructions based on oxygen isotope compositions. In this context, to improve our understanding of the effects of diagenetic isotope exchange on biocalcites, this thesis aims to:

1. Establish how ambient porewaters penetrate into and isotopically exchange with biocalcites.
2. Determine whether different species of biocalcites experience diagenetic isotope exchange equally or if there are species-specific or taxon-specific differences in diagenetic susceptibility.
3. Determine whether fossil shells remain susceptible to diagenesis after the degradation of shell organic matter.
4. Identify the organic components most relevant to diagenetic isotope exchange in biocalcites.

1.7 Approach and organization of the thesis

The experimental methodology of this thesis follows a similar experimental protocol to that of Bernard and colleagues (2017), who demonstrated that the incubation of shell material with artificial seawaters highly enriched in ^{18}O in combination with NanoSIMS isotopic imaging can be used to visualize how porewaters interact with shell calcite. In this thesis, the calcitic tests of three species of modern benthic foraminifera and one species of fossil foraminifera, and the calcitic prismatic layer of two species of bivalve mollusks were incubated with ^{18}O-labeled artificial

seawaters at 90 °C for 6 days, at chemical equilibrium with calcite. The resulting distribution of ^{18}O-exchange was visualized and quantified with a NanoSIMS ion microprobe. This was combined with bulk isotope measurements and a variety of micro- and nano-analytical techniques to correlate the diagenetic isotope exchange with chemical and structural heterogeneities within the shells. The Chapters of this thesis are thus summarized as follows:

Chapter 2 identifies the ultrastructural pathways through which diagenetic fluids permeate the tests of three benthic foraminifera, *Ammonia confertitesta*, *Haynesina germanica* and *Amphistegina lessonii* as a result of incubation in an ^{18}O-enriched sea water analogue, in combination with NanoSIMS imaging and scanning and transmission electron microscopy (SEM and TEM).

Chapter 3 utilizes the same methods as in chapter 2 in combination with electron backscatter diffraction (EBSD), atomic force microscopy (AFM), and cathodoluminescence (CL) imaging to compare the ultrastructures, crystallography and extent of diagenetic O-isotope exchange between modern *Ammonia confertitesta* and a fossil equivalent, *Ammonia beccarii*.

Chapter 4 uses a combination of NanoSIMS imaging, SEM, EBSD, and a new-frontier technique Photo-induced Force Microscopy (PiFM) to examine the identity and investigate the distribution of organic matter in the calcitic prismatic layer of modern bivalve *Pinctada margaritifera.*

Chapter 5 builds on the results of chapter 4 and compares the distribution of organic components and diagenetic isotope exchange between the calcitic prismatic layer of modern bivalves *Pinctada margaritifera* and *Pinna nobilis* to identify the organic biomacromolecules most relevant to diagenesis in bivalves.

Chapter 6 presents the overall conclusions an outlook.

2 *Fast and pervasive diagenetic isotope exchange in foraminifera tests is species-dependent*

Deyanira Cisneros-Lazaro[1*], Arthur Adams[1], Jinming Guo[1], Sylvain Bernard[2], Lukas P. Baumgartner[3], Damien Daval[4], Alain Baronnet[5], Olivier Grauby[5], Torsten Vennemann[6], Jarosław Stolarski[7], Stéphane Escrig[1], Anders Meibom[1,3*]

[1] Laboratory for Biological Geochemistry, School of Architecture, Civil and Environmental engineering, Ecole Polytechnique Fédérale de Lausanne (EPFL), Lausanne, CH-1015 Switzerland

[2] Museum National d'Histoire Naturelle, Sorbonne Université, CNRS UMR 7590, IMPMC, 75005 Paris, France

[3] Center for Advanced Surface Analysis, Institute of Earth Science, University of Lausanne, CH-1015 Lausanne, Switzerland

[4] ISTerre, Univ. Grenoble Alpes, Univ. Savoie Mont Blanc, CNRS, IRD, IFSTTAR, 38041, Grenoble, France

[5] CNRS, CINaM, Aix-Marseille Université, 13009 Marseille, France

[6] Institute of Earth Surface Dynamics, University of Lausanne, CH-1015 Lausanne, Switzerland

[7] Institute of Paleobiology, Polish Academy of Sciences, PL-00-818 Warsaw, Poland

This chapter has been published in Nature Communications as:

Cisneros-Lazaro, D., Adams, A., Guo, J., Bernard, S., Baumgartner, L.P., Daval, D., Baronnet, A., Grauby, O., Vennemann, T., Stolarski, J. and Escrig, S., 2022. Fast and pervasive diagenetic isotope exchange in foraminifera tests is species-dependent. Nature Communications, **13**(1), p.113.https://doi.org/10.1038/s41467-021-27782-8

Author contribution statement

DC-L, AA, JG, SB, LPB, DD, JS and AM designed the experimental study; AA performed the isotope exchange experiments; AA and TV acquired the bulk enrichment data; DC-L and AA acquired the SEM images; JG, AB and OG acquired TEM data; DC-L and SE acquired NanoSIMS data; DC-L, AA and AM drafted the manuscript. All co-authors contributed to the writing of the manuscript.

Abstract

Oxygen isotope compositions of fossil foraminifera tests are commonly used proxies for ocean paleotemperatures, with reconstructions spanning the last 112 million years. However, the isotopic composition of these calcitic tests can be substantially altered during diagenesis without discernible textural changes. Here, we investigate fluid-mediated isotopic exchange in pristine tests of three modern benthic foraminifera species (*Ammonia sp*., *Haynesina germanica*, and *Amphistegina lessonii*) following immersion into an ^{18}O-enriched artificial seawater at 90 °C for hours to days. Reacted tests remain texturally pristine but their bulk oxygen isotope compositions reveal rapid and species-dependent isotopic exchange with the water. NanoSIMS imaging reveals the 3-dimensional intra-test distributions of ^{18}O-enrichment that correlates with test ultra-structure and associated organic matter. Image analysis is used to quantify species level differences in test ultrastructure, which explains the observed species-dependent rates of isotopic exchange. Consequently, even tests considered texturally pristine for paleo-climatic reconstruction purposes may have experienced substantial isotopic exchange; critical paleo-temperature record re-examination is warranted.

2.1 Introduction

Biogenic calcite chemical and isotopic compositions offer scientists a broad range of proxies for past environmental conditions (Katz *et al.*, 2010). Arguably the most important among these proxies is the oxygen isotope composition, which was developed as a paleothermometer by Urey and colleagues more than six decades ago (Urey, 1948; McCrea, 1950; Epstein *et al.*, 1951; Urey *et al.*, 1951). Since then, the oxygen isotopic composition of carbonate has been systematically used to reconstruct past ocean temperatures. In particular, the oxygen isotope composition of fossil calcitic tests of benthic foraminifera has produced a reconstruction of the paleotemperature of the deep ocean with high temporal resolution as far back as 112 My (Friedrich *et al.*, 2012).

The oxygen isotopic composition of biogenic carbonate reflects both the oxygen isotope composition and the temperature of the seawater in which the biomineralizing organisms live, as well as the biological mechanisms involved in their biomineralization process (so-called vital effects) (Urey *et al.*, 1951; Shackleton, 1967; Meibom *et al.*, 2006; Allison *et al.*, 2010; Pearson, 2012). The use of the oxygen isotope paleothermometer relies on the widely accepted paradigm that fossil foraminifera tests collected from ocean sediments have retained their original elemental and isotopic compositions; at least those tests that appear pristine when observed with optical microscopy or scanning electron microscopy (SEM) (Pearson *et al.*, 2001; Wilson *et al.*, 2002; Sexton *et al.*, 2006b; Edgar *et al.*, 2013, 2015; Schneider *et al.*, 2017). However, from the moment a marine organism dies, diagenetic processes may begin to alter the original isotopic and chemical composition of its biocarbonate remains (Pearson and Burgess, 2008) and might thus introduce bias in subsequent paleo-environmental reconstructions.

Calcium carbonate skeletons, shells, and tests formed by marine animals have a nanocomposite organo-mineral structure (Cuif *et al.*, 2010b). The tests of planktonic and benthic foraminifera — the latter being the focus of this study — are made up of irregular (sub-spherical) nanocrystallites of calcite 10–100 nm in diameter (Debenay *et al.*, 2000; Cuif *et al.*, 2010b; Dubicka *et al.*, 2018). Furthermore, these tests are compositionally heterogenous at the mesoscale, incorporating elements such as Mg, Na, P, and S (Erez, 2003; Geerken *et al.*, 2019; van Dijk *et al.*, 2019). The banded distributions of these elements reflect, to different degrees, the presence and distribution of organic matter within the test wall (Nagai *et al.*, 2018a, 2018b; Geerken *et al.*, 2019; Glock *et al.*, 2019).

This ultrastructure creates a very large internal surface on which elemental and isotopic exchange with sediment porewater can take place, provided that this water can penetrate deep enough into the structure, which seems to be the case according to several recent studies (Bernard *et al.*, 2017; Chanda *et al.*, 2019).

Bernard *et al.* (2017) subjected planktonic foraminifera tests to elevated temperature and pressure (300 °C, 200 bar) in pure $H_2{}^{18}O$ artificial seawater at chemical equilibrium with calcite and demonstrated that, within months, the tests had exchanged up to 15 vol% of their ^{18}O with the seawater analogue without observable (by SEM) changes to test ultrastructure and morphology. Assuming solid state diffusion as the dominant process, these authors showed that substantial bulk oxygen isotopic exchange of a fossil foraminifera tests can take place on a timescale of 10 My under ambient conditions in ocean sediments, resulting in paleotemperature overestimations and explaining the unrealistically flat inferred temperature gradients in the paleo-ocean as a result of diagenetic bias.

Rapid isotopic exchange between carbonate and an aqueous phase has subsequently been experimentally confirmed for a series of carbonate minerals at much lower temperature (down to room temperature), on time scales never exceeding a few months. Chanda *et al.* (2019) used ^{45}Ca as a radiotracer to investigate recrystallization of planktonic foraminifera tests in seawater analogues in equilibrium with calcite at 25 °C. The radiotracer was incorporated into the biocalcite within days with minimal structural change and it was concluded that intra-test chemical heterogeneities played a key role in the recrystallization of these tests. Other experiments with micrometer-sized abiotic carbonates – including calcite – in chemical equilibrium with surrounding fluids have demonstrated that isotopic exchange can proceed at room temperature even in the absence of chemical heterogeneities (Mavromatis *et al.*, 2015; Oelkers *et al.*, 2018, 2019; Géhin *et al.*, 2021).

In this study, we expose three species of foraminifera to precisely controlled experimental conditions simulating diagenesis to evaluate how biogenic calcites interact with surrounding fluids. A combination of NanoSIMS imaging and scanning- and transmission electron microscopy (SEM and TEM) investigations permits to visualize and quantify isotope exchange inside the experimentally fossilized calcitic tests while documenting relevant ultrastructural features. We

show that isotopic exchange rates vary consistently across the three species studied, and we relate this to species-specific differences in ultrastructure. Together, these observations provide insight into the processes that drive isotopic exchange in fossil foraminifera tests and, by analogy, other fossil biocalcites.

2.2 Methods

Three species of foraminifera, *Ammonia sp.*, *A. lessonii* and *H. germanica,* were used in the autoclave experiments. *Ammonia sp.* and *H. germanica* were collected from recent sediment on tidal mudflats in the Bay of Bourgneuf, France. Two morphological features visible on the surfaces of tests, suture elevation and average pore diameter, were used to identify *Ammonia sp.* tests as phylotypes T1 and T6 as per the classification in Richirt *et al.* (2019). *A. lessonii* were picked at depths of 15–45 m from the Gulf of Aqaba in Eilat, Israel.

2.2.1 Test cleaning and oxygen isotope exchange experiments

Before the experiments, foraminifera tests were cleaned following the standard methanol and oxidative cleaning procedures from Barker *et al.* (2003): clays adhered to foraminifera tests were removed through ultrasonication in methanol and deionized (MilliQ) water. Organic matter was removed by placing foraminifera tests in an alkali buffered 1% H_2O_2 solution in a boiling water bath for 20 minutes, followed by several rinses with deionized water and finally technical grade ethanol before overnight desiccation at 50 °C. Subsequently the three species of foraminifera and mm-sized cleaved single crystals of untreated Iceland spar were individually placed within flame-sealed glass ampules or welded gold capsules, hereby collectively referred to as autoclaves, along with ~100 µL of a seawater analogue ($\Omega_{calcite}$ = 1; 0.6 M NaCl, 0.05 M $MgCl_2$). The seawater analogue was enriched in ^{18}O to a $^{18}O/^{16}O$ ratio of about 0.30. Each autoclave was placed in an oven at 90 °C for 4 hours or 6 days. Upon removal from the autoclaves, foraminifera and Iceland spar were rinsed in artificial seawater, distilled and deionized water, and technical grade ethanol and desiccated at 50 °C overnight, followed by 24 hours of vacuum desiccation.

For bulk foraminifera analysis, 10–15 aliquots of 70 µg of dried and desiccated foraminifera per species (about 7–10 foraminifera) were analyzed using a GasBench linked to a Finnigan Delta V

(Thermo Fisher Scientific) mass spectrometer at the University of Lausanne according to a method adapted after Spötl and Vennemann (2003). Measured isotope ratios of desiccated foraminifera tests were identical to those of tests where the desiccation steps have been omitted, indicating that the measured isotope ratios are not influenced by any absorbed ^{18}O-enriched water. Isotope ratios were normalized to the VSMOW scale using a Carrara marble in-house standard calibrated against NBS-19. Oxygen isotopic compositions are reported in per mil Vienna Standard Mean Ocean Water (VSMOW).

2.2.2 NanoSIMS preparation and imaging

For NanoSIMS analyses, the dried and vacuum desiccated samples were embedded in resin (EpoThin2, Struers) in aluminum rings. The resin was vacuum pumped to remove air bubbles and allowed to harden overnight. Sample surfaces were then polished using increasingly finer grained diamond paste (from 15 to 0.25 µm) producing a smooth cross section of the chamber walls. The polished samples were coated with ca. 15 nm Au and the surface imaged with backscattered electrons using a Zeiss Gemini 500 SEM (University of Lausanne, UNIL) operating at an acceleration voltage of 20 kV and a working distance of 10–17 mm. NanoSIMS imaging of the resulting distribution of ^{18}O-enrichment in the tests was carried out with a 16 keV Cs^+ primary ion beam focused to a spot-size of about 120 nm (ca. 0.7 pA on the sample surface). Positive charge build-up on the surface was compensated by the use of an electron gun. The multi-collector system simultaneously counted the following ions in individual electron-multiplier detectors with a mass resolving power of ~9000 (Cameca definition): $^{16}O^-$, $^{18}O^-$, $^{28}Si^-$, $^{31}P^-$, $^{32}S^-$, $^{16}O^{24}Mg^-$, and $^{16}O^{40}Ca^-$. Areas of 25×25 µm or 30×30 µm were imaged with a raster of 256×256 pixels and a dwell-time of 5 milliseconds per pixel. Up to 25 sequential images were produced for each area and were accumulated and drift corrected using L'IMAGE (developed by Dr. Larry Nittler, Carnegie Institution of Washington, USA). A threshold was applied to the images using the $^{16}O^{40}Ca^-$ counts, to only select for the calcitic test surface. $^{28}Si^-$ counts were used to eliminate rare clay particles adhering to the outer test surface. Oxygen isotope compositions were reported as $\delta^{18}O$ (in parts-per-thousand) relative to tests of pristine *Ammonia sp., A. lessonii, H. germanica*, or Iceland spar calcite that were not exposed to the experimental solutions:

$$\delta^{18}O = \left\{\left[\left(^{18}O/^{16}O\right)_{\text{sample}} - \left(^{18}O/^{16}O\right)_{\text{standard}}\right]/\left(^{18}O/^{16}O\right)_{\text{standard}}\right\} \times 1000 \qquad (1)$$

2.2.3 TEM preparation and imaging

For the TEM analyses of *Ammonia* sp., test surfaces were precoated with a 10-nm thick layer of carbon (for improved conduction and protection of the sample surface). Subsequent extraction and milling of lamellae that were parallel to the test surface were performed with a dual-beam Gemini NVision 40 Focused Ion Beam machine. The initial thick sections were milled with 30 kV Ga ions at 6.5 nA and then thinned down using progressively lower currents until reaching a minimum of 80 pA, with the final smoothing of the lamellae utilizing 5 kV Ga ions at 80 pA. Bright-field images were recorded using a Thermo Fisher Tecnai Osiris machine operated at 200 kV accelerating voltage, with dark contrasts showing areas with strongly diffracting incident electrons.

2.2.4 Calculating cogwheel interface densities and diagenesis resistance ratios

Cogwheel interface densities were calculated using the ImageJ macro from van Dijk *et al.* (2020). Secondary electron SEM images at 5000× magnification were taken of the outer surface of the second to last chamber of tests from all three species studied here. The raw SEM images were imported into ImageJ and the images cropped such that only areas in sharp focus were selected. Gray value thresholding was used to individually select pore spaces and cogwheel interfaces. The net surface area is the total surface area imaged minus the area of the pores. The total cogwheel interface length is the total length of all cogwheel interfaces excluding pore-calcite interfaces and pixels along the image frame. The cogwheel interface density is calculated as the ratio of the total cogwheel interface length to the net test surface area (i.e., in μm per μm^2). Supplementary Fig. 2.11 provides an overview of this process.

The diagenesis resistance ratio was calculated using a modified version of the ImageJ macro from van Dijk *et al.* (2020) (Supplementary Software). Foraminifera tests were embedded in epoxy and polished down to the widest cross section of the test (using diamond polishing pastes with a final grain size of 0.25 μm) and imaged using backscattered electrons (BSE) SEM. Gray value thresholding was used to select the test area to create a binary image. The paintbrush tool was used to remove extraneous pixels and to fill in fractured and broken parts of the test. The diagenesis resistance ratio is the ratio of the cross-sectional test surface area to the number of chambers, which is equal to the number of organic linings.

2.3 Results

2.3.1 Oxygen isotope exchange experiments

Initially pristine tests of three species of recently collected modern benthic foraminifera, *Ammonia sp.*, *H. germanica*, and *A. lessonii*, as well as abiotic Iceland spar calcite crystals, were incubated for 6 days in a highly ^{18}O-enriched ($^{18}O/^{16}O = 0.30$) seawater analogue in chemical equilibrium with calcite at 90 °C; additional experiments lasting only 4 hours were conducted on *Ammonia sp.* and *A. lessonii* tests under the same conditions. Before these experiments, the tests were treated with a standard methanol and oxidative cleaning procedure, which removes the organic cell materials (mostly proteins and polysaccharides) as well as a large fraction of inter-crystalline organic materials (Sykes *et al.*, 1995). This procedure mimics the natural fossilization process, in which the majority of organic material is rapidly degraded upon death of the organism (Sykes *et al.*, 1995; Bernard and Papineau, 2014; Malinverno and Martinez, 2015; Alleon *et al.*, 2017; Wheeler *et al.*, 2021). Bulk measurements of the O-isotope composition (i.e., the $^{18}O/^{16}O$ ratio) of experimentally fossilized tests were performed to precisely quantify isotopic exchange.

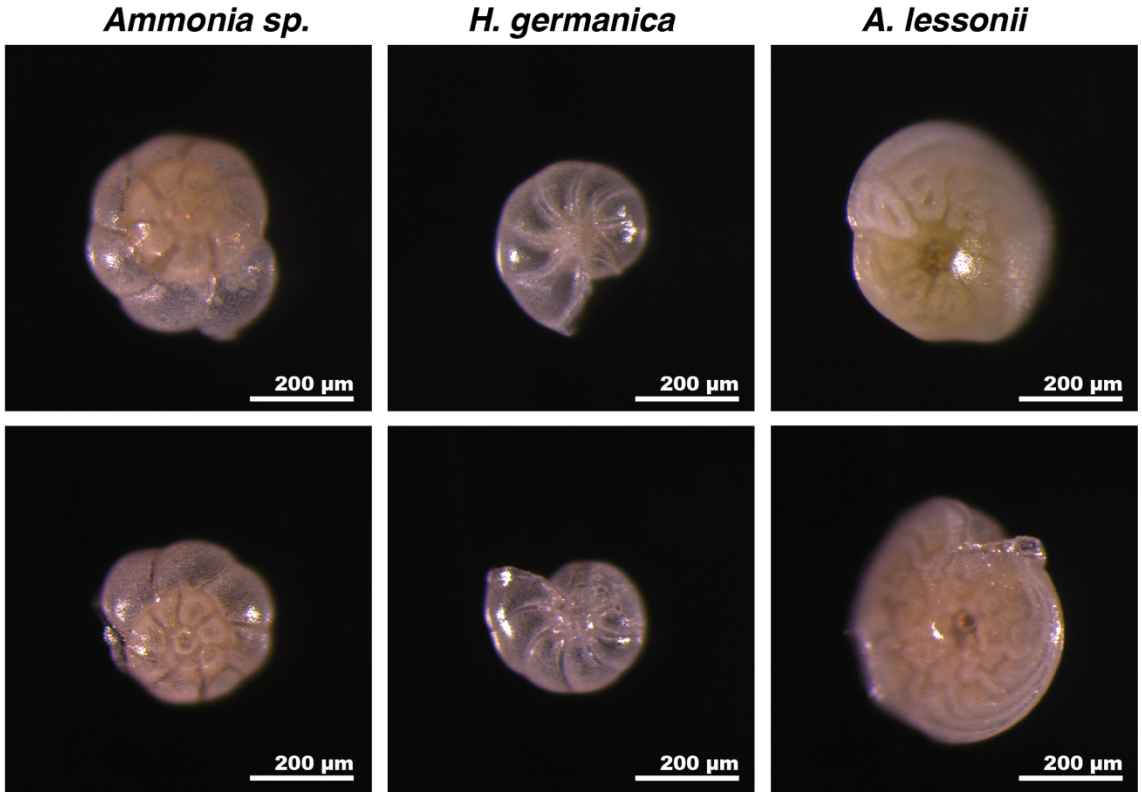

Figure 2.1 Appearance of tests before and after incubation. Stereo microscopy images of *Ammonia* sp., *H. germanica, and A. lessonii* tests before (top row) and after (bottom row) incubation for 6 days at 90 °C in in artificial seawater (ASW) with a $^{18}O/^{16}O$ ratio of 0.30. All images were taken at the same scale, under identical illumination conditions, and using the same microscope and camera.

2.3.2 Ultrastructure of the starting materials

The spiraled, multi-chambered, calcitic tests of the pristine benthic species used in this study are similar to the tests of benthic foraminifera species most frequently used for paleo-environmental reconstructions. In their natural pristine state, they are semi-transparent (i.e., hyaline or glassy) and perforated by pores (hence the name foraminifera, which in Latin means hole bearer, Figs. 2.1 and 2.2d, f, g, h). At the formation of each new test chamber, a calcitic layer is formed on top of pre-existing chambers, separated by a layer of organic matter; the so-called organic linings (Erez, 2003; Nehrke *et al.*, 2013; de Nooijer *et al.*, 2014b; Nagai *et al.*, 2018b, 2018a; Geerken *et al.*, 2019).

This creates a test wall consisting of calcite-dominated layers separated by relatively thin (100–300 nm) sheets of organic linings oriented parallel to the wall surface (Spero, 1988; Branson *et al.*, 2016; Geerken *et al.*, 2019); these organic linings and the calcite layers they separate are clearly seen in fractured test walls (Fig. 2.2b). The test wall is further divided into domains that resemble interlocking cogwheels when observed on the outer wall surface, or in the interior of the wall in sections cut parallel to the wall surface (Towe and Cifelli, 1967; van Dijk *et al.*, 2020) (Fig. 2.2d–i). The cogwheel-like domains are 3-dimensional structures that extend throughout the thickness of the wall (Fig. 2.2c). Each of these cogwheel-like structures consists of 10–100 nm sub-spherical calcite-dominated particles sharing a common crystal-orientation, which makes each cogwheel domain appear as a single crystal in bright-field TEM images (Fig. 2.2e, i). The interfaces between individual cogwheel structures, which are also enriched in organic matter (Cuif *et al.*, 2010a), are readily imaged with SEM (Fig. 2.2d, f, h, g). Therefore, in addition to the organic linings, the test wall also contains organic-rich interfaces separating individual cogwheel domains, albeit with the latter oriented perpendicular to the surface of the test wall; i.e., parallel to the local pore axis (Fig. 2.2c). These key features are illustrated schematically in Fig. 2.2a. Importantly, the size and organization of cogwheel structures, as well as the density and tortuosity of their interfaces, vary from one species of foraminifera to another, as Fig. 2.2 illustrates. Finally, at the nanoscale, the 10–100 nm sub-spherical calcite dominated particles (Supplementary Fig. 2.1) have been shown through atomic force microscopy (AFM) to be separated by organic-rich grain boundaries (Cuif *et al.*, 2010b). Due to the cleaning procedures (cf. Methods) a large fraction of these organic materials was broken down and partly removed before exposure to the experimental fossilization conditions.

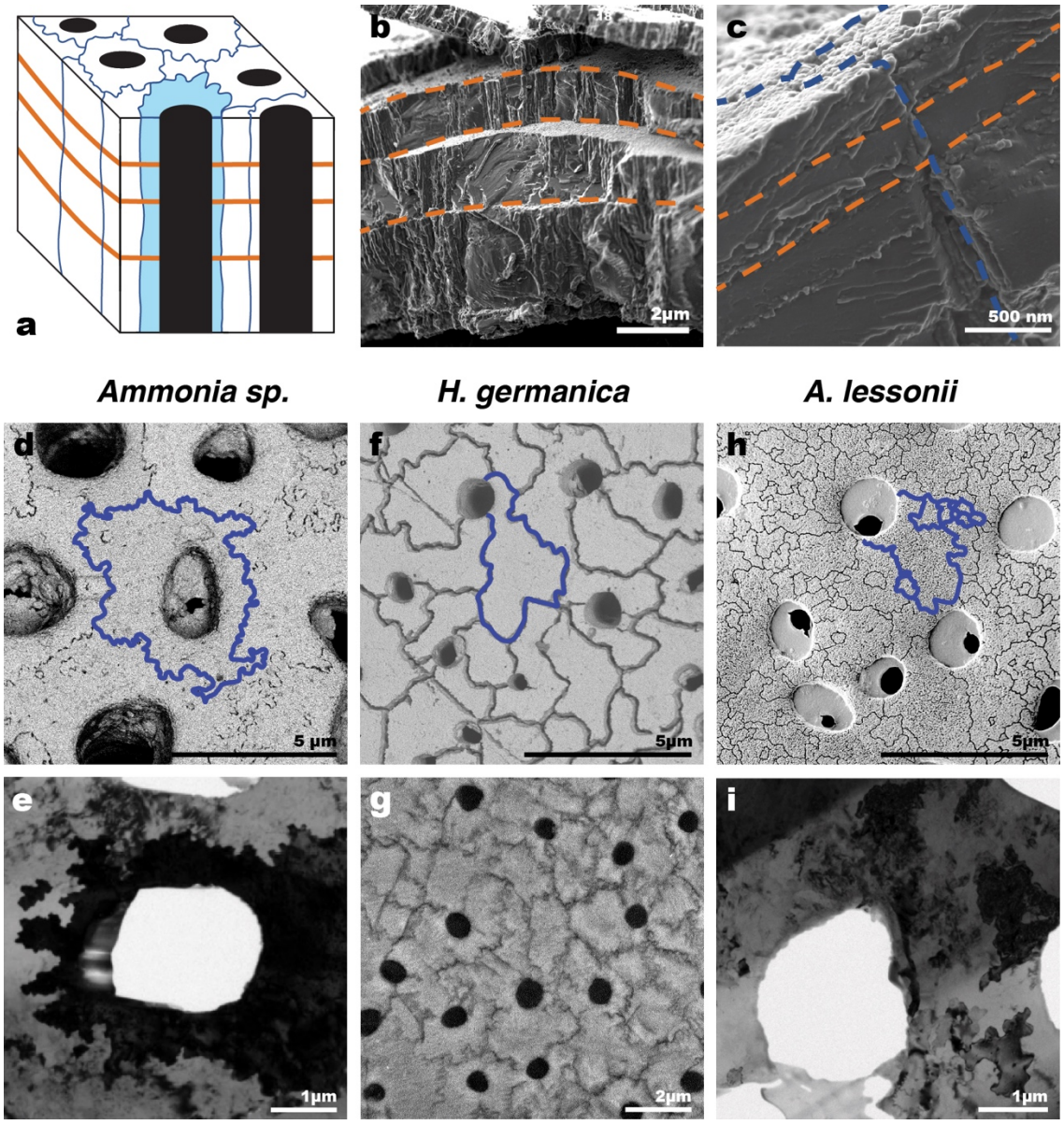

Figure 2.2 Ultrastructural organization. Organic linings and cogwheel structures in *Ammonia* sp.*, H. germanica and A. lessonii.* (a) Schematic diagram showing the spatial location of cogwheel structures and organic linings on the surface and inside benthic foraminifera test walls. Cogwheel interfaces are outlined in blue, a single cogwheel structure is shaded in light blue, pore-spaces are black, and organic linings are marked by orange lines. (b) SEM image of the edge of a broken *Ammonia* sp. test wall. The step-like fractures running parallel to the test surface (highlighted in orange hatched lines) correspond to the organic

linings. (c) SEM image of the surface and interior of an *Ammonia* sp. test wall showing a cogwheel interface (outlined with dashed blue lines) extending throughout the thickness of the wall, perpendicularly to the organic linings (dashed orange lines). (d) SEM image of cogwheels on the surface of an *Ammonia* sp. test. (e) Bright field (BF) TEM image centred on a single cogwheel in a FIB thin-section obtained from the interior of an *Ammonia* sp. test wall (cut parallel to the wall surface). The dark cogwheel in the center has a slightly different crystallographic orientation relative to surrounding cogwheels (light grey). (f) SEM image of the surface of *H. germanica* showing large, irregularly-shaped cogwheels. (g) SEM image of a lightly EDTA etched section from the interior of a *H. germanica* test, which is parallel to the wall surface, demonstrating that cogwheel structures are continuous throughout the test walls. (h) SEM image of the surface of a lightly EDTA etched *A. lessonii* test exhibiting cogwheels with variable surface areas. (i) BF TEM image of a FIB thin section obtained from the interior of an *A. lessonii* test wall (cut parallel to the test surface). The small cogwheels have jig-saw like interfaces between them.

2.3.3 Ultrastructure of the experimentally incubated materials

The first and fundamentally important observation from the 6-days-long experiments at 90 °C was that it was practically impossible to distinguish between pristine tests (i.e., the starting materials) and tests having been exposed to diagenetic conditions (i.e., the experimentally incubated materials) (Fig. 2.1, Supplementary Figs. 2.1–2.7). Both the pristine and experimentally incubated tests appeared translucent and glassy, with chamber divisions and pores easily recognizable using transmitted light and a stereo microscope. Even at the level of SEM imaging, it is not possible to distinguish between uncleaned foraminifera tests and tests that were exposed to the experimental solution (Supplementary Figs. 2.1, 2.5–2.7).

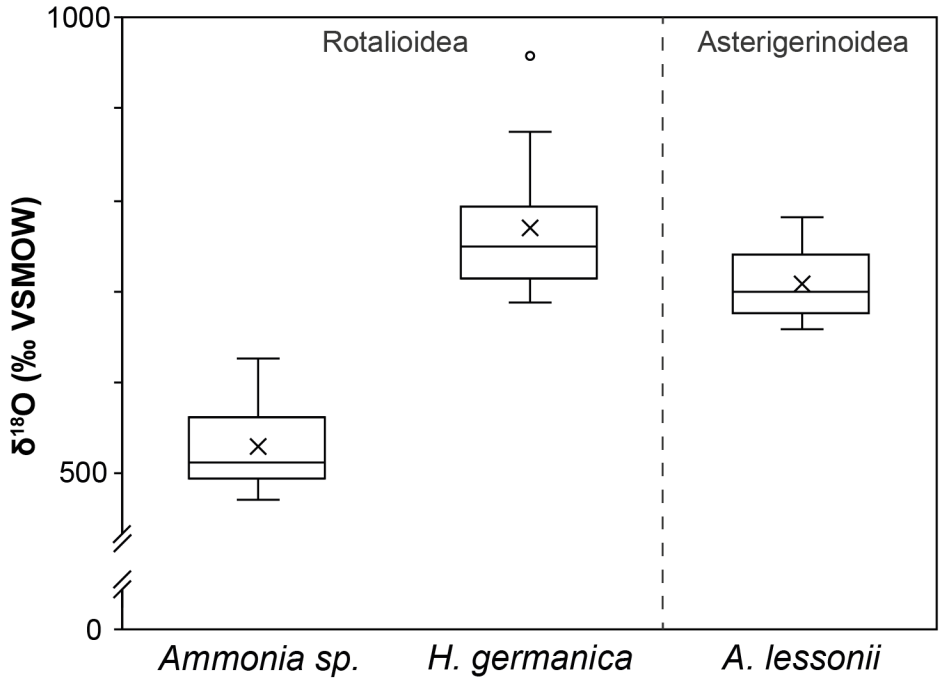

Figure 2.3 Bulk ^{18}O-enrichment after incubation. Box plot distributions of bulk ^{18}O-enrichment in tests of the three benthic foraminifera species incubated for 6 days at 90 °C in seawater analogue with a $^{18}O/^{16}O$ ratio of 0.30. The average ^{18}O-enrichments are shown with crosses. The superfamily that the foraminifera species belong to are indicated at the top of the figure. Middle lines = medians, boxes = interquartile ranges, whiskers = minimum and maximum values, empty circle = outlier.

2.3.4 Species-specific bulk ^{18}O-enrichments

Bulk oxygen isotope measurements were made on calcite tests that have been exposed to the experimental solution for 6 days, with each batch containing 70–100 µg of foraminifera. The bulk ^{18}O-enrichment reported in parts-per-thousand relative to VSMOW ± 1 standard deviation (SD) 529 ± 49 ‰ (n = 10) for *Ammonia* sp., 769 ± 80 ‰ (n = 10) for *H. germanica*, and 709 ± 36 ‰ (n = 12) for *A. lessonii* (Fig. 2.3, Supplementary Table 2.1). To determine whether the bulk ^{18}O-enrichments per species were significantly different ($p < 0.05$) from one another, unpaired two-tailed t-tests were made after testing for variance with F-tests. *Ammonia* sp. bulk ^{18}O-enrichments were significantly different, $p = 9 \times 10^{-9}$ and $p = 5 \times 10^{-7}$, between *H. germanica* and *A. lessonii*

respectively, but those between *H. germanica* and *A. lessonii* ($p = 0.06$) were not. Overall, these results demonstrate that substantial O-isotopic exchange occurred between the seawater analogue and the calcitic tests during the experiments and that the degree of isotopic exchange is species-specific. Note that organic compounds remaining within the tests should not significantly contribute to these measured values (Wacker *et al.*, 2016; Löffler *et al.*, 2019).

2.3.5 NanoSIMS imaging of ^{18}O-enrichments

The $^{18}O/^{16}O$ ratio variations in the tests exposed to the experimental solutions for 6 days were imaged with a NanoSIMS ion microprobe (Hoppe *et al.*, 2013), on surfaces both perpendicular and parallel to the local axis of pores, revealing localized ^{18}O-enrichments that explain the bulk measurements. Note that the ^{18}O-enrichments measured with the NanoSIMS are reported in parts-per-thousand relative to a foraminifera test with natural isotopic composition and that the measured $^{18}O/^{16}O$ ratios are completely dominated by secondary ions of O^- derived from calcite. The secondary ion yield of O^- differs for calcite and organics, but neither in NanoSIMS images nor in line-scans were changes in the $^{16}O^-$ count rate across the test observed to correlate with regions enriched in P, which point to remains of organic linings (Geerken *et al.*, 2019). In *Ammonia* sp., surfaces parallel to the pore axis (i.e., perpendicular to the test surface) show thin (~0.3 µm) bands of ^{18}O-enrichment that followed the curvature of the test wall (Fig. 2.4a). These ^{18}O-enriched bands correlated systematically with P-enrichments (Fig. 2.4a, d) indicating remains of organic linings that had withstood the oxidative cleaning procedure (Geerken *et al.*, 2019). Consistently, the number of ^{18}O-enrichment bands correspond to the number of organic linings expected from the specific location of the section within the test and the total number of chambers (Supplementary Fig. 2.8). All three investigated species thus had qualitatively similar correlation between P-enrichments and ^{18}O-enrichment bands (Fig. 2.4). However, it is noted that within most imaged *Ammonia* sp. tests ($n = 18$) there was one additional band of ^{18}O-enrichment close to the inner edge of the shell not associated with a band of P-enrichment (Fig. 2.4a, d). Perpendicular to these thin P- and ^{18}O-enriched bands were broader, more irregular zones of ^{18}O-enrichments of varying thickness running across the full width of the test (Fig. 2.4a).

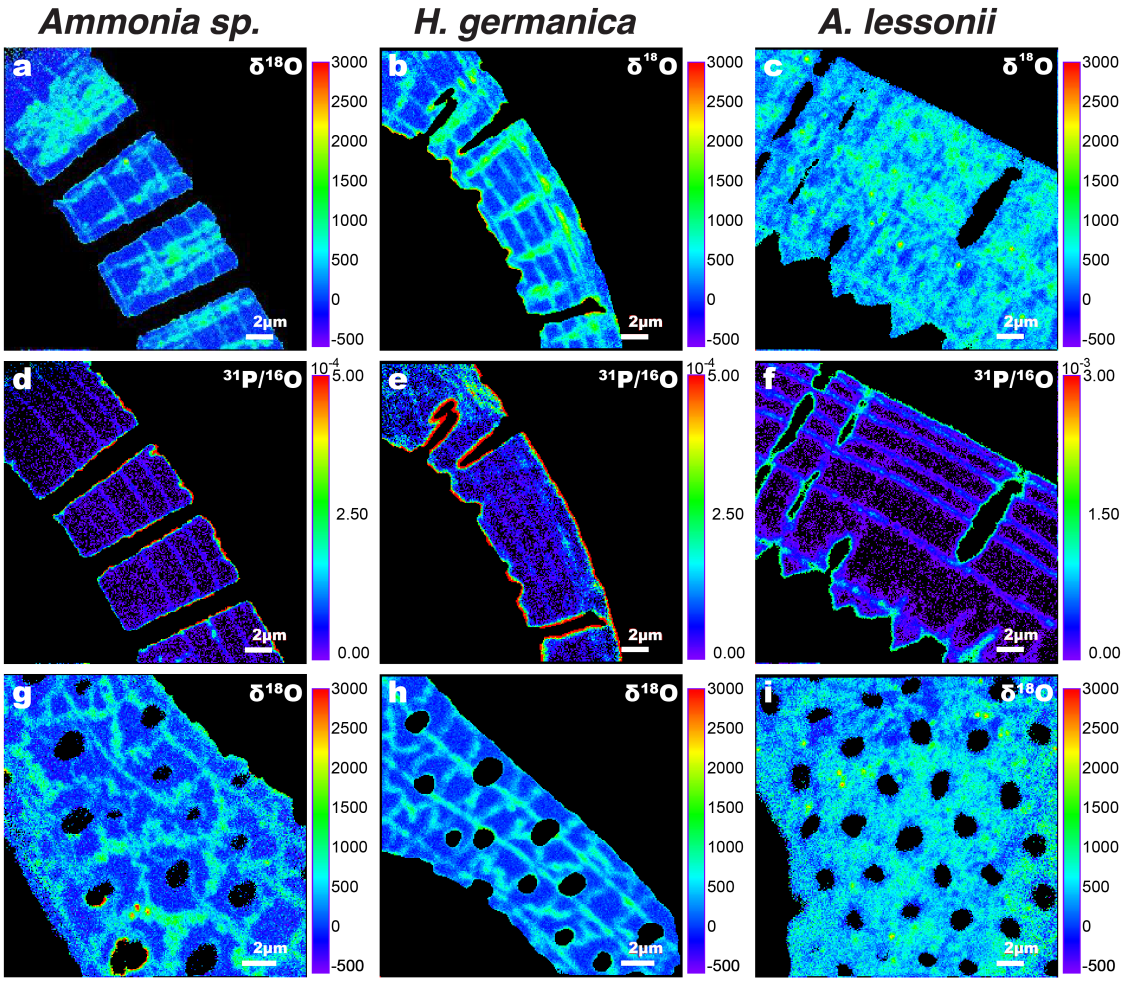

Figure 2.4 Direct imaging of ^{18}O-enrichments in foraminifera tests after incubation. NanoSIMS images of *Ammonia* sp., *H. germanica, and A. lessonii* tests after incubation for 6 days at 90 °C in seawater analogue with a $^{18}O/^{16}O$ ratio of 0.30. (a-c) Surfaces exposing the interior of test walls show high ^{18}O-enrichments occurring as thin parallel bands following the curvature of the test walls and elongated zones of variable thickness running perpendicular to the test surface. (d-f) Same view of the same samples showing the $^{31}P/^{16}O$ ratio, which reveals P-rich bands following the curvature of the test walls. (g-i) Surfaces from the interior of the same samples, but cut parallel to the wall surface, show ^{18}O-enrichments occurring as thin, tortuous and cogwheel-shaped lines in *Ammonia* sp. and *H. germanica*, which merge into patchy areas of higher ^{18}O enrichment in *A. lessonii*.

On surfaces oriented perpendicular to the local pore axis, i.e., parallel to the test surface, the ^{18}O-enrichments in *Ammonia* sp. formed tortuous line-patterns around the pores, identical in appearance to those outlined by the interfaces between cogwheel domains (compare Figs. 2.4g and 2.2d). Qualitatively similar ^{18}O-enrichment patterns were observed in *H. germanica* and *A. lessonii* tests experimentally incubated under identical conditions (i.e., 6 days at 90 °C) (Fig. 2.4), and these ^{18}O-enrichments directly reflect the species-specific differences in density and tortuosity of the cogwheel domain interfaces (Figs. 2.2 and 2.4).

Furthermore, NanoSIMS line-scans were made parallel to the pore axis in tests of *Ammonia* sp. and *H. germanica* to investigate the level of ^{18}O-enrichment in test material in-between organic linings and cogwheel interfaces (Fig. 2.5). These line-scans showed that the ^{18}O-enrichments reached 1500 ‰ where P concentrations indicated remains of organic linings. In addition, the adjacent test calcite (i.e., in-between organic linings) was also clearly enriched by about 100 ‰ above the ^{18}O/^{16}O value of an isotopically unlabeled control sample measured under identical conditions.

Taken together, these observations indicate that isotopic exchange occurred between the foraminifera calcite particles and the ^{18}O-enriched seawater analogue, not only along the organic linings and cogwheel interfaces, but also throughout the test, albeit to a lesser extent. A series of short 4-hour experiments with *Ammonia* sp. and *A. lessonii* tests were conducted under the same conditions and provided qualitatively similar results, but with correspondingly lower ^{18}O-enrichments (Supplementary Fig. 2.9). This demonstrated that isotopic exchange took place on a timescale of minutes and hours.

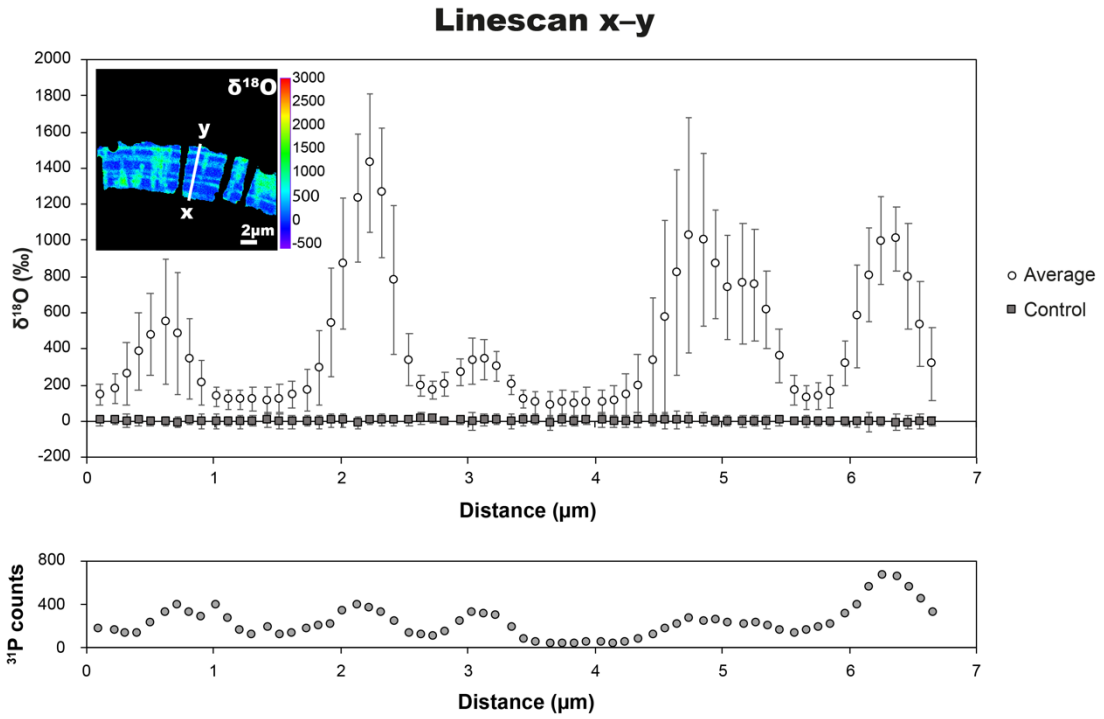

Figure 2.5 ^{18}O-enrichments in test walls between organic linings and cogwheel interfaces. Top: NanoSIMS line-scans across the width of a *H. germanica* test wall after incubation for 6 days at 90 °C in seawater analogue with a $^{18}O/^{16}O$ ratio of 0.30 (white circles), compared to a control sample with natural $^{18}O/^{16}O$ ratio (dark squares); error bars are 2σ. NanoSIMS image inset shows the location of the line going from x to y. Bottom: corresponding ^{31}P-counts over the same line-scan indicating the location of organic linings.

2.3.6 The difference in reactivity between biogenic and abiotic calcite

The exact same 6-day-long experiment was conducted with cleaved, mm-sized single crystals of Iceland spar yielding strikingly different results (Supplementary Fig. 2.10). No ^{18}O-enrichments were measured in NanoSIMS images in the interior of these Iceland spar crystals analyzed under identical conditions and at the same scale as the foraminifera tests (Fig. 2.4, Supplementary Fig. 2.8). This underlines the fundamental difference in reactivity between a biogenic calcite, here in

the form of foraminiferal tests with their intricate organo-calcite composite internal structures (e.g., linings and cogwheel interfaces), and a purely abiotic calcite crystal.

2.4 Discussion

2.4.1 Localized ^{18}O-enrichments

NanoSIMS images and line-scans on surfaces oriented parallel to the local pore axis show that the bands of high ^{18}O-enrichment follow the curvature of the test wall, and are correlated to bands rich in P (Figs. 2.4 and 2.5). Phosphorous enriched bands in foraminifera tests are exclusively associated with organic linings and the P-enriched bands measured here point to remains of organic linings having withstood oxidative cleaning (Geerken *et al.*, 2019). During the life of foraminifera, these organic linings play a key role in directing calcite nucleation during the process of foraminifera test chamber formation (Weiner and Erez, 1984; Addadi and Weiner, 1985; Langer, 1992; Fhlaithearta *et al.*, 2013; Giuffre *et al.*, 2013). Indeed, the number of ^{18}O-enriched bands found in the test wall at specific positions matches the number of organic linings expected at these positions within the tests (Supplementary Fig. 2.8).

At the location of these ^{18}O-enrichment bands, there are often (but not always) also bands with higher concentrations of S and Mg (Supplementary Fig. 2.8). Sulphur can be hosted by organic molecules or incorporated within the calcite lattice as SO_4^{2-} (Paris *et al.*, 2014). Magnesium can substitute for Ca in the calcite lattice (Branson *et al.*, 2013), but is also concentrated within the organic linings (Branson *et al.*, 2016). Chanda *et al.* (2019) argued that stable mineral recrystallization of foraminifera tests proceeds through the preferential dissolution of Mg- and Sr-rich calcite by a dissolution-precipitation mechanism. However, our NanoSIMS images indicate that Mg- and S-rich bands are broader and more numerous than the ^{18}O-enrichment bands, and the tests do not show evidence of any significant dissolution or precipitation (Supplementary Figs. 2.5–2.7).

The close association between ^{18}O-enrichment and P-rich bands demonstrates that organic linings are sites of preferential isotopic exchange as H_2O penetrates into the spaces created by the partial breakdown of the organic molecules caused by oxidative cleaning. This is analogous to what will

occur postmortem inside a foraminifera test in natural settings, where intercrystalline organic matter will be (at least partially) degraded (Sykes *et al.*, 1995; Bernard and Papineau, 2014; Malinverno and Martinez, 2015; Alleon *et al.*, 2017; Wheeler *et al.*, 2021), paving the way for water penetration and subsequent isotopic exchange.

On surfaces perpendicular to the local pore axis (i.e., parallel to the surface), the tortuous lines of ^{18}O-enrichment in all three species (Fig. 2.4g, h, i) are clearly correlated to the shape, distribution, and density of the cogwheel structures and their interfaces (Fig. 2.2d, f, h). Consistently, on surfaces parallel to the local pore axis, the cogwheel interfaces were apparent as undulating sheet-like zones of ^{18}O-enrichments (Fig. 2.4a–c). Interfaces between cogwheel structures initially contain abundant organic matter and therefore, by analogy with the organic linings, represent another site for preferential H_2O penetration and isotopic exchange; H_2O penetrates into the spaces created by the partial breakdown of the organic molecules during oxidative cleaning and by extension, during diagenesis.

2.4.2 Pervasive ^{18}O-enrichments

Partially broken-down organic linings and organic materials at cogwheel interfaces provide highways for H_2O penetration and efficient isotopic exchange with adjacent calcite, and therefore exhibit the highest ^{18}O-enrichments. However, line-scans across *Ammonia* sp. and *H. germanica* (Fig. 2.5) revealed ^{18}O-enrichments averaging 100 ‰ (compared to unlabeled test calcite) in regions between organic linings and without apparent cogwheel interfaces, demonstrating that isotopic exchange also took place elsewhere in the test, at least down to a length-scale below the resolution of the NanoSIMS instrument (i.e., about 100 nm).

At the ultrastructural level, away from linings and cogwheel interfaces, organic matter is concentrated (Cuif *et al.*, 2010b) between the 10–100 nm sub-spherical calcite particles that make up the bulk of the foraminifera tests (Supplementary Fig. 2.1). Partial breakdown of this organic matter will, by analogy with the organic linings and organic compounds along the cogwheel interfaces, also create pathways for H_2O penetration and surfaces for isotopic exchange with calcite everywhere in the tests at <100 nm length scales. Using P as a proxy for the presence of remaining organic compounds after oxidative cleaning, we observed that the P-counts did not decrease to zero

anywhere in the tests, indicating the presence of organic matter in regions between organic linings and away from cogwheel interfaces at length scales below the resolution of the NanoSIMS; a finding also reported by Geerken *et al.* (2019). At the atomic scale, the presence of these organic molecules causes anisotropic distortion of the crystal lattice of biogenic calcite (Pokroy *et al.*, 2006a). Compared to abiotic calcite, biogenic calcite thus has significantly longer and weaker C–O bonds (Zolotoyabko *et al.*, 2010; Stolarski *et al.*, 2016). Consequently, where H_2O preferentially penetrates the tests because of the partial breakdown of organic compounds, it also preferentially exchanges O-isotopes with the calcite surfaces it encounters.

The role of inter- and intra-crystalline organic matter in permitting water penetration and promoting isotopic exchange is further supported by the measured ^{18}O-enrichments in the foraminifera tests exposed to the experimental solutions compared to O-isotope measurements in macroscopic (i.e., mm-sized) abiotic Iceland spar calcite exposed to the very same experimental conditions (Supplementary Fig. 2.8). No ^{18}O-enrichment was measurable in the interior of these Iceland spar crystals, in which water simply could not penetrate because of the lack of structural pathways that, in contrast, are ubiquitous in biogenic calcites in general (Lowenstam and Weiner, 1989; Nudelman *et al.*, 2007; Cuif *et al.*, 2010a; Schenk and Kim, 2015).

2.4.3 Species-specific susceptibility to isotope exchange

Organic linings and cogwheel structures are fundamental structural features in the tests of both benthic and planktonic foraminifera (van Dijk *et al.*, 2020), and can become the main pathways for H_2O penetration and hence also induce isotopic exchange after the (partial) degradation of the organic matter (Figs. 2.3–2.5). In addition to chamber walls of variable thickness, tests of different foraminifera species have different cogwheel structures in terms of size, distribution, and density (van Dijk *et al.*, 2020), as is the case for the species studied here (Fig. 2.2). This would then also result in a species-specific susceptibility for the penetration of water and subsequent isotopic exchange. In other words, the different susceptibilities of biogenic carbonates to diagenesis appears directly correlated with differences in ultrastructure.

The cogwheel structures and the organic linings are the main sites for preferred isotopic exchange, therefore, a higher proportion of these structures in a foraminifera test supports a higher bulk ^{18}O

enrichment. The surface density of the cogwheel interfaces was calculated for all three species of foraminifera used in this study (Supplementary Fig. 2.11, Supplementary Table 2.2) using the methodology described in van Dijk *et al.* (2020). *Ammonia* sp. and *H. germanica* had comparable average cogwheel interface densities (measured in μm per μm^2) of 1.80 ± 0.36 (1σ) and 1.78 ± 0.10 (1σ) respectively, which were approximately half that of *A. lessonii*, 3.52 ± 0.18 (1σ). This higher cogwheel interface density of *A. lessonii* compared to *Ammonia* sp. is likely a contributing factor to this species having a higher average bulk ^{18}O-enrichment than Ammonia sp.

Despite *Ammonia* sp. and *H. germanica* having similar cogwheel interface densities, the average bulk ^{18}O-enrichment in *H. germanica* was 45% higher than in *Ammonia* sp. (Fig. 2.3, Supplementary Table 2.2). All three species belong to the same order, Rotaliida, but are differentiated at the Superfamily level, with *Ammonia* sp. and *H. germanica* belonging to Rotalioidea and *A. lessonii* to Asterigerinoidea. Consistent with this classification *Ammonia* sp. and *H. germanica* have similar test geometry (Supplementary Fig. 2.8, Supplementary Software), but *Ammonia* sp. test chambers appear thicker than in *H. germanica*. To quantify this, tests from both species were embedded in epoxy, ground down to the widest portion of the test and polished, imaged in SEM, and the images analyzed using the image processing software ImageJ (Supplementary Software). For both species, there is a good statistical correlation between the number of chambers and the cross-sectional test area measured in μm^2; *Ammonia* sp. $R^2 = 0.85$ and *H. germanica* $R^2 = 0.89$ (Fig. 2.6a). For the same number of chambers, *Ammonia* sp. tests occupy a larger area, indicating that test chambers are thicker than in *H. germanica*. Assuming these two species have organic linings of similar thicknesses (which is consistent with observations), the ratio of the cross-sectional test area to the number of chambers is both a proxy for chamber thickness and a measure of the density of calcite-organic interfaces. On average, *H. germanica* tests are 48% thinner than *Ammonia* sp. tests for the same number of calcite-organic interfaces (Supplementary Table 2.3), which is consistent with *H. germanica* having an average bulk ^{18}O-enrichment that is 45% higher than in *Ammonia* sp. (Fig. 2.2, Supplementary Table 2.1).

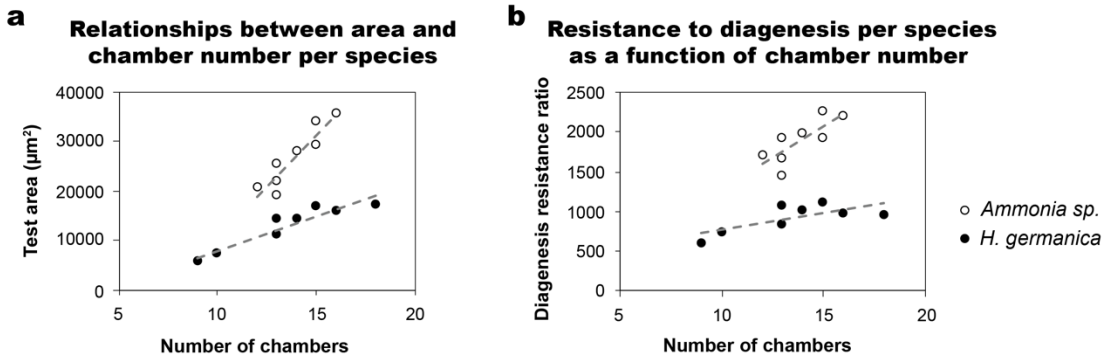

Figure 2.6 Variation in diagenetic susceptibility to isotopic exchange per species and during ontogeny. Relationship between the number of chambers and foraminifera test cross-sectional area (a) and diagenesis resistance ratio for *Ammonia* sp. and *H. germanica,* calculated as a ratio of the foraminifera test cross-sectional area to the number of chambers (b). (a) The cross-sectional test wall area (µm^2) and the number of chambers show a good statistical correlation for both *Ammonia* sp. ($R^2 = 0.85$) and *H. germanica* ($R^2 = 0.89$). For the same number of chambers, *Ammonia* sp. test walls have larger cross-sectional areas than *H. germanica* tests because the walls are thicker in this species. (b) Plotting the diagenesis resistance ratio to the number of chambers shows that *H. germanica* has a lower resistance to diagenesis than *Ammonia* sp. and that, as foraminifera from both species grow more chambers, their diagenetic resistance ratio increases.

The similar test geometry and cogwheel interface densities in *Ammonia* sp. and *H. germanica* offer the opportunity to study variations in diagenetic susceptibility to isotopic exchange during ontogeny. The ratio of the estimated maximum cross-sectional area of a test to its total number of chambers, which is equal to the number of organic linings separating consecutive layers in the test as it grows, was used to calculate a diagenesis resistance ratio. If this ratio is small, it indicates a relatively high number of organic linings for a given amount of calcite and therefore low resistance to isotopic exchange. Importantly, this ratio increases during ontogeny, i.e., with the number of completed chambers (Fig. 2.6b). From Fig. 2.6b, it is clear that *H. germanica* is relatively more susceptible to diagenesis than *Ammonia* sp. due to its thinner chambers. Additionally, smaller tests from younger foraminifera have fewer chambers and are therefore more susceptible to diagenesis. This is because later added chambers are proportionally larger and their walls have fewer organic linings. Therefore, as foraminifera tests grow larger, their diagenetic resistance increases. This

ontogenetic effect on diagenetic susceptibility can help explain some of the variability in the bulk isotopic enrichment measurements, if foraminifera from a range of sizes are included in a single batch of analyzed tests.

2.4.4 Paleo-environmental reconstructions based on biogenic calcites – an outlook

The effects of sediment lithology and sedimentation rate have been recognized as having an influence on foraminifera test preservation (Sexton and Wilson, 2009), with tests hosted in clay-rich sediments without significant breaks in sedimentation thought to be protected from porewaters with a different chemical and isotopic compositions (Pearson *et al.*, 2001; Wilson *et al.*, 2002; Sexton *et al.*, 2006b; Sexton and Wilson, 2009). However, even these clay-rich oceanic sediments exhibit average porosities of 40% at burial depths up to 500 m (Velde, 1996), and thus contain abundant porewater. Even if the porewater surrounding the foraminifera tests maintain a constant chemical and isotopic composition, increased temperatures during burial will lead to isotopic disequilibrium between the test calcite and the porewater, which drives isotopic exchange (Bernard *et al.*, 2017). Therefore, consistent with the results of Bernard *et al.* (2017) and Chanda *et al.* (2019), our results make the case that partial isotopic exchange of foraminifera tests is unavoidable under natural conditions during diagenesis. We furthermore demonstrate that susceptibility to isotopic exchange is species-specific. Over millions of years, as carbonate skeletons approach isotopic equilibrium with the surrounding pore fluids in the sediments, this species-specific susceptibility to diagenesis will become less pronounced, which may partly explain the reduced variability of oxygen isotope ratios between different species over geological time (Zachos *et al.*, 2001; e.g. Friedrich *et al.*, 2012). It is common practice to correct compiled paleo O-isotopic records for assumed biological disequilibrium effects (the so-called vital effect) (Urey *et al.*, 1951; Shackleton *et al.*, 1984; Zachos *et al.*, 1994, 2001; Cramer *et al.*, 2009). Species-specific susceptibility to diagenesis should also be corrected for once its evolution over time is well established and quantifiable.

Furthermore, glassy fossil foraminifera tests should no longer be considered as isotopically pristine. In modern paleo-environmental reconstruction studies, the collection of fossil foraminifera tests from ocean sediments for chemical or isotopic analysis involves a selection based on their appearance in optical microscopy: glassy tests are used in preference to frosty tests (Wilson *et al.*,

2002; Sexton *et al.*, 2006b; Edgar *et al.*, 2013, 2015; Pearson *et al.*, 2015; Schneider *et al.*, 2017). Frosty tests are those that appear opaque when observed with an optical microscope because they have experienced extensive secondary crystallization; they are therefore generally discarded (Sexton *et al.*, 2006b; Pearson and Burgess, 2008). In contrast, glassy tests, i.e., those that appear transparent when observed with an optical microscope, are assumed to have undergone minimal diagenetic alteration in the form of neomorphism or cementation; i.e., replacement of original biogenic calcite with abiotic calcite or direct precipitation of calcite onto the tests (Sexton *et al.*, 2006b). But, as we demonstrate here, it is highly likely that glassy tests have also partially exchanged oxygen with a pore fluid. In fact, the benthic foraminifera tests exposed to the experimental incubations in this study can be considered to be texturally pristine, with no observable evidence of dissolution/precipitation or neomorphism. Yet, bulk measurements and quantitative NanoSIMS imaging demonstrate that even though they appear visually pristine, these tests have undergone extensive isotopic exchange (Figs. 2.3–2.5). Additionally, since isotope exchange is ubiquitous throughout the entire tests, no amount of cleaning or fragmentation would remove their enriched isotopic compositions.

Moreover, even a cursory look at the literature shows that most (if not all) fossil foraminifera tests selected from geologically older ocean sediments (i.e., millions of years) and included in standard paleo-environmental reconstructions have been modified in terms of their initial texture, crystallinity, and ultrastructures during fossilization. Compare Fig. 2.1 and Supplementary Figs. 2.5–2.7 with Supplementary Fig. 2.12; the latter shows SEM images of fossil tests from the DSDP Site 522. Deeply etched pores and abundant secondary calcite cementation are features typical for the majority of tests from Paleogene ocean sediment sections (Sexton *et al.*, 2006a) and this relatively poor level of preservation is certainly not the worst among fossil foraminifera tests for which the stable isotope compositions have been measured.

The results of the present study indicate that texture-based assessments of the degree of diagenetic alteration of foraminifera tests is by itself not a sufficient criterium to exclude partial isotopic exchange after the sedimentation of the test. It also demonstrates that the effects of diagenetic isotopic exchange are species-specific. This needs to be considered and potentially corrected for in paleo-environmental reconstructions. In general, until diagenetic processes on different types of

marine biocalcites are better understood and quantified, the existing paleo-seawater temperature reconstructions based on, for example, O-isotopic compositions cannot be considered unbiased.

2.4.5 Code Availability Statement

The ImageJ macro used in this study have been deposited in the EarthChem database accessible at https://doi.org/10.26022/IEDA/112180 (Cisneros-Lazaro *et al.*, 2021).

2.5 Supplementary information

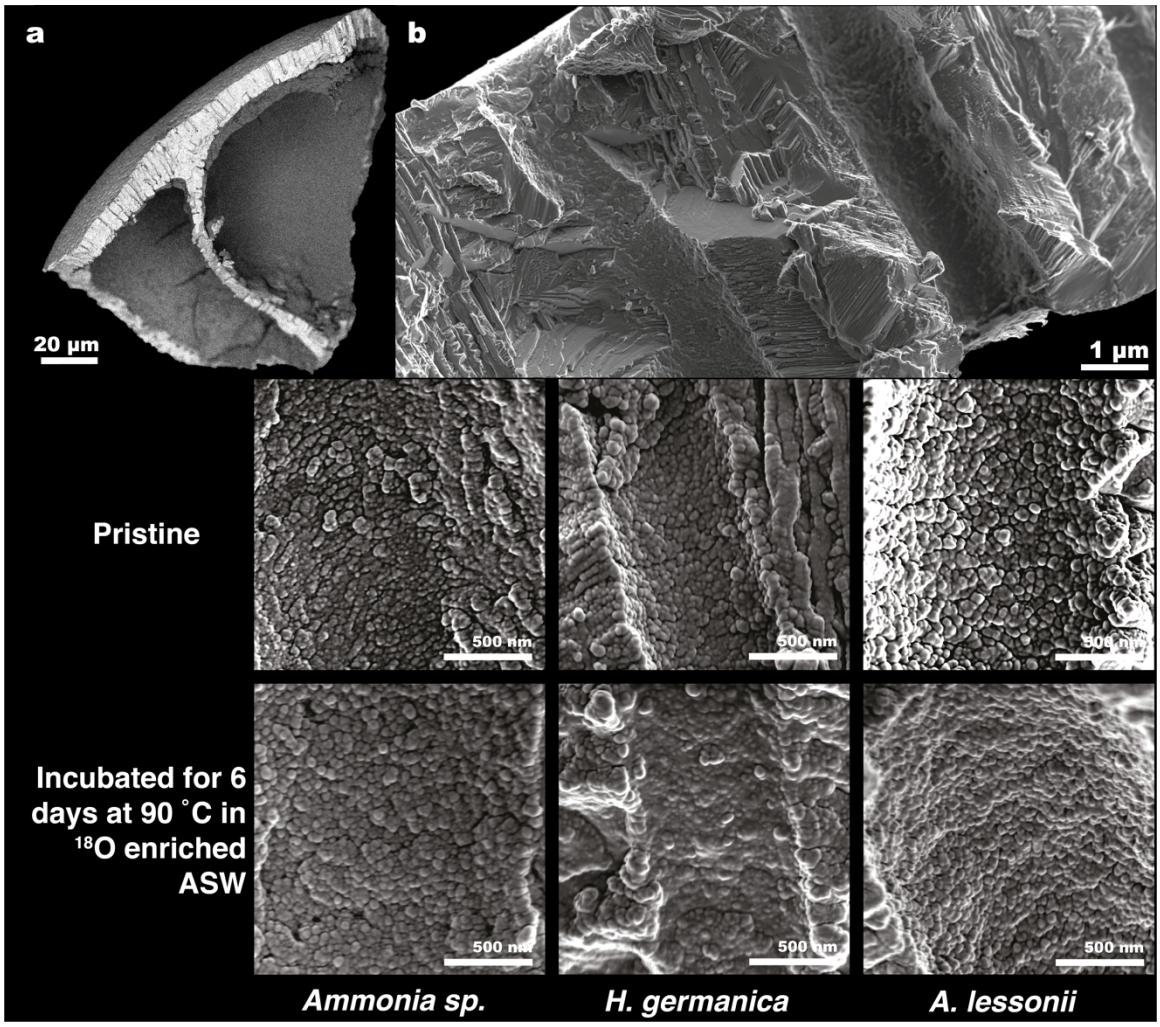

Supplementary Figure 2.1 High magnification (35 000×) SEM images of the sub-spherical calcite particles that make up the test wall of three species of foraminifera, as seen on the surfaces of broken test chambers (a and b). There are no clear differences in the texture of the nanoparticles in pristine foraminifera tests of *Ammonia sp., H. germanica* and *A. lessonii* compared to tests that were incubated for 6 days at 90 °C in a seawater analogue with a $^{18}O/^{16}O$ ratio of 0.30. Notice that all high magnification images were taken at the same scale.

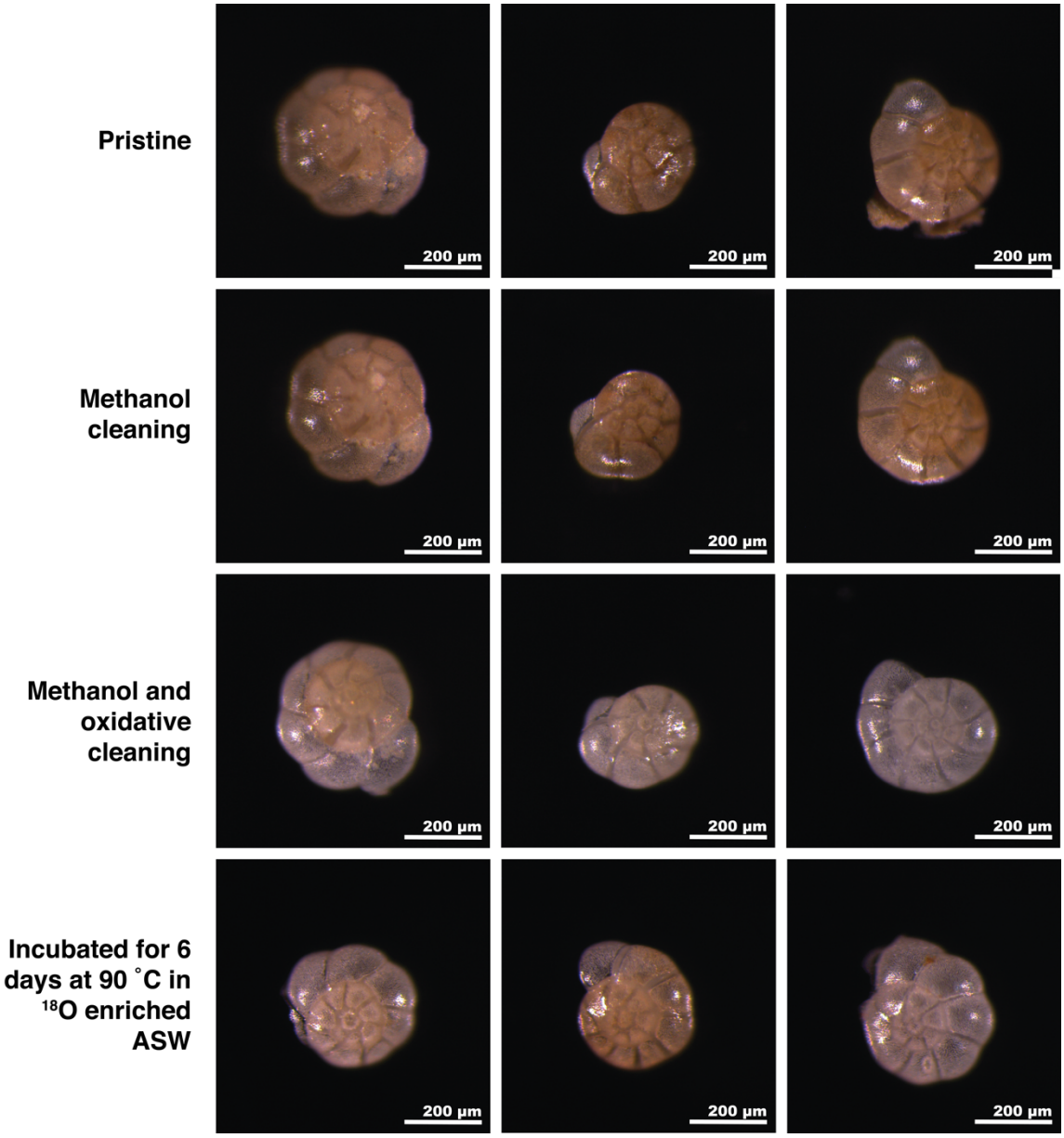

Supplementary Figure 2.2 Stereo microscope images of *Ammonia sp.* tests that are pristine (1st row), cleaned only with methanol (2nd row), cleaned with methanol and an oxidative treatment (3rd row) and tests that were incubated for 6 days at 90 °C in artificial seawater (ASW) with a $^{18}O/^{16}O$ ratio of 0.30 after methanol cleaning and an oxidative treatment. All images were taken at the same scale, under identical illumination conditions, and with the same microscope and camera.

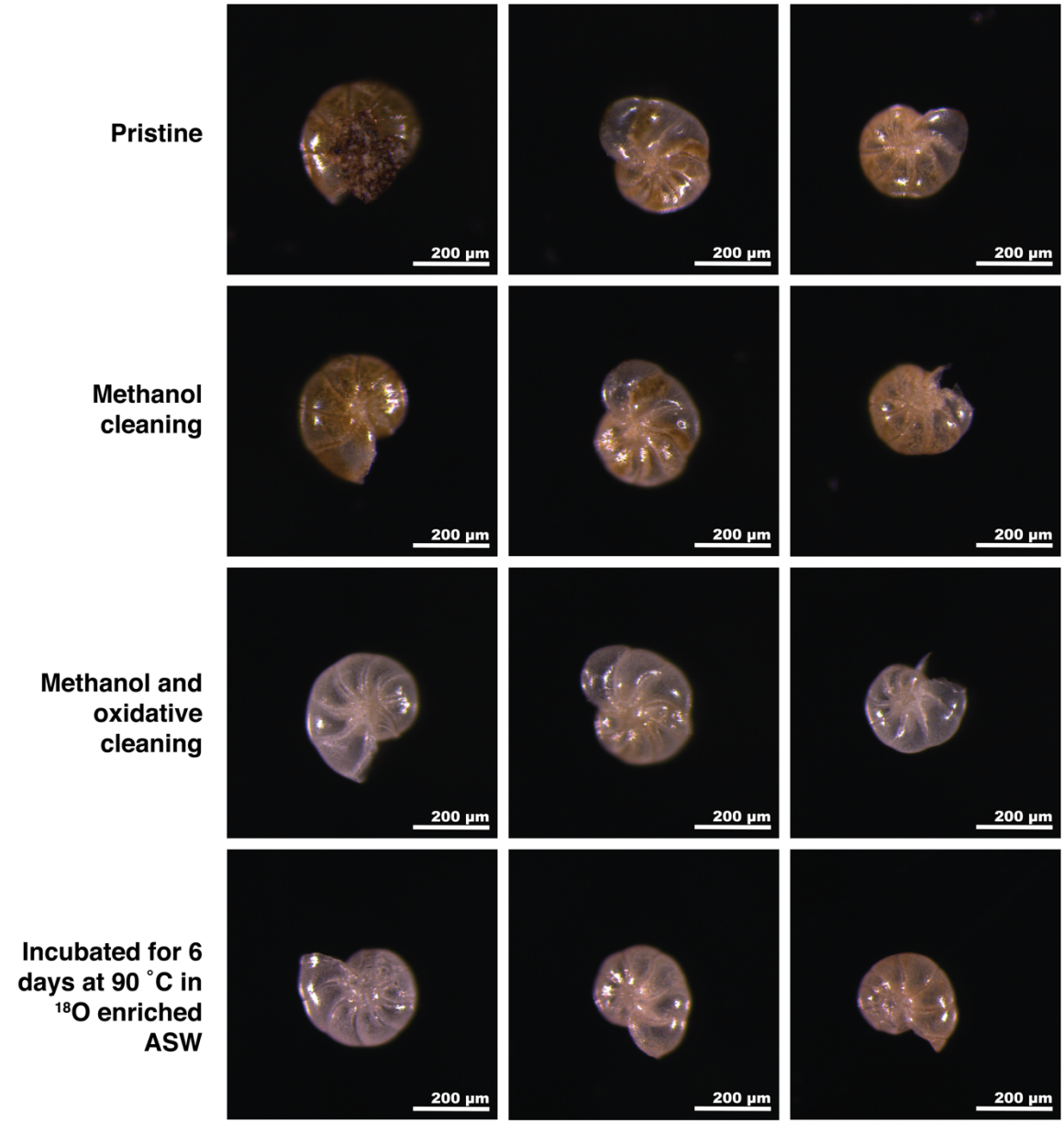

Supplementary Figure 2.3 Optical images of *H. germanica* tests that are pristine (1st row), cleaned only with methanol (2nd row), cleaned with methanol and an oxidative treatment (3rd row) and tests that were incubated for 6 days at 90 °C in artificial seawater (ASW) with a $^{18}O/^{16}O$ ratio of 0.30 after methanol cleaning and an oxidative treatment. All images were taken at the same scale, under identical illumination conditions, and with the same microscope and camera.

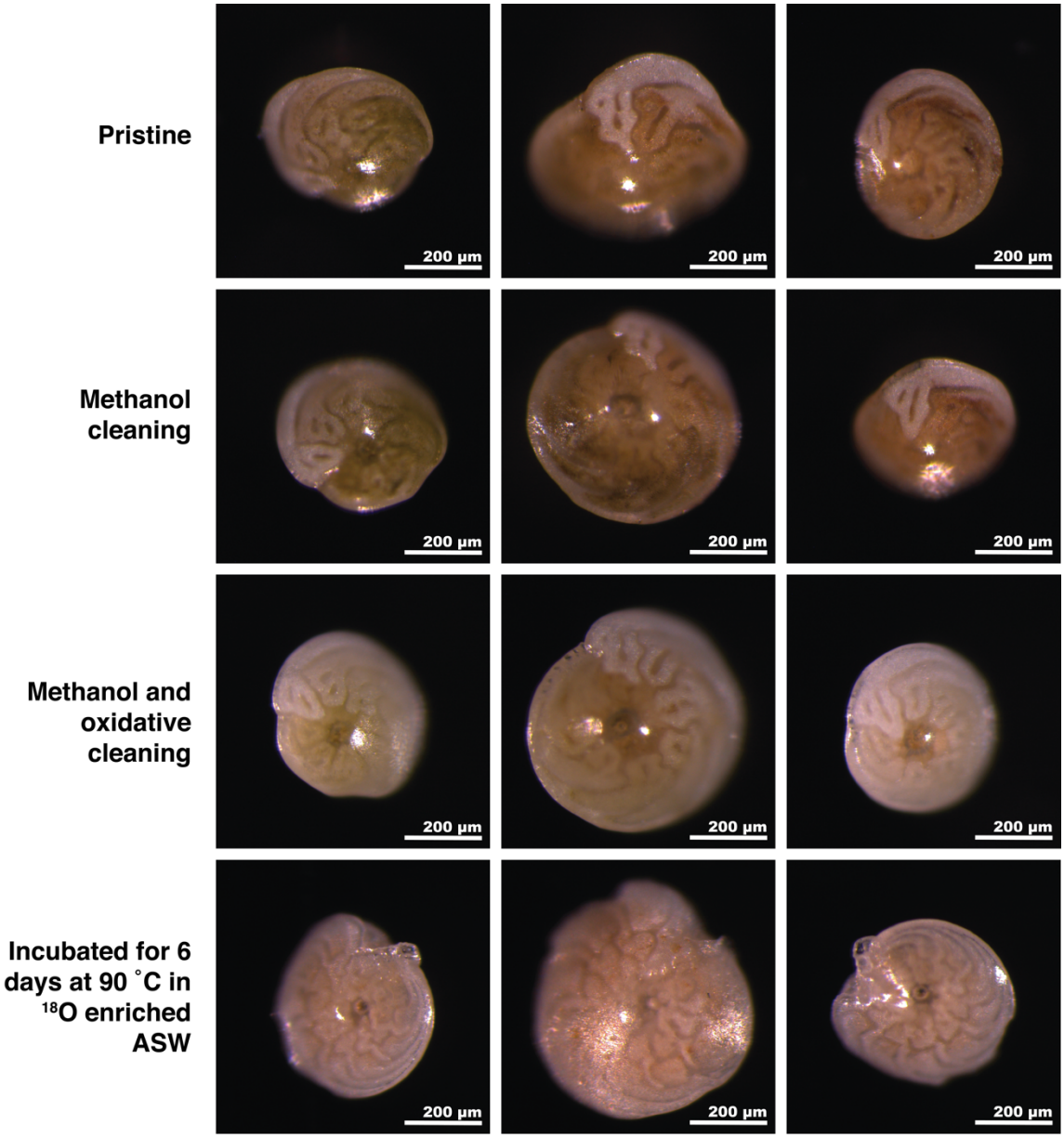

Supplementary Figure 2.4 Optical images of *A. lessonii.* tests that are pristine (1st row), cleaned only with methanol (2nd row), cleaned with methanol and an oxidative treatment (3rd row) and tests that were incubated for 6 days at 90 °C in artificial seawater (ASW) with a $^{18}O/^{16}O$ ratio of 0.30 after methanol cleaning and an oxidative treatment. All images were taken at the same scale, under identical illumination conditions, and with the same microscope and camera.

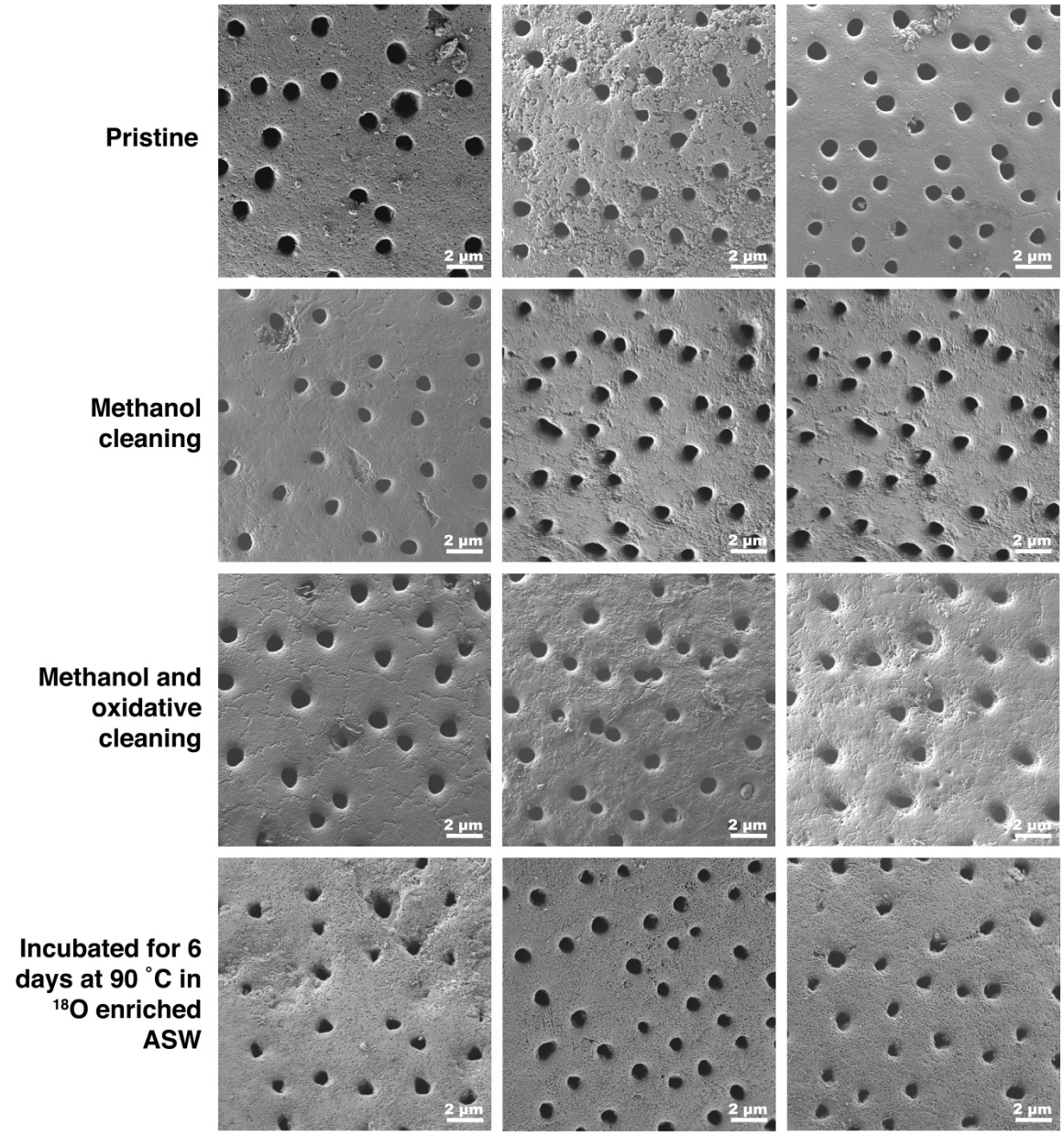

Supplementary Figure 2.5 High magnification (5000×) SEM images of the surfaces of the penultimate chamber of *Ammonia* sp. comparing tests that are pristine (1st row), cleaned only with methanol (2nd row), cleaned with methanol and an oxidative treatment (3rd row) to tests that were incubated for 6 days at 90 °C in artificial seawater (ASW) with a $^{18}O/^{16}O$ ratio of 0.30 after methanol cleaning and an oxidative treatment. All images were taken at the same scale.

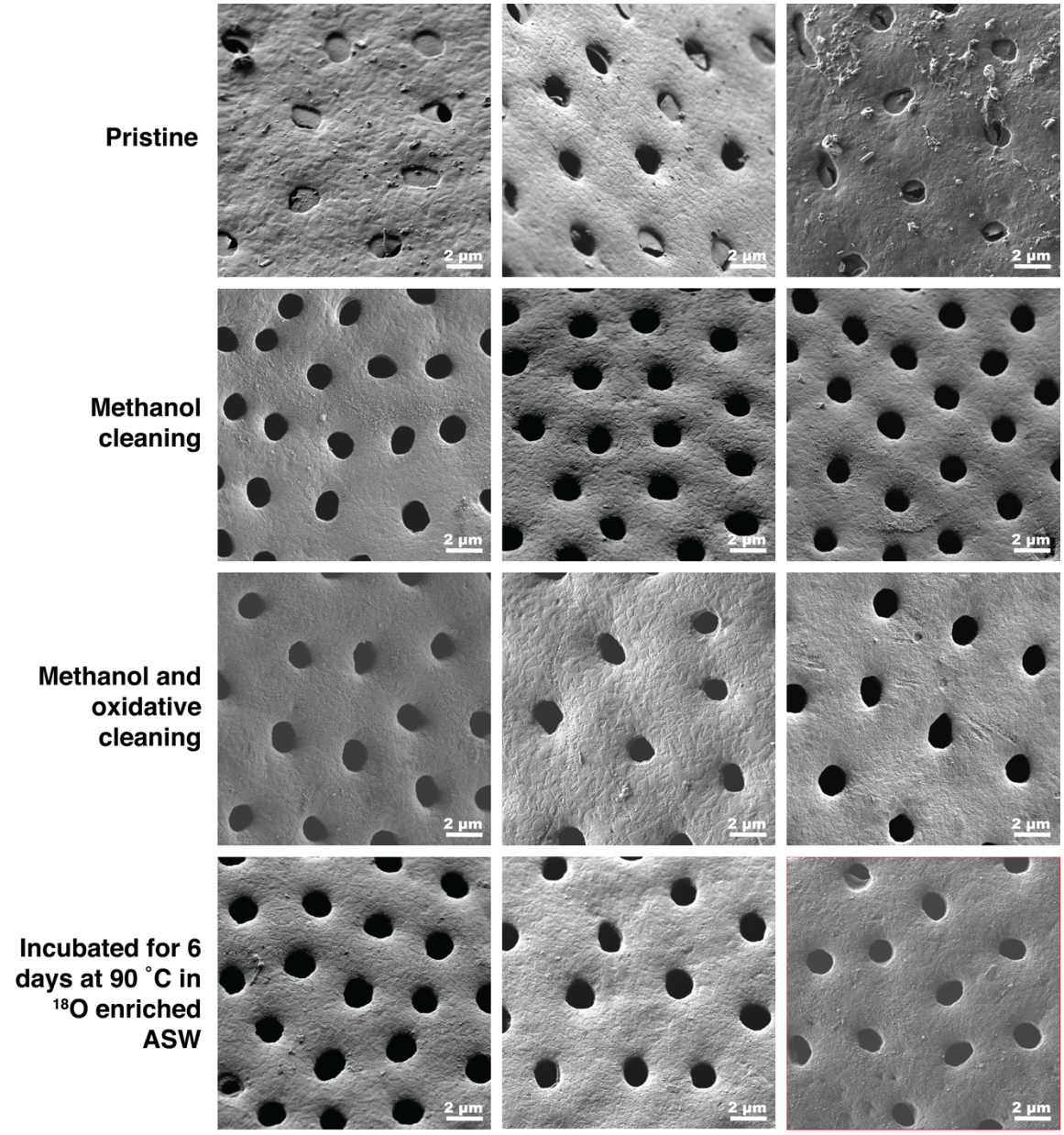

Supplementary Figure 2.6 High magnification (5000×) SEM images of the surfaces of the penultimate chamber of *H. germanica* comparing tests that are pristine (1st row), cleaned only with methanol (2nd row), cleaned with methanol and an oxidative treatment (3rd row) to tests that were incubated for 6 days at 90 °C in artificial seawater (ASW) with a $^{18}O/^{16}O$ ratio of 0.30 after methanol cleaning and an oxidative treatment. All images were taken at the same scale.

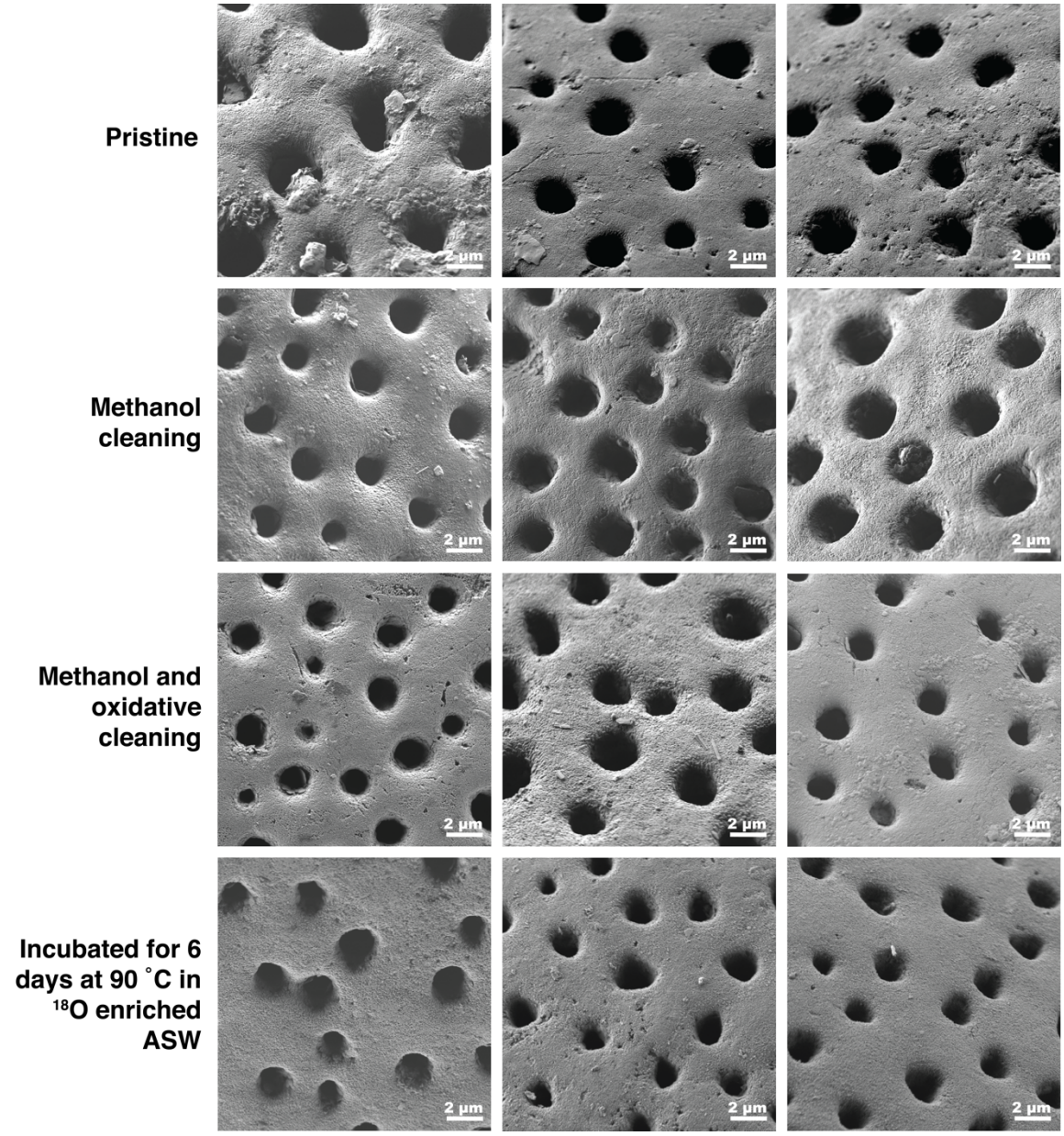

Supplementary Figure 2.7 High magnification (5000×) SEM images of the surfaces of the penultimate chamber of *A. lessonii* comparing tests that are pristine (1st row), cleaned only with methanol (2nd row), cleaned with methanol and an oxidative treatment (3rd row) to tests that were incubated for 6 days at 90 °C in artificial seawater (ASW) with a $^{18}O/^{16}O$ ratio of 0.30 after methanol cleaning and an oxidative treatment. All images were taken at the same scale.

Foram $\delta^{18}O$ (‰ VSMOW)			
Species	*Ammonia* sp.	*H. germanica*	*A. lessonii*
	508	722	782
	614	874	741
	499	761	726
	518	959	691
	472	687	674
	627	716	677
	483	743	747
	521	758	738
	507	705	676
	543	768	694
			657
			705
Average	529	769	709
Standard Deviation	49	80	36
Variance	2437	6398	1288

Supplementary Table 2.1 Summary table of the bulk oxygen isotope measurements of foraminifera tests that were incubated for 6 days at 90 °C in artificial seawater with a $^{18}O/^{16}O$ ratio of 0.30. Each measurement consists of 70–100 μg of foraminifera tests. The average, standard deviation and variance are reported for each species.

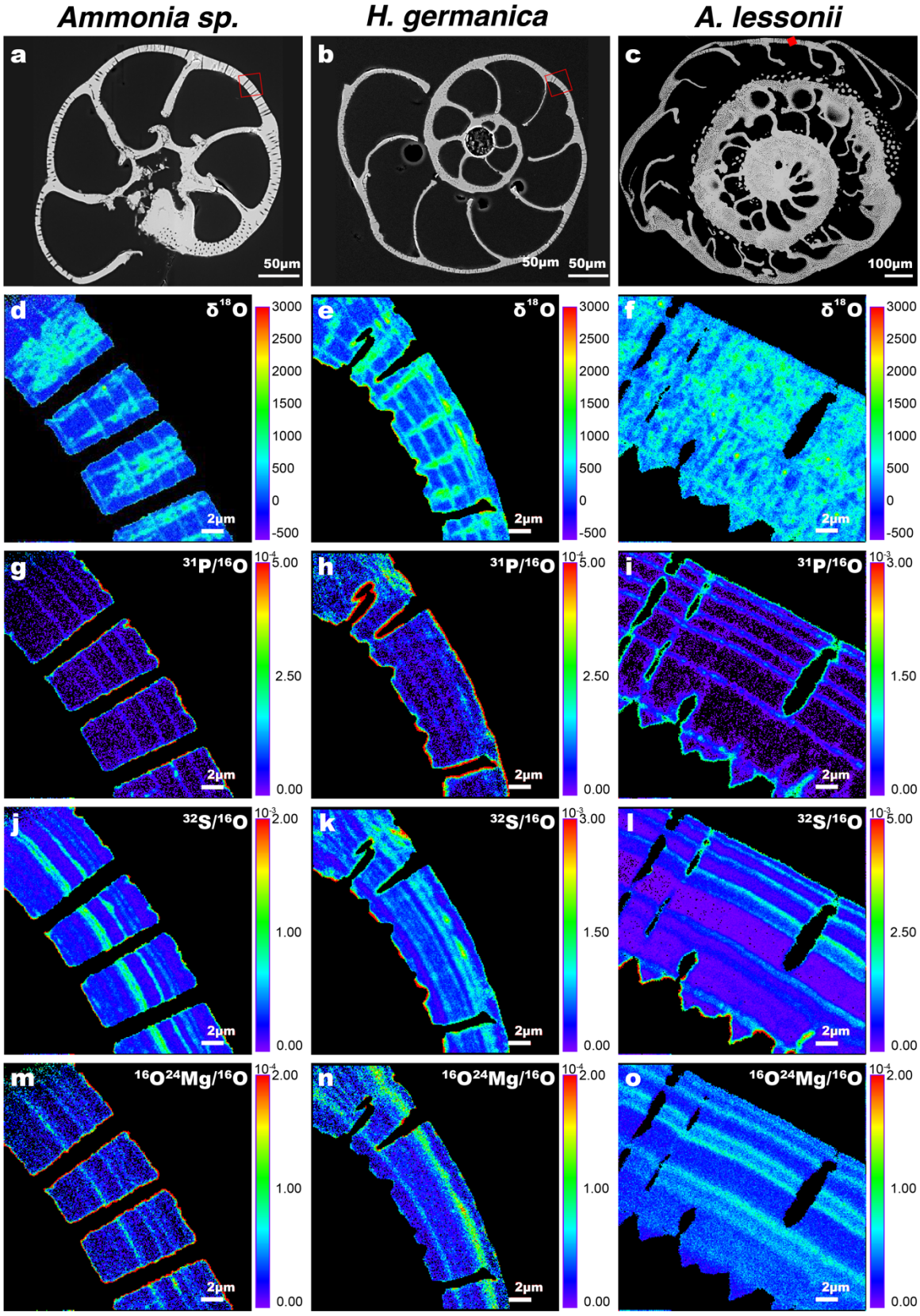
Ammonia sp.
H. germanica
A. lessonii
a
b
c
50µm
50µm
50µm
100µm
d
δ18O
e
δ18O
f
δ18O
3000
2500
2000
1500
1000
500
0
-500
2µm
g
31P/16O
h
31P/16O
i
31P/16O
10-4
5.00
2.50
0.00
10-3
3.00
1.50
j
32S/16O
k
32S/16O
l
32S/16O
2.00
1.00
3.00
1.50
5.00
2.50
m
16O24Mg/16O
n
16O24Mg/16O
o
16O24Mg/16O

Supplementary Figure 2.8 (Preceding page) NanoSIMS images of *Ammonia sp., A. lessonii* and *H. germanica* tests after incubation for 6 days at 90 °C in artificial seawater (ASW) with a $^{18}O/^{16}O$ ratio of 0.30. (a-c) shows SEM images of polished tests with the red square indicating the location of the NanoSIMS images in rows 2 to 5 that show surfaces parallel to pore axes. (d-f): $\delta^{18}O$. (g-i): $^{31}P/^{16}O$ ratio. (j-l): $^{32}S/^{16}O$ ratio. (m-o): $^{24}Mg^{16}O$ $/^{16}O$ ratio. In all three species it is clear that ^{18}O-enrichment is best correlated with bands of P, as bands of S and Mg are thicker and more numerous than the bands of P. Additionally, the number of ^{18}O-enrichment bands correspond to the number of organic linings expected from the position of the chamber in question relative to the total number of chambers.

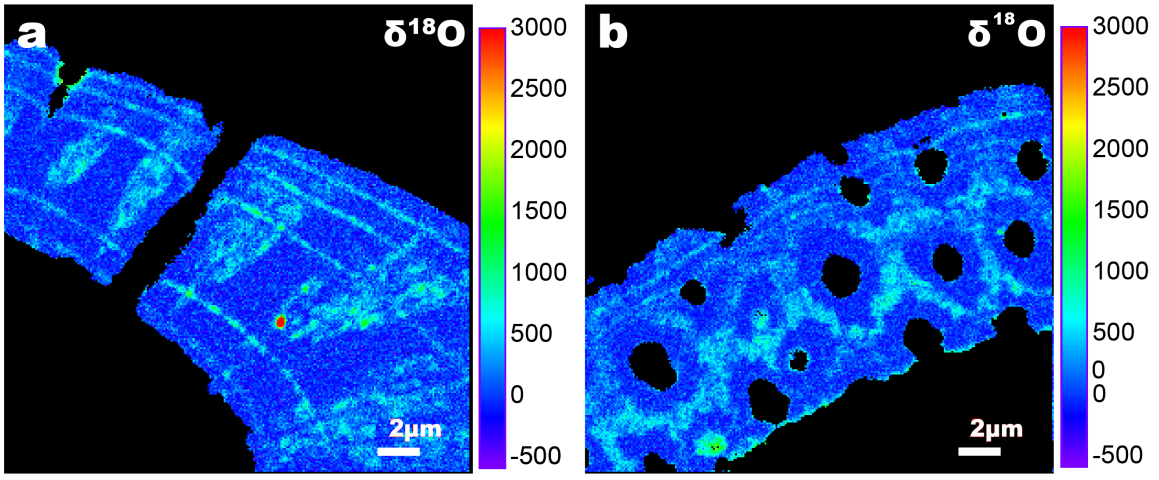

Supplementary Figure 2.9 NanoSIMS images of an *Ammonia* sp. test after incubation for 4 hours at 90 °C in artificial seawater with a $^{18}O/^{16}O$ ratio of 0.30 after methanol cleaning and an oxidative treatment. Tests incubated for only 4 hours show the same heterogenous spatial pattern of ^{18}O-enrichment as experiments lasting 6 days, but with correspondingly lower ^{18}O-enrichments.

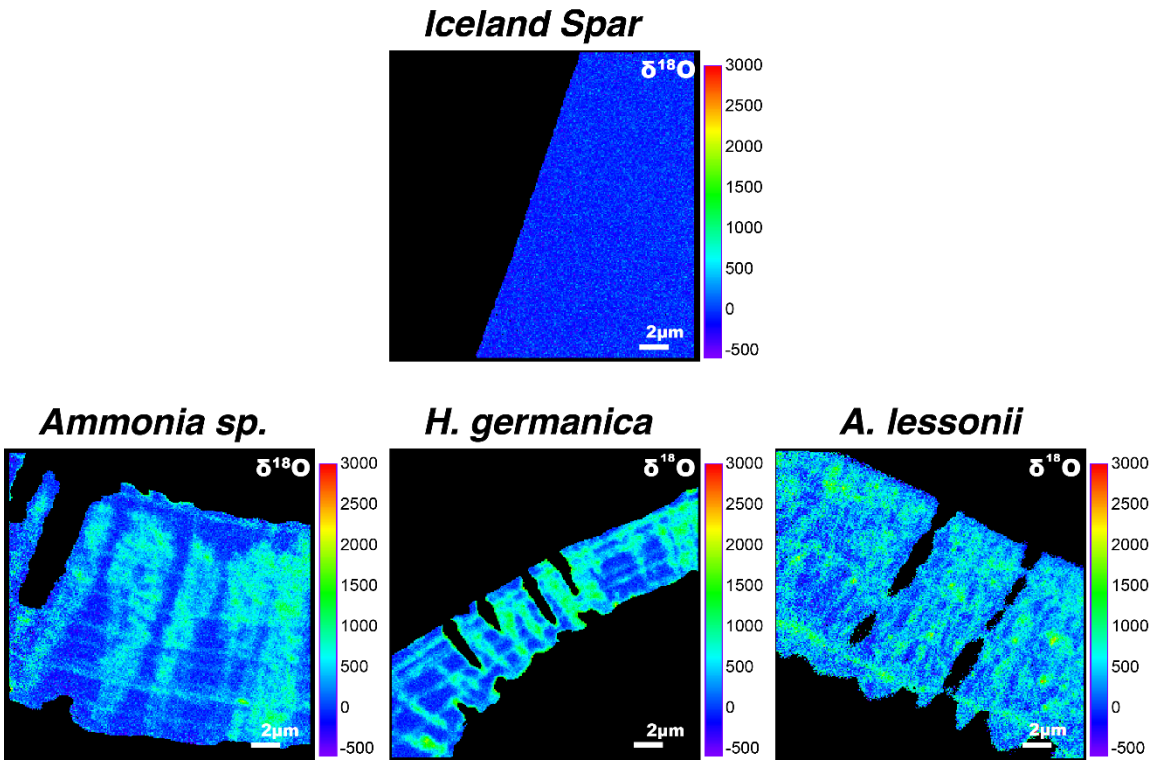

Supplementary Figure 2.10 NanoSIMS $\delta^{18}O$-image of an Iceland spar crystal, in direct comparison with $\delta^{18}O$-images of *Ammonia* sp., *H. germanica* and *A. lessonii* tests after incubation for 6 days at 90 °C in artificial seawater with a $^{18}O/^{16}O$ ratio of 0.30 after methanol cleaning and an oxidative treatment. The interior of Iceland spar crystals did not become enriched in ^{18}O despite being incubated for the same time, in the same fluid, and at the same temperature as the benthic foraminifera tests.

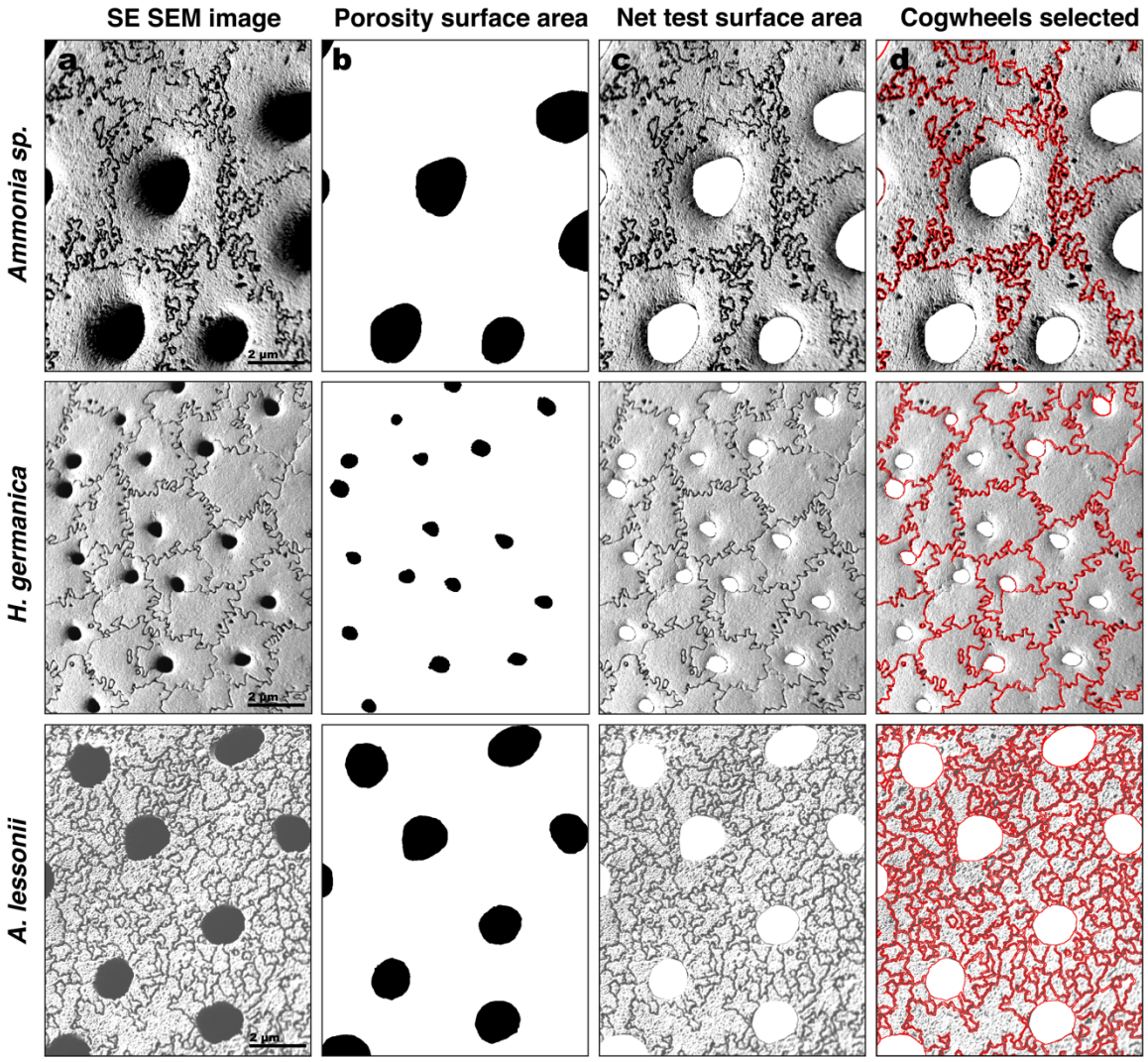

Supplementary Figure 2.11 Images illustrating the 4 key steps of the ImageJ cogwheel quantification macro from van Dijk *et al.* (2020) with an example from each of the three species used in this study: *Ammonia* sp., *H. germanica*, and *A. lessonii*. (a) The raw SEM images of external test surface areas were imported into ImageJ, and the images cropped such that only areas in sharp focus were used. (b) Gray value thresholding was used to select the pore spaces and the paintbrush tool was used to remove any pixels that do not form part of the pore surface area. (c) The net test surface area was obtained by removing the pores from the cropped SEM image. (d) All cogwheel interfaces were registered and their total length measured.

Species	Image area dimensions	Porosity surface area (μm^2)	Net test surface area (μm^2)	Number of cogwheels	Total cogwheel interface length (μm)	Cogwheel interface density (μm per μm^2)
Ammonia sp.	21.79 um x 10.85 μm	24.59	211.83	95	381.4	1.8
Ammonia sp.	10.37 um x 11.33 μm	7.93	109.56	70	236.09	2.15
Ammonia sp.	15.23 um x 9.94 μm	25.26	126.13	49	180.95	1.43
					Av. ± (1σ):	**1.80 ± 0.36**
H. germanica	22.22 um x 14.91 μm	13.05	318.25	155	603.12	1.9
H. germanica	19.31 um x 13.19 μm	10.87	243.83	108	425.62	1.75
H. germanica	13.63 um x 11.24 μm	6.75	146.45	69	251.01	1.71
					Av. ± (1σ):	**1.78 ± 0.10**
A. lessonii	9.30 um x 11.57 μm	13.72	93.88	324	349.01	3.72
A. lessonii	10.90 um x 10.36 μm	17.14	95.78	282	322.17	3.36
A. lessonii	11.37 um x 10.36 μm	15.45	102.34	284	357.43	3.49
					Av. ± (1σ):	**3.52 ± 0.18**

Supplementary Table 2.2 Cogwheel interface density quantification parameters calculated using ImageJ for three foraminifera tests of *Ammonia* sp.*, H. germanica,* and *A. lessonii* obtained by the procedure described in van Dijk *et al.* (2020). The net surface area was calculated by subtracting the area of the pores from the total area of the frame. The total cogwheel interface length (μm) is the total length of all cogwheel interfaces excluding pore-calcite interfaces and pixels along the image frame; cf. Supplementary Fig. 2.11. Cogwheel interface density (μm per μm^2) is calculated as the ratio of the total cogwheel interface length to the net test surface area. The average cogwheel surface density for each species is provided ± one standard deviation.

Species	Test surface area (μm^2)	Maximum diameter	Number of chambers	Diagenesis resistance ratio
Ammonia sp.	35447	403	16	2215
Ammonia sp.	18967	364	13	1459
Ammonia sp.	25148	362	13	1934
Ammonia sp.	33922	423	15	2261
Ammonia sp.	20593	344	12	1716
Ammonia sp.	21661	368	13	1666
Ammonia sp.	27920	365	14	1994
Ammonia sp.	28960	404	15	1931
			Av. ± (1σ):	**1897 ± 274**
H. germanica	5428	214	9	603
H. germanica	14122	269	13	1086
H. germanica	10896	258	13	838
H. germanica	7320	212	10	732
H. germanica	16778	434	15	1119
H. germanica	15619	353	16	976
H. germanica	14190	333	14	1014
H. germanica	17168	393	18	954
			Av. ± (1σ):	**915 ± 178**

Supplementary Table 2.3 Parameters used to calculate the diagenesis resistance ratio, which is the ratio of the maximum cross-sectional test area (μm^2) to the number of chambers for *Ammonia* sp. and *H. germanica.* The average diagenesis resistance factor for each species is provided ± one standard deviation.

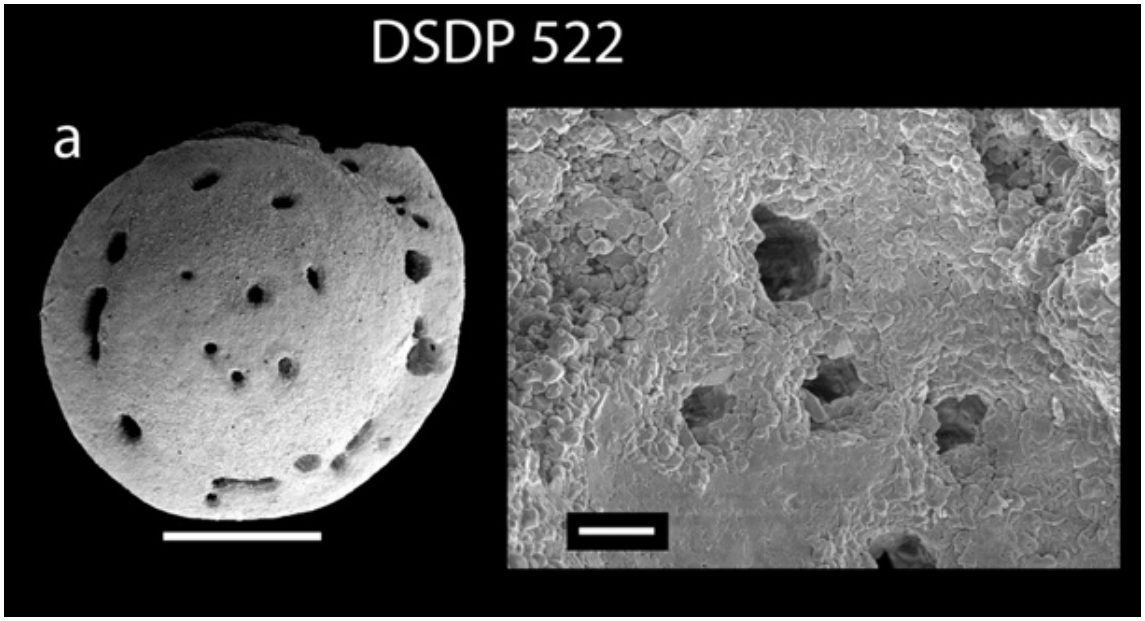

Supplementary Figure 2.12 SEM image of the spiral side and high-magnification view of the wall texture of benthic foraminifera *Cibicidoides havanensis* from DSDP Site 522 (Walvis Ridge). Note the etching of pores and/or secondary calcite deposits on the surface. Scale bars are 100 μm (left side) and 10 μm (right side). Modified from Sexton *et al.* (2006a).

3 *Fossil biocalcite remains open to isotopic exchange with seawater for tens of millions of years*

Deyanira Cisneros-Lazaro[1*], Arthur Adams[1], Jarosław Stolarski[2], Sylvain Bernard[3], Damien Daval[4], Alain Baronnet[5], Olivier Grauby[5], Lukas P. Baumgartner[6], Torsten Vennemann[7], Jo Moore[6], Claudia Baumgartner[6], Cristina Martin Olmos[1], Stéphane Escrig[1] and Anders Meibom[1,6,*]

[1] Laboratory for Biological Geochemistry, School of Architecture, Civil and Environmental engineering, Ecole Polytechnique Fédérale de Lausanne (EPFL), Lausanne, CH-1015 Switzerland

[2] Institute of Paleobiology, Polish Academy of Sciences, PL-00-818 Warsaw, Poland

[3] Museum National d'Histoire Naturelle, Sorbonne Université, CNRS UMR 7590, IMPMC, 75005 Paris, France

[4] ISTerre, Univ. Grenoble Alpes, Univ. Savoie Mont Blanc, CNRS, IRD, IFSTTAR, 38041, Grenoble, France

[5] CNRS, CINaM, Aix-Marseille Université, 13009 Marseille, France

[6] Institute of Earth Science, University of Lausanne, CH-1015 Lausanne, Switzerland

[7] Institute of Earth Surface Dynamics, University of Lausanne, CH-1015 Lausanne, Switzerland

This chapter was submitted to PNAS.

Author contribution statement

DC-L, AA, JS and AM designed the experimental study; DC-L acquired the optical and SEM images, CB acquired the CL images, DC-L and JM acquired the EBSD data, DC-L and CMO acquired the AFM data, AA performed the isotope exchange experiments; DC-L and SE acquired NanoSIMS data; DC-L, AA and AM drafted the manuscript. All co-authors contributed to the writing of the manuscript.

Abstract

Fossilized remains of marine calcifiers constitute the physical basis for reconstructions of both deep ocean and sea-surface temperatures going back millions of years, but paleoclimate records derived from their isotope and trace-element geochemistry can be biased by diagenesis. Experiments simulating diagenesis in the presence of an ^{18}O-rich seawater analogue were conducted with modern and 14 m.y. old foraminifera (*Ammonia* sp.) tests to investigate their susceptibility to oxygen isotope exchange. The fossilized tests were of exceptional preservation and similar to modern tests in terms of structure and crystalline organization, but had experienced partial loss of embedded organic structures, thus *a priori* offering less preferential pathways for porewaters to penetrate the test. NanoSIMS imaging revealed that oxygen isotope exchange was pervasive in fossil tests, which were approximately half as susceptible to isotopic exchange as modern tests. The results unequivocally show that fossil biocalcites remain susceptible to isotopic exchange millions of years after sedimentation and burial.

3.1 Introduction

The elemental and isotopic composition of fossil carbonate skeletons of marine calcifiers, such as foraminifera, bivalves and brachiopods, are essential archives for understanding the evolution of marine environments, and hence global changes in climate over geological time (Urey, 1948; Brand *et al.*, 2003; Katz *et al.*, 2010; Schone and Surge, 2012; Immenhauser *et al.*, 2016). The oxygen isotope paleothermometer (Urey, 1948; Urey *et al.*, 1951) has permitted reconstruction of deep-water and sea-surface temperatures from the present to the Phanerozoic (Veizer and Prokoph, 2015). However, accurately reconstructing past ocean environments is predicated on the assumption that there has been minimal isotopic exchange between the fossil biogenic carbonates and the surrounding porewaters during or after sedimentation. The potential for diagenesis to affect the preservation of elemental or isotopic compositions of biogenic carbonates was recognized already in the infancy of paleoclimate reconstructions (Urey, 1948), with most subsequent work focusing on physio-chemical alterations: for example, the conversion of biogenic aragonite into abiotic calcite for bivalves (Casella *et al.*, 2017; Pederson *et al.*, 2019; Forjanes *et al.*, 2022), changes in luminescence, mineralogy and elemental compositions for brachiopods (Perez-Huerta *et al.*, 2007; Casella *et al.*, 2018), and structural modifications brought on by dissolution, overgrowth and secondary precipitation for foraminifera (Shieh *et al.*, 2002; Sexton *et al.*, 2006b; Pearson and Burgess, 2008; Fehrenbacher and Martin, 2014).

Bernard and colleagues (2017) recognized that significant modification of the isotopic composition of foraminifera tests can take place without observable (by optical or scanning electron microscopy) ultrastructural changes to foraminifera tests. Subsequent experiments designed to quantify the rates of biogenic calcite-fluid exchange showed that a ^{45}Ca radiotracer can be rapidly incorporated into foraminifera test calcite (Chanda *et al.*, 2019) and that oxygen isotope compositions of foraminifera tests can be significantly altered through (rapid) grain-boundary diffusion (Adams *et al.*, 2023), all without any accompanying ultrastructural changes. In addition, it was demonstrated that calcium, carbon and oxygen isotope exchange between nano- to micrometer sized abiotic calcite crystals and fluid occur at ambient temperatures without any change in grain size (Harrison *et al.*, 2022, 2023). These studies indicate that low-temperature diagenesis can change the original isotope and

chemical composition of biocalcites, even on geologically short time scales, thus potentially biasing paleoenvironmental reconstructions without leaving any noticeable evidence of this alteration.

In a previous study (Cisneros-Lazaro *et al.*, 2022), diagenesis was simulated in experiments with ^{18}O-labelled artificial seawater combined with NanoSIMS high spatial resolution isotopic imaging to understand how fluids interact with calcitic tests of modern hyaline rotaliid foraminifera, the order most commonly used in paleoclimate reconstructions (Adams *et al.*, 2023). Pore fluids were found to pervasively penetrate the entire test via organic-rich conduits (common to all rotaliid foraminifera) that act as preferential pathways: cogwheel interfaces and organic linings. The 'cogwheel' interfaces, visible on the surfaces of test walls of both modern and fossil foraminifera, separate 3-dimensional domains of distinct crystallographic orientation (Debenay *et al.*, 2000; Nakajima *et al.*, 2016; van Dijk *et al.*, 2020). Organic linings, architecturally similar for all rotaliid foraminifera, are layers that serve as templates for calcification. During growth, foraminifera extrude an organic template outlining the new chamber and covering the rest of the outer surface of the test (Nehrke *et al.*, 2013; Nagai *et al.*, 2018a; Geerken *et al.*, 2019). The walls of previously formed – and hence overgrown – chambers thus contain a number of organic linings corresponding to their position in the test. Both cogwheel interfaces and organic linings act as penetration 'highways' that bring pore fluids close to all internal parts of the tests, facilitating isotope exchange with the entirety of the test structure, the bulk of which is composed of 10–100 nm sub-spherical calcite particles coated by organic materials (Cisneros-Lazaro *et al.*, 2022). Such nano-scale granular texture is common to most biominerals from disparate taxa and phyla (Rodríguez-Navarro *et al.*, 2016). Given that the organic linings are generally degraded (at least partially) in fossil biocalcitic structures (95% of the initial stock of proteins can be degraded in less than 120 kyr (Walton, 1998)), it could be surmised that fossil biocalcites do not remain susceptible to diagenetic isotope exchange. In order to investigate this hypothesis, we incubated 14 m.y. old *Ammonia* tests (Rögl *et al.*, 2008; Zágoršek *et al.*, 2012) for 6 days in ^{18}O-enriched seawater analogue at chemical equilibrium and 90 °C to establish the degree to which fluids can penetrate into and isotopically exchange with fossil tests with partially degraded organic matter. Modern, pristine *Ammonia* tests were incubated under identical conditions, offering a basis for direct comparison.

3.2 Methods

Two species of *Ammonia* were used for the incubation experiments, modern *Ammonia confertitesta* (previously named *Ammonia tepida* T6) and fossil *Ammonia beccarii*. *Ammonia confertitesta* specimens were obtained from recent tidal sediment in the mudflats of the Bay of Bourgneuf, France. The fossils were collected from the Korytnica Clays at Mt. Łysa (located at GPS position: 50°39′50″ to 50°40′50″ N and 20°31′20″ to 20°33′00″ E), which are part of a fossil rich facies deposited between 14.8–14.6 Mya (Rögl *et al.*, 2008; Zágoršek *et al.*, 2012) in the Korytnica Basin (Stolarski, 1991; Zágoršek *et al.*, 2012; Stolarski *et al.*, 2023). Fossils from the Korytnica Clays are exceptionally well preserved due to their rapid deposition in water-impermeable clays, and coral, gastropod and fish otolith fossils often maintain their original aragonitic mineralogy as well as their original nanostructural textures (Stolarski and Mazur, 2005; Stolarski *et al.*, 2023). Fossil specimens from the same collection are housed at the Institute of Paleobiology, Polish Academy of Sciences, Warsaw (abbreviation ZPAL).

3.2.1 Cleaning procedures and incubation experiments

The procedure below is similar to that for our previous work (Bernard *et al.*, 2017; Cisneros-Lazaro *et al.*, 2022; Adams *et al.*, 2023). Prior to the incubation experiments, the foraminifera tests were cleaned as recommended by Barker and colleagues (Barker *et al.*, 2003), which involved ultrasonication in methanol and subsequently deionized water (MilliQ) before rinsing in technical grade ethanol and drying overnight at 50 °C. We omitted the oxidative cleaning step that removes organic matter as we previously found that this did not make a significant difference to the O-isotope exchange (Cisneros-Lazaro *et al.*, 2022). For the incubation experiments, a dozen modern and fossil tests were placed in separate arc-welded gold capsules filled with ~40 µL of artificial seawater ($\Omega_{calcite}$ = 1; 0.6 M NaCl, 0.05 M $MgCl_2$), which was enriched in ^{18}O to a $^{18}O/^{16}O$ ratio of about 0.30, and placed in ovens at 90 °C for 6 days. After removing the samples from the gold capsules, the tests were rinsed successively in artificial seawater, distilled and deionized water, and technical grade ethanol. The tests were then dried overnight at 50 °C and subjected to 24 hours of vacuum desiccation at room temperature. Previous work has confirmed that the addition or omission of desiccation steps does not change the $\delta^{18}O$ value of the incubated foraminifera tests (Adams *et al.*, 2023).

3.2.2 Imaging by SEM, AFM, CL, NanoSIMS and EBSD

Uncoated whole and broken tests were imaged using secondary electrons on a Zeiss Gemini 500 SEM operating at an acceleration voltage of 1 kV and a working distance of 5 mm. For the rest of the analyses a flat imaging surface was required. To produce a smooth cross-sectional surface of the tests, dried and vacuum-desiccated tests were embedded in resin (EpoThin2, Struers) and polished with a series of increasingly finer-grained diamond pastes (15 to 0.25 μm). This was followed by a brief (3 minute) colloidal silica polish using a Vibromet2 to achieve a mirror finish.

For SEM and AFM imaging of internal test textures mirror polished samples were briefly immersed in 2 vol % glutaraldehyde + 0.1 vol % acetic acid. Samples for SEM imaging were immersed in this solution for 10 seconds and those destined for AFM imaging were immersed in the solution for 3 seconds.

AFM images were taken using an Asylum Research Cypher VRS instrument (Oxford Instruments, United Kingdom) with an ARC2 controller. The silicon AFM probes used for non-contact tapping mode were uncoated and had a resonant frequency of 150 kHz and a spring constant of 9 N/m (supplier Oxford Instruments, model AC200TS).

Optical cathodoluminescence (CL) imaging was performed on polished sample surfaces using the electronics and electron gun of OPEA adapted to the vacuum chamber of CTTL, Technosyn 8200 MkII, mounted on an Olympus light microscope BX51 equipped with a static stage and a high-sensitivity Olympus DP74. The OPEA was operated at 15–20 kV and 0.4–0.6 mA with an unfocused cold cathode electron beam under an air atmosphere at 0.2 torr (about 26.6 Pa). In biogenic calcite, a yellow-orange CL colour (λ = 600–650 nm) usually results from the incorporation of Mn^{2+} (10–1000 ppm) in the crystal lattice (Baumgartner-Mora and Baumgartner, 1994). In contrast, a dark blue CL colour (λ= ± 400 nm) corresponds to the intrinsic luminescence of high-purity calcite, that characterizes unaltered biogenic carbonate (Wendler *et al.*, 2012). The quenching effect of Fe^{2+} was not considered here, as it requires high concentrations (>10’000 ppm) absent in foraminifera.

EBSD imaging was conducted using an Oxford Instrument Tescan Mira LMU on samples that were coated with approximately 5 nm of carbon. During measurements the SEM was operated with a beam energy of 20 keV, a working distance of 23 mm, and a tilt angle of 70°. EBSD maps were acquired with a 200 nm step size. Kikuchi patterns were acquired with a Symmetry EBSD detector and indexed with AzTec analysis software (Oxford Instruments). Map processing was done with CHANNEL 5 HKL software. Individual crystal boundaries (black lines) were defined as having a misorientation angle larger than 10° and subgrain boundaries (grey lines) as having a misorientation angle larger than 2°.

For NanoSIMS imaging, the procedures followed Cisneros-Lazaro *et al.* (2022). The polished samples were coated with ca. 15 nm Au to reduce charging on the sample surface. A 16 keV Cs^+ primary ion beam with a focused spot size of approximately 120 nm (~ 3.7 pA on the sample surface) was used to visualize the distribution of ^{18}O-enrichment and elemental banding within the tests. Ions of $^{16}O^-$, $^{18}O^-$, $^{12}C^{14}N^-$, $^{31}P^-$, $^{32}S^-$, $^{16}O^{24}Mg^-$ were simultaneously counted in the multi-collector system in individual electron multiplier detectors with a mass resolving power of ~9000 (Cameca definition). An electron gun was used to compensate for the positive charges that build up on the surface. 25×25 μm^2 images were generated as a raster of 256×256 pixels with a dwell-time of 5 milliseconds per pixel. The resulting images were processed using L'IMAGE (Dr. Larry Nittler, Carnegie Institution of Washington, USA). The oxygen isotope compositions of the tests were reported as $\delta^{18}O$ (in parts-per-thousand) relative to tests of the same species that were not incubated with the ASW, i.e., pristine:

$$\delta^{18}O = \left\{\left[\left(^{18}O/^{16}O\right)_{\text{sample}} - \left(^{18}O/^{16}O\right)_{\text{standard}}\right]/\left(^{18}O/^{16}O\right)_{\text{standard}}\right\} \times 1000 \quad (1)$$

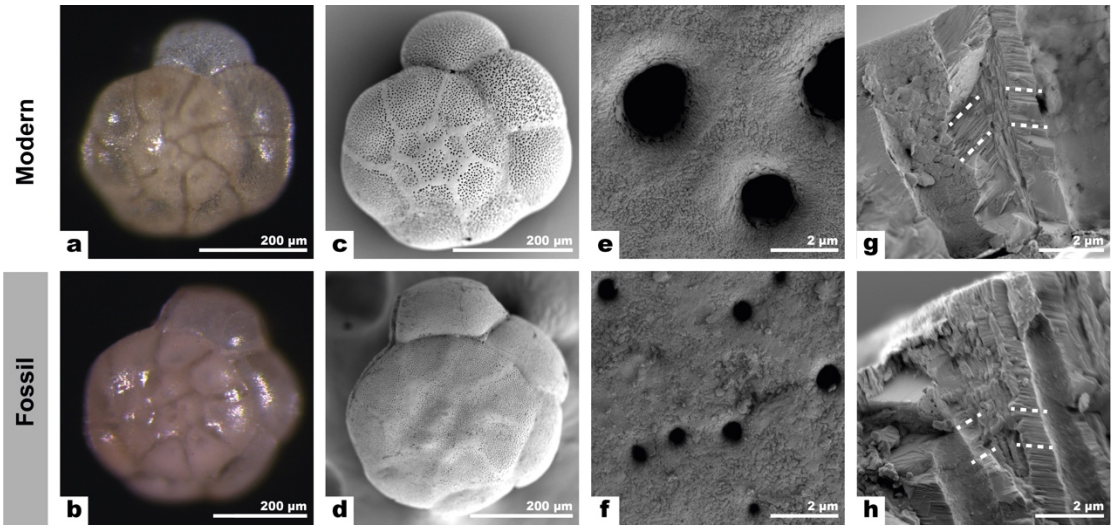

Figure 3.1. Stereo microscopy and secondary electron SEM images comparing representative modern *Ammonia confertitesta* (top row) and fossil *Ammonia beccarii* (bottom row) tests used in the incubation experiments. (a–b) Optical images show that both modern and fossil *Ammonia* appear 'glassy and pristine', with pores and chamber divisions clearly outlined. (c–d) SEM images of the same tests as in (a–b), demonstrating an absence of overgrowths. (e–f) High-magnification SEM images of the surfaces of the same tests. Modern and fossil tests have comparable surface textures. (g–h) SEM images of a cross-sectional view of broken chamber walls. Both modern and fossil tests show step-like fractures in opposite directions either side of a vertical cogwheel boundary, as indicated by dashed white lines.

3.3 Results

3.3.1 *Comparing the ultrastructures and crystallography of modern and fossil Ammonia*

A combination of scanning electron microscopy (SEM), atomic force microscopy (AFM), cathodoluminescence (CL) and electron backscatter diffraction (EBSD) imaging were used to compare the ultrastructures of modern *Ammonia confertitesta* and fossil *Ammonia beccarii* used in the incubation experiments, which will henceforth collectively be referred to as *Ammonia.* Optical and SEM images showed that pristine fossil and modern tests had comparable external textures

(Fig. 3.1). Both modern and fossil *Ammonia* tests appeared 'glassy and translucent' (Sexton *et al.*, 2006b) when viewed with an optical microscope (Fig. 3.1a, b). Fossil tests with an opaque appearance, a different coloration, or clear signs of damage (Supplementary Fig. 3.1) were not selected for the incubation experiments. Selected modern and fossil tests thus had minimal overgrowths (Supplementary Fig. 3.1), with pore and chamber divisions easily recognizable (Fig. 3.1c, d). The final (i.e., youngest) chamber(s) of fossil tests were fragile, often breaking during handling. Modern tests had significantly larger pores than fossil tests, but in both cases, pores were empty when viewed from the outside (Fig. 3.1c–h, Supplementary Fig. 3.1). High-resolution SEM images of modern and fossil tests showed comparable surface textures (Fig. 3.1e, f). SEM images of cross-sections of chambers on broken tests showed similar textures for both modern and fossil tests, with step-like fractures in opposite directions either side of vertical cogwheel boundaries (Fig. 3.1g, h).

SEM images of the surfaces of modern tests clearly exhibited a number of organic linings as ridges emerging from the surrounding (etched) calcite; the number of linings corresponding to the position of the chamber relative to the last precipitated chamber (Geerken *et al.*, 2019) (Fig. 3.2a, Supplementary Fig. 3.2). The bulk texture between the organic linings – revealed by AFM imaging – showed a nanocrystalline ultrastructure typical of all *Rotaliid* foraminifera (Fig. 3.2b). Fossil tests exposed to the same etching and fixation treatment did not show the same organic lining patterns (Fig. 3.2c, Supplementary Fig. 3.2), but had preserved their nanocrystalline structure (Fig. 3.2b, d).

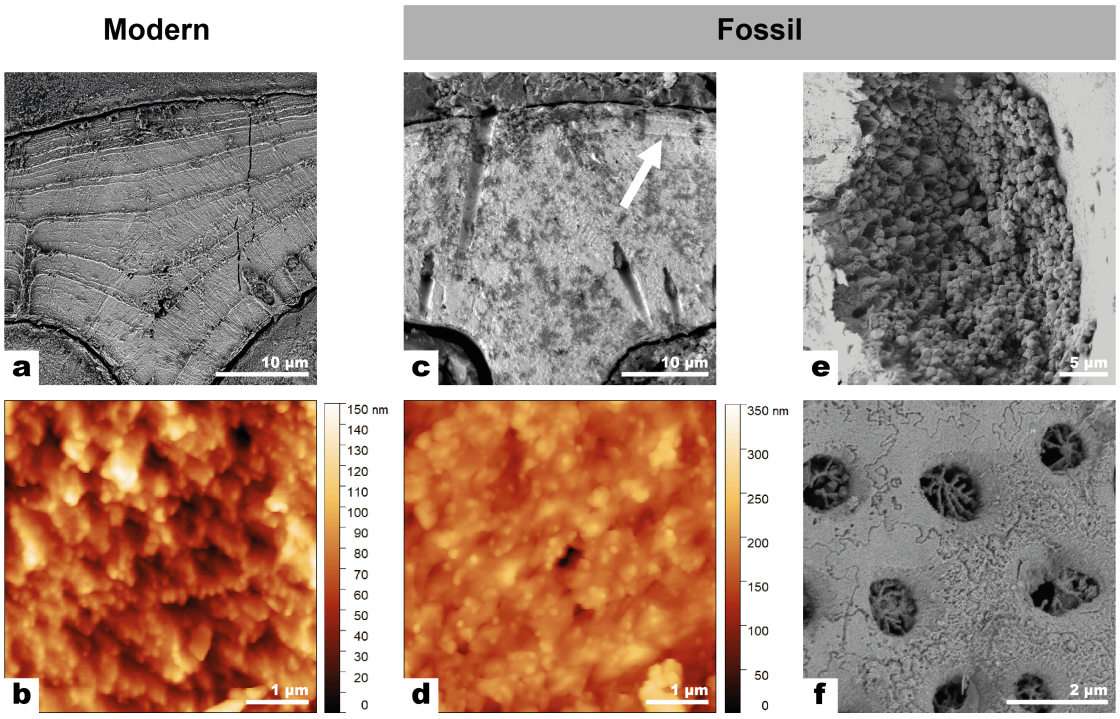

Figure. 3.2 SEM and AFM images of the internal textures of modern and fossil *Ammonia* embedded in epoxy, polished and briefly fixed and etched in a solution of glutaraldehyde and acetic acid (see Methods). (a) Organic linings were clearly visible in modern tests as fine ridges. (b) AFM imaging showed the nanogranular texture of a modern test. (c) SEM image of a fossil test showed an absence of ridges from organic linings, apart from a few regions, as indicated with the white arrow. (d) AFM imaging of fossil tests showed a nanogranular texture comparable to that of the modern test in (b). (e-f) SEM images of the insides of fossil test chambers. (e) Euhedral ca. 1 µm sized secondary calcite grains within the inside of a test. (f) Thin irregular coating of secondary calcite on the inside of a test. A dendritic secondary calcite infilling of the pores was also observed.

In contrast to their relatively pristine outer surfaces, several forms of secondary calcite precipitation were observed on the inner surfaces of fossil tests (Fig. 3.2e, f, and Fig. 3.3c, d): as large blocky crystals of secondary calcite (tens of micrometers) partly filling some chambers (Fig. 3.3d), as ~1 µm euhedral crystals attached to the inside of tests (Fig. 3.2e), as thin irregular coatings of calcite (Fig. 3.2f), and as a dendritic infilling inside some pores (Fig. 3.2f).

Modern tests showed a blue cathodoluminescence with bands of orange that followed the shape of the organic linings and within pores (Fig. 3.3a). Foraminifera can incorporate soluble Mn^{2+} when it is present in their environment under oxygen-depleted conditions, and this banding could indicate that these foraminifera grew in Mn-rich waters with fluctuating oxygen concentrations (Barras *et al.*, 2018; van Dijk *et al.*, 2019). The modern tests also showed orange luminescence within pores, indicating some amount of early secondary calcite coating of pore spaces (Baumgartner-Mora and Baumgartner, 1994) (Fig. 3.3a), although SEM images show that pores are not completely infilled (Fig. 3.3b). The fossil tests luminesced blue and similarly exhibited orange luminescence within pores, with additional bright orange luminescence of the coatings along the inside surfaces of tests (Fig. 3.3c). The large blocky pieces of secondary calcite exhibited strongly zoned CL patterns (Fig. 3.3c, d).

It was previously shown that the cogwheel structures visible on external surfaces (Fig. 3.2f) or inner etched surfaces of tests (Supplementary Fig. 3.2) correspond to 3D domains of different crystallographic orientations. (Nakajima *et al.*, 2016; van Dijk *et al.*, 2020; Cisneros-Lazaro *et al.*, 2022) and EBSD was used to examine potential crystallographic changes due to recrystallization between modern and fossil tests. EBSD maps and pole figures were obtained of surfaces both perpendicular and parallel to the local axis of pores in modern and fossil tests (Fig. 3.3e–l). In these EBSD crystal orientation maps, similar colors indicate regions with similar crystallographic orientations, while contrasting colors indicate adjacent areas with different crystallographic orientations (i.e., where the crystallographic axes misaligned by more than 10°, see Methods). When the imaging surface was perpendicular to the local axis of the pores, the cogwheels formed approximately circular mesocrystals centered around pores in both modern and fossil *Ammonia* (Fig. 3.3e, g). The fine-scale interfingering of cogwheels visible in SEM (van Dijk *et al.*, 2020), TEM (Cisneros-Lazaro *et al.*, 2022) and AFM (Supplementary Fig. 3.2) was not resolvable with EBSD imaging, which was limited to a lateral resolution of ca. 200 nm. The areas between cogwheels were rarely continuously indexed, resulting in an apparent absence of continuous crystal boundaries (black lines in Fig. 3.3e, g, i, k).

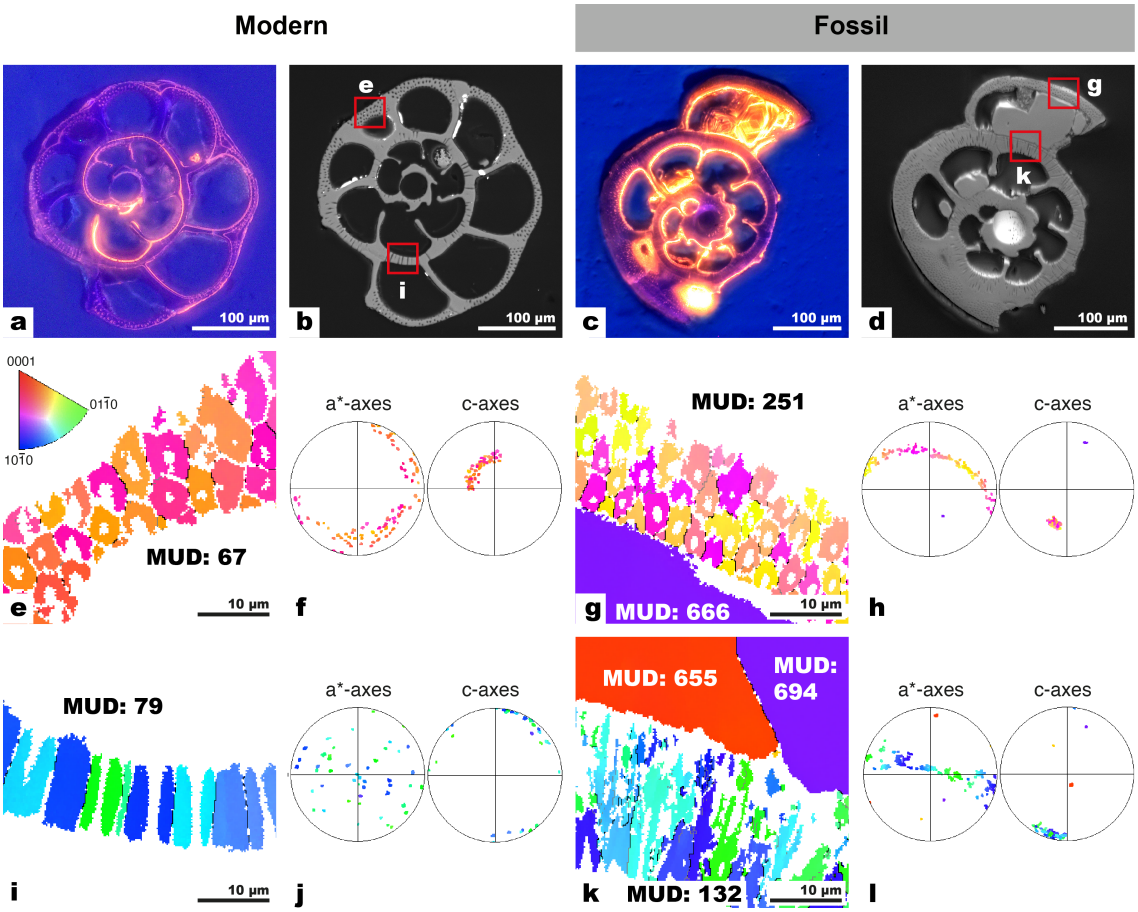

Figure 3.3 CL and SEM images, along with EBSD maps of polished surfaces comparing modern and fossil *Ammonia*. (a–d) CL and SEM images of modern (a, b) and fossil tests (c, d). (a) The bulk of the modern calcite exhibited blue luminescence apart from orange luminescent bands following the pattern of the organic linings, as well as some orange luminescence around pores. (b) SEM image of the same test as in (a) with the location of subsequent EBSD maps marked with red boxes. (c) The bulk of the fossil test calcite luminesced blue, while the pores, coatings along the insides of tests and the zoned blocky secondary calcite showed bright orange luminescence. (d) SEM image of the same test as in (c) with the with the location of EBSD maps marked with red boxes. (e–l) EBSD maps and pole figures of modern and fossil tests showed the cogwheel structures in two orientations: (e–h) the surface perpendicular to the local pore axis, and (i–l) the surface parallel to the local pore axis. Note that while the cogwheel domains were generally smaller in fossil tests, the general shape and orientations of the cogwheel domains were similar to modern tests. EBSD maps of fossil tests (g, k) also showed large blocks of secondary calcite, with

different orientations. The EBSD map in (k) has some areas within the test (in white) that could not be indexed. Multiple of uniform distribution (MUD) values, a measure of crystal co-orientation, are indicated on the maps for both biogenic and secondary calcite.

Despite the large differences in mean pore size and density between modern and fossil tests (Supplementary Table 3.1), the mean cogwheel size for modern tests was only slightly larger than in fossil tests (Table 3.1). When the surface imaged by ESBD was parallel to the local axis of the pores, the cogwheels appeared as elongated domains parallel to axis of the pores (Fig. 3.3i, k). The cogwheel length was greater in fossil tests compared with the modern counterparts (Table 3.1), reflecting the greater thickness of fossil tests (compare Figs. 3.3b and d). For both modern and fossil tests, the c-axis shows a clear preferred orientation perpendicular to the test surface, such that the c-axis rotates with the curvature of the test with the a*-axis randomly oriented on the plane normal to the c-axis (Fig. 3.3f, h, j, l). The large blocks of secondary calcite infilling in fossil tests (Fig. 3.3c, d, g, k) had orientations distinct from the adjacent biogenic calcite (Fig. 3.3h, l).

Several parameters could be quantified from the EBSD data, which differentiated modern, fossil, and secondary calcite. Multiple of uniform (MUD) distribution is a measure of the co-orientation of the crystallographic axes. A MUD value of 1 indicates a random crystallographic orientation whereas MUD values upwards of 600 are found in inorganically precipitated single crystals of calcite (Yin *et al.*, 2019). Modern tests had MUD values of 67 and 79 and fossil tests had MUD values of 132 and 251, perpendicular and parallel to the axes of the pores respectively (Fig. 3.3). MUD values of the secondary calcite precipitated on the inside of fossil tests ranged from 655 to 694 (Fig. 3.3). Mean angular deviation (MAD) is a measure of how well the EBSD patterns were indexed, with a lower MAD indicating higher confidence in indexing. The modern tests showed a relatively high mean MAD value around 1, while the fossil tests showed MAD values (~0.6) closer to that of the secondary calcite (~0.4, Table 3.1).

	Viewing plane relative to pores	Number of grains	Mean cogwheel size (µm^2)	Max length (µm)	S-W p-value	K-S p-value	Mean MAD	SC mean MAD
Modern	Perpendicular	61	12.55 ± 1.31		**<0.01**	0.27	1.10	
	Parallel	22		14.10 ± 0.79	0.05	0.07	0.98	
Fossil	Perpendicular	38	11.67 ± 1.44		**<0.01**	0.21	0.66	0.46
	Parallel	92		23.35 ± 0.39	**<0.01**	**<0.01**	0.61	0.40

Table 3.1 Cogwheel sizes calculated from EBSD data. Reported as mean ± standard error (SE). S-W: Shapiro-Wilk normality test. K-S: Kolmogorov–Smirnov normality test. MAD: Mean angular deviation. SC: Secondary calcite. Bold values indicate a non-normal distribution.

3.3.2 NanoSIMS imaging of ^{18}O-enrichments in modern and fossil Ammonia tests exposed to identical diagenetic conditions

Modern and fossil *Ammonia* tests were exposed to experimental conditions similar to those of a previous study (Cisneros-Lazaro *et al.*, 2022), namely incubation at 90 °C for 6 days in a highly ^{18}O-enriched artificial seawater at chemical equilibrium ($^{18}O/^{16}O$ = 0.30, $\Omega_{calcite}$ = 1). NanoSIMS imaging subsequently permitted the quantitative visualization of the amount of isotopic exchange with the seawater. Because of the chemical equilibrium between tests and artificial seawater, no significant changes to test textures resulted from these incubations, i.e., the tests remained visually pristine (Supplementary Fig. 3.3), consistent with observations from similar previous experiments (Bernard *et al.*, 2017; Cisneros-Lazaro *et al.*, 2022; Adams *et al.*, 2023). NanoSIMS images were obtained of surfaces parallel and perpendicular to the local pore axis (Fig. 3.4). Consistent with previous results (Cisneros-Lazaro *et al.*, 2022), modern *Ammonia* tests exchanged oxygen isotopes

efficiently with the artificial seawater, as demonstrated by the pervasive ^{18}O-enrichment of the entire test relative to control samples (Fig. 3.4a). The highest measured ^{18}O-enrichments occurred along two main penetration pathways: cogwheel interfaces and organic linings (Fig. 3.4a), which are common to all rotaliid foraminifera and visualized here with nitrogen measured as $^{12}C^{14}N^-$ (Fig. 3.4b). Fossil tests also showed extensive O-isotope exchange throughout the test structure (Fig. 3.4e, i). However, in contrast to modern tests, the fossil tests had a lower level of O-isotope exchange along organic linings (Fig. 3.4e, i) and there was no evidence for effective exchange along cogwheel structures (Fig. 3.4i). Sulfur and magnesium bands (comparable in modern and fossil tests) were not correlated with ^{18}O-enrichments (Fig. 3.4c, d, g, h, k, l). Secondary, blocky calcite in fossil tests was enriched in Mg (Fig. 3.4l) but did not show detectable ^{18}O-enrichment (Fig. 3.4i).

The average ^{18}O-enrichment, relative to control (i.e., unlabeled) tests of the same species, was 325 ± 58 ‰ (n = 20) for modern *Ammonia* and 186 ± 76 ‰ (n = 28) for fossil *Ammonia* (Fig. 3.5, Supplementary Table 3.2), which was statistically different (t (46) = 6.8, $p < .001$). Comparing the average ^{18}O-enrichments of individual tests showed that some fossil tests were more reactive than others, with some fossil tests as susceptible to diagenetic isotope exchange as modern tests (Fig. 3.5). The average $\delta^{18}O$ of secondary calcite was 10 ± 24 ‰ (n = 10), i.e., effectively zero enrichment within the roughly 30 ‰ (conservative) detection limit of the NanoSIMS operating in this imaging mode.

Figure 3.4. (Following page) NanoSIMS images of the polished surfaces of modern and fossil *Ammonia* after exposure to artificial seawater (ASW) with a $^{18}O/^{16}O$ ratio of 0.30 for 6 days at 90 °C. (a–d) ^{18}O-enrichments and elemental bandings in modern tests. (a) ^{18}O-enrichments were heterogenous but occurred predictably along cogwheel structures and organic linings. (e–l) ^{18}O-enrichments and elemental bandings in fossil tests. (e) ^{18}O-enrichments in fossil tests were also heterogenous but did not show increased ^{18}O-enrichment along recognizable ultrastructures. In (e) relatively low ^{18}O-enrichments were observed in the areas where the organic linings are normally situated (see CN banding in f). Note the generally low-to-negligible ^{18}O-enrichment of the secondary calcite infilling on either side of the test in (i) and the relatively high Mg-content of this secondary calcite (l).

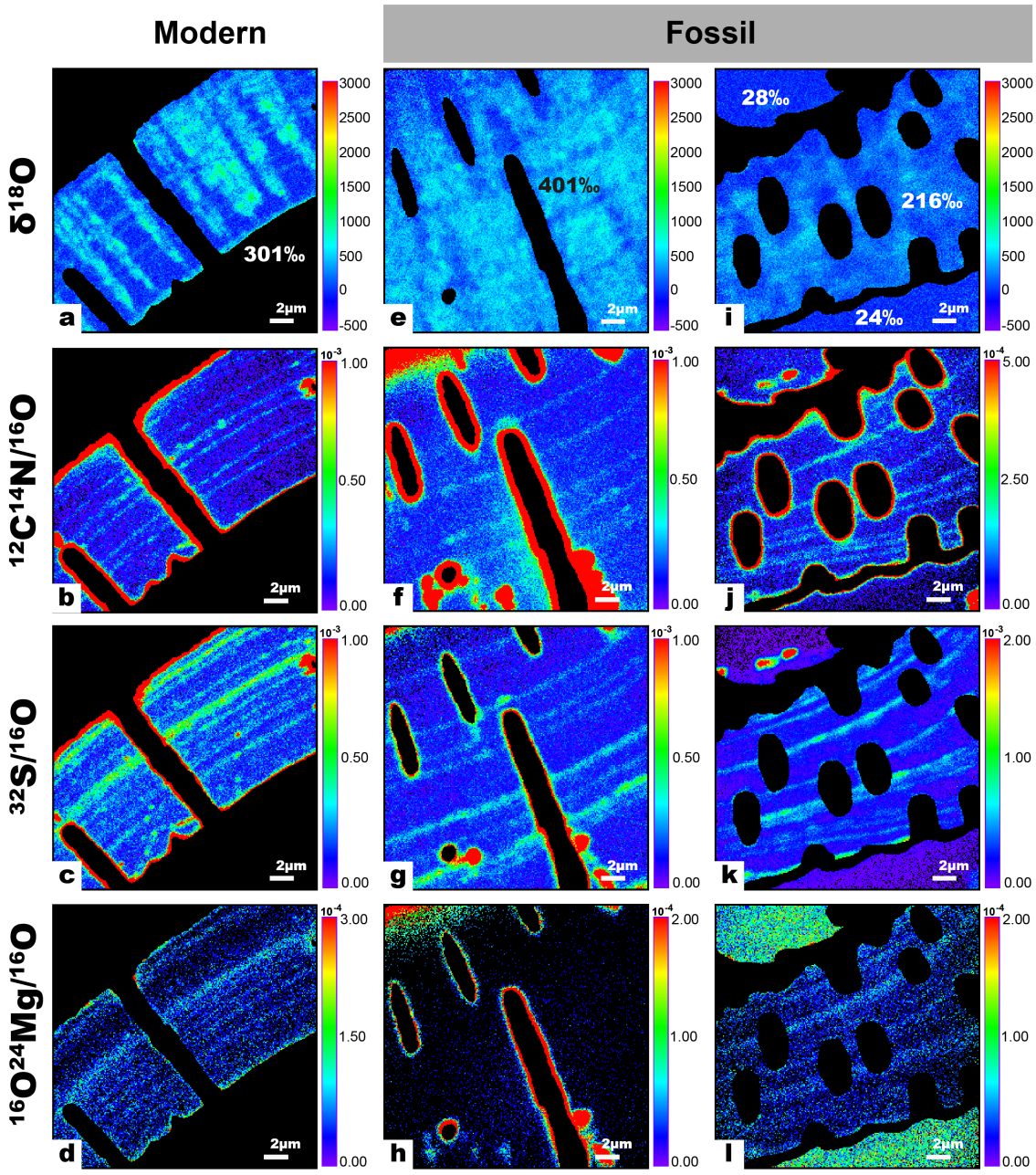
Modern
Fossil
δ18O
12C14N/16O
32S/16O
16O24Mg/16O
301‰
401‰
28‰
216‰
24‰
2μm
a
b
c
d
e
f
g
h
i
j
k
l
3000
2500
2000
1500
1000
500
0
-500
10-3
1.00
0.50
0.00
10-4
5.00
2.50
2.00
1.00
3.00
1.50

3.4 Discussion

3.4.1 Preservation state of fossil tests used in this study

The multi-analytical imaging approach (SEM, AFM, CL, EBSD, NanoSIMS) employed here demonstrates that the fossil foraminifera tests used in this study were exceptionally preserved, though there are some caveats to consider. First, the external textures of tests, which is one of the main criteria for identifying diagenetically altered/unaltered foraminifera to be accepted/rejected for paleo-temperature reconstructions, were highly similar between these fossil and modern tests (Fig. 3.1). The glassy-frosty paradigm has established that fossil tests that appear 'frosty' under optical microscopy are recrystallized and generally yield strongly biased $\delta^{18}O$-based seawater temperatures reconstructions because of secondary carbonate precipitation, in contrast to 'glassy' tests that are typically derived from hemipelagic clay-rich sites and have preserved a translucent appearance (Pearson *et al.*, 2001; Wilson *et al.*, 2002; Sexton *et al.*, 2006b). However, even the glassy fossil tests used here showed clear evidence for internal secondary calcite precipitation (Fig. 3.2e, f); this would not disqualify these fossil tests from inclusions in paleoclimate reconstruction studies. Recently, researchers have been using microspatial in-situ techniques to identify authigenic overprints and select the more pristine parts of tests for these analyses (Kozdon *et al.*, 2011, 2013; Stainbank *et al.*, 2020; Staudigel *et al.*, 2022).

The secondary calcite in this study was highly luminescent and occurred within pores of both modern and fossil tests, as well as large blocky calcite infilling of fossil tests (Fig. 3.3a, c). However, the fossil test calcite itself was not luminescent, which is a strong indication that recrystallization did not occur (Baumgartner-Mora and Baumgartner, 1994). Furthermore, NanoSIMS imaging showed that this blocky secondary calcite is Mg-rich (Fig. 3.4l) while the test calcite contained very little Mg, beyond the naturally occurring Mg-banding in foraminifera (Geerken *et al.*, 2019) (Fig. 3.4d, h, l). Overall, the evidence from optical and SEM images of the outer surfaces of tests, CL and NanoSIMS imaging attest to the excellent preservation state of the fossil tests.

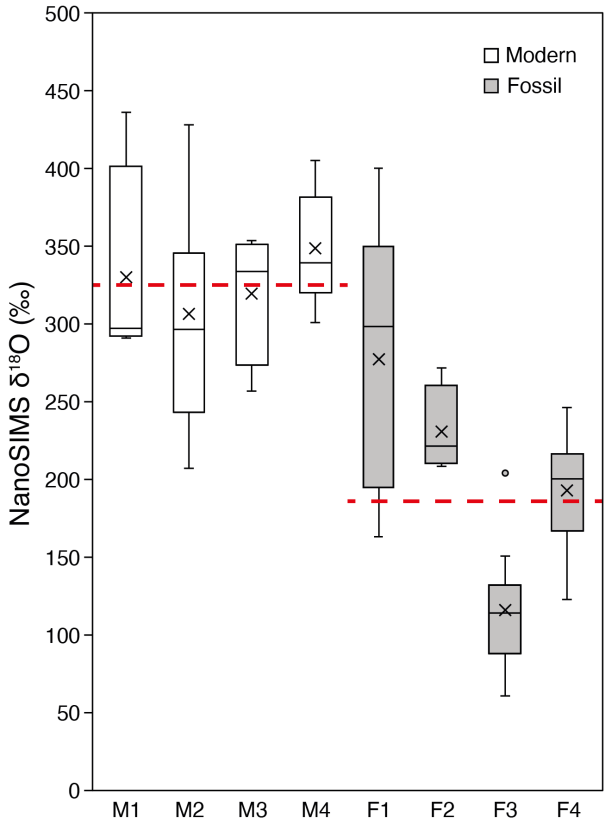

Figure 3.5 ^{18}O-enrichments measured with NanoSIMS in modern and fossil tests after exposure to ASW with a $^{18}O/^{16}O$ ratio of 0.30 for 6 days at 90 °C. NanoSIMS ^{18}O-enrichments per test show similar variability for modern and fossil *Ammonia*. NanoSIMS ^{18}O-enrichment, relative to pristine tests of the same species, was on average 325 ± 58 ‰ (n = 20) for modern *Ammonia* and 186 ± 76 ‰ (n = 28) for fossil *Ammonia*, as indicated by the red dashed lines. The × sign indicates average ^{18}O-enrichments for individual tests. Middle lines = medians, boxes = interquartile ranges, whiskers = minimum and maximum values, empty circle = extreme outlier.

However, SEM images of the internal textures of tests revealed differences between modern and fossil test calcite, primarily related to the degradation of organic matter. Fixation and etching of modern tests showed prominent ridges at the location of the organic linings (Fig. 3.2a). Apart from occasional ridges (e.g., white arrow in Fig. 3.2c), similar regions in fossil tests did not show much evidence for the preservation of organic linings. NanoSIMS maps nevertheless showed that CN-

bandings were preserved in fossil tests in a manner similar to that of modern tests (Fig. 3.4). Foraminiferal organic linings are predominantly made up of proteins and polysaccharides (Fhlaithearta *et al.*, 2013) and are known to persist in some form for millions of years (Stancliffe, 1989). However, proteins in fossils invariably partially degrade into smaller peptides over time (Drake *et al.*, 2020; Warinner *et al.*, 2022; Stolarski *et al.*, 2023). In a study of the degradation of intracrystalline proteins in fossil brachiopods, Walton (1998) found that 95 % of proteins were degraded into their constituent amino acids after only 120 kyrs. Proteins that are bound to mineral surfaces, such as the charged proteins in organic linings thought to be responsible for directing nucleation of calcite (de Nooijer *et al.*, 2014b), are among the most resistant to degradation (Demarchi *et al.*, 2016). The lack of relief in etched samples in the SEM and NanoSIMS images suggests that the bulk of the organic linings was degraded, but the organic molecules bound to the test calcite were preserved and are the source of the nitrogen (CN^-) counts in the NanoSIMS maps (Fig. 3.4). Since no obvious gaps in the tests occur where the organic matter would normally be found (Fig. 3.2c), it is possible that the voids created by the loss of organic matter were either sealed due to pressure or filled by trace amounts of secondary calcite, although this is not observable as enhanced cathodoluminescence. Despite the differences in the internal textures observed with SEM, the AFM imaging indicated no difference between the nanogranular structures of modern and fossil tests (Fig. 3.2b, d).

EBSD mapping offered another relevant comparison between modern and fossil tests and is increasingly being used to identify diagenetic overprints in biominerals, often centered on the question of overprinting of biogenic aragonite with secondary calcite (Cusack *et al.*, 2008b; Dalbeck *et al.*, 2011; Casella *et al.*, 2017; Pederson *et al.*, 2019, 2020). In simulated diagenesis experiments on bivalves, gastropods and corals, EBSD was used to track the subtle reorganization of the aragonitic microstructure well before transformation into calcite (Forjanes *et al.*, 2022). Similarly, Casella and colleagues (2018) used EBSD to compare the textures of naturally and experimentally altered calcitic brachiopod shells.

The MUD (multiple of uniform distribution) value, a measure of crystal co-orientation strength, is increasingly used to quantify the degree of diagenetic alteration in biogenic carbonates. Whether diagenesis leads to an increase or decrease in the degree of co-orientation seemingly depends on

the microstructure, which is a function of the genus. Casella and colleagues (2018) found that MUD values in fossil and hydrothermally altered calcitic brachiopods were lower relative to modern pristine brachiopods. Consistently, Forjanes and colleagues (2022) found that the hydrothermally altered aragonitic bivalve *Artica islandica* had lower MUD values compared to pristine samples. Yet, these authors also found that diagenetic overprints to aragonitic nacre in gastropod *Haliotis ovina* led to a sharp increase in MUD values (Forjanes *et al.*, 2022). In our study, modern *Ammonia* tests had MUD values between 67 and 79 (Fig. 3.3), which is roughly similar to MUD values of pristine bivalves and gastropods (Forjanes *et al.*, 2022), brachiopods (Casella *et al.*, 2018), and foraminifera (Yin *et al.*, 2021). Fossil tests had higher MUD values between 132 and 251, with the secondary calcite crystals occurring as blocks of a uniform orientation and showing the highest MUD values between 655 and 694 (Fig. 3.3), consistent with MUD values of inorganically precipitated calcite (Yin *et al.*, 2019).

Differences in MAD values (mean angular deviation, calculated from the EBSD data) between modern and fossil tests and secondary calcite offered another point of comparison. Fossil tests had MAD values of ca. 0.6, closer to secondary calcite (~0.4) than to modern tests values (~1). This could potentially be explained by the degradation of organic matter and potential infilling of these gaps with secondary calcite (Fig. 3.2c and Supplementary Fig. 3.2), which would decrease the MAD value compared to modern tests. If there was secondary calcite infilling of the gaps created by the loss of organic matter, it either grew epitaxially on the test calcite or was too small to be distinguished by the electron beam in EBSD maps (surface spot-size of 200 nm, but with a larger interaction volume due to the high voltage used). Both MUD and MAD indicate that the fossil calcite tests were somewhere along a continuum between biogenic and abiotic calcite.

In summary, the geometry of cogwheel structures was similar between fossil and modern tests (Fig. 3.3) but quantification of EBSD parameters, such as MUD and MAD, indicates that fossil tests have some similarity with inorganically precipitated calcite. Altogether, NanoSIMS, SEM, AFM, CL and EBSD observations suggest that the fossil *Ammonia* tests used in this study are well-preserved specimens, yet close inspection reveals some subtle alteration, mostly related to the degradation of organic matter and associated, subtle re-ordering of the crystallography.

The similarity in cogwheel structures as seen on EBSD maps of modern and fossil foraminifera tests separated in time by 14 m.y. suggests a highly consistent biomineralization process in the *Ammonia* genus through geological time.

3.4.2 The difference in diagenetic susceptibility between modern and fossil calcite

Previous work has established that fluids will exploit two organic-rich ultrastructures common to all hyaline rotaliid foraminifera – cogwheel structures and organic linings – to pervasively penetrate and isotopically exchange with foraminiferal test calcite (Cisneros-Lazaro *et al.*, 2022). It was also postulated that beyond the large surface areas created by the nanogranular structure inherent to foraminifera tests, it is partly the inter- and intracrystalline organic matter that facilitates this isotopic exchange. Biogenic calcite has longer and weaker C-O bonds than abiotic calcite due to the anisotropic lattice distortions caused by intracrystalline organic macromolecules (Pokroy *et al.*, 2006a; Zolotoyabko *et al.*, 2010; Stolarski *et al.*, 2016; Zolotoyabko, 2017). Thus, this organic matter not only creates pathways for fluids to penetrate into the test structure, but also makes this organic matter-associated calcite more reactive. With the gradual degradation of organic matter in biogenic carbonates during fossilization, some authors have proposed that the anisotropic strain induced by organic molecules may relax and the lattice parameters of biogenic calcite will approach that of inorganically precipitated calcite (Pokroy *et al.*, 2006b; Zolotoyabko, 2017; Lang *et al.*, 2020). Additionally, as organic matter degrades, oxidative reactions producing CO_2 could lower the local pH, which may increase calcite reactivity at these sites (van der Weijden, 1992). However, even with a rapid degradation of intercrystalline organics (Bernard and Papineau, 2014; Malinverno and Martinez, 2015; Wheeler *et al.*, 2021) and a – presumably slower – decay of intracrystalline organics over time (Sykes *et al.*, 1995; Walton, 1998), the question remains how fast fossil biocarbonates continue to exchange isotopically with porewaters.

From NanoSIMS images of the experimentally incubated fossil tests, it is clear that despite the diminished organic matter content, diagenetic fluids can still penetrate into and exchange with fossil calcite (Fig. 3.4e, i). The observed ^{18}O-enrichment was pervasive with areas of preferential O-isotope exchange, but these patchy enrichments bore no relationship to ultrastructural features such as organic linings, cogwheel structures or elemental banding (Fig. 3.4). In fact, there seemed to have been a lower rate of exchange at the locations of the partially degraded organic linings (Fig.

3.4e, f). This contrasts with modern tests that exhibit with preferential O-isotope exchange along cogwheel structures and organic linings (Fig. 3.4a). As shown here and in previous work, secondary abiotic calcite is much less susceptible to isotopic exchange than biogenic calcite (Cisneros-Lazaro *et al.*, 2022). Internal secondary calcite precipitation filling the space after degradation of organic linings (Fig. 3.2c) could therefore explain the lower O-isotope exchange at these sites (Fig. 3.4e).

Comparing average NanoSIMS ^{18}O-enrichments in experimentally incubated modern and fossil tests, the fossil tests were about 40 % less enriched (Fig. 3.5). The lack of overt recrystallization as documented with AFM and EBSD, suggests that the main difference between the modern and fossil tests used in this study was the reduced amount of organic matter in fossil tests. In other words, the organic matter lost was contributing to around half of the reactivity of foraminiferal calcite. Chanda and colleagues (2019) similarly found differences in the reactivities of modern and fossil foraminiferal calcite to ^{45}Ca-spiked fluids, with modern tests reacting about ten times faster than fossil tests. They compared modern tests and 3 populations of fossil tests at drill core depths of 0–100, 100–200, and 200–300 meters below seafloor, with the latter dated to the middle/late Miocene (ca. 10.4 Ma) (Kroenke *et al.*, 1991), i.e., similar to the fossil tests used in this study. These authors found that shallowly buried (younger) fossil tests incorporated more of the ^{45}Ca tracer than more deeply buried (older) tests, and proposed that these differences could be due to these tests having different reactive histories, i.e., that some tests have partially been recrystallized (Chanda *et al.*, 2019). If the preservation state of the fossil specimens in the Chanda and colleagues (2019) study is comparable to the fossil tests in the present study, we propose that these differences in diagenetic susceptibility could also be due to the progressive degradation of the inter- and intracrystalline organic material in fossil specimens over time.

3.4.3 The role of organic matter degradation in fossil calcite diagenesis and the implications for paleo-environmental reconstructions

Following the death of a marine calcifier, diagenetic processes begin to alter the original isotopic and chemical composition of its biocarbonate remains (Pearson and Burgess, 2008). As shown here and in our previous work (Cisneros-Lazaro *et al.*, 2022), seawater will exploit organic-rich ultrastructures during early diagenesis to rapidly and pervasively penetrate the bulk of the shell calcite. During burial, as temperatures increases and/or pore fluid isotope (and chemical)

compositions deviate from those of the original seawater, the isotope disequilibrium between these early diagenetic fluids and the buried biominerals increases, leading to a modification of the isotopic composition of the shells (Bernard *et al.*, 2017; Adams *et al.*, 2023). As fossilization progresses, the degradation of intercrystalline organics, such as organic linings in foraminifera, creates secondary porosity, which could be infilled with early diagenetic calcite that may partially reduce the susceptibility of fossil calcite to further diagenetic isotope exchange. But clearly, as shown in this work, fossil biocalcite does not lose its capability to exchange isotopically with surrounding porewaters. A schematic model for the relationship between the degradation of inter- and intracrystalline organics and diagenetic isotope exchange is shown in Fig. 3.6.

The present study and that of Chanda and colleagues (2019) show that despite age-related reductions in diagenetic susceptibility, fossil calcite remains much more susceptible to diagenetic isotope exchange than abiotic calcites. AFM images in this study revealed no changes in the nanogranular structure between modern and fossil foraminifera. The small sizes of the nanograins (20 to 150 nm) that constitute the bulk of the majority of biocalcites (Wolf *et al.*, 2016), means that grain boundary and lattice diffusion can measurably alter the isotopic composition of the biocalcite used for paleoclimate reconstructions. The effects of grain boundary diffusion alone can, on timescales of hundreds of years, bias paleotemperature reconstructions by up to 1 °C and, given enough time, the effects of lattice diffusion can cause even more under- or overestimates of the true paleotemperature calculated from oxygen isotope compositions (Bernard *et al.*, 2017; Adams *et al.*, 2023). The oxygen diffusion coefficients derived from biocalcites are larger than for abiotic minerals, probably as a consequence of embedded organic matter (Adams *et al.*, 2023). Conducting similar simulated diagenesis experiments on excellently preserved fossil calcites of different ages may allow for an evaluation of whether the oxygen diffusion coefficient of biocalcites changes as a function of the remaining organic content. The susceptibility of biocalcites to diagenetic isotope exchange over time could be calculated, and the bias to paleoclimate records based on oxygen isotope composition could be corrected.

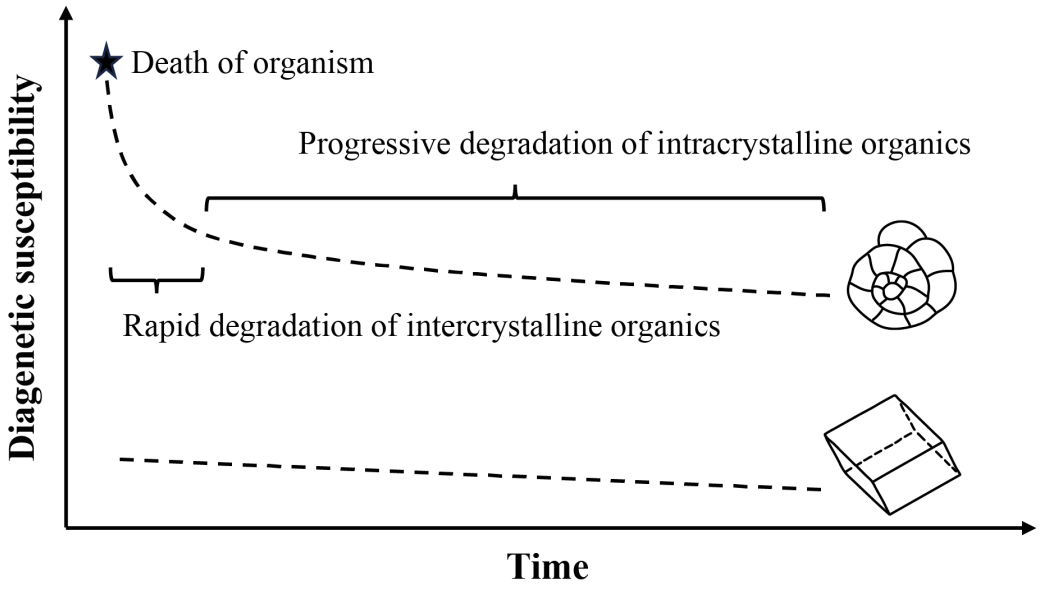

Figure 3.6 Conceptual model for the diagenetic susceptibility of fossil biocalcite compared to abiotic calcite over time.

In this study, we used a multi-analytical screening approach (SEM, AFM, CL, EBSD, NanoSIMS) to compare the ultrastructure and crystallography of modern and fossil *Ammonia* species. We investigated oxygen isotope exchange with highly controlled incubation experiments on these materials. Despite substantial (but not complete) degradation of organic matter-rich pathways that facilitate fluid penetration in modern tests and offer more reactive sites for O-isotope exchange, fossil tests exhibited around half the ^{18}O-enrichment compared with pristine modern foraminifera. This demonstrates that, while early diagenesis will proceed along organic-rich structures in the carbonate skeletons of recently deceased organisms, fossilized tests with diminished amounts of organic matter are far from impervious to the effects of long-term diagenesis. The best (and perhaps only) way to remove this bias from paleo-ocean temperature records calculated from oxygen isotope compositions of carbonate fossils is to better understand the diagenetic susceptibility of biogenic carbonates and to apply the necessary correction factors to existing data.

3.5 Supplementary information

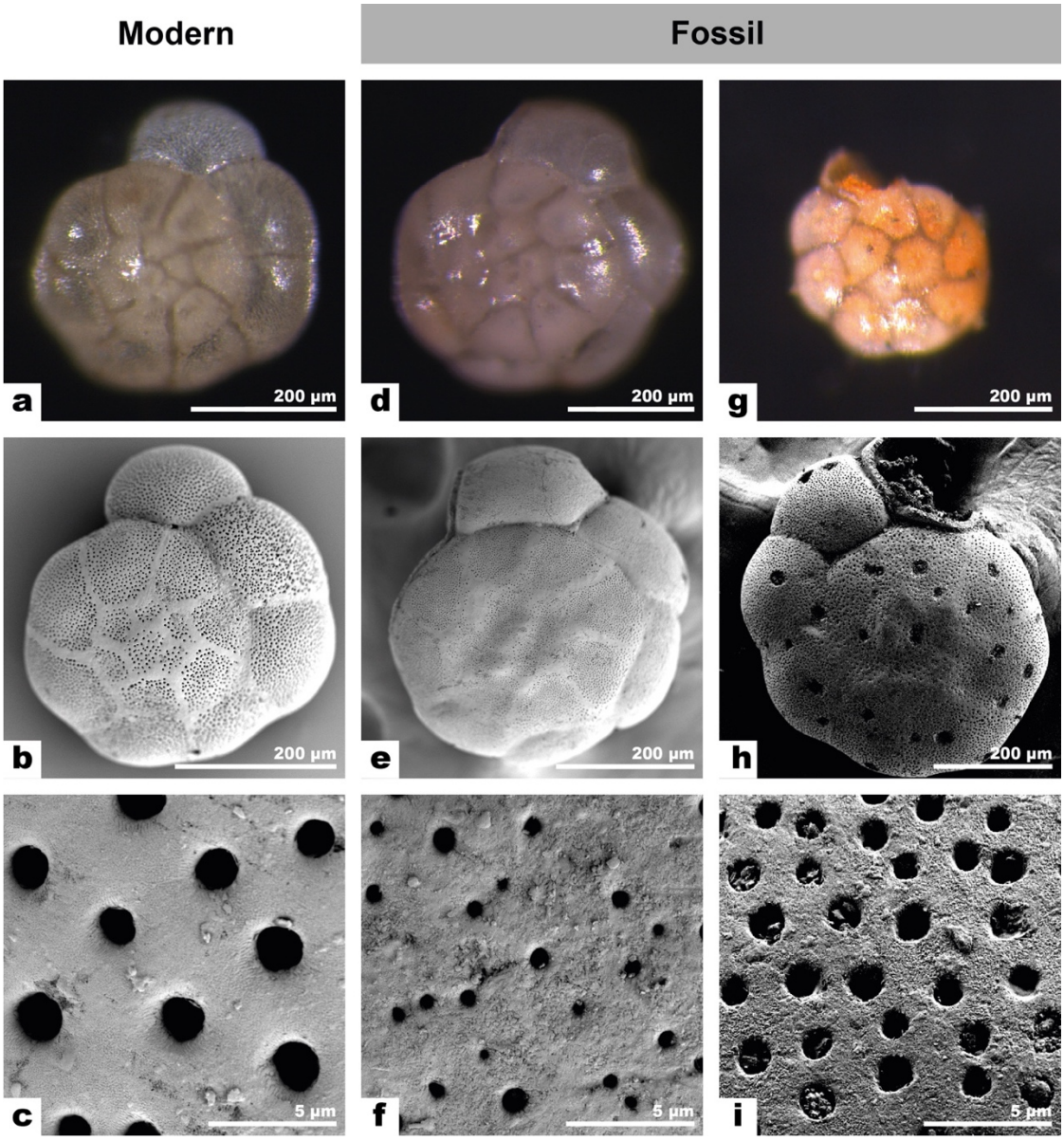

Supplementary Figure 3.1 (Preceding page) Stereo microscopy and SEM images comparing modern *Ammonia confertitesta* and fossil *Ammonia beccarii* tests. (a–c) A modern test appearing glassy under optical microscopy and exhibiting pristine surface textures, revealing the underlying nanogranular texture in close-up SEM images. Some small overgrowths can be observed (c). (d–f) Only fossil tests that appeared similarly glassy under optical microscopy were selected for the incubation experiments. Most pores were free of infilling and there were only small amounts of overgrowths on the outside surface. (g–i) Fossil tests that appeared 'frosty' and showed clear evidence of damage were not selected for the incubation experiments. These tests showed more evidence for pore infilling than more glassy-looking fossil tests.

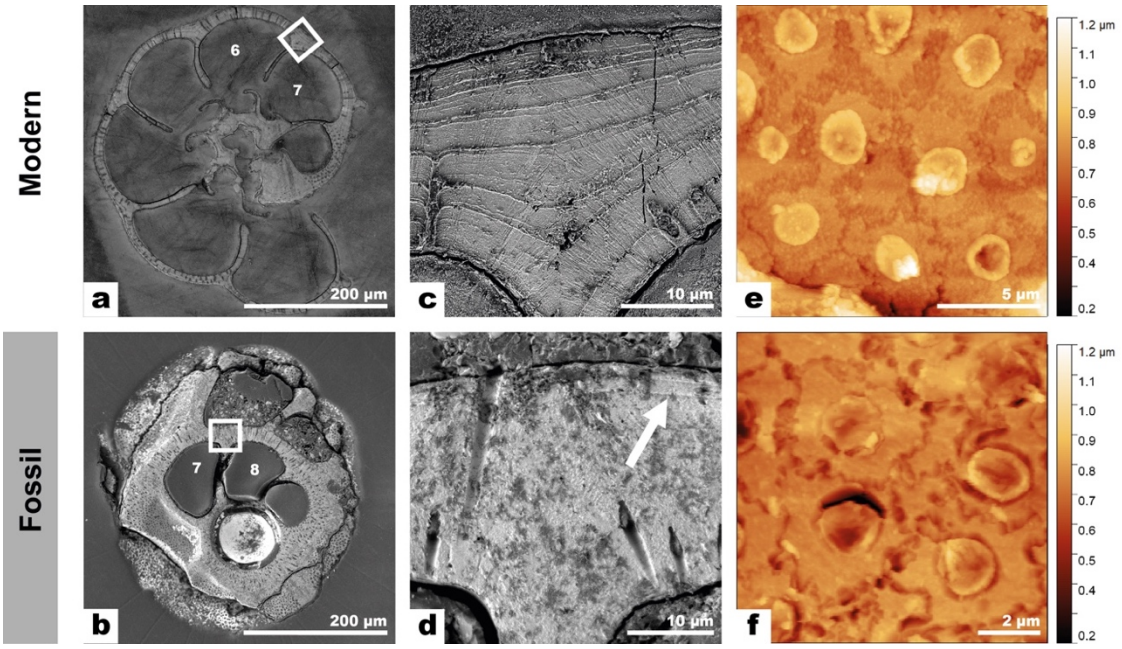

Supplementary Figure 3.2 SEM and AFM images of modern and fossil tests embedded in epoxy, polished and briefly fixed and etched in a solution of glutaraldehyde and acetic acid. (a-d) SEM images of whole tests showing the number of organic linings expected for the chamber position, with the white squares in (a–b) indicating the location of images (c–d). (c–d) Close-up SEM image showing the organic linings clearly standing out as ridges in modern tests, which are not visible in fossil tests apart from at the location of the white arrow. (e–f) AFM images of cogwheel structures in modern and fossil tests. Cogwheel boundaries are present as depression in the surface.

	Porosity %	Number of pores	Mean pore size (μm^2)	Shapiro-Wilk p-value	Kolmogorov-Smirnov p-value
Modern	12.79	18	2.11 ± 0.12	0.36	0.89
	18.45	24	2.04 ± 0.18	0.93	1
	9.60	12	2.40 ± 0.22	0.59	1
Fossil	3.81	35	0.31 ± 0.02	**<0.01**	0.42
	5.94	37	0.46 ± 0.03	0.11	0.87
	9.56	33	0.97 ± 0.05	0.95	1

Supplementary Table 3.1 Porosity and pore size were determined by analysis of SEM images of the penultimate chamber of 3 modern and fossil *Ammonia* tests following Petersen *et al.* (2016) and van Dijk *et al.* (2020). Shapiro-Wilk and Kolmogorov-Smirnov tests, as well as visual inspection of Q-Q plots were used to test for normality of distribution. Bold values indicate a non-normal distribution. Modern tests had larger, more closely spaced pores (i.e., greater porosity) in contrast to fossil tests which had smaller, more sparsely spaced pores (i.e., lower porosity).

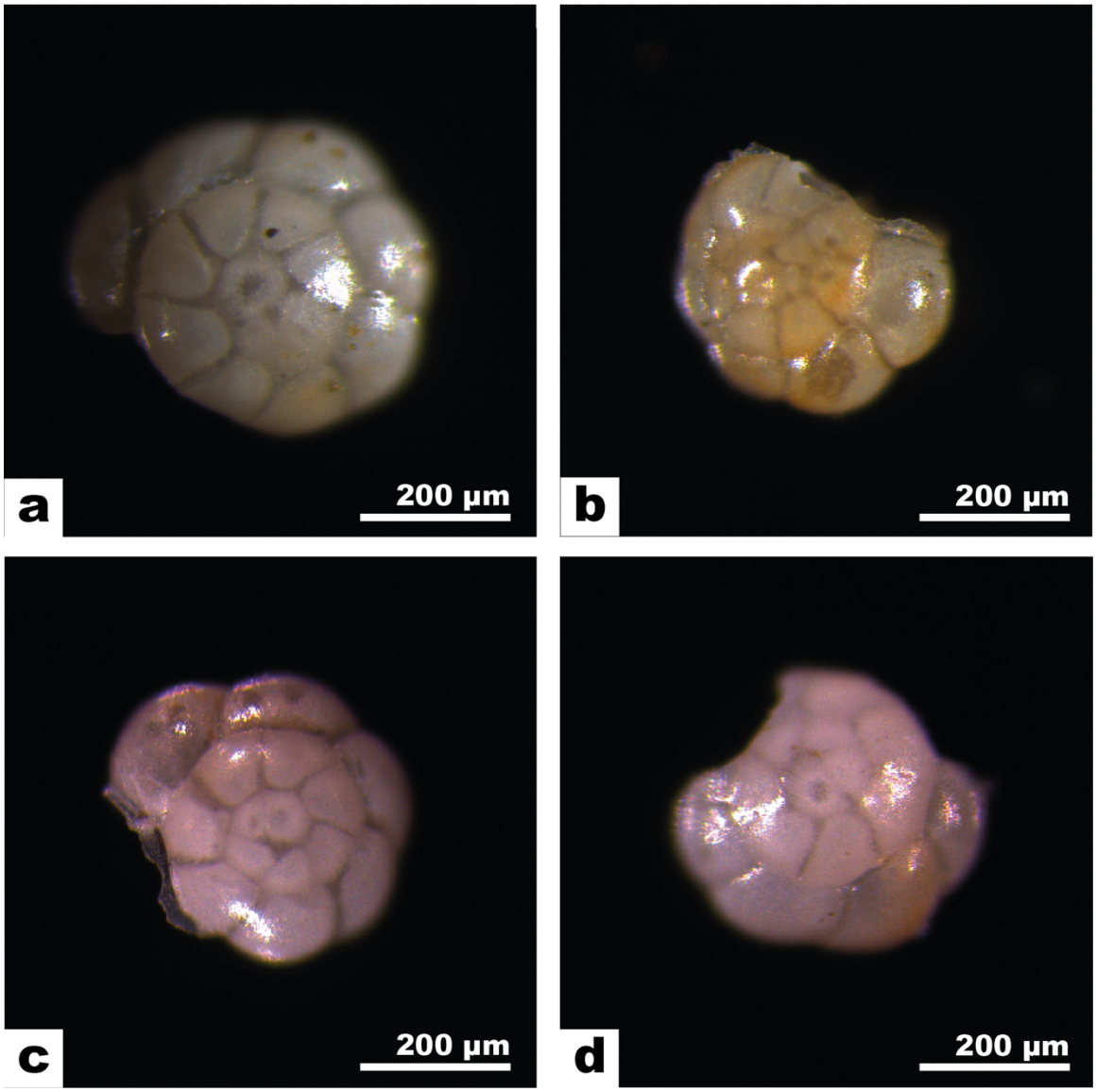

Supplementary Figure 3.3 Stereo microscopy images of two *Ammonia beccarii* tests before (top row) and after (bottom row) exposure to artificial seawater with a $^{18}O/^{16}O$ ratio of 0.30 for 6 days at 90 °C. Note that after the incubation experiment the tests were more fragile and younger chambers were often lost. All images were taken under comparable imaging conditions with the same camera and at the same scale.

Average NanoSIMS $\delta^{18}O$ (‰)

Species	Modern		Fossil		Secondary calcite in fossil tests
	M1	299	F1	401	28
	M1	437	F1	300	24
	M1	296	F1	299	6
	M1	291	F1	226	16
	M2	429	F1	163	-12
	M2	243	F2	227	3
	M2	345	F2	208	-20
	M2	279	F2	272	39
	M2	207	F2	216	44
	M2	346	F3	122	-29
	M2	297	F3	204	
	M3	257	F3	125	
	M3	346	F3	60	
	M3	354	F3	106	
	M3	323	F3	150	
	M4	359	F3	67	
	M4	340	F3	113	
	M4	340	F3	114	
	M4	406	F3	94	
	M4	301	F4	246	
			F4	173	
			F4	122	
			F4	225	
			F4	200	
			F4	204	
			F4	208	
			F4	198	
			F4	160	
Average		325		186	10
SD		58		76	24
n		20		28	10

Supplementary Table 3.2 (Preceding page) Summary table of the oxygen isotope measurements and average $\delta^{18}O$ of modern and fossil *Ammonia* tests as well as secondary calcite precipitations (associated with fossil tests) incubated for 6 days at 90 °C in artificial seawater with a $^{18}O/^{16}O$ ratio of 0.30. The NanoSIMS measurements each reflect the $\delta^{18}O$ measured over a 25 by 25 um^2 area. M# and F# refer to individual modern and fossil tests respectively.

4 *Abundant intracrystalline saccharides within the calcitic prisms of bivalve Pinctada margaritifera: Insights into biomineralization and bioinspired structural materials*

Deyanira Cisneros-Lazaro[1*], Arthur Adams[1], Laura M. Otter[2], Jarosław Stolarski[3], Sylvain Bernard[4], Damien Daval[5], Alain Baronnet[6], Lukas P. Baumgartner[7], Torsten Vennemann[8], Hemant K. Raut[1], Stéphane Escrig[1] and Anders Meibom[1,7*]

[1] Laboratory for Biological Geochemistry, School of Architecture, Civil and Environmental engineering, Ecole Polytechnique Fédérale de Lausanne, Lausanne, CH-1015 Switzerland

[2] Research School of Earth Sciences, Australian National University, Canberra, ACT 2601, Australia

[3] Institute of Paleobiology, Polish Academy of Sciences, PL-00-818 Warsaw, Poland

[4] Museum National d'Histoire Naturelle, Sorbonne Université, CNRS UMR 7590, IMPMC, 75005 Paris, France

[5] ISTerre, Univ. Grenoble Alpes, Univ. Savoie Mont Blanc, CNRS, IRD, IFSTTAR, 38041, Grenoble, France

[6] CNRS, CINaM, Aix-Marseille Université, 13009 Marseille, France

[7] Center for Advanced Surface Analysis, Institute of Earth Science, University of Lausanne, CH-1015 Lausanne, Switzerland

[8] Institute of Earth Surface Dynamics, University of Lausanne, CH-1015 Lausanne, Switzerland

This chapter will be submitted to Biomaterials.

Author contribution statement

DC-L, AA, LMO, JS and AM designed the experimental study; DC-L acquired the SEM images, DC-L acquired the EBSD data, DC-L and SE acquired the NanoSIMS data, DC-L and LMO acquired the PiFM data, DC-L, AA and AM drafted the manuscript. All co-authors contributed to the writing of the manuscript.

Abstract

The calcitic prismatic layer of nacroprismatic bivalves is a biogenic composite material with high compressive strength, hardness, and toughness that serves as an effective defense against predators. However, the composition and spatial organization of the occluded organic phases, which is key to attaining these beneficial mechanical properties, remains poorly documented. Here, NanoSIMS imaging and Photo-induced Force Microscopy (PiFM) are used to chemically map and fingerprint the inter- and intracrystalline organic moiety in *Pinctada margaritifera* shells. It is shown that proteins are mostly confined to the interprismatic organic membranes and intracrystalline saccharides dominate within the prims, where they are heterogeneously distributed. Our findings suggest that intracrystalline saccharides are much more important to the biomineralization processes of marine calcifying organism than previously appreciated. It also suggests that saccharides could be an important additive for improving damage tolerance in bioinspired high-performance structural materials.

4.1 Introduction

The shells of nacroprismatic bivalves have an outer calcitic layer, which provides protection against mechanical and chemical attacks from predators and the environment, and a highly fracture resistant inner nacreous layer, which provides the shell with high mechanical strength (Currey, 1989; Marin *et al.*, 2012; Gim *et al.*, 2019; Wan *et al.*, 2019). These shells are mineral-organic composites that can be significantly stronger, harder, and tougher than the minerals from which they are comprised, in part due to the hierarchal organization of embedded organic components across multiple length scales (Schenk and Kim, 2015; Deng *et al.*, 2022). Nacre has been particularly well-studied due to its superior mechanical properties (Currey, 1977; Jackson *et al.*, 1988; Gim *et al.*, 2019; Liang *et al.*, 2023). Conversely, the calcitic prismatic layer has long been studied for its use as a paleoclimate archive of past oceanic conditions (Immenhauser *et al.*, 2016), but more recently there has also been significant interest regarding the mechanical properties of its single crystals (Kunitake *et al.*, 2013; Metzger *et al.*, 2014; Deng *et al.*, 2020; Wallis *et al.*, 2022). Despite making up less than 1 wt. % of the prismatic layer, embedded nanoscopic intracrystalline organics simultaneously strengthen and toughen prisms by directing fractures along non-cleavage planes (Nudelman *et al.*, 2007; Li *et al.*, 2011; Deng *et al.*, 2020; Wallis *et al.*, 2022). However, a great variation exists in both the nanoscale organization of organic components (Okumura *et al.*, 2012) and the mechanical properties of different species of bivalves (Olson *et al.*, 2013). Understanding the composition and spatial organization of the organic components in the prismatic layer of bivalve shells would not only improve the current understanding of biomineralization in these important paleoclimate archives, but also aid efforts to generate synthetic materials with tailored mechanical properties.

The columnar prismatic layer in nacroprismatic bivalves typically consists of variably sized (10–200 μm in diameter) elongated polygonal calcite prisms that have their long-axis oriented perpendicular to the shell surface. Individual prisms are separated by 0.5–8 μm thick organic walls (Dauphin, 2003; Checa *et al.*, 2005, 2016; Cuif *et al.*, 2014; Harper and Checa, 2017; Dauphin *et al.*, 2019; Strag *et al.*, 2019) and can be characterized as either single- or poly-crystalline in terms of crystallographic preferred orientation at the mesoscale, but — as with most biominerals — at the nanometer scale, each individual prism is fundamentally composed of 20–150 nm subspherical

nanograins (Wolf *et al.*, 2016). Members of the Pinnidae genus, which includes *Pinna nobilis* and *Atrina rigida*, form a shell consisting of prisms with a single, uniform crystallographic orientation with the c-axis perpendicular to the shell surface, i.e., parallel to the length of the prisms (Dauphin, 2003; Checa *et al.*, 2005; Reich *et al.*, 2019). In contrast, the *Pinctada* genus produces poly-crystalline calcite prisms that are subdivided into regions with different crystallographic orientations at the level of individual prisms (Okumura *et al.*, 2010, 2013; Checa *et al.*, 2013, 2016; Dauphin *et al.*, 2019). In some Pinctada species such as *P. margaritifera,* prism growth starts out single-crystalline before becoming poly-crystalline during ontogeny (Checa *et al.*, 2013, 2016; Cuif *et al.*, 2014; Dauphin *et al.*, 2019).

Gilbert and colleagues (2011) hypothesized that poly-crystalline shells could be more fracture resistant than single-crystalline shells due to the inhibition of longer-range cleavage in biogenic calcite. This was later experimentally confirmed by correlated microdiffraction imaging and nano-indentation, which showed that poly-crystalline calcitic prisms from the *Pinctada* genus are significantly stronger than single-crystalline calcitic prisms from other mollusks (Olson *et al.*, 2013; Wallis *et al.*, 2022). Dauphin and colleagues (2019) compared the sulfur contents of *P. nobilis* and *P. margaritifera*, and suggested that the differences in crystallography are related to differences in the composition of sulfur-containing intra-crystalline organic materials. Based on transmission electron microscopy (TEM), Okumura and co-authors also argued that differences between single- and poly-crystalline prisms originate from the spatial distribution of the intra-crystalline organic matrices (Okumura *et al.*, 2012, 2013). These studies thus strongly imply that even subtle differences in composition or organization of organic material, which predominantly consists of proteins, chitin, polysaccharides, and lipids (Dauphin, 2003; Suzuki *et al.*, 2007; Farre and Dauphin, 2009; Furuhashi *et al.*, 2009b; Cuif *et al.*, 2010a; Agbaje *et al.*, 2017), can profoundly affect the mechanical properties of the prismatic layer. Much work has gone into incorporation of shell-derived proteins into synthetic calcites, whereby synthetic organo-mineral composites have been manufactured with crystal parameters, morphologies, and even toughness comparable to their biogenic counterparts (Albeck *et al.*, 1993; Aizenberg, 2006; Okumura *et al.*, 2013; Kim *et al.*, 2016). Typically, the organic moiety is analyzed by decalcification of the mineral component followed by bulk characterization techniques, such as infrared spectroscopy and electrophoresis, liquid and gas chromatography, and nuclear magnetic resonance (NMR) (Dauphin, 2003; Suzuki

et al., 2007; Farre *et al.*, 2011; Okumura *et al.*, 2013; Agbaje *et al.*, 2017; Huang *et al.*, 2021). While significant progress has been made towards understanding the composition of shell organic components through bulk characterization techniques, in situ methods are highly warranted as the distributions of the organic fraction is not homogeneous (Nudelman *et al.*, 2007; Huang *et al.*, 2021). Additionally, the chemical mapping techniques employed until now to visualize and fingerprint these organic materials in situ have been limited in spatial resolution to the higher micron scale (Dauphin *et al.*, 2003b, 2008, 2010, 2013; Suzuki *et al.*, 2007; Farre *et al.*, 2011), while electron microscopy has shown that the organic components are distributed at the nanometer scale (Nudelman *et al.*, 2007; Farre *et al.*, 2011; Li *et al.*, 2011; Okumura *et al.*, 2013; Deng *et al.*, 2020).

Here, we apply Photo-induced Force Microscopy (PiFM) to map and chemically fingerprint the biomacromolecules hosted within the calcitic prismatic layer in *Pinctada margaritifera*. PiFM is capable of simultaneously acquiring in situ 3D topographic and molecular distribution of both the biomacromolecules and the inorganic component of the biominerals at high spatial (~ 5 nm) and spectral (~ 1 cm^{-1}) resolution (Otter *et al.*, 2021, 2023). We combine this with scanning electron microscopy (SEM), electron backscatter diffraction (EBSD), and Nanoscale secondary ion mass spectrometry (NanoSIMS) imaging to correlate the distribution of organic components to the crystallography, chemistry, and ultrastructural features within prisms. By bridging the gap between nanoscale organic characterization and mesoscale mineral analysis, this study simultaneously sheds light on the complex biomineralization processes of nacroprismatic bivalves and provides observations that guide future biomimetic engineering strategies.

4.2 Methods

The *Pinctada margaritifera* shell investigate here is from the collection of the Institute of Paleobiology, Polish Academy of Sciences, Warsaw (specimen number ZPAL V.31/11/R-BIV07). They were harvested in October 2006 at 7–12 meters depth at Marutea Sud Atoll, French Polynesia. For the PiFM analysis of the pristine, unembedded shell piece, a Tahitian *Pinctada margaritifera* shell was provided by Pearls of Australia Pty Ltd. Shell pieces including the prismatic layer, the nacreous layer and the nacroprimatic transition zone were cut with a wire saw, embedded in epoxy (EpoThin2, Buehler) and polished with increasingly finer-grained diamond pastes (15 to 0.25 µm), before a final chemical-mechanical polish with colloidal silica using a Vibromet2. Specimens for SEM imaging were immersed in a modified composition of Mutvei's solution (Dunca *et al.*, 2005) (12.5 vol% glutaraldehyde + 0.5 vol% acetic acid) for 4 minutes. Samples for nanoscale molecular imaging were immersed in a weaker formulation (2 vol% glutaraldehyde + 0.1 vol% acetic acid) for 1–3 seconds.

4.2.1 SEM and EBSD

Both polished and etched samples were imaged using a Zeiss Gemini 500 SEM, operating at an acceleration voltage of 1 kV and a working distance of 5 mm. After PiFM imaging, samples intended for EBSD imaging were lightly repolished, to remove the topography due to the etching procedure, and coated with approximately 5 nm of carbon. EBSD imaging was conducted using an Oxford Instrument Tescan Mira LMU operating with a beam energy of 20 keV, a working distance of 23 mm, and a tilt angle of 70°. EBSD maps were acquired with an 800 nm step size. Kikuchi patterns were captured with an Oxford Instruments Symmetry EBSD detector, indexed with AzTec analysis software (Oxford Instruments) and processed with CHANNEL 5 HKL software. Black lines on EBSD maps show individual crystal boundaries with a misorientation angle larger than 10° and grey lines indicate sub-grain boundaries with a misorientation angle larger than 2°.

4.2.2 NanoSIMS

For NanoSIMS imaging (Hoppe *et al.*, 2013), polished samples were coated with ca. 15 nm Au to reduce surface charging. After about 5 mins of pre-sputtering with a 200 pA defocused Cs^+ beam

to remove the Au-coating locally prior to data acquisition, a primary cesium (Cs^+) beam was focused to a spot size of approximately 120 nm (~ 3.7 pA on the sample surface) to map areas 25×25 µm with a raster of 256×256 pixels and a dwell-time of 5 milliseconds per pixel. The multi-collector system counted the incoming secondary ions of $^{16}O^-$, $^{12}C^{14}N^-$, $^{32}S^-$, and $^{16}O^{24}Mg^-$ simultaneously using individual electron multiplier detectors with a mass resolving power of ~9000 (Cameca definition). Typically, 10 sequential images were acquired for each area that were then combined and drift corrected using L'IMAGE software (Dr. Larry Nittler, Carnegie Institution of Washington, USA).

4.2.3 PiFM

Nanoscale molecular maps were acquired via PiFM using a VistaOne (Molecular Vista Inc., CA-USA) system at the Australian National University (ANU) Research School of Earth Sciences (Otter *et al.*, 2023). The system is equipped with a tunable infrared (IR) excitation source consisted of four serially connected gap-free quantum cascade lasers (QCLs) in a QCL-module from Block Engineering LLC, that provided a continuous range from 770 to 1860 cm^{-1} at a spectral resolution of 1 cm^{-1}. Non-contact platinum-iridium coated 300 kHz Nanosensor™ AFM probes (NanoWorld AG, Switzerland) were used for all measurements. Map sizes ranged from 1×1 to 25×25 µm and were acquired as rasters of 256×256 or 512×512 pixels with a spatial resolution of about 5 nm. A laser power profile was taken at the start of each imaging session to normalize all PiFM spectra. Initial processing of PiFM data was done using SurfaceWorks 3.0 Release 30, where spectra were smoothed with a factor of 17. Drift between maps were corrected when necessary, using the bUnwarpJ plugin in ImageJ. For additional information regarding PiFM instrumentation and methodology, see Otter *et al.* (2021). In addition to the shell specimens, we also analyzed pure chemicals with the PiFM that we obtained from Sigma Aldrich (Merck, Germany) namely chitin, D-(+)-glucose, and N-Acetyl-D-Glycosamine. These chemicals came in powdered and flake form and small quantities were individually prepared on double-sided carbon tape on a metal AFM holder. Each chemical was analyzed using a fresh PiFM tip and these tips were never used in combination with either other pure chemicals or the shell specimens to avoid cross-contamination.

4.3 Results

4.3.1 The hierarchical structural arrangements of calcitic prisms in Pinctada margaritifera

The shell of *P. margaritifera* consists of an outer calcitic prismatic layer and an inner aragonitic nacreous layer (Fig. 4.1a). SEM images of polished transversal sections of the prismatic layer show the thick organic interprismatic membranes outlining prisms with long aspect ratios and irregular polygonal cross-sections. (Fig. 4.1b) Some organic membranes protrude into prisms and partially divide them, whereas others appear isolated within prisms (Fig. 4.1b). Simultaneous partial decalcification and fixation of the organic components with a modified Mutvei's solution (a mixture of a weak solution of acetic acid and glutaraldehyde, cf. Methods), reveals recessed sinuous grooves separating prisms into intraprismatic domains (white arrow Fig. 4.1c), while the thick interprismatic organic membranes are topographically raised relative to the etched calcite. In secondary electron (SE) images of the longitudinal view, the transition from the prismatic outer layer to the nacreous inner layer is clearly defined (Fig. 4.1d). Surficial decalcification shows that the prismatic and nacreous layers are separated by a fibrous aragonitic layer (Fig. 4.1e). The sinuous grooves revealed by the etching in the transversal view (white arrow Fig. 4.1c), delineate elongated intraprismatic domains in the longitudinal view (white arrow Fig, 4.1e). Additionally, a weak layering in the prismatic layer perpendicular to the long axis of the prisms becomes apparent after partial decalcification (Fig. 4.1e).

4.3.2 Crystallography and chemistry of the calcitic prismatic shell architecture

Results of chemical mapping and crystallography of the prismatic layer in transversal view are shown in Figure 4.2. EBSD maps reveal that the c-axis is preferably oriented within the plane of the transversal sample surface, with sharp changes in crystallographic orientations between neighboring prisms (Fig. 4.2a). In addition, the prisms are sub-divided into different intraprismatic crystallographic domains that are not outlined by organic membranes (Fig. 4.2a, b). The boundaries between these crystallographically-distinct domains correspond to the sinuous grooves visible after partial decalcification (Fig. 4.1c, e). Within some of these domains, the orientation of the c-axis rotates progressively (Supplementary Fig. 4.1).

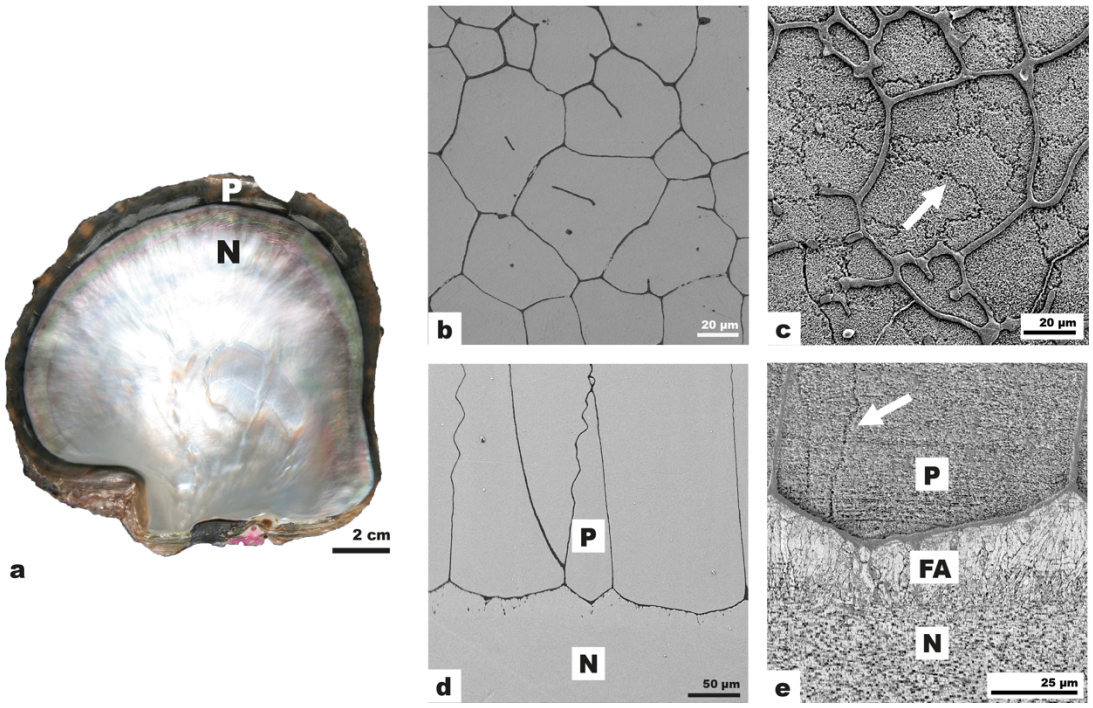

Figure 4.1 Microstructures in the shell of *Pinctada margaritifera*. (a) Photo of the left shell valve showing the nacreous inner layer (N) and the outer prismatic layer (P). (b–e) Secondary electron SEM images of polished cross-section of the prismatic layer. (b) Transversal view with the organic interprismatic membranes appearing as dark lines which outline the prisms. (c) Partial decalcification and fixation (cf. Methods) of an area similar to (b) reveals the interprismatic organic membranes standing out from the surrounding etched calcite. Note that the prisms are split into intraprismatic domains separated by sinuous grooves (white arrow). (d) Longitudinal view showing the transition from the prismatic (P) to nacreous layer (N). (e) Partial decalcification and organic fixation of an area similar to (d) shows that the prismatic (P) and nacreous (N) layer are separated by a thick organic membrane as well as a fibrous aragonitic (FA) layer. The white arrow indicates the separation of the prismatic layer into intraprismatic domains that run the length of the prisms.

We obtained an overview PiFM map (Fig. 4.2c) from the same location as previously obtained by EBSD that encompasses one of the boundaries between two intraprismatic domains (Fig. 4.2a). Surfaces for PiFM mapping were carefully etched and fixed for 1–3 seconds solution (cf. Methods). In this process, the acetic acid and pure deionized water lightly etch the calcium carbonate, while

the glutaraldehyde component of the solution fixes the organic components. This procedure results in the organic components sitting slightly topographically higher than the calcium carbonate and being thus easier to visualize with the PiFM, whereas in samples that were only polished and not fixed and etched, the organics sit slightly recessed between the mineral components due to their softness and the resulting preferential removal during mechanical polishing (Otter *et al.*, 2021). Shorter treatment times were used for PiFM imaging than SEM imaging, with the goal of minimizing topographic differences in line with sample requirements for PiFM (Otter *et al.*, 2021). The PiFM maps are presented as 3-color composite maps in which each color represents a distinct molecular compound or phase that was mapped using a characteristic absorption band (Fig. 4.2c). The individual single wavenumber maps underpinning the composite map were acquired sequentially using the exact same acquisition parameters and setup with only the laser energy being optimized for each phase. Three phases were distinguished: proteinaceous material (absorption band related to Amide I) is shown in red (1663 cm^{-1}), calcite is shown in blue (1420 cm^{-1}), and an organic phase showing absorption bands in the region typically attributed to saccharides, hence referred to as a saccharide-rich phase, is shown in green (1050 cm^{-1}) (Dauphin, 2003; Dauphin *et al.*, 2013; Agbaje *et al.*, 2017; Otter *et al.*, 2021). The proteinaceous material is mostly restricted to the interprismatic organic membranes, with some isolated occurrences within the prisms. The saccharide-rich organic moiety is distributed within the prisms as micrometer-sized aggregates with no clear pattern to their distribution. No differences in topography or concentration of organic phases are visible along the intraprismatic domain boundary (Figs. 4.2a–c, Supplementary Fig. 4.1).

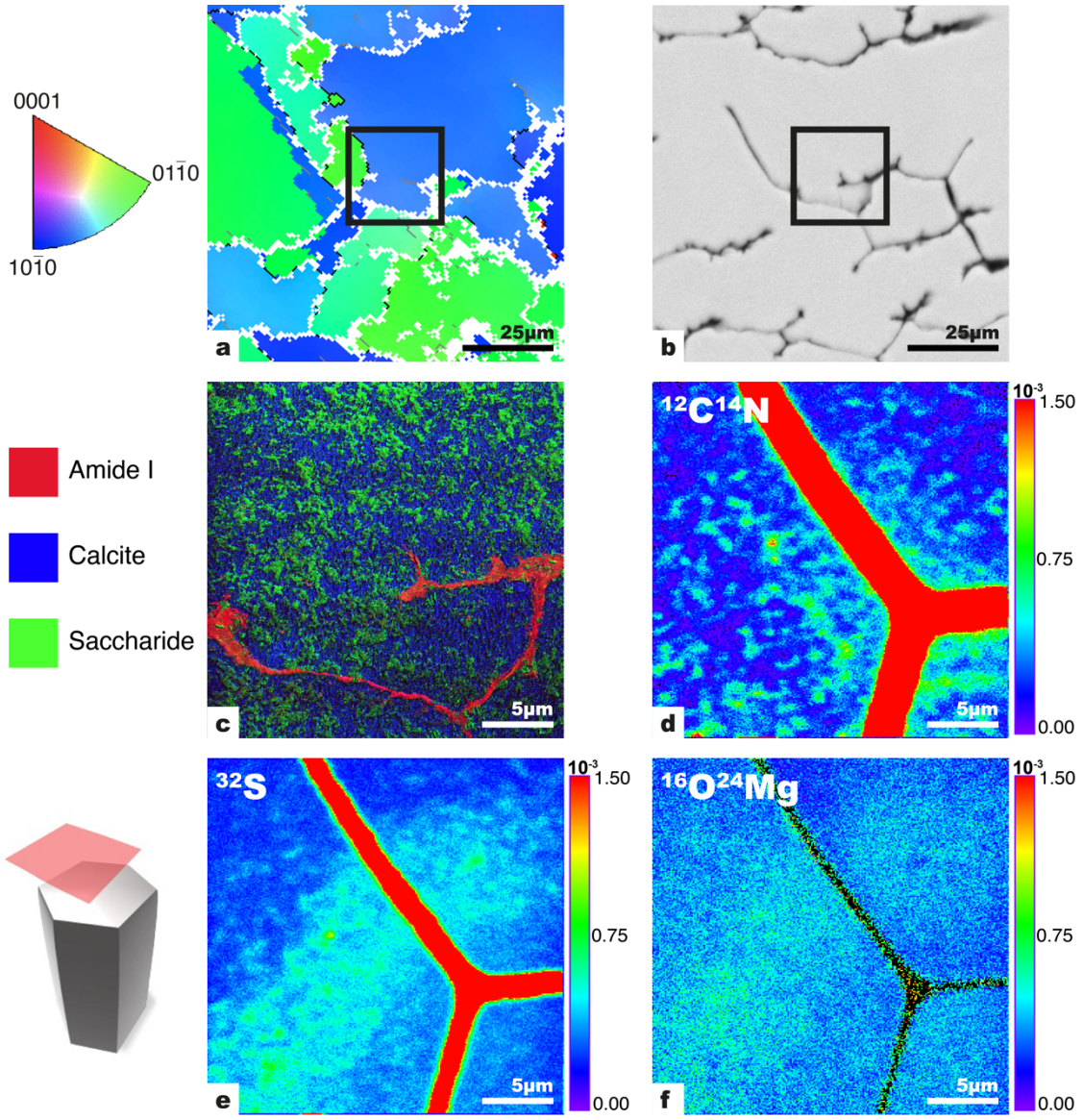

Figure. 4.2 Crystallography and chemical mapping of prisms in transversal view. (a) EBSD map showing sharp changes in the orientation visible as different colors of the c-axis across interprismatic organic membranes as well as the splitting of prisms into intraprismatic domains of variable orientation. (b) Backscattered electron SEM image of the same region. (c) 3-color composite PiFM map (region indicated by black square in a and b) obtained at the characteristic absorption band for each phase: amide I is shown in red (1663 cm^{-1}), calcite is shown in blue (1420 cm^{-1}), and the saccharide-rich phase is shown in green (1050 cm^{-1}). The amide I signal is confined to interprismatic membranes, whereas the saccharide-rich

phase is distributed as patches within the calcite domains. (d) NanoSIMS map of a similar region showing that nitrogen is found both within the interprismatic membrane as well as dispersed within the prisms as micrometer-sized patches. (e) NanoSIMS map of sulfur showing that sulfur is highly enriched within the interprismatic membrane as well as occurring as a broad band that continues across adjacent prisms. (f) NanoSIMS maps of magnesium showing no enrichment in the interprismatic membrane. However, within the prisms, higher magnesium concentrations are co-located with increased sulfur concentrations in (e). The schematic prism shows the orientation of the viewing plane.

Nitrogen, sulfur, and magnesium NanoSIMS maps were made of the surface areas also observed by PiFM and EBSD. In the prismatic layer of bivalves, magnesium ideally substitutes for calcium in the calcite crystal lattice, whereas sulfur and nitrogen are thought to be exclusively associated with organic phases (Dauphin *et al.*, 2003a, 2003b, 2010). Hence its unsurprising that the interprismatic membranes are highly enriched in nitrogen and sulfur but not in magnesium (Fig. 4.2d–f). Within the prisms, however, increased concentrations of nitrogen were observed, distributed as elliptical micrometer-sized patches (Fig. 4.2d). Sulfur and magnesium (Fig. 4.2e, f) show a banded distribution with no clear visual correlation to the 'patchy' nitrogen distribution (Fig. 4.2d).

Results of chemical mapping, both molecular and isotopic species, as well as visualizing the crystallography of the prismatic layer in longitudinal view are shown in Figure 4.3. Similar to EBSD maps of the transversal view, longitudinal EBSD maps show sharp changes in crystallographic orientation across interprismatic organic membranes (Fig. 4.3a). Most prisms are oriented with the c-axis perpendicular to the imaging surface (Supplementary Fig. 4.2). Intraprismatic splitting of individual prisms is also visible in the longitudinal view and preferentially oriented parallel to the long axis of the prisms (Fig. 4.3a, Supplementary Fig. 4.2). SE images of the same region as the EBSD maps (Fig. 4.3b) exhibit faint textural banding perpendicular to the length of the prisms.

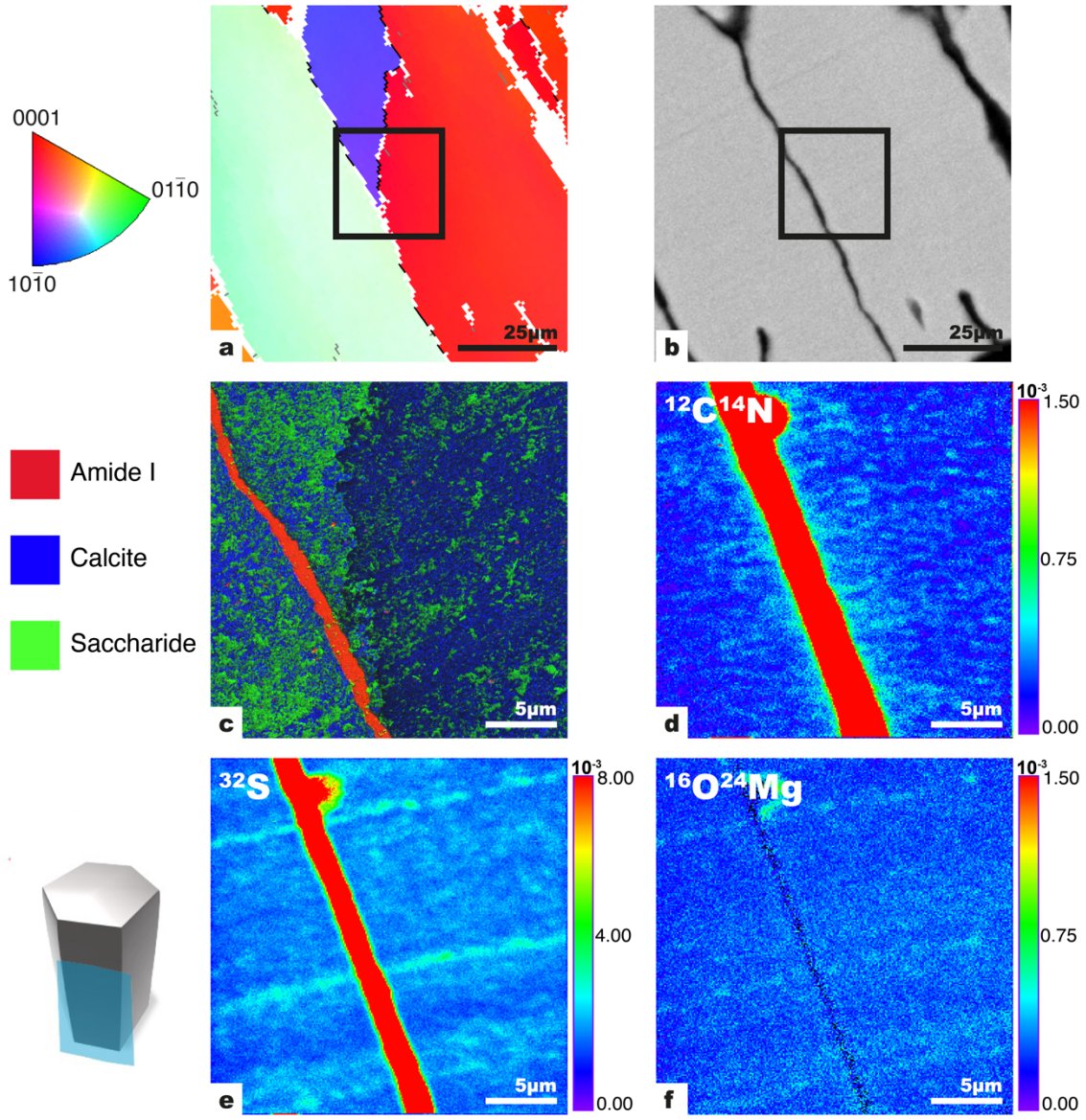

Figure 4.3 Crystallography and chemical mapping of prisms in longitudinal view. (a) EBSD map showing sharp changes in crystallography visible as different colors across interprismatic membranes as well as splitting of the prism at the center of the map into two intraprismatic domains of distinct orientation (colored red and purple) that are elongated parallel to the long axis of the prisms. (b) Backscattered electron SEM image of the same region showing a faint banding perpendicular to the organic interprismatic membrane. (c) 3-color composite PiFM map (region indicated by black square in a and b) obtained at the characteristic absorption band for each phase: amide I is shown in red (1663 cm^{-1}), calcite is shown in

blue (1420 cm^{-1}), and the saccharide-rich phase is shown in green (1050 cm^{-1}). The amide signal is confined to the interprismatic membrane, whereas the saccharide-rich phase occurs mostly intraprismatically as patches. (d) NanoSIMS map of a similar region showing that nitrogen is found both within the interprismatic membrane as well as dispersed within the prisms showing a weak layering perpendicular to the interprismatic organic membrane. (e) NanoSIMS map of sulfur showing a clear banding perpendicular to the interprismatic membrane. (f) NanoSIMS maps of magnesium showing weak banding perpendicular to the interprismatic membrane, which is correlated to the sulfur banding in (e). The schematic prism shows the orientation of the viewing plane.

The PiFM map in Fig. 4.3c was acquired across the interprismatic organic membrane and the splitting of the prism into two intraprismatic domains with two distinct c-axis orientations, colored in red and purple in the EBSD map (Fig. 4.3a). Although not quantifiable, we observe that the PiFM intensities obtained for the main calcite band are indeed sensitive to differences in crystallographic orientation. This is visible in the PiFM map as differences in the blue shading of the main calcite absorption band at 1420 cm^{-1} across the two intraprismatic domains (Fig. 4.3a, c, Supplementary Fig. 4.2), which correlates to the domains of different c-axis orientations visualized in the corresponding EBSD map (Fig. 4.3a). The differential effect of etching on different crystal orientations is also visible in the corresponding AFM topography image: here, the leftmost intraprismatic domain was more etched (Supplementary Fig. 4.2) and hence the amount of organic moiety revealed is greater (Fig. 4.3c). A weak banding is visible in topography images (Supplementary Fig. 4.2) similar to that observed in SEM images but this does not appear to be correlated to any major differences in the distribution of organic phases (Fig. 4.3c), apart from a small number of protein-rich particles weakly orientated along the layering (Supplementary Fig. 4.2). Similar to the transversal view, the protein signal is mostly confined to the interprismatic linings. In contrast, the PiFM data show that the saccharide-rich phase is dispersed as micrometer-sized patches within the prisms that are more abundant where more calcite was removed due to etching (Fig. 4.3c).

NanoSIMS mapping of the longitudinal view show the distribution of nitrogen as a weak fabric perpendicular to the interprismatic organic membranes (Fig. 4.3d), instead of the elliptical micrometer-sized patches observed in the transversal orientations (compare Figs. 4.2d and 4.3d).

Sulfur and magnesium maps show a banded distribution perpendicular to the interprismatic membranes (Fig. 4.3e, f).

4.3.3 Nanoscale mapping of organic components with PiFM

High-resolution PiFM maps were made of both the transversal and longitudinal sections to map the distribution of the organic components (Fig. 4.4). Topographic images show no great difference between transversal and longitudinal sections (Fig. 4.4a, b). In the transversal and longitudinal views, the phase images provide contrast between the organic and mineral shell components (Fig. 4.4c, d). AFM phase images are known to reflect differences in material properties including elasticity and have hence historically been attributed to reflect local changes in chemical composition and structure of the materials probed (Cuif *et al.*, 2010a) and have played a key role in identifying nanoscale mineral-organic interfaces across many biomineral systems (Wolf *et al.*, 2016). In transversal view, the interprismatic organic membrane (Fig. 4.4c, bottom of image) has the same phase contrast as the organic patches distributed within the adjacent intraprismatic domain. Surprisingly, this is however not the case for the longitudinal view (Fig. 4.4d), which raises important concerns about the reliability of phase images in the context of biological composite materials. In the transversal view, the PiFM composite map shows the saccharide-rich phase distributed as well-defined patches hosted within areas that are largely calcite-dominated domains (Fig. 4.4e). In the longitudinal view, these saccharide-rich areas appear highly intercalated with the calcite-dominated areas. A few small areas (50–200 nm), with of a proteinaceous signal (amide I), are dispersed within the prisms (red in Fig. 4.4e–h). In the longitudinal view these sometimes appear weakly aligned in layers perpendicular to the interprismatic membrane (Supplementary Fig. 4.2). High-resolution composite PiFM maps show that this proteinaceous signal is in the form of particles that are closely associated with the saccharide-rich phase (Fig. 4.4g, h; Supplementary Figs. 4.3, 4.4). At the highest magnification, the individual calcite nanograins are resolvable and the PiFM maps clearly show the intricately intertwined mineral and organic phases (Fig. 4.4g, h).

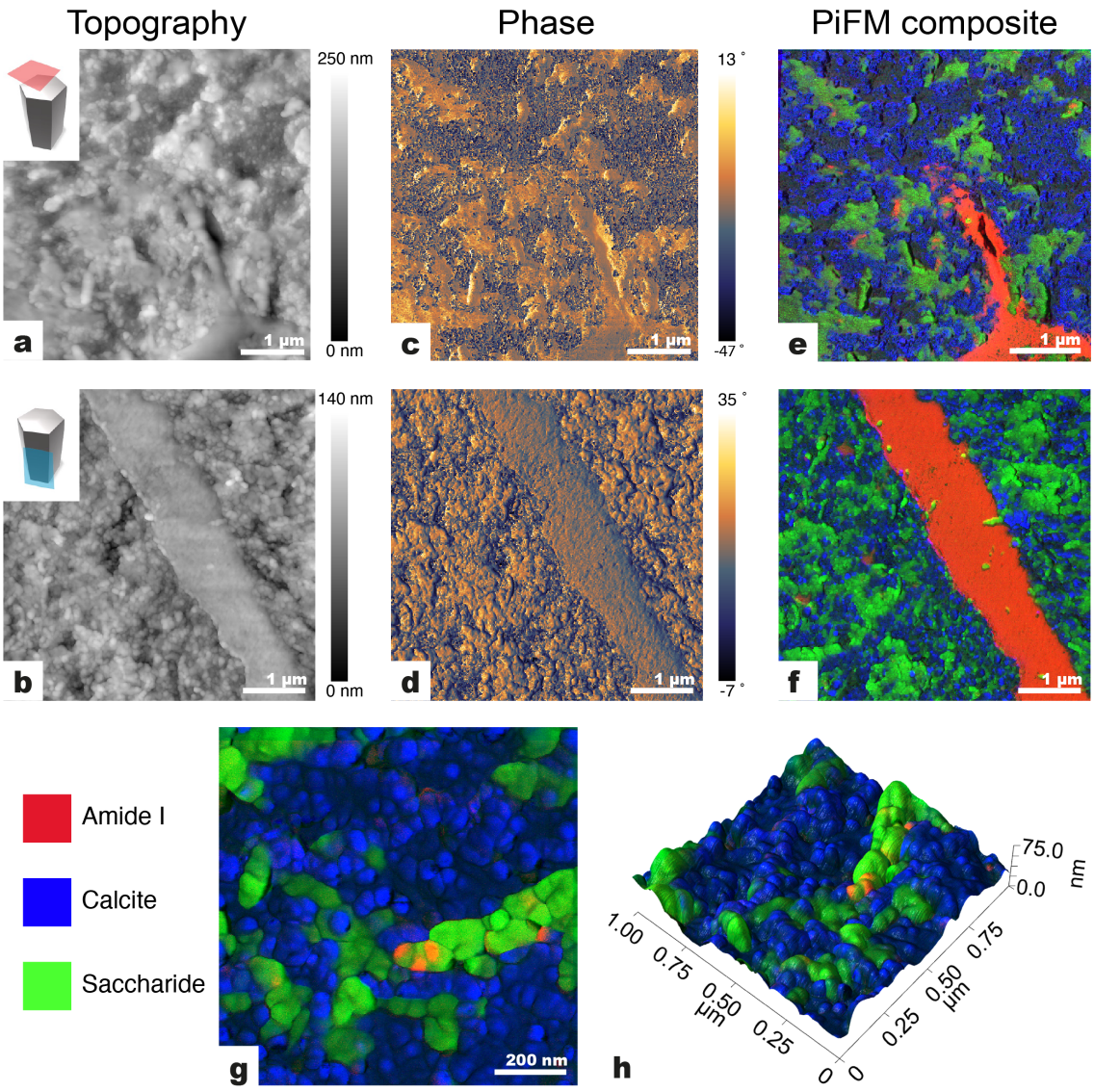

Figure 4.4 AFM topography, phase, and PiFM composite maps of the transversal and longitudinal view of prisms that were briefly fixed and etched (cf. Methods). (a–d) Topography and phase maps showing the structural organization and differences in material properties of the different components. Note that in the transversal view the patches of organics have the same phase contrast as the interprismatic membrane, whereas in the longitudinal view this is, however, not the case. (e–f) 3-color composite PiFM maps showing the characteristic absorption band for each phase: amide I is shown in red (1663 cm^{-1}), calcite is shown in blue (1420 cm^{-1}), and the saccharide-rich phase is shown in green (1050 cm^{-1}). The amide signal

(red) is mostly confined to the interprismatic organic membrane apart from some small particles associated with the saccharide-rich phase (green). (g–h) Composite PiFM map in (g) is shown superimposed on the topography in (h).

Representative PiFM spectra obtained from both mineral- and organic moiety-dominated regions in the prismatic layer of *P. margaritifera* are shown in Figure 4.5a. The spectrum from calcite in *P. margaritifera* shows a main absorption band centered around 1420 cm^{-1}, with some smaller absorption bands between 1465 and 1415 cm^{-1}, and a small absorption band around 873 cm^{-1}. This compares well to a pure abiotic calcite reference spectrum, apart from the smaller absorption bands in the shell calcite spectrum between 1465 and 1415 cm^{-1} (Supplementary Fig. 4.6). Spectra obtained from the saccharide-rich phase and the protein-like particles show the same absorption bands as calcite, as well as additional absorption bands at 1613, 1584, and several intermediate absorption bands from 1383 to 1000 cm^{-1} , with the most prominent absorption band centered around 1070 cm^{-1}. The interprismatic organic membrane is characterized by prominent absorption bands from 1518 to 1555 cm^{-1}, which are not found in the other spectra, and many intermediate absorption bands from 1455 to 1019 cm^{-1}. Only the protein-like particles and the interprismatic organic membrane have prominent absorption bands around 1650 cm^{-1}.

To identify the saccharide-rich phase, we compared its spectra to polysaccharide chitin, a long-chain polymer of N-acetyl-glucosamine (an amide derivate of glucose), and to the monosaccharides N-acetyl-glucosamine and glucose, all of which have been previously identified within the shells of bivalves (Suzuki *et al.*, 2007; Furuhashi *et al.*, 2009a; Agbaje *et al.*, 2019) (Fig. 4.5b). These saccharides have several prominent absorption bands between 975 and 1157 cm^{-1} that correlate well to the broad absorption bands centered at 1070 cm^{-1} in the saccharide-rich phase and in the protein-like particles. Chitin and glucosamine have prominent absorption bands in the amide I and II region, and chitin has a prominent absorption band at 1875 cm^{-1}, that are not found in the other spectra.

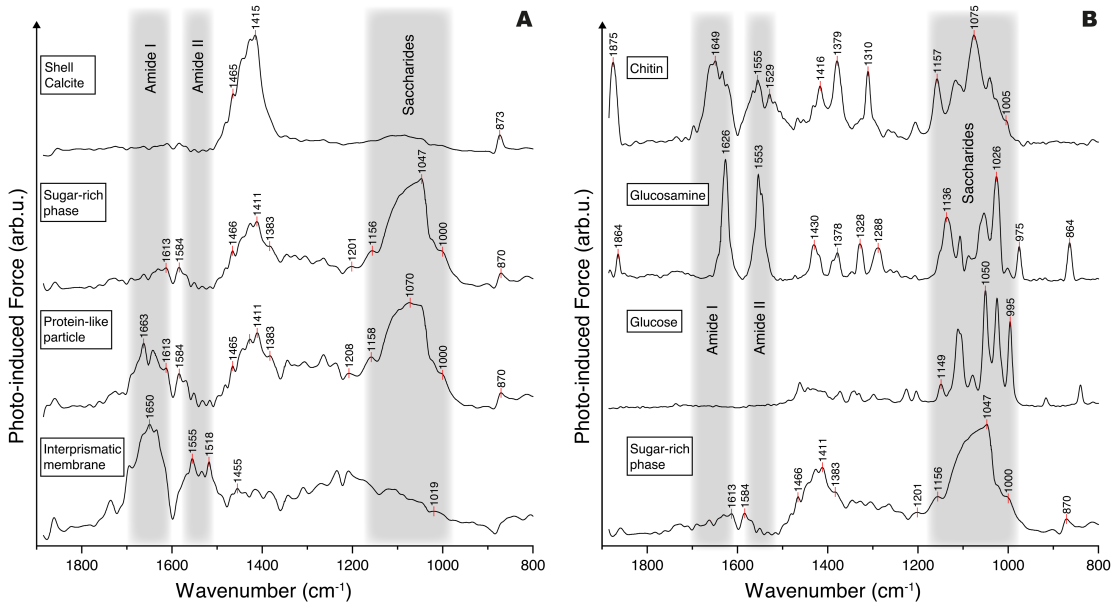

Figure 4.5 Representative PiFM spectra of various shell components in *P. margaritifera* (a) and their comparison with reference spectra, chitin, D-(+)-glucose, and N-Acetyl-D-Glucosamine, obtained using the same PiFM instrument and analytical set up (b). All PiFM spectra are averages of 3–5 spectra and are shown normalized to their highest intensity. Shaded areas indicate absorption bands associated to amide I and II, and saccharides.

To ensure that the process of fixing and etching the sample surface did not change the structure or chemistry of the prism surfaces, we analyzed the surface of a transversal section near the inner edge of a pristine piece of shell (Supplementary Fig. 4.5). It was not possible to analyze the thick interprismatic walls as these appeared to have dehydrated and lost volume which made them regress behind the prisms and were too deep for the cantilever to reach and the IR laser to illuminate. Despite this, we show that the intraprismatic regions are indeed calcite-dominated with interspersed saccharide-rich patches and minor amounts of protein (Supplementary Fig. 4.5), with a distribution highly similar to the polished, fixed and etched samples (Fig. 4.4), significantly boosting our confidence in this approach. The lack of spectral differences between pristine, and fixed and etched mineral and organic phases (Supplementary Fig. 4.5) thus validate the fixation and etching protocol followed in this study.

4.4 Discussion

4.4.1 Composition of the organic moiety

NanoSIMS maps show that the interprismatic organic wall is strongly enriched in both sulfur and nitrogen (Figs. 4.2, 4.3). This, together with the PiFM spectra showing prominent amide absorption bands (Fig. 4.5a), indicate that the interprismatic organic membranes are compositionally dominated by proteins. Dauphin (2003) examined the composition of the soluble organic matrices (SOM) in the prismatic layer of *P. margaritifera* using bulk characterization methods, including FTIR, chromatographic analyses, and XANES. Their characterization process, which involved crushing the prismatic layer, fully decalcifying the shell, and extracting the organic components, meant that they analyzed both the inter- and intracrystalline organic matrices together in bulk. Their results therefore mostly characterized the interprismatic organic membranes due to their greater abundance relative to the intraprismatic compounds (Dauphin, 2003). The FTIR spectra for the SOM in *P. margaritifera* in their study is similar to the spectra for the interprismatic organic membrane in the present study. In their spectra, prominent amide I and II bands also indicated the proteinaceous nature of the SOM. They identified the absorption band at 1245 cm^{-1} as sulfate and the absorption bands between 1000 and 1150 cm^{-1} as sugars and, using XANES and electrophoretic data, they concluded that the sugars are sulfated. In our study, no strong saccharide absorption bands were found in the interprismatic membrane, instead the strong saccharide signal was found in intraprismatic regions (Figs. 4.2–4.4). This demonstrates the benefits of using in situ nano-analysis to elucidate the composition of spatial and compositionally heterogenous organic components.

Several authors have linked the presence of sulfur in biominerals to sulfated polysaccharides (Dauphin, 2003, 2005; Dauphin *et al.*, 2003b; Cuif *et al.*, 2012; Huang *et al.*, 2021). In our NanoSIMS maps, sulfur is heterogeneously distributed and mostly concentrated in the interprismatic membranes, but also occurs as banding within the prisms (Figs. 4.2e, 4.3e). Sulfur, however, does not correlate with nitrogen (Figs. 4.2, 4.3). The distribution of nitrogen matches the patchy distribution of the saccharide-rich phase, whereas sulfur does not (Figs. 4.2, 4.3). This could suggest that the main saccharide-rich phase seen in the PiFM maps is not sulfated or that the amount of sulfur is below the detection limit of the NanoSIMS. Additionally, the lack of organic phases

showing a banded distribution in the PiFM similar to that of sulfur in the NanoSIMS maps could indicate that the spectral region studied here does not capture all organic components.

The shell calcite spectrum compares well to that of the abiotic calcite, but there are some additional secondary absorption bands between 1415 and 1465 cm^{-1} (Fig. 4.5a, Supplementary Fig. 4.6). These additional absorption bands most likely result from small amounts of organic moiety, but nonetheless the areas that appear in blue in the PiFM maps are predominantly composed of calcite with only minor amounts of organic material (Figs. 4.2–4.4). The saccharide-rich phase on the other hand also has calcite mineral absorption bands, with a broad absorption band centered at 1420 and a small absorption band at 870 cm^{-1}, as well as prominent additional absorption bands stemming from the presence of organic phases (Fig. 4.5). This implies that the saccharide-rich phase, shown in green in the PiFM maps, shows higher concentrations of organic moieties than the adjacent calcite-dominated areas shown in blue (Figs. 4.2–4.4). This distribution of intracrystalline regions rich- and poor in organic moieties, respectively, has previously been reported in bivalves. Using bright-field TEM imaging Deng and colleagues (2020) found 5–10 nm sized intracrystalline organic inclusions in *A. rigida* that were organized spatially into high- and low-density regions that measured hundreds of nanometers, consistent with this study.

The prominent absorption band centered around 1070 cm^{-1} in the saccharide-rich phase is in the region assigned to saccharides (Dauphin, 2003; Dauphin *et al.*, 2013; Agbaje *et al.*, 2017) (Fig. 4.5). To identify the organic molecules contributing to additional absorption bands in the saccharide-rich phase, comparisons were drawn to spectra from pure poly- and monosaccharides (Fig. 4.5b). Chitin, and sulfated- and neutral mono- and polysaccharides have all been proposed as saccharides that could occur intraprismatically in mollusks (Dauphin, 2003; Nudelman *et al.*, 2007; Suzuki *et al.*, 2007; Furuhashi *et al.*, 2009b). The absorption band centered around 1070 cm^{-1} corresponds well to the numerous absorption bands from 975 to 1157 cm^{-1} present in the spectra of saccharides glucose, glucosamine, and chitin (Fig. 4.5b). In studies that identified chitin in the prismatic layer from *P. fucata* using FTIR, the saccharide absorption bands appear broad, like those in this study, compared to reference spectra such as chitin (Suzuki *et al.*, 2007). This could be the result of the presence of different saccharides, all with slightly different absorption bands that would contribute to a broad absorption band in this region. The saccharide-rich phase has several

intermediate absorption bands from 1201 to 1383 cm^{-1}. The spectra of the three saccharides studied here have small (glucose) or prominent (glucosamine and chitin) absorption bands in this region. Chitin and glucosamine have distinctive absorption bands in the amide I and II region, and chitin also has a prominent absorption band at 1875 cm^{-1}, that are absent from the saccharide-rich phase. The additional absorption bands in the saccharide-rich phase therefore best match those of glucose, and less well the prominent absorption bands in both chitin and glucosamine.

Previous studies have used diverse methods to identify chitin in the prismatic layer of bivalves (Suzuki *et al.*, 2007; Nudelman and Sommerdijk, 2012; Kintsu *et al.*, 2017). Suzuki and colleagues (2007) used bulk FTIR and NMR spectral analyses of extracted organics as well as Calcofluor White staining on decalcified pieces of *P. fucata* shell and found that the interprismatic membrane fluoresces, indicating the presence of chitin. On the other hand, Nudelman (2007) used a fluorescent chitin-binding protein and found that chitin was distributed intraprismatically in *A. rigida*. Kintsu and colleagues (2017) treated the prismatic layer of *P. fucata* with sodium hypochlorite, removing the interprismatic membranes to only analyze the intracrystalline organic fraction. Their FTIR spectra strongly resemble that of chitin, with the amide I and II bands present, which is not the case in the present study (Fig. 4.5). This set of observations, indicative of both the inter- and intraprismatic presence of chitin obtained by a large suit of different analytical techniques, are all relevant, but difficult to completely reconcile at this stage. The characterization of the saccharide-rich phase remains ambiguous and warrants future work.

Intimately associated with the saccharide-rich phase in the intraprismatic domains are globular structures with a strong amide I spectral signature (Fig. 4.4g, h; Supplementary Fig. 4.3, 4.4), that we refer to as protein-like particles. Nudelman and colleagues (2007) identified a similar structure following partial decalcification of *A. rigida*, which revealed a network of chitin fibers decorated with globular structures. Treatment with sodium hypochlorite removed these globular structures but did not affect the chitin fibers, so these authors concluded that the globular structures consisted of proteinaceous material. Kintsu and colleagues (2017) identified a similar fiber + globular structure in *P. fucata*. If this is the same structure that Nudelman and colleagues (2007) observed in *A. rigida*, the PiFM spectra seem to confirm their inference that these globular structures are indeed proteinaceous.

Overall, this work highlights that volumetrically-speaking, intracrystalline saccharides may be more abundant in the prismatic calcite layer of nacroprismatic bivalves than intracrystalline proteins. As pointed out by Furuhashi and colleagues (2009b), a strong focus on the role of proteins in biomineralization has perhaps been to the detriment of research into other organic components, such as lipids and saccharides. More recently, focus has shifted to how polysaccharides can act to direct biomineralization and influence the morphological and mechanical characteristics of biogenic or bio-inspired abiotic calcite (Giuffre *et al.*, 2013; Kintsu *et al.*, 2017; Knight *et al.*, 2023). The saccharide component of glycoproteins has long been known to be directly involved in the selection of the morphology and crystallography of biologically formed calcite (Albeck *et al.*, 1996), yet the results of this study show that the majority of saccharide components are not necessarily spatially associated with proteins.

4.4.2 Morphology of intracrystalline organic moieties

The distribution of nitrogen in the NanoSIMS maps is heterogenous and anisotropic with regards to the viewing plane. In the transversal view, nitrogen is distributed as elliptical micrometer-sized patches (Fig. 4.2d), whereas in the longitudinal view this patchy elliptical geometry is not visible, but instead a weak fabric parallel to the sulfur and magnesium banding is apparent (Fig. 4.3d–f). These observations suggest that the nitrogen-rich intracrystalline organic phase component is distributed as disk-like patches flattened perpendicular to the length of prisms and weakly oriented parallel to the growth banding. The distribution of nitrogen in the NanoSIMS maps and the PiFM maps and spectra in this study mirrors the work of Deng and colleagues (2020) on *A. rigida*, in which high- and low-density regions of intracrystalline organics were found to be distributed randomly in the traversal view but in a layered fashion in the longitudinal view. Li and colleagues (2011) used annular dark-field scanning transmission electron microscopy and electron tomography to visualize organic moieties in *A. rigida* in 3D and found that the organics were distributed as disk-like nanopatches measuring around 10 nm. These disk-like nano-patches were preferentially oriented with their largest dimension perpendicular to the growth direction of the prisms, consistent with other TEM studies (Okumura *et al.*, 2012, 2013; Deng *et al.*, 2020). We therefore propose that the PiFM map areas appearing in blue are calcite-dominated with few intracrystalline inclusions, whereas the areas in green have high densities of intracrystalline

inclusions (Figs. 4.2–4.4). This is reflected in the PiFM spectra that show a mixed signal of calcite and organic moieties, identified in this study as saccharide-rich (Fig. 4.5). A proposed hierarchical organization of organic components at various spatial scales as schematically illustrated in Fig. 4.6 potentially resolves the disconnect between SEM and TEM based studies, while simultaneously identifying these organic components as saccharide-rich rather than protein-based.

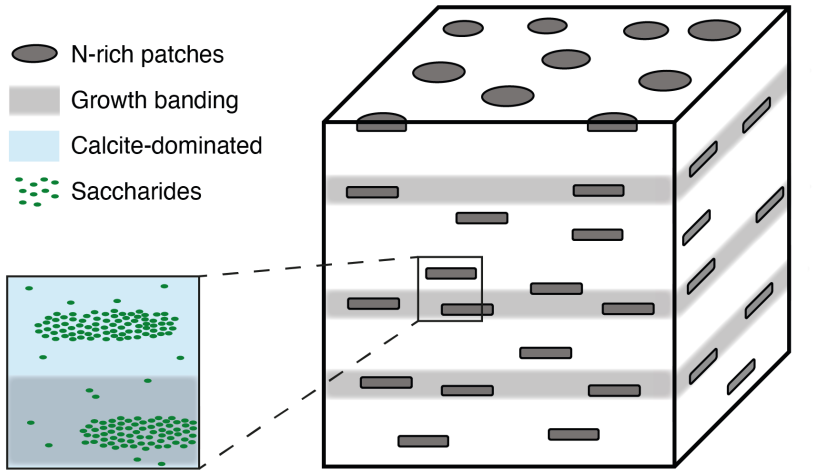

Figure 4.6 Conceptual model of the distribution of intraprismatic organic phases in *P. margaritifera* based on the anisotropic distribution of nitrogen in NanoSIMS maps and the saccharide-rich phase in the PiFM maps. The saccharide-rich organic moiety is represented as dark green disks and growth banding shaded in light grey.

4.4.3 Relationship between intracrystalline organic moieties and the crystallography of prisms

Dauphin (2003) was the first to suggest that unlike single-crystalline prismatic *P. nobilis*, the prisms in *P. margaritifera* are poly-crystalline. EBSD, microdiffraction, and TEM subsequently demonstrated that the Pinctada genus is characterized by a higher level of crystallographic complexity that not only shows gradients in crystallographic orientation within intraprismatic domains, but also abrupt changes in crystallography across these domains (Okumura *et al.*, 2010; Checa *et al.*, 2013, 2016; Olson *et al.*, 2013; Dauphin *et al.*, 2019; Strag *et al.*, 2019). The preferential etching of crystallographic domain boundaries and the heterogenous distribution of sulfate (obtained with XANES chemical mapping) indicated to Dauphin and co-authors that the intraprismatic domain boundaries in *P. margaritifera* host sinuous intraprismatic organic membranes (Dauphin, 2003; Dauphin *et al.*, 2003b, 2019). However, TEM imaging of closely related *P. fucuta* did not show continuous membranes at the site of intraprismatic boundaries (Okumura *et al.*, 2010). Similarly to previous work (Dauphin, 2003; Dauphin *et al.*, 2003b; Okumura *et al.*, 2010; Checa *et al.*, 2016), the intraprismatic domain boundaries studied here were preferentially etched (Fig. 4.1c) yet correlated NanoSIMS, PiFM and EBSD mapping did not show evidence for continuous organic membranes at the site of these intraprismatic boundaries (Figs. 4.2, 4.3). The patchy distribution of organic moieties does not exhibit a clear relationship to the crystallography of the prisms they are hosted in.

Work on single-crystalline species such as *P. nobilis* and *A. rigida* that have their c-axes parallel to the long-axis of prisms led to the idea that organics are preferentially oriented along positively charged (001) planes in calcite (Li *et al.*, 2011; Metzger *et al.*, 2014), which are thought to interact with the negatively charged functional groups of intracrystalline proteins (Gilow *et al.*, 2011). However, poly-crystalline Pteriomorph bivalves that have their c-axes perpendicular to the length of prisms, such as the *Pinctada* genus, challenge this notion (Dauphin *et al.*, 2019). Although the patches of organic moieties traced with nitrogen in NanoSIMS maps in this study are significantly larger, the disk-like morphology perpendicular to the length of prisms is similar in shape and orientation to the high-density intracrystalline organics regions seen in single-crystalline bivalves (Li *et al.*, 2011; Deng *et al.*, 2020). This points to either a fundamental difference between how

single-crystalline Pinnidae and poly-crystalline Pinctada bivalves construct their shells, or that the orientation of intracrystalline organic moieties in nacroprismatic bivalves is the result of actively controlled prism growth dynamics, and not a (passive) function of crystallographic orientation.

4.4.4 Conclusions

We investigated the relationship between ultrastructural features, crystallography and the composition and distribution of organic moieties in poly-crystalline nacroprismatic bivalves using the model species *Pinctada margaritifera*. Combining NanoSIMS and electron backscatter diffraction (EBSD) mapping of both transversal and longitudinal prism sections shed new light on the distribution of organic moieties and its relationship to the crystallography of prisms. We used a novel high-resolution molecular imaging technique, Photo-induced Force Microscopy (PiFM), to show that intercrystalline organics are primarily protein-rich whereas intracrystalline organics are dominated by saccharides *in situ*. These results provide insights into how Pteriomorph bivalves construct their shells but also highlight the key role of intracrystalline saccharides in contributing to high-performance bioinspired structural materials. Further work should be directed at unambiguously identifying the saccharide-rich organic phases in *P. margaritifera*., which may have implications for bioinspired high-performance structural materials.

4.5 Supplementary information

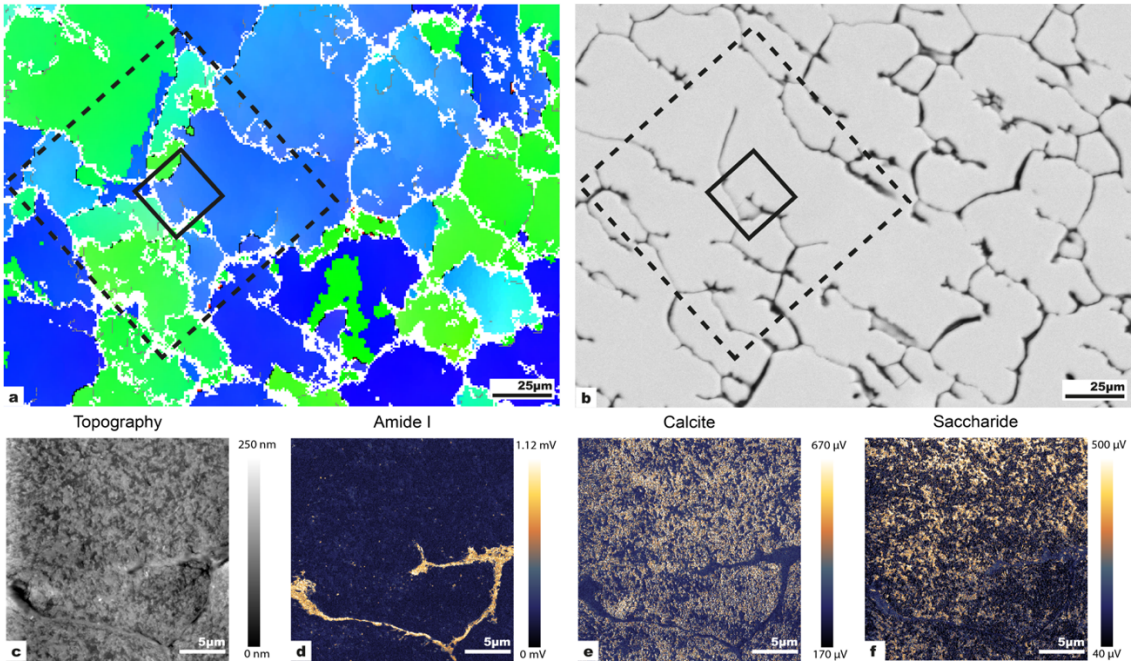

Supplementary Figure 4.1 Overview EBSD and backscattered electron SEM images providing context for the AFM topography and PiFM phase maps (locations indicated by black boxes). (a–b) EBSD and SEM images obtained from the same location. Dotted squares show the location of the high-resolution EBSD and backscattered electron SEM images in Figs. 4.2a and b in the main text. Black squares with solid outlines indicate the location of the PiFM maps. (c–f) AFM topography and single-wavenumber PiFM phase maps for amide I (d, 1663 cm^{-1}), calcite (e, 1420 cm^{-1}) and the saccharide-rich phase (f, 1050 cm^{-1}), respectively.

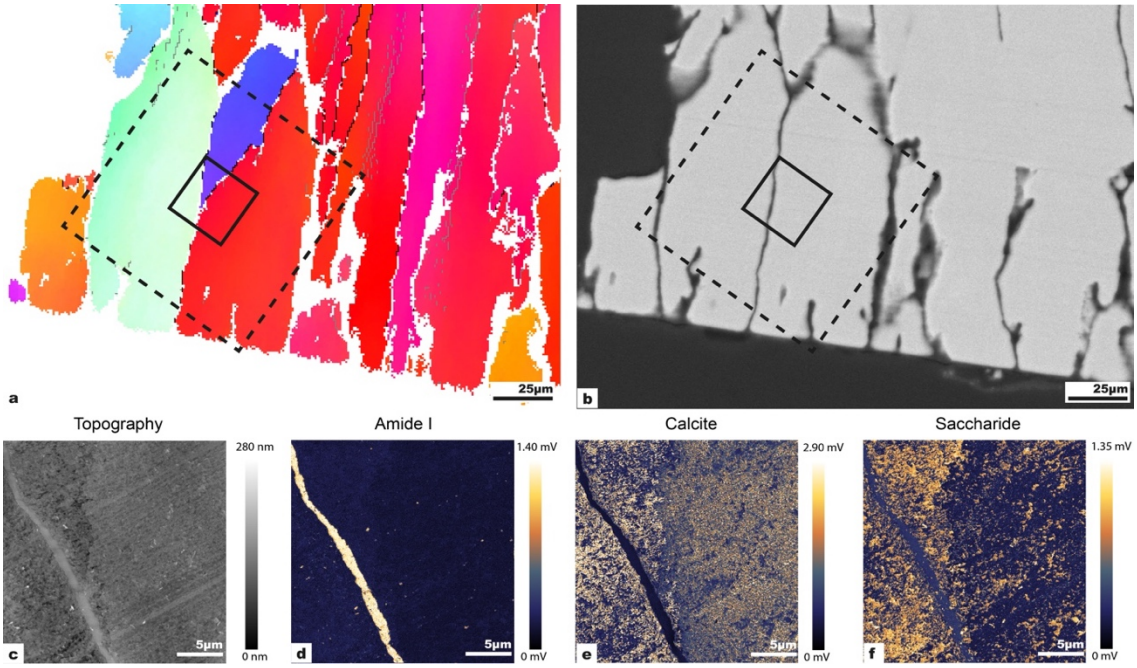

Supplementary Figure 4.2 Overview EBSD and backscattered electron SEM images providing context for the location of AFM topography and PiFM phase maps (locations indicated by black boxes). (a–b) EBSD and SE images in the same location. Dotted squares show the location of the high-resolution EBSD and backscattered electron SEM images in Figs. 4.3a and b in the main text. Black squares with solid outlines highlight the location of the PiFM phase maps. (c–f) AFM topography and single-wavenumber PiFM phase maps for amide I (d, 1663 cm−1), calcite (e, 1420 cm−1) and the saccharide-rich phase (f, 1050 cm−1), respectively.

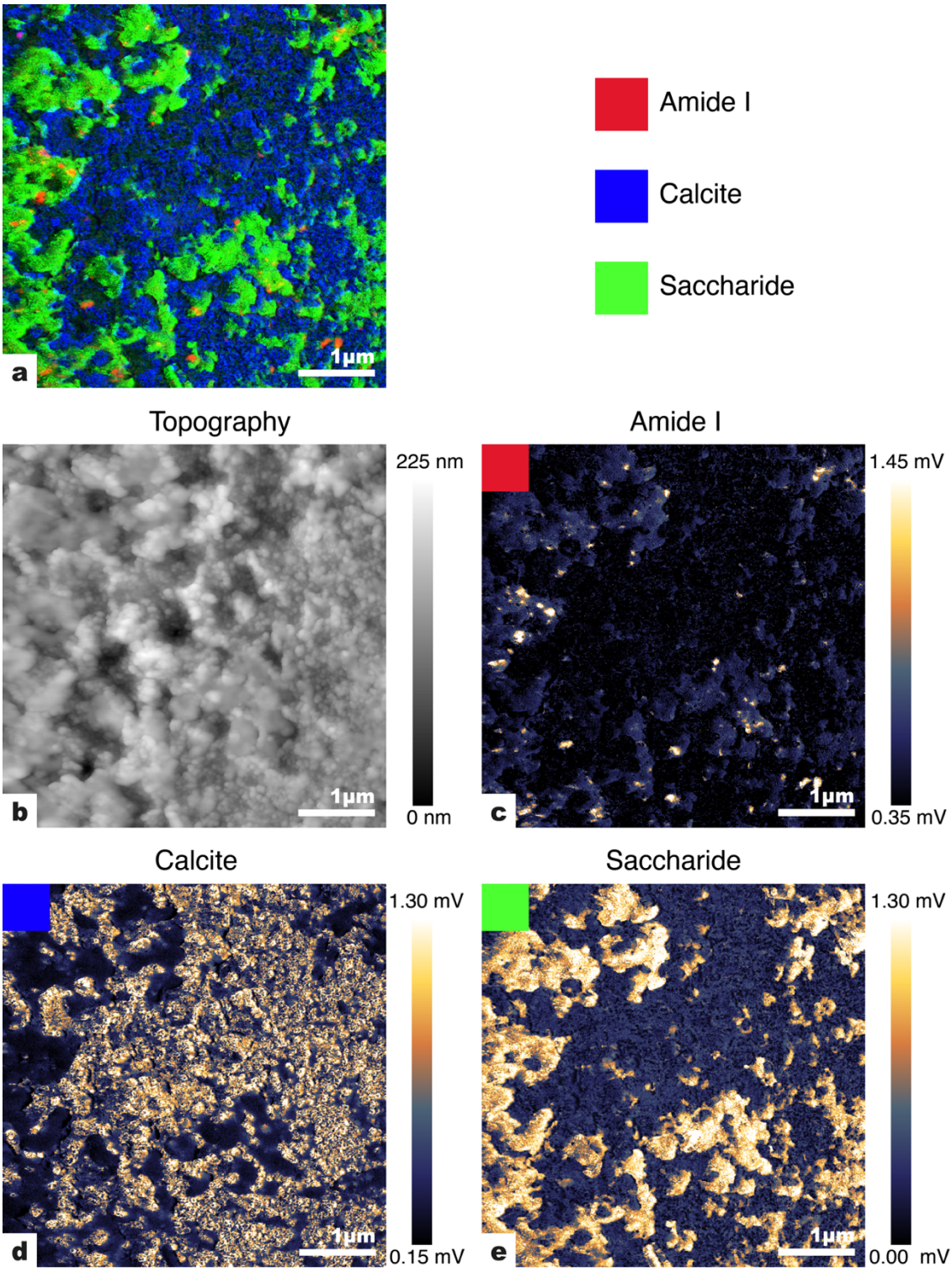
a
1µm
Amide I
Calcite
Saccharide
Topography
225 nm
0 nm
b
1µm
Amide I
1.45 mV
0.35 mV
c
1µm
Calcite
1.30 mV
0.15 mV
d
1µm
Saccharide
1.30 mV
0.00 mV
e
1µm

Supplementary Figure 4.3 (Preceding page) AFM topography and PiFM phase and composite maps showing the close association between the isolated protein-like particles and the saccharide-rich phase within the carbonate matrix. (a) 3-color composite PiFM map. (b) AFM topography map. (c-e) Single-wavenumber PiFM phase maps for amide I (c, 1663 cm^{-1}), calcite (d, 1420 cm^{-1}) and the saccharide-rich phase (e, 1050 cm^{-1}), respectively.

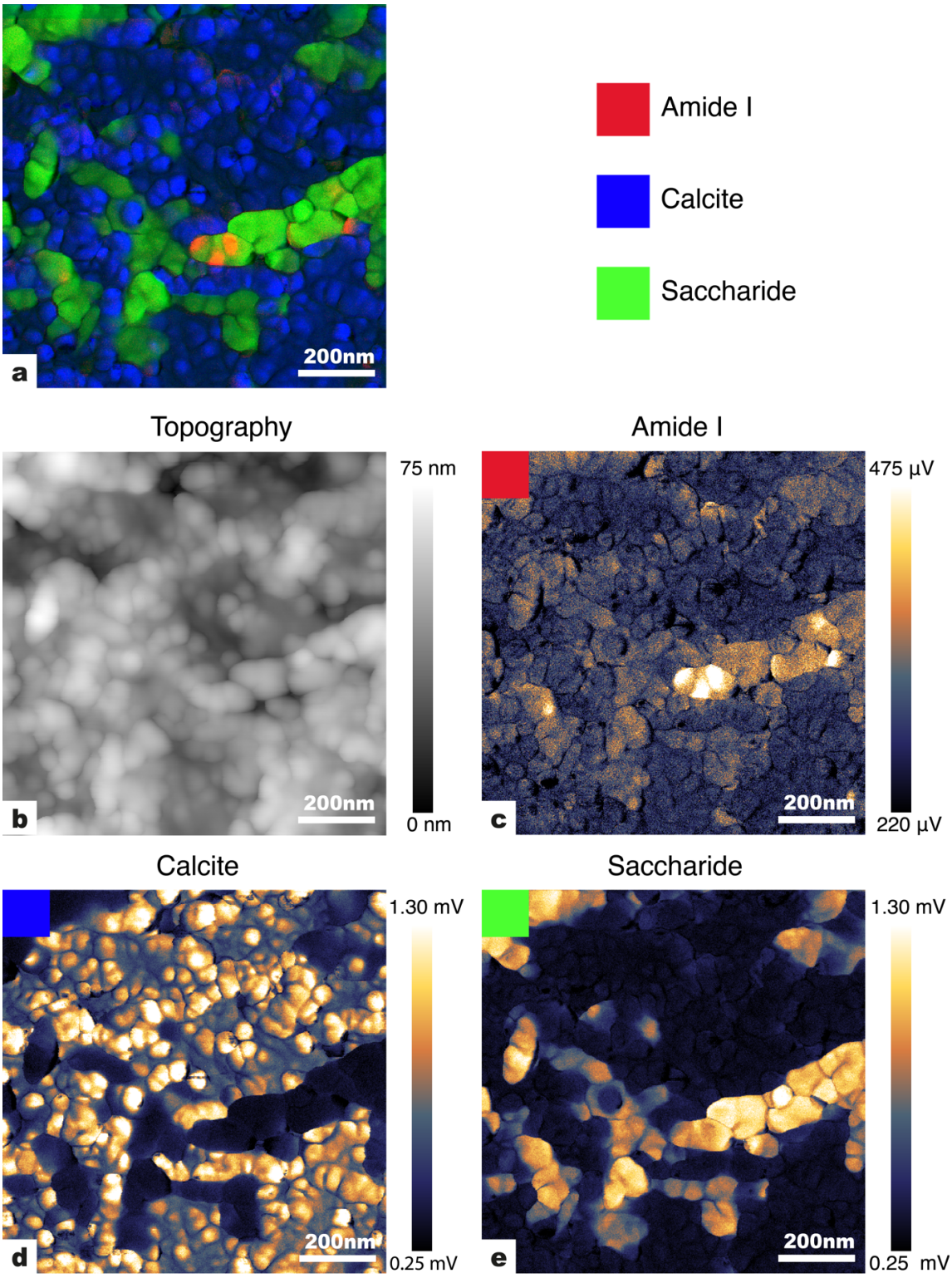
a
200nm
Amide I
Calcite
Saccharide
Topography
75 nm
0 nm
b
200nm
Amide I
475 µV
220 µV
c
200nm
Calcite
1.30 mV
0.25 mV
d
200nm
Saccharide
1.30 mV
0.25 mV
e
200nm

Supplementary Figure 4.4 (Preceding page) High-resolution AFM topography and PiFM phase and composite maps showing the close association between the protein-like particles and the saccharide-rich phase. (a) 3-color composite PiFM map. (b) AFM topography map. (c-e) Single-wavenumber PiFM phase maps for amide I (c, 1663 cm^{-1}), calcite (d, 1420 cm^{-1}) and the saccharide-rich phase (e, 1050 cm^{-1}), respectively.

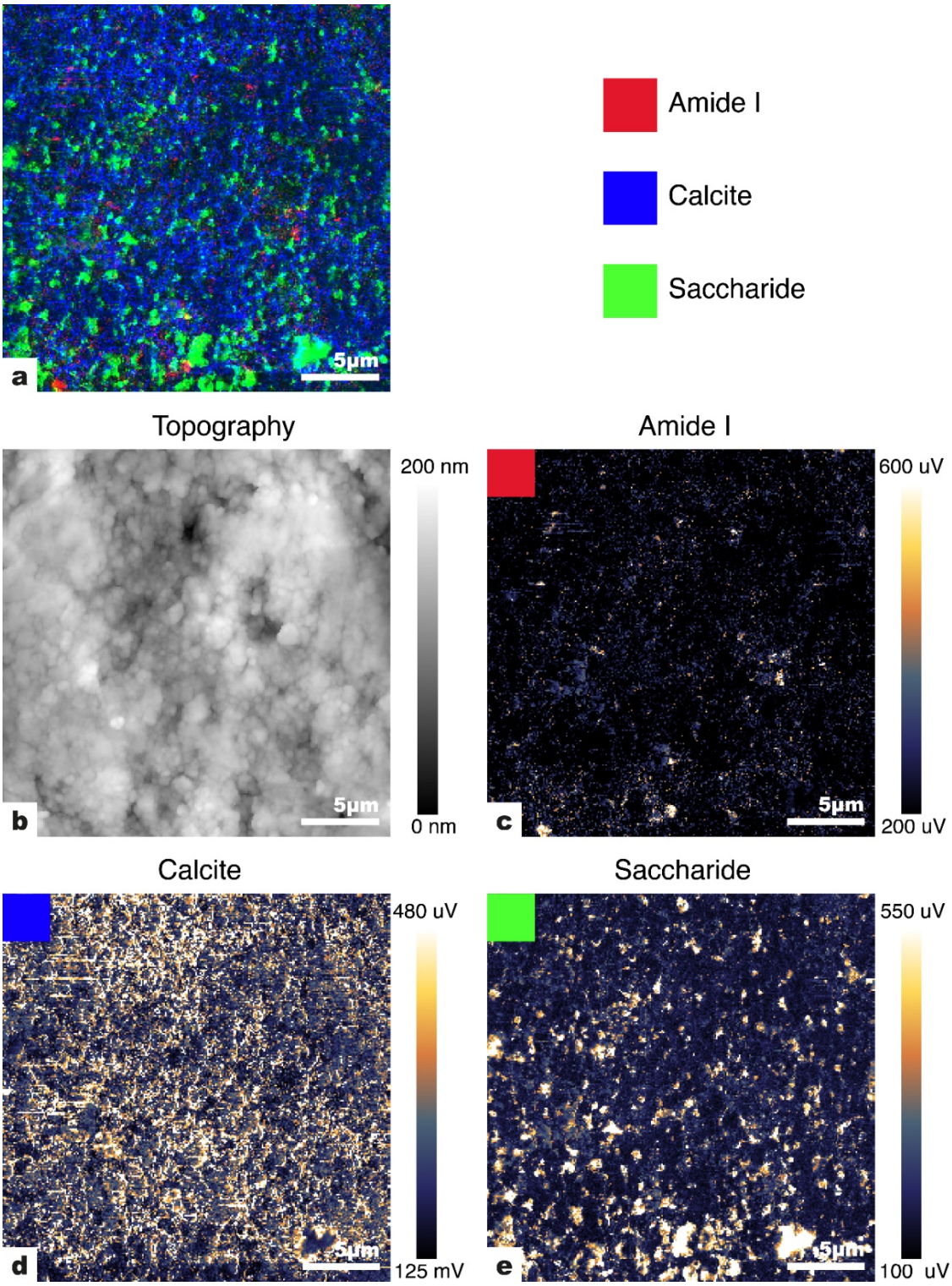
Amide I
Calcite
Saccharide
5μm
a
Topography
200 nm
0 nm
b
Amide I
600 uV
200 uV
c
Calcite
480 uV
125 mV
d
Saccharide
550 uV
100 uV
e

Supplementary Figure 4.5 (Preceding page) AFM topography and PiFM phase and composite maps of the transversal view of a pristine (i.e., not etched) shell piece showing that the saccharide-rich phase is abundant and heterogenous in distribution. (a) 3-color composite PiFM map. (b) AFM topography map. (c-e) Single-wavenumber PiFM phase maps for amide I (c, 1663 cm^{-1}), calcite (d, 1420 cm^{-1}) and the saccharide-rich phase (e, 1050 cm^{-1}), respectively.

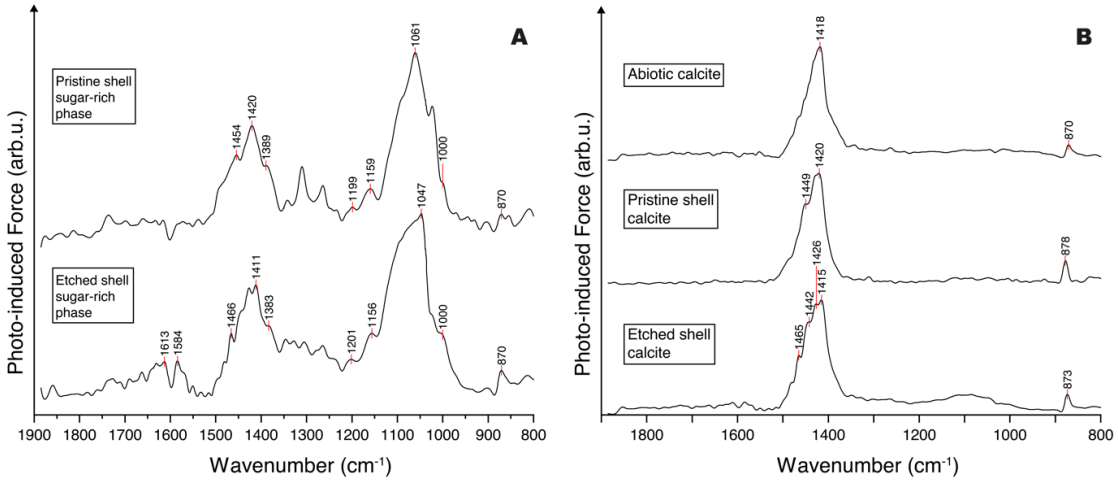

Supplementary Figure 4.6 Representative PiFM spectra comparing embedded, fixed and etched shell calcite and organic spectra to unembedded (i.e., pristine) shell calcite and organic spectra, as well as to abiotic pure calcite spectra, using the same PiFM instrument and analytical set up. All PiFM spectra are averages of 3–5 spectra and are shown normalized to their highest intensity.

5 *In-situ identification of the biomacromolecules relevant to diagenetic isotope exchange in bivalves*

Deyanira Cisneros-Lazaro[1*], Arthur Adams[1], Laura. M. Otter[2], Jarosław Stolarski[3], Sylvain Bernard[4], Damien Daval[5], Alain Baronnet[6], Olivier Grauby[6], Lukas P. Baumgartner[7], Torsten Vennemann[8], Stéphane Escrig[1] and Anders Meibom[1,7*]

[1] Laboratory for Biological Geochemistry, School of Architecture, Civil and Environmental engineering, Ecole Polytechnique Fédérale de Lausanne, Lausanne, CH-1015 Switzerland

[2] Research School of Earth Sciences, Australian National University, Canberra, ACT 2601, Australia

[3] Institute of Paleobiology, Polish Academy of Sciences, PL-00-818 Warsaw, Poland

[4] Museum National d'Histoire Naturelle, Sorbonne Université, CNRS UMR 7590, IMPMC, 75005 Paris, France

[5] ISTerre, Univ. Grenoble Alpes, Univ. Savoie Mont Blanc, CNRS, IRD, IFSTTAR, 38041, Grenoble, France

[6] CNRS, CINaM, Aix-Marseille Université, 13009 Marseille, France

[7] Center for Advanced Surface Analysis, Institute of Earth Science, University of Lausanne, CH-1015 Lausanne, Switzerland

This chapter will be shortened for submission to Geology.

Author contribution statement

DC-L, AA, JS and AM designed the experimental study; AA performed the isotope exchange experiments, AA and TV acquired the bulk O-isotope enrichment data, DC-L acquired the SEM images, DC-L and SE acquired the NanoSIMS data, DC-L and LMO acquired the PiFM data, DC-L, AA and AM drafted the manuscript. All co-authors contributed to the writing of the manuscript.

Abstract

The oxygen isotope compositions of fossil biocalcites, such as foraminifera, bivalves, brachiopods, and belemnites represent a comprehensive proxy for ocean temperatures stretching back into the Phanerozoic. Here we experimentally simulated the effects of fluid-mediated isotope exchange on the prismatic layer of two species of bivalve mollusks, *Pinna nobilis* and *Pinctada margaritifera*, by incubating pieces of shell material in ^{18}O-labeled artificial seawaters. The resulting fluid penetration and O-isotope exchange was visualized using NanoSIMS imaging and quantified with bulk isotope mass spectrometry, revealing species-specific differences in shell ^{18}O-enrichments that appear associated with the distribution and composition of intracrystalline organic matter. In *P. nobilis*, ^{18}O-enrichments were preferentially associated with sulfur-rich growth banding, whereas ^{18}O-enrichments in *P. margaritifera* were associated to the occurrence of micrometer-sized, approximately disk-shaped nitrogen-rich patches of organic matter. Photo-induced force microscopy (PiFM) was used to identify the intracrystalline organic compounds most relevant to diagenesis in each of the investigated species. Both species showed abundant intracrystalline saccharide-rich ultrastructures. In *P. margaritifera* these could be clearly linked to the distribution of nitrogen-rich patches. In *P. nobilis* the saccharide-rich ultrastructures showed a weak banding parallel to the growth banding, potentially linked to the sulfur banding. Neither species contained abundant intracrystalline proteinaceous material, suggesting that saccharides play a more significant role than proteins in facilitating fluid penetration and O-isotope exchange. Chemically fingerprinting the organo-mineral ultrastructures relevant to diagenesis advances our understanding of the role biomacromolecules play during the diagenesis of biocalcites.

5.1 Introduction

Understanding and contextualizing anthropogenic climate change in a geological perspective relies in large part on accurate models of past oceanic conditions, as oceans cover 70% of Earth's surface area and represent the main source of thermal inertia in the climate system (Resplandy *et al.*, 2019). The oxygen isotope compositions of the fossilized calcitic shells of foraminifera, bivalves, and brachiopods have been used to reconstruct ocean temperatures from the present to as far back as 500 Mya (Veizer and Prokoph, 2015). However, the accuracy and precision of these paleoclimatic records is challenged by the effects of diagenesis, which can introduce errors in temperature reconstructions.

A common feature of the biocalcites used for paleoclimatic reconstructions is that at the nano-scale, they are composed of 10–150 nm sub-spherical calcite nanograins surrounded by sheaths of organic matter (Wolf *et al.*, 2016). This ultrastructural organization represents an enormous surface area for interactions between the nanograins and porewaters, beginning at the death of the organism and continuing during subsequent burial in ocean sediments. Recent experiments have shown that the small sizes of these nanograins means that, given sufficient time, grain boundary and lattice diffusion of oxygen between fluid and calcite can cause measurable under- or overestimations of the true paleotemperature, depending on burial conditions (Bernard *et al.*, 2017; Adams *et al.*, 2023). In our previous works, we investigated how sediment porewaters interact with foraminifera shells, also called tests, by incubating tests with ^{18}O-enriched artificial seawaters (Bernard *et al.*, 2017; Cisneros-Lazaro *et al.*, 2022; Adams *et al.*, 2023). The investigated foraminifera species showed species-specific differences in the amount of diagenetic isotope exchange related to the proportion of organic-rich ultrastructures, despite similar sized nanograins in all species. These results mirror diagenesis experiments conducted on the aragonitic layer of bivalves, where the generation of secondary porosity due to the degradation of shell organic matter and the release of aqueous fluids bound to this organic matter increases the pathways through which diagenetic fluid can migrate and subsequently reset the original geochemistry of the shells (Pederson *et al.*, 2019, 2020; Forjanes *et al.*, 2022). These studies all point to the importance of embedded organic matter to diagenetic isotope exchange.

Here, we expand our work to the calcitic prismatic layer of bivalve mollusks to understand the influence of embedded organic matter on the diagenesis of biocalcites. *Pinna nobilis* and *Pinctada margaritifera* are two well-characterized species of bivalves that, despite being composed of similarly sized nanograins and having similar wt% of intracrystalline organic matter (Wallis *et al.*, 2022), exhibit key differences in the distribution and composition of intracrystalline organic matter (Dauphin, 2003). Furthermore, the calcitic prisms in *P. nobilis* shells are single-crystalline, as opposed to the prisms in *P. margaritifera* which are poly-crystalline (Checa *et al.*, 2013). These differences in crystallography are thought to relate to differences in the composition and distribution of intracrystalline organic matter (Okumura *et al.*, 2013), notably sulfated compounds (Dauphin *et al.*, 2019). Conducting simulated diagenesis experiments with shell pieces from these two species with contrasting organic matter compositions and distributions can shed light on the nature of organic macromolecules of relevance to diagenetic isotope exchange in biocalcites (Dauphin *et al.*, 2003a).

5.2 Methods

Pinna nobilis and *Pinctada margaritifera* shells were obtained from collections of the Institute of Paleobiology, Polish Academy of Sciences, Warsaw (specimen numbers ZPAL V.31/13/R-BIV06 and ZPAL V.31/11/R-BIV07 respectively). *P. nobilis* shells were collected at 5 meters depth in the eastern Adriatic Sea, Slovenia. *P. margaritifera* shells were harvested at a depth of 7–12 meters at Marutea Sud Atoll, French Polynesia. Shell pieces were cut with a wire saw, epoxy-embedded, diamond-polished (15 to 0.25 μm) and finally mirror-polished on a Vibromet2 using colloidal silica. For SEM imaging, mirror polished samples were immersed in a modified composition of Mutvei's solution (Dunca *et al.*, 2005) (12.5 vol% glutaraldehyde + 0.5 vol% acetic acid) for 4 minutes.

To understand how the calcitic prismatic layer of modern bivalves interacts with surrounding porewaters, we exposed pieces of *P. margaritifera* and *P. nobilis* shells to artificial seawaters that were highly ^{18}O-enriched, and visualized and quantified the resulting distribution of ^{18}O-exchange with a NanoSIMS ion microprobe (Hoppe *et al.*, 2013). In an experimental procedure similar to previous studies (Bernard *et al.*, 2017; Cisneros-Lazaro *et al.*, 2022; Adams *et al.*, 2023) (for

technical details see Chapter 2, section 2.2.1), shell pieces from both species were incubated at 90 °C for 6 days in a highly ^{18}O-enriched artificial seawater ($^{18}O/^{16}O = 0.30$, $\Omega_{calcite} = 1$). Within the NanoSIMS images, the oxygen isotope compositions of the shells are reported as $\delta^{18}O$ (in parts-per-thousand) relative to pristine shells of the same species:

$$\delta^{18}O = \left\{\left[\left(^{18}O/^{16}O\right)_{sample} - \left(^{18}O/^{16}O\right)_{standard}\right]/\left(^{18}O/^{16}O\right)_{standard}\right\} \times 1000 \quad (1)$$

We combined NanoSIMS isotopic imaging with Photo-induced Force Microscopy (PiFM) to correlate areas of higher ^{18}O-exchange to the distribution of organic matter. PiFM is a new-frontier technique with the required spatial (~ 5 nm) and spectral (~ 1cm^{-1}) resolution necessary to map and fingerprint the nanoscale organic matter associated with diagenesis (Otter *et al.*, 2021, 2023). For PiFM imaging, mirror-polished pristine shell pieces were briefly (1–10 seconds) immersed in a modified Mutvei's solution weaker than that used for SEM imaging to (2 vol% glutaraldehyde + 0.1 vol% acetic acid) to avoid excessive topography, as per the PiFM sample requirements (Otter *et al.*, 2021) (for technical details see Chapter 4, section 4.2.3).

5.3 Results

5.3.1 Ultrastructures of the prismatic layer in P. nobilis and P. margaritifera

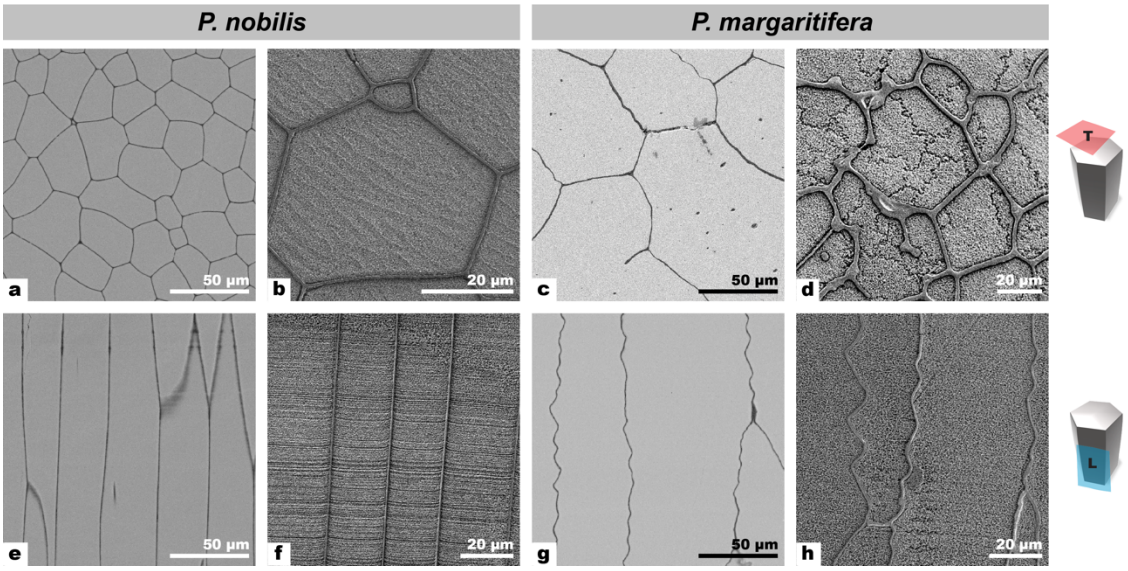

Figure 5.1 SEM images of polished cross-sections of the calcitic prismatic layer of *Pinna nobilis* and *Pinctada margaritifera*. Schematic diagrams indicate the viewing planes: (a–d) Transversal view, e–h) Longitudinal view. (a) Prisms in *P. nobilis* are polygonal with straight edges formed by the interprismatic organic membranes, which appear as dark lines. (b) Partially decalcified *P. nobilis* shells (cf. Methods) show a pattern of regularly spaced parallel crests. (c) Prisms in *P. margaritifera* are irregularly shaped and have interprismatic organic membranes that partially divide some prisms. (d) Partially decalcified *P. margaritifera* shows prisms that are split into intraprismatic domains separated by sinuous grooves. (e) Longitudinal view showing that prisms in *P. nobilis* have straight edges. (f) Partially decalcified *P. nobilis* shows banding perpendicular to the length of prisms. (g) *P. margaritifera* has interprismatic membranes with a wavy appearance. (h) Longitudinal view of partially decalcified *P. margaritifera* prisms shows only weak banding perpendicular to the length of prisms.

SEM images were made of transversal (Fig. 5.1a–d) and longitudinal sections through the prismatic layer (Fig. 5.1e–h) and show differences in ultrastructure between *P. nobilis* and *P. margaritifera* shells. In the transversal view, *P. nobilis* has polygonal shaped prisms with straight interprismatic membranes (Fig. 5.1a). Partial decalcification with a modified Mutvei's solution (Dunca *et al.*,

2005) (cf. Methods) etches calcite while simultaneously fixing organic components, thereby revealing the underlying organization of intraprismatic organic matter. Partially decalcified *P. nobilis* prisms show a pattern of regularly spaced parallel crests, which relate to the lateral extension during prism growth (Cuif *et al.*, 2020) (Fig. 5.1b). *P. margaritifera* has irregular shaped prisms, with interprismatic membranes that partially divide some prisms and in places exhibit wavy morphology (Fig. 5.1c). Partial etching reveals that prisms in *P. margaritifera* are split into intraprismatic domains, separated by sinuous grooves (Fig. 5.1d). These sinuous grooves are also crystallographic domain boundaries, which are believed to result from the recession of the interprismatic membrane during shell growth (Checa *et al.*, 2016). The longitudinal view of *P. nobilis* shows regularly shaped prisms with a well-expressed topographical banding perpendicular to the length of prisms when partially decalcified (Fig. 5.1e, f), whereas etched *P. margaritifera* shows a much fainter topographical banding perpendicular to the length of prisms (Fig. 5.1h). These layered structures are thought to be the result of the cyclical deposition of mineral-rich and organic-rich layers during prism growth (Cuif *et al.*, 2012).

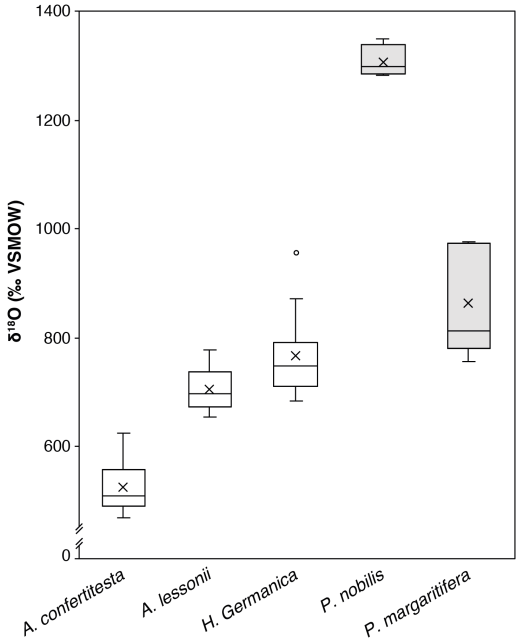

Figure 5.2 Box plot distributions of bulk ^{18}O-enrichment in tests of the three species of benthic foraminifera (Cisneros-Lazaro *et al.*, 2022) and *P. nobilis and P. margaritifera* shells (this study) incubated for 6 days at 90 °C in seawater analogue with a $^{18}O/^{16}O$ ratio of 0.30. Average ^{18}O-enrichments are shown with crosses. Middle lines = medians, boxes = interquartile ranges, whiskers = minimum and maximum values.

5.3.2 Oxygen isotope exchange experiments

Bulk oxygen isotope measurements were made on shell pieces from both species that were exposed to the experimental solution during 6 days at 90 °C. The bulk ^{18}O-enrichments reported as parts-per-thousand relative to VSMOW ± 1 standard deviation (SD) were 1311 ± 26‰ (n = 4) for *P. nobilis* and 868 ± 92‰ (n = 5) for *P. margaritifera* (Fig. 5.2, Supplementary Table 5.1). For comparison, Fig. 5.2 also shows the bulk ^{18}O-enrichments of *Ammonia confertitesta., Haynesina germanica* and *Amphistegina lessonii*, three species of modern benthic foraminifera incubated under identical conditions (Cisneros-Lazaro *et al.*, 2022). The bivalve shells are generally more enriched in ^{18}O than the foraminifera tests.

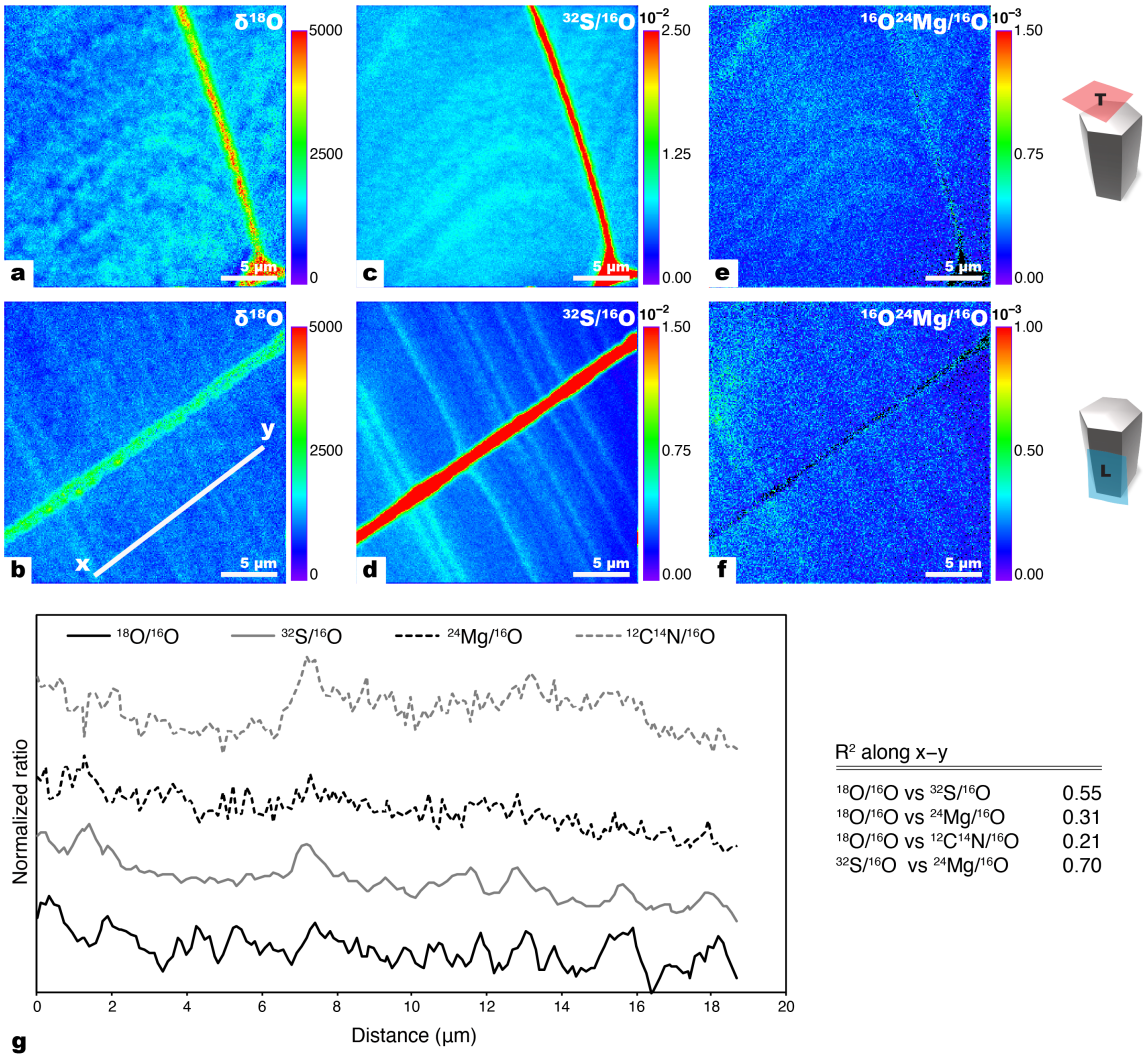

Figure 5.3 NanoSIMS images and line-profiles of polished cross-sections of *P. nobilis* after exposure to artificial seawater with a $^{18}O/^{16}O$ ratio of 0.30 for 6 days at 90 °C. (a–b) Areas of ^{18}O-enrichments are banded and appear curved in the transversal view, and as straight-lines perpendicular to the interprismatic membrane in the longitudinal view. (c–d) The distribution of sulfur appears as curved bands in the transversal view and straight bands in the longitudinal view. (e–f) The distribution of magnesium generally follows the same patterns as the ^{18}O-enrichment and sulfur. (g) NanoSIMS line-profiles showing the correlation, or lack thereof, between ^{18}O-enrichments and sulfur, magnesium, and nitrogen in *P. nobilis* in decreasing order of correlation.

NanoSIMS images of ^{18}O-enrichment in *P. nobilis* and *P. margaritifera* shell pieces exposed to the ^{18}O-enriched artificial seawater show pervasive and heterogeneous ^{18}O-enrichment throughout the shells (Figs. 5.3, 5.4). In *P. nobilis,* the ^{18}O-enrichment appears banded in both transversal and longitudinal sections (Fig. 5.3a, b). In the transversal view, the ^{18}O-enrichment appears as curved bands, whereas in the longitudinal view, the banding is straight and perpendicular to the length of prisms. Sulfur and magnesium bands are correlated to ^{18}O-enrichment in both the longitudinal and transversal view (Fig. 5.3c–f). Weak banding in nitrogen appears only weakly correlated to ^{18}O-enrichments (Supplementary Fig. 5.1). The line-profiles in Figure 5.3g show that in *P. nobilis* the ^{18}O-enrichment is best correlated to sulfur ($R^2 = 0.55$), weakly correlated to magnesium ($R^2 = 0.31$), and poorly correlated to nitrogen ($R^2 = 0.21$), albeit sulfur and magnesium are well correlated to each other ($R^2 = 0.70$).

In *P. margaritifera,* the distribution of ^{18}O-enrichment is different between the transversal and longitudinal view (Fig. 5.4). In the transversal view, there are micrometer-sized patches of increased ^{18}O-enrichment with a distribution similar to the observed patches enriched in nitrogen (Fig. 5.4a, c). Sulfur and magnesium show a banded distribution that is not correlated to areas that are enriched in ^{18}O or nitrogen (Fig. 5.4e, f, Supplementary Fig. 5.2). In the longitudinal view, the micrometer-sized patches of higher ^{18}O-enrichment are not visible, but there is instead a weak fabric perpendicular to the banding (Fig. 5.4d), that is correlated to the distribution of nitrogen (Fig. 5.4d) but not to the sulfur and magnesium bands (Fig. 5.4f, Supplementary Fig. 5.2). Line-profiles of the transversal view (Fig. 5.4g) show that ^{18}O-enrichment is correlated to nitrogen ($R^2 = 0.64$), but not correlated to sulfur ($R^2 = 0.03$) nor magnesium ($R^2 = 0.01$). As in *P. nobilis*, sulfur and magnesium are fairly well correlated ($R^2 = 0.55$). In both species the interprismatic membrane is highly enriched in sulfur and nitrogen but not in magnesium (Figs. 5.3 and 5.4, Supplementary Figs. 5.1 and 5.2).

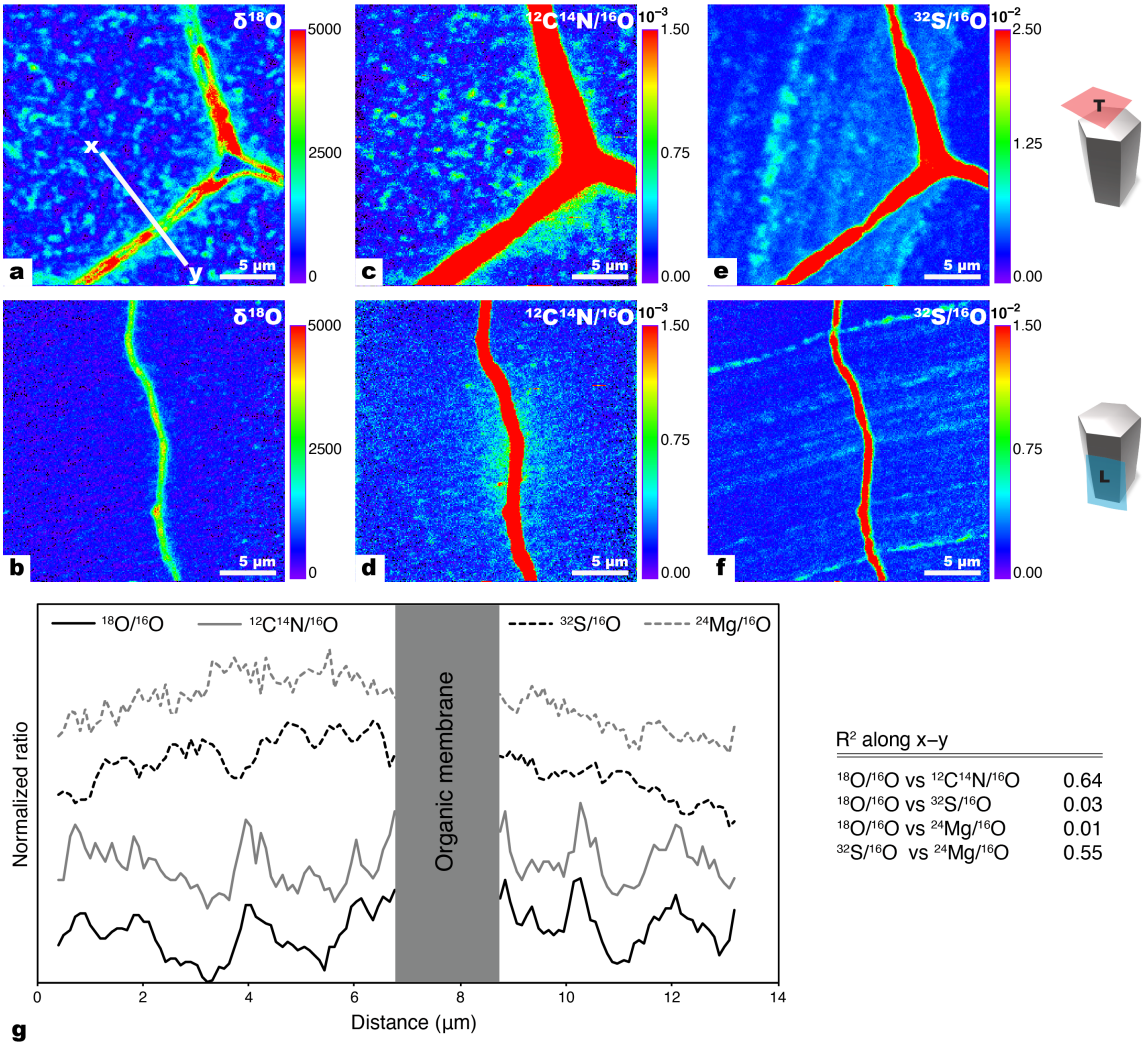

Figure 5.4 NanoSIMS images of the polished cross-sections of *P. margaritifera* after exposure to artificial seawater with a $^{18}O/^{16}O$ ratio of 0.30 for 6 days at 90 °C. (a) ^{18}O-enrichment shows a patchy distribution in the transversal view. (b) ^{18}O-enrichment shows a weak fabric perpendicular to the interprismatic membrane in the longitudinal view. (c) Nitrogen-rich patches are approximately elliptical and distributed randomly in the transversal view. (d) Nitrogen-rich areas show a weak fabric perpendicular to the interprismatic membrane in the longitudinal view. (e–f) Sulfur shows a banded distribution. (g) NanoSIMS line-profiles showing the correlation, or lack thereof, between ^{18}O-enrichment and nitrogen, sulfur, and magnesium in *P. margaritifera* in decreasing order of correlation.

5.3.3 Distribution of organic components in P. nobilis and P. margaritifera

NanoSIMS ^{18}O-enrichment maps (Fig. 5.5a, b) were compared with PiFM and AFM topography maps (Fig. 5.5c–f) from polished shell sections from both species in the transversal view, following brief immersion in the weaker modified Mutvei's solution (cf. Methods). *P. nobilis* was immersed in the solution for 10 seconds and *P. margaritifera* for 1–3 seconds to achieve similar etching effects in both species and orientations. PiFM maps (Fig. 5.5c, d) are shown as 3-color composite maps of three single-wavenumbers maps acquired at the characteristic absorption band for the different phases: (1) proteinaceous material is shown in red (Amide I, 1663 cm^{-1}), (2) calcite is shown in blue (1420 cm^{-1}), and (3) in green is an organic phase with absorption bands in the region assigned to saccharides (1050 cm^{-1}) that we refer to as saccharide-rich (Dauphin, 2003; Dauphin *et al.*, 2013; Agbaje *et al.*, 2017; Otter *et al.*, 2021). Both species show a similar distribution of organic components: proteins are mostly confined to the interprismatic walls and saccharides are the dominant component within prisms (Fig. 5.5c, d). The saccharide-rich phase occurs as micrometer-sized patches that are randomly distributed in both species in the transversal view (Fig. 5.5). Despite the significantly longer etching time applied to *P. nobilis* (10 seconds compared to 1–3 seconds in *P. margaritifera)*, the amount of organic matter revealed was lower and did not follow any discernible pattern (Fig 5c). In *P. margaritifera* these aggregates appeared to clump closer together (Fig. 5.5d). The random distribution of the saccharide-rich patches matched the distribution of ^{18}O-enrichments *in P. margaritifera* (Fig. 5.5b), but was distinctly different from the well banded distribution of ^{18}O in *P. nobilis.* (Fig. 5.5a).

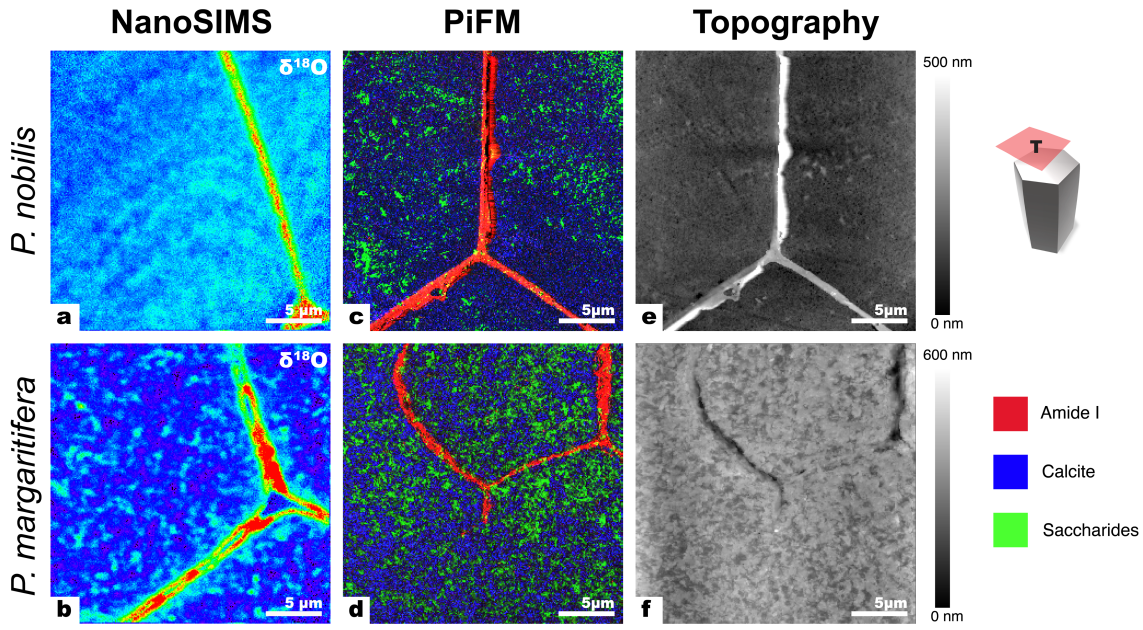

Figure 5.5 NanoSIMS (a, b) and PiFM maps (c–f) of similar regions in the transversal view of *P. nobilis* (top row) and *P. margaritifera* (bottom row). Samples for NanoSIMS imaging were exposed to artificial seawater with a $^{18}O/^{16}O$ ratio of 0.30 for 6 days at 90 °C, whereas samples for PiFM were pristine mirror-polished samples that were briefly (1–10 seconds) fixed and etched (cf. Methods). PiFM maps are shown as 3-color composite maps of three single-wavenumbers characteristic of the different phases: in red 1663 cm^{-1} is an absorption band typical for proteins (Amide I), in blue 1420 cm^{-1} is the main absorption band for calcite, and in green 1050 cm^{-1} is an absorption band typically for saccharides. (c–d) PiFM maps show a similar distribution of organic phases in both species. The protein signal is confined to the interprismatic membranes and the saccharide signal is intraprismatic and distributed randomly. (e–f) Topography maps for both species do not reveal any clear patterns.

In comparisons between NanoSIMS ^{18}O-enrichment maps (Fig. 5.6a, b) and PiFM and AFM topography maps of polished shell sections (Fig. 5.6c–f) in the longitudinal view, both species showed a distribution of the saccharide-rich phase that was weakly aligned parallel to the growth banding. This observation was better seen between the ^{18}O-enrichment and PiFM maps of *P. nobilis* (Fig. 5.6a, c) than in *P. margaritifera* (Fig. 5.6b, d). In *P. nobilis*, the saccharide-rich phase appears weakly banded in some places (Fig. 5.6c). In *P. margaritifera* the saccharide-rich phase is more

homogenously distributed with a weak alignment to the growth banding (Fig. 5.6d). The topography maps of *P. nobilis* show many fine-scale rhythmical topographical differences (Fig. 5.6e), whereas *P. margaritifera* shows only few bands raised in topography (Fig. 5.6f).

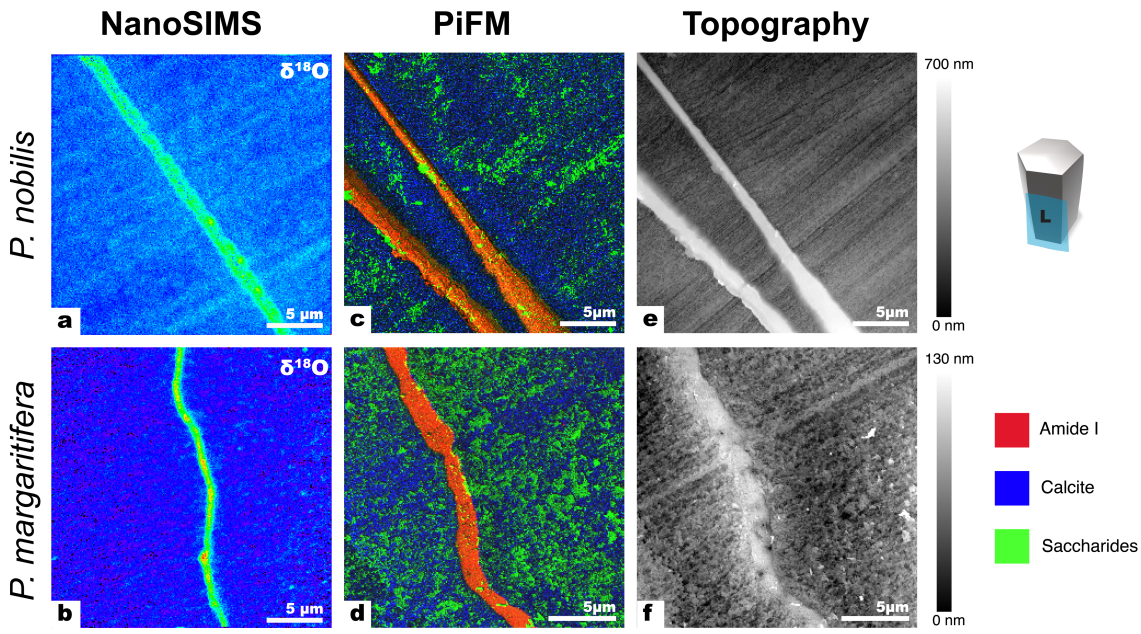

Figure 5.6 NanoSIMS (a, b) and PiFM maps (c–f) of similar regions in the longitudinal view of *P. nobilis* (top row) and *P. margaritifera* (bottom row). Samples for NanoSIMS imaging were exposed to artificial seawater with a $^{18}O/^{16}O$ ratio of 0.30 for 6 days at 90 °C whereas samples for PiFM were pristine mirror-polished samples that were briefly (1–10 seconds) fixed and etched (cf. Methods). PiFM maps are shown as 3-color composite maps of three single-wavenumbers characteristic of the different phases: in red 1663 cm^{-1} is an absorption band typical for proteins (Amide I), in blue 1420 cm^{-1} is the main absorption band for calcite, and in green 1050 cm^{-1} is an absorption band typical for saccharides. (c) In *P. nobilis* the distribution of the saccharide-rich phase appears in some places weakly banded parallel to the growth banding. (d) In *P. margaritifera* the saccharide-rich phase is more homogenously distributed but also appears weakly oriented parallel to the growth banding. (e–f) PiFM topography images show that *P. nobilis* (e) is strongly banded, whereas *P. margaritifera* (f) only shows isolated banding.

PiFM spectra were acquired for each of the organic and mineral components mapped above for both species (Fig. 5.7). The spectra for shell calcite, the saccharide-rich phase, and the interprismatic membranes were highly similar between the two species. Shell calcite spectra had a prominent absorption band at 1420 cm^{-1} and a smaller absorption band at 876 cm^{-1} (Fig. 5.7a, b). The saccharide-rich phases had the same absorption bands as calcite, with some additional absorption bands, most notably a prominent absorption band centered on 1050 cm^{-1} (Fig. 5.7c, d). The interprismatic membranes were characterized by prominent amide I and II absorption bands, attesting to their dominantly proteinaceous nature (Fig. 5.7e, f).

5.4 Discussion

5.4.1 Species-specific diagenetic isotope exchange in the prismatic layer of bivalves

The bulk oxygen isotope measurements on *P. nobilis* and *P. margaritifera* prisms incubated with the experimental solution (Fig. 5.2) allow for two observations: (1) The prismatic layer of bivalves is significantly more susceptible to diagenetic isotope exchange than the tests of benthic foraminifera and, (2) like foraminifera, bivalves show a species-specific susceptibility to fluid penetration and subsequent exchange (Cisneros-Lazaro *et al.*, 2022). From the NanoSIMS maps and line-profiles (Fig. 5.3, 5.4), it is clear that the artificial seawater penetrated into and isotopically exchanged with the prism calcite of both species in a pervasive and heterogenous manner, showing distinct species-dependent patterns.

In *P. nobilis,* areas of increased O-exchange in both orientations are present as bands that are most strongly correlated with the distribution of sulfur, and to a lesser extent magnesium and nitrogen (Fig. 5.3). Note that the curved banding seen in the transversal view (Fig. 5.3a, c, e) is mostly likely due to a cutting angle effect. The ^{18}O-enrichment in *P. nobilis* therefore appears correlated to growth banding perpendicular to the length of prisms (Cuif *et al.*, 2012) (Fig. 5.1f). In *P. margaritifera*, areas of increased O-exchange were primarily associated with micrometer-sized disk-shaped patches of nitrogen, and less with the growth banding pattern (Fig. 5.4). The higher ^{18}O-exchange seen in *P. nobilis* compared to *P. margaritifera* is potentially linked to the geometry and distribution of organic components: strongly layered organic matter, as in *P. nobilis*, potentially

offers more interconnected pathways through which fluids can migrate, compared with the patchy – and hence more disconnected – distribution of organic matter in *P. margaritifera*. These observations strongly indicate that the observed species-specific susceptibility of calcitic bivalve mollusks to diagenetic isotope exchange (Fig. 5.2) is linked with both the distribution and composition of organic components within their prisms.

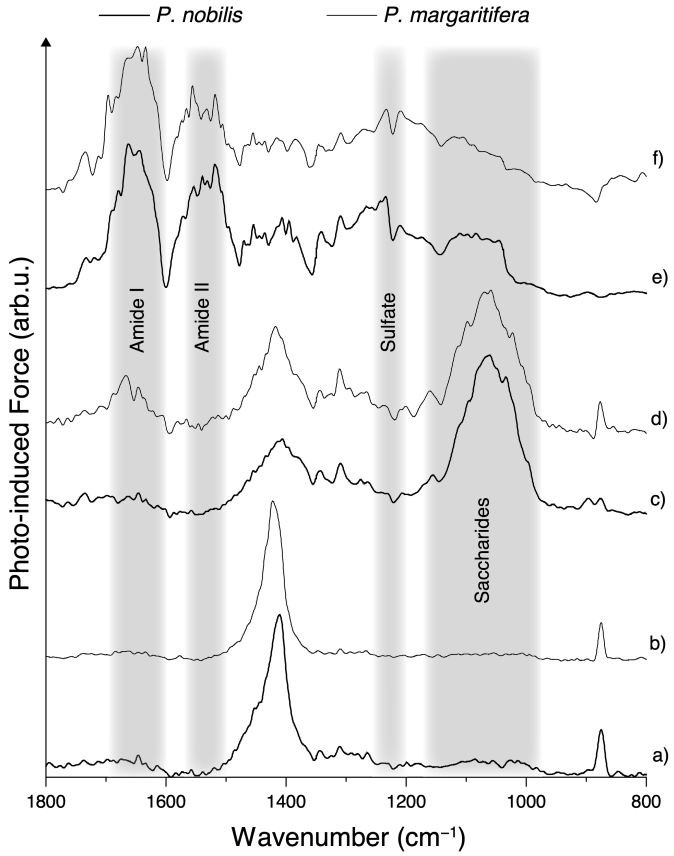

Figure 5.7 PiFM spectra of the various organic and mineral components in the shells of *P. nobilis* and *P. margaritifera*. (a–b) Shell calcite. (c–d) Saccharide-rich phase. (e–f) Interprismatic membrane. Shaded areas highlight spectral regions associated to proteins (amide I and I), sulfate and saccharides.

Previous O-isotope exchange experiments on foraminifera tests, with the same experimental protocol, also found strong correlations between ^{18}O-enrichments and ultrastructures rich in organic material(s) (Cisneros-Lazaro *et al.*, 2022). All three species of foraminifera used in those experiments had prominent sulfur and magnesium banding that were not significantly correlated with high ^{18}O-enrichments. The speciation of sulfur in different biominerals is heterogenous. Using XANES chemical species mapping, Dauphin and co-authors found that in the prismatic layer of *P. nobilis* and *P. margaritifera,* sulfur occurs both within the prisms and in the interprismatic organic membranes in the form of sulfated polysaccharides (Dauphin, 2003; Dauphin *et al.*, 2003a, 2003b). Conversely, Yoshimura and co-authors (2013) found inorganic sulfate to be the dominant sulfur species in two species of aragonitic and calcitic bivalves, substituting for carbonate. Foraminifera tests are also thought to primarily host sulfur within the calcite lattice due to the substitution of carbonate for sulfate ions (van Dijk *et al.*, 2017). In other species including calcitic brachiopods, aragonitic bivalves, and corals, sulfur occurs both as carbonate-associated sulfate incorporated within the mineral phase as well as organic sulfur, i.e., as intracrystalline organic matter (Cusack *et al.*, 2008a; Tamenori *et al.*, 2014; Fichtner *et al.*, 2018). The NanoSIMS maps here show that the relationship between sulfur and ^{18}O-enrichment is different in the two species: In *P. nobilis* sulfur showing a growth distribution is clearly linked to ^{18}O-enrichment, whereas in *P. margaritifera* this is not the case. This appear to be odds with the XANES results of Dauphin and co-authors, which showed that sulfur in both species is primarily hosted by organic molecules rather than within the calcite crystal lattice (Dauphin, 2003; Dauphin *et al.*, 2003a, 2003b). The pattern of ^{18}O-exchange in *P. margaritifera* matches best with that previously seen in foraminifera (Cisneros-Lazaro *et al.*, 2022), where increased ^{18}O-exchange was best correlated with nitrogen-associated organic matter, but *not* to the presence of sulfur.

5.4.2 The role of saccharide-rich organic matter in diagenetic isotope exchange

Consistent with the present work, previous studies have mapped the distribution of organic components in the prismatic layer of bivalve mollusks and found that the composition of organic components is heterogenous, with the interprismatic membranes mostly associated to proteins, whereas saccharides are mostly found intraprismatically (Dauphin *et al.*, 2003a; Farre *et al.*, 2011; Huang *et al.*, 2021). The PiFM maps of both species indicate that proteins are mostly confined to

the interprismatic membrane, whereas a saccharide-rich phase is distributed randomly throughout the prisms as micrometer sizes patches (Fig. 5.6, 6). PiFM spectra of this saccharide-rich phase are similar for both species and show the same peaks as calcite as well as some prominent peaks in the region typically attributed to saccharides (Fig. 5.7a–d). This suggests that regions mapped in blue in PiFM maps are largely calcite-dominated, whereas the regions mapped in green are saccharide-rich (Figs. 5.5c, d and 5.6c, d). Intracrystalline saccharides in bivalve mollusks are thought to be sulfated, as evidenced by techniques such as colloidal iron staining, electrophoresis, and XANES spectra and mapping (Dauphin, 2003; Dauphin *et al.*, 2003b; Huang *et al.*, 2021). The patchy distribution of this saccharide-rich phase matches the patchy distribution of nitrogen in *P. margaritifera*, but is not linked to the strongly layered distribution of sulfur-rich (and nitrogen-rich in the case of *P. nobilis*) organic components as mapped with NanoSIMS in both species (Figs. 5.5, 5.6); only occasionally in *P. nobilis* could weak banding of the saccharide-rich phase potentially be associated to sulfur banding (Fig. 5.6c). Moreover, sulfate FTIR absorption bands in the 1200–1250 range (Dauphin, 2003; Agbaje *et al.*, 2017, 2021) are absent in the PiFM spectra of the saccharide-rich phase (Fig 7c, d). Consequently, the bulk of the evidence found here suggests that the intracrystalline saccharides associated with prismatic layer in both species are not sulfated.

The highly heterogenous distribution of increased O-exchange in bivalve shells shown here represents a challenge to paleoclimatic reconstructions, even in the best preserved fossil shells. Discussing the effects of diagenesis on the $\delta^{18}O$ values of pristine-looking bivalve shells, Ivany and Runnegar (2010) proposed, that after screening for diagenesis with conventional methods, if shell $\delta^{18}O$ values exhibit clear seasonal variations, the $\delta^{18}O$ values are likely to be primary, as diagenesis would likely obliterate this original pattern. However, as shown by the results here, the heterogenous, and in the case of *P. nobilis*, even banded ^{18}O-enrichments in areas with relatively high susceptible to diagenesis show that some cyclicity could potentially be created during diagenesis, rendering the final O-isotope composition a mix of the primary signal and diagenesis.

5.5 Conclusions

Two bivalve mollusks, *Pinna nobilis* and *Pinctada margaritifera*, were experimentally simulated to study how differences in the composition and distribution of intracrystalline organic matter affect how these shells are modified by post-burial diagenesis. Taxon-specific differences in the amount of bulk O-isotope exchange were observed with *P. nobilis* showing greater bulk O-isotope exchange than *P. margaritifera*. In *P. nobilis*, regions of increased O-isotope exchange were linked to sulfur-rich organic matter present in the growth banding, whereas in *P. margaritifera* O-isotope exchange was correlated to the occurrence of micrometer-sized patches of nitrogen-rich organic matter. Chemical characterization of organic matter in both species with Photo-induced Force Microscopy (PiFM) revealed that proteins are predominantly restricted to the interprismatic membranes, whereas saccharide-rich areas were abundant within the interior of prisms.

This study raises questions regarding identification and the role of different sulfur components, i.e., organic matter-hosted vs carbonate-hosted, during the biomineralization and diagenesis of biocalcites. With the methods used in this study it was not possible to fully characterize these saccharides, but interesting comparisons could be made between the two species of bivalves studied here, which are thought to primarily host organic sulfur, and the calcitic bivalve found to primarily host inorganic sulfur by Yoshimura and co-authors (2013). Future work should aim to characterize the intracrystalline saccharides in bivalve mollusks through methods such as High-Performance Anion-Exchange chromatography with Pulsed-Amperometric-Detection (HPAE-PAD) or solid state nuclear magnetic resonance (SS-NMR), which can identify and quantify mono- and polysaccharides found within intracrystalline matter (Immel *et al.*, 2016; Oudot *et al.*, 2020).

The apparent relatively low presence of intracrystalline proteins and the apparent high abundance of intracrystalline saccharides point to the importance of the latter to facilitate fluid penetration into and exchange isotopes with calcitic bivalve shells. Further research should therefore aim to investigate the bulk composition as well as the decomposition potential of intracrystalline saccharides. The results of this work provide strong inspiration for such research, as better understanding of fine-scale diagenetic isotope exchange in biocalcites is of fundamental importance for paleoclimatic and paleophysiological reconstructions.

5.6 Supplementary information

Shell $\delta^{18}O$ (‰ VSMOW)		
Species	*P. nobilis*	*P. margaritifera*
	1354	980
	1306	976
	1287	760
	1298	817
		807
Average	1311	868
SD	26	92
Variance	652	8459

Supplementary Table 5.1. Summary table of the bulk oxygen isotope measurements of *P. nobilis* and *P. margaritifera* shells after exposure to artificial seawater with a $^{18}O/^{16}O$ ratio of 0.30 for 6 days at 90 °C.

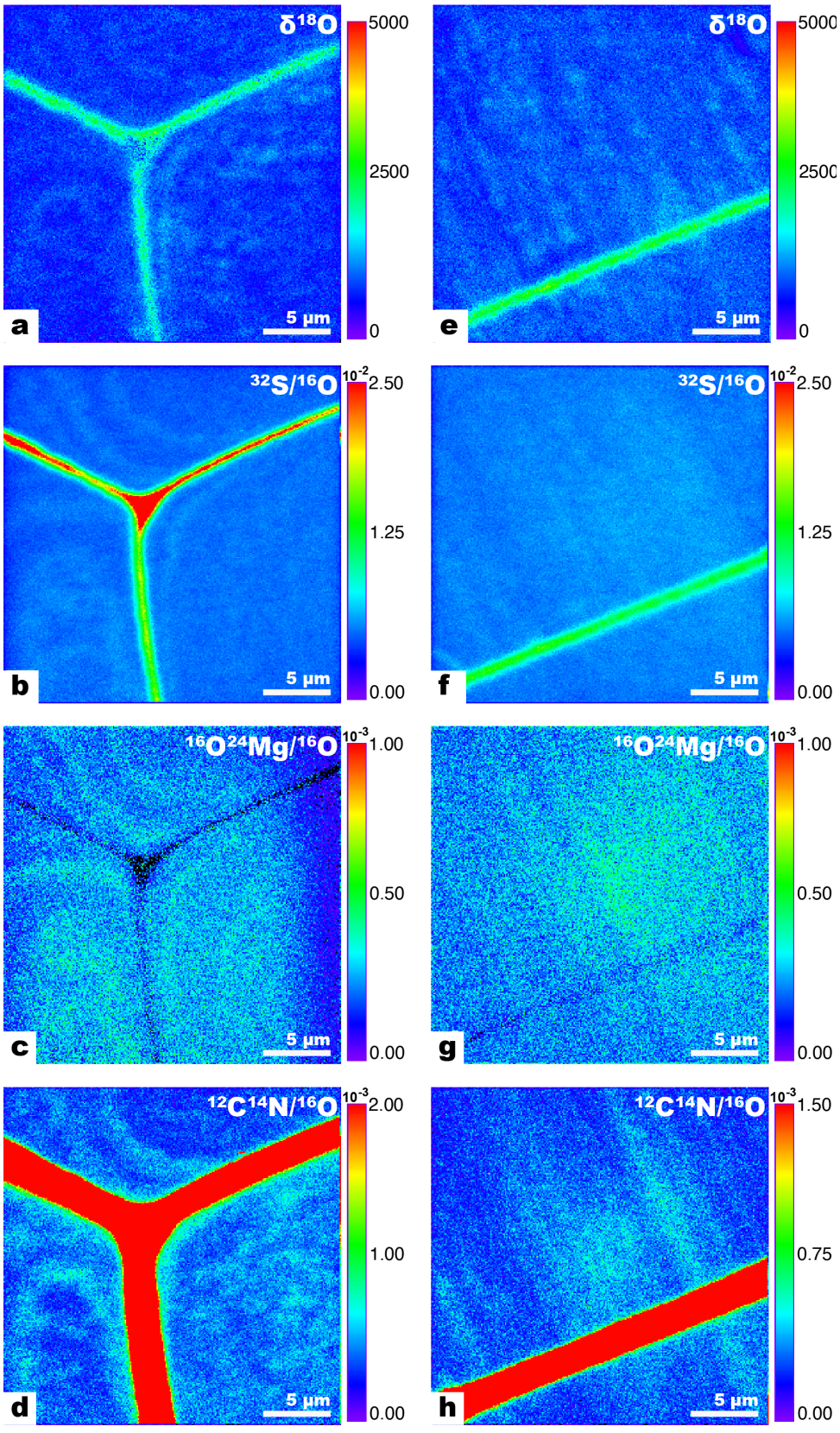
δ18O
5000
2500
0
5 µm
a
δ18O
5000
2500
5 µm
e
32S/16O
10-2
2.50
1.25
0.00
5 µm
b
32S/16O
10-2
2.50
1.25
0.00
5 µm
f
16O24Mg/16O
10-3
1.00
0.50
0.00
5 µm
c
16O24Mg/16O
10-3
1.00
0.50
0.00
5 µm
g
12C14N/16O
10-3
2.00
1.00
0.00
5 µm
d
12C14N/16O
10-3
1.50
0.75
0.00
5 µm
h

Supplementary Figure 5.1. (Preceding page) NanoSIMS images of polished cross-sections of *P. nobilis* after exposure to artificial seawater with a $^{18}O/^{16}O$ ratio of 0.30 for 6 days at 90 °C. (a–d) Transversal view. (e–h) Longitudinal view.

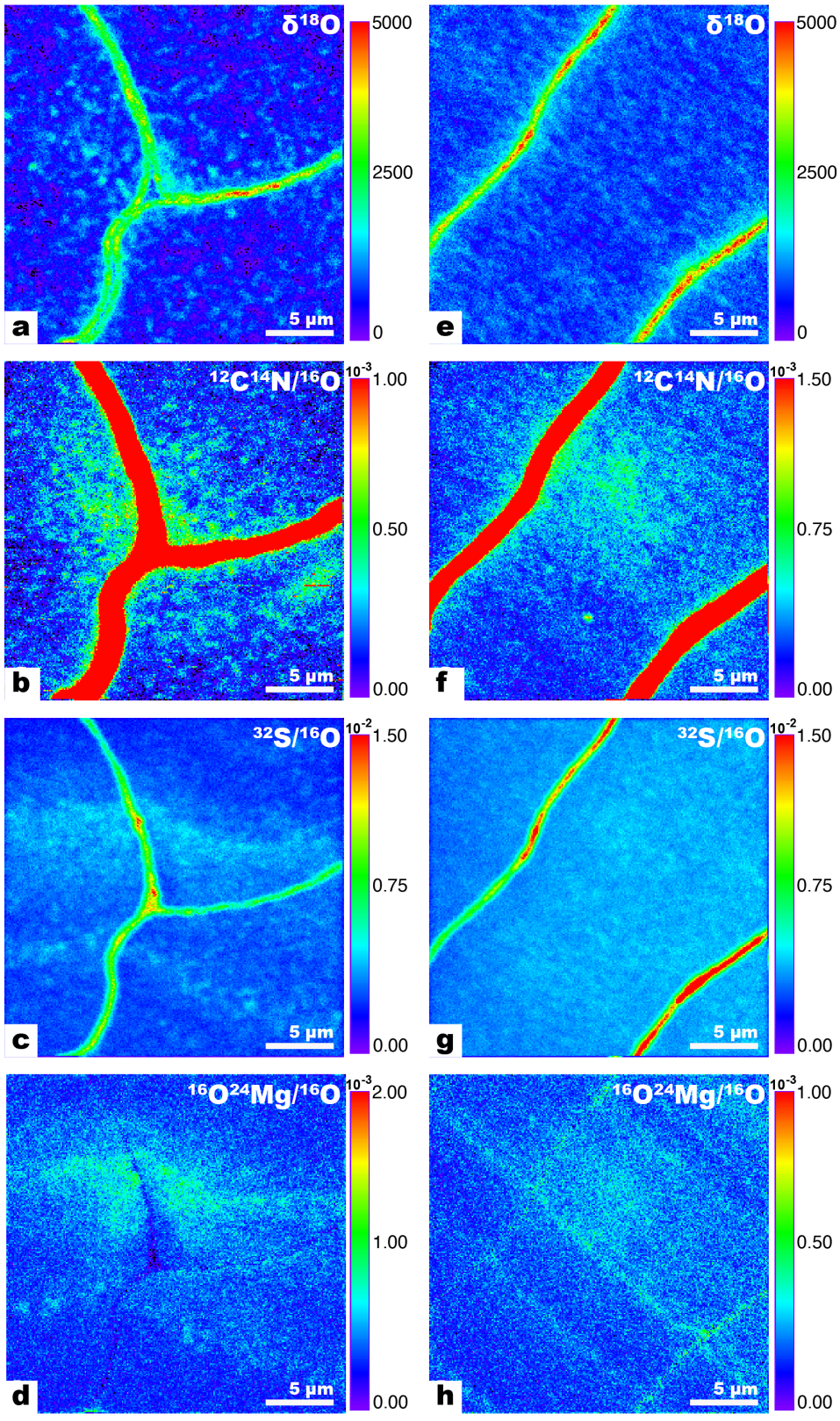
δ18O
5000
2500
0
5 µm
a
δ18O
5000
2500
0
5 µm
e
12C14N/16O
10-3
1.00
0.50
0.00
5 µm
b
12C14N/16O
10-3
1.50
0.75
0.00
5 µm
f
32S/16O
10-2
1.50
0.75
0.00
5 µm
c
32S/16O
10-2
1.50
0.75
0.00
5 µm
g
16O24Mg/16O
10-3
2.00
1.00
0.00
5 µm
d
16O24Mg/16O
10-3
1.00
0.50
0.00
5 µm
h

Supplementary Figure 5.2 (Preceding page) NanoSIMS images of polished cross-sections of *P. margaritifera* after exposure to artificial seawater with a $^{18}O/^{16}O$ ratio of 0.30 for 6 days at 90 °C. (a–d) Transversal view. (e–h) Longitudinal view.

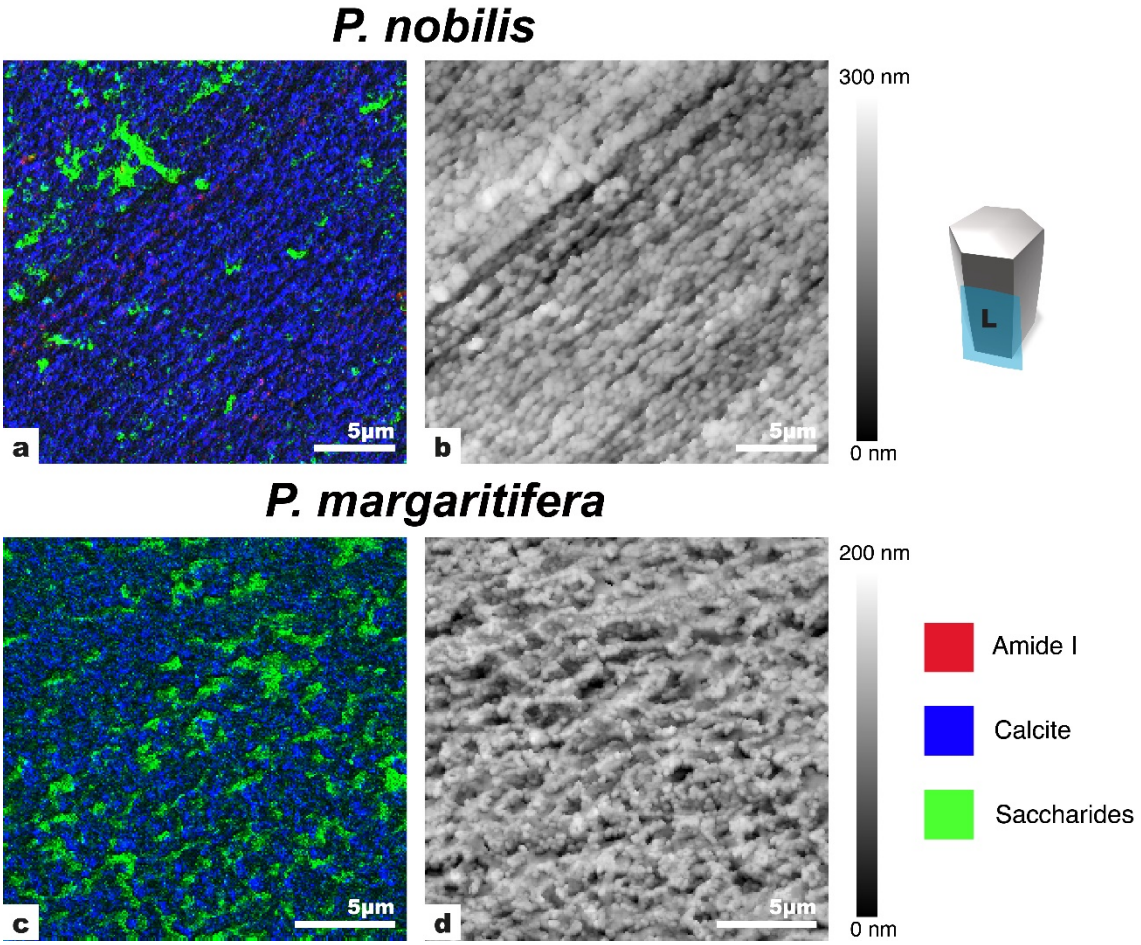

Supplementary Figure 5.3 PiFM maps of similar regions in the longitudinal view of *P. nobilis* and *P. margaritifera*. These are pristine mirror-polished samples that were briefly (1–10 seconds) fixed and etched (cf. Methods). PiFM maps are shown 3-color composite maps of three single-wavenumbers characteristic of the different phases: in red 1663 cm^{-1} is an absorption band typical for proteins (Amide I), in blue 1420 cm^{-1} is the main absorption band for calcite, and in green 1050 cm^{-1} is an absorption band typical for saccharides.

6 Conclusions

6.1 Species-specific diagenetic isotope exchange

The biocalcites investigated here are all composed of sub-spherical calcite domains 20–150 nm in diameter. The effects of diagenetic isotope exchange could therefore be expected to be similar across species. However, as demonstrated through the simulated diagenesis experiments conducted in this thesis (chapters 2, 3 and 5) this is not the case, with both bulk O-isotope ratios and NanoSIMS imaging showing species-specific rates and patterns of O-isotope exchange. In all five modern species of foraminifera tests and prismatic bivalve shells, the observed O-isotope exchange was closely linked with the occurrence and distribution of the inter- and intracrystalline organic materials.

In the foraminifera tests, the highest ^{18}O-enrichments were spatially correlated with organic linings and cogwheel domain boundaries, which differ in distribution the three species investigated, explaining species-specific differences in bulk O-isotope exchange. In the prismatic layer of bivalves, the observed O-isotope exchange was likewise linked to the organic moiety, with clear differences between species. In *P. nobilis*, the ^{18}O-enrichment exhibited a banded distribution that was well correlated to distribution of sulfur in growth bands. In *P. margaritifera*, O-isotope exchange was well correlated to the occurrence of micrometer-sized disk-shaped patches of nitrogen-rich organic matter. The observed bulk ^{18}O-enrichments were attributed to such differences in the distribution of the organic moiety between the two species: a well-defined layering of organic matter in *P. nobilis* provides more interconnected pathways for fluid penetration compared with *P. margaritifera*, in which the organic matter is more fragmented, offering less connectivity for water penetration.

These results demonstrate how diagenesis is influenced by the species-specific differences in the abundance and distribution of shell organic moieties, potentially explaining why different species may experience different degrees of diagenesis, despite similar diagenetic conditions. Furthermore, the observed heterogenous O-isotope compositions resulting from incubation experiments in this thesis indicate that even well-preserved fossil shells with strong intra-shell variations in their O-

isotope composition that would normally be interpreted as primary, may have been affected by diagenetic isotope exchange.

6.2 Diagenetic isotope exchange in fossil biocalcites

A combination of scanning electron imaging, electron backscatter diffraction, and cathodoluminescence imaging was used to compare the ultrastructures and crystallography between modern *Ammonia confertitesta* and a fossil equivalent, *Ammonia beccarii*. These results demonstrated the excellent preservation state of the fossil tests and the high degree of ultrastructural similarity between modern and fossil tests, with the exception that the organic moiety within fossil tests was partially degraded by natural fossilization processes. The O-isotope exchange visualized and quantified by NanoSIMS mapping showed that fossil foraminifera tests were about half as susceptible to diagenetic isotope exchange as modern foraminifera tests. NanoSIMS imaging of the fossil tests showed no evidence for increased O-isotope exchange at the location of the organic linings and cogwheel structures, suggesting that the organic matter here was degraded. The lack of porosity at the site of the organic linings suggested that the voids created by the degradation of the organic moiety were filled with secondary calcite. As the results of this thesis have established, abiotic calcite is significantly less susceptible to O-isotope exchange than biogenic calcite. This diagenetic infilling at the sites of organic matter degradation is thus consistent with the lower susceptibility of fossil biocalcite to O-isotope exchange. However, the measured isotope exchange in fossil biocalcites clearly demonstrates that they remain susceptible to burial diagenesis for millions of years, and hence even well-preserved fossil biocalcites may have bulk O-isotopic compositions compromised by diagenesis, resulting in biased paleo-temperature reconstructions.

I therefore propose that similar simulated diagenesis experiments should be conducted on tests from the foraminifera species dominantly utilized for paleoclimate reconstructions, to better constrain the diagenetic O-isotope exchange on these key samples. Recent work by Adams and colleagues (2023) demonstrated that paleoclimatic records can be corrected for the effects of grain-boundary diffusion of oxygen. Species-specific correction for diagenesis would not be unlike the species-specific vital effect corrections that are now commonplace.

Although this thesis has only investigated the effects of O-isotope exchange, the NanoSIMS images presented here show that fluids can penetrate into the entirety of the shell structure, even in fossil biocalcites with less organo-mineral interfaces to facilitate fluid migration. This may have implications for the interpretation of paleoclimate records based on other elemental and isotopic paleoproxies, such as Mg/Ca and Sr/Ca ratios, carbon and boron isotopes etc.

6.3 Outlook

By utilizing the methodology for simulating diagenesis in biocalcites through the exposure to highly ^{18}O-enriched fluids, future work could investigate fluid-mediated isotopic exchange in other key fossil groups such as brachiopods and belemnites. This would help establish whether diagenesis in other biocalcites is also principally facilitated by the organic moiety rather than (or in addition to) trace-element variations, e.g., of magnesium. A limitation of this thesis was that only one species of modern foraminifera was compared to a fossil equivalent with a narrowly constrained age. It would be important to compare the extent of diagenetic O-isotope exchange in other excellently preserved fossil foraminifera tests and bivalve shells for a range of ages, and from similar paleoenvironmental settings, with modern equivalents. The susceptibility of different fossil biocalcites, in which the organic moiety is significantly degraded, should be thoroughly investigated.

This thesis raises interesting questions regarding the role that different sulfur reservoirs — carbonate-hosted vs organics-hosted — play during the diagenesis of biocalcites. All investigated species of biocalcites showed prominent sulfur banding. In foraminifera tests, sulfur banding was associated to organic linings, but also exhibited additional banding seemingly unrelated to the organic linings; this sulfur banding was preserved in the fossil specimens. In the prismatic layer of both bivalves, *P. nobilis* and *P. margaritifera*, sulfur banding was associated to the growth banding that develops perpendicular to long axis of the prisms. In *P. nobilis* increased O-isotope exchange was clearly linked to the sulfur banding, but this was not the case in any of the foraminifera tests studied or, notably, in *P. margaritifera*. Sulfur in foraminifera tests is thought to be primarily carbonate-hosted, whereas in prisms from both bivalve species studied here, sulfur is thought to be hosted within the organic moiety. It is therefore somewhat surprising that the two bivalve species

show a clear difference in the association between shell sulfur concentrations and rate of O-isotope exchange. Future simulated diagenesis experiments on different biocalcite species with distinct sulfur reservoirs could establish whether organics-hosted sulfur, but not carbonate-hosted sulfur, can generally be linked to increased O-isotopic exchange and help clarify why *P. nobilis* and *P. margaritifera* prisms show such pronounced differences in the association between the presence of sulfur and O-isotope exchange.

A final proposed avenue for future research likewise concerns sulfur. This thesis identified abundant intracrystalline saccharide-rich organic matter in the prismatic layer of bivalves. Intracrystalline saccharides in bivalves are thought to be sulfated, yet the distribution of sulfur in the NanoSIMS maps did not match the distribution of the saccharide-rich phase in the PiFM maps. PiFM spectra of the saccharide-rich phase likewise did not show the absorption bands typically associated with sulfated compounds. Moreover, much of the research into saccharide components in shells has been focused on polysaccharides, such as chitin, yet the PiFM spectra of the saccharide-rich phase point to simple sugars akin to glucose. Establishing whether this saccharide-rich phase is composed of mono- and/or polysaccharides and whether it is sulfated or not would provide insights into the biomineralization process of bivalve mollusks as well as assist in finding suitable additives to improve the mechanical properties of bio-inspired calcites.

7 References

Adams, Arthur, Daval, Damien, Baumgartner, Lukas P., Bernard, Sylvain, Vennemann, Torsten, Cisneros-Lazaro, Deyanira, Baronnet, Alain, Grauby, Olivier, Guo, Jinming and Meibom, Anders (2023) 'Rapid grain boundary diffusion in foraminifera tests biases paleotemperature records', *Communications Earth and Environment*, 4(144), pp. 1–11. doi: 10.1038/s43247-023-00798-2.

Addadi, L. and Weiner, Stephen (1985) 'Interactions between acidic proteins and crystals: Stereochemical requirements in biomineralization', *PNAS*, 82, pp. 4110–4114.

Addadi, Lia, Joester, Derk, Nudelman, Fabio and Weiner, Steve (2006) 'Mollusk Shell Formation : A Source of New Concepts for Understanding Biomineralization Processes', *Chemistry, a European Journal*, 12, pp. 980–987. doi: 10.1002/chem.200500980.

Agbaje, Oluwatoosin B. A., Dominguez, J. Gabriel and Jacob, Dorrit E. (2021) 'Organic biopolymers of venus clams : Collagen-related matrix in the bivalve shells with crossed-lamellar ultrastructure', *Biochemistry and Biophysics Reports*, 26, pp. 1–8. doi: 10.1016/j.bbrep.2021.100939.

Agbaje, Oluwatoosin B. A., Thomas, D., McInerney, B. V, Molloy, Mark P. and Jacob, Dorrit E. (2017) 'Organic macromolecules in shells of Arctica islandica : comparison with nacroprismatic bivalve shells', *Marine Biology*. Springer Berlin Heidelberg, 164(11), pp. 1–13. doi: 10.1007/s00227-017-3238-2.

Agbaje, Thomas, Denise E., Dominguez, J. Gabriel, McInerney, B. V, Kosnik, Matthew A. and Jacob, Dorrit E. (2019) 'Biomacromolecules in bivalve shells with crossed lamellar architecture', *Journal of Materials Science*. Springer US, 54(6), pp. 4952–4969. doi: 10.1007/s10853-018-3165-8.

Aizenberg, J. (2006) 'Nanomechanics of Biological Single Crystals', in Chuang, T. J., Anderson, P. M., Wu, M. K., and Hsieh, S. (eds) *Nanomechanics of Materials and Structures*. Dordreecht: Springer, pp. 99–108.

Al-Aasm, I. and Veizer, J. (1986) 'Diagenetic stabilization of aragonite and low-Mg calcite, I. Trace elements in rudists', *Journal of Sedimentary Petrology*, 56(1), pp. 138–152.

Albeck, S., Addadi, L. and Weiner, S. (1996) 'Regulation of Calcite Crystal Morphology by Intracrystalline Acidic Proteins and Glycoproteins', *Connective Tissue Research*, 35, pp. 365–370.

Albeck, S., Aizenberg, J., Addadi, L. and Weiner, S. (1993) 'Interactions of Various Skeletal Intracrystalline Components with Calcite Crystals', *Journal of American Chemical Society*, 115, pp. 11691–11697.

Alleon, Julien, Bernard, Sylvain, Guillou, Corentin Le, Daval, Damien, Skouri-panet, Feriel, Kuga, Maïa and Robert, François (2017) 'Organic molecular heterogeneities can withstand diagenesis', *Scientific Reports*, 7(1508), pp. 1–9. doi: 10.1038/s41598-017-01612-8.

Allison, Nicola, Finch, Adrian A. and EIMF (2010) 'The potential origins and palaeoenvironmental implications of high temporal resolution δ18O heterogeneity in coral skeletons', *Geochimica et Cosmochimica Acta*, 74, pp. 5537–5548. doi: 10.1016/j.gca.2010.06.032.

Anderson, Thomas F. (1969) 'Self-Diffusion of Carbon and Oxygen in Calcite by Isotope Exchange with Carbon Dioxide', *Journal of Geophysical Research*, 74(15), pp. 3918–3932.

Banner, F. T., Sheehan, R. and Williams, E. (1973) 'The organic skeletons of Rotaline foraminifera: A review', *Journal of Foraminiferal Research*, 3(1), pp. 30–42.

Barker, S., Greaves, M. and Elderfield, H. (2003) 'A study of cleaning procedures used for foraminiferal Mg/Ca paleothermometry', *Geochemistry, Geophysics, Geosystems*, 4(9), pp. 1–20. doi: 10.1029/2003GC000559.

Barras, Christine, Mouret, Aurelia, Pia Nardelli, Maria, Metzger, Edouard, Petersen, Jassin, La, Carole, Filipsson, Helena L. and Jorissen, Fran (2018) 'Experimental calibration of manganese incorporation in foraminiferal calcite', *Geochimica et Cosmochimica Acta*, 237, pp. 49–64. doi: 10.1016/j.gca.2018.06.009.

Bauch, D., Carstens, J. and Wefer, G. (1997) 'Oxygen isotope composition of living Neogloboquadrina pachyderman (sin.) in the Arctic Ocean', *Earth and Planetary Science Letters*, 146, pp. 47–58.

Baumgartner-Mora, C. and Baumgartner, P. O. (1994) 'Shell structure of fossil foraminifera studied by cathodoluminiscence', *Microscopy and Microanalysis*, 3, pp. 35–38.

Bentov, Shmuel, Brownlee, Colin and Erez, Jonathan (2009) 'The role of seawater endocytosis in the biomineralization process in calcareous foraminifera', *PNAS*, 106(51), pp. 21500–21504. doi: 10.1073/pnas.0906636106.

Bentov, Shmuel and Erez, Jonathan (2006) 'Impact of biomineralization processes on the Mg content of foraminiferal shells: A biological perspective', *Geochemistry, Geophysics, Geosystems*, 7(1), pp. 1–11. doi: 10.1029/2005GC001015.

Bernard, S., Daval, D., Ackerer, P., Pont, S. and Meibom, A. (2017) 'Burial-induced oxygen-isotope re-equilibration of fossil foraminifera explains ocean paleotemperature paradoxes', *Nature Communications*, 8(1), pp. 1–10. doi: 10.1038/s41467-017-01225-9.

Bernard, Sylvain and Papineau, Dominic (2014) 'Graphitic Carbons and Biosignatures', *Elements*, 10, pp. 435–440. doi: 10.2113/gselements.10.6.435.

Bernasconi, Stefano M., Schmid, Thomas W., Grauel, Anna-lena and Mutterlose, Joerg (2011) 'Applied Geochemistry Clumped-isotope geochemistry of carbonates : A new tool for the reconstruction of temperature and oxygen isotope composition of seawater', *Applied Geochemistry*, 26, pp. S279–S280. doi: 10.1016/j.apgeochem.2011.03.080.

Boersma, Anne (1998) 'Foraminifera', in Bilal, U. and Boersma, Anne (eds) *Introduction to Marine Micropaleontology*. Elsevier B.V., pp. 19–77.

Boussetta, S., Bassinot, F., Sabbatini, A., Caillon, N., Nouet, J., Kallel, N., Rebaubier, H., Klinkhammer, G. and Labeyrie, L. (2011) 'Diagenetic Mg-rich calcite in Mediterranean sediments : Quantification and impact on foraminiferal Mg / Ca thermometry', *Marine Geology*, 280(1–4), pp. 195–204. doi: 10.1016/j.margeo.2010.12.011.

Brand, Uwe, Logan, Alan, Hiller, Norton and Richardson, Joyce (2003) 'Geochemistry of modern brachiopods: applications and implications for oceanography and paleoceanography', *Chemical Geology*, 198, pp. 305–334. doi: 10.1016/S0009-2541(03)00032-9.

Branson, Oscar, Bonnin, Elisa A., Perea, Daniel E., Spero, Howard J., Zhu, Zihua, Winters, Maria and

Hönisch, Bärbel (2016) ‘Nanometer-Scale Chemistry of a Calcite Biomineralization Template : Implications for Skeletal Composition and Nucleation’, *PNAS*, 113(46), pp. 12934–12939. doi: 10.1073/pnas.1522864113.

Branson, Oscar, Redfern, Simon A. T., Tyliszczak, Tolek, Sadekov, Aleksey, Langer, Gerald, Kimoto, Katsunori and Elderfield, Henry (2013) ‘The coordination of Mg in foraminiferal calcite’, *Earth and Planetary Science Letters*, 383, pp. 134–141. doi: 10.1016/j.epsl.2013.09.037.

Briard, J., Pucéat, E., Vennin, E., Daëron, M., Chavagnac, V., Jaillet, R., Merle, D. and Rafélis, M. De (2020) ‘Seawater paleotemperature and paleosalinity evolution in neritic environments of the Mediterranean margin: Insights from isotope analysis of bivalve shells’, *Palaeogeography, Palaeoclimatology, Palaeoecology*, 543, pp. 1–19. doi: 10.1016/j.palaeo.2019.109582.

Butler, Paul G., Wanamaker, Alan D., Scourse, James D., Richardson, Christopher A. and Reynolds, David J. (2011) ‘Long-term stability of δ 13 C with respect to biological age in the aragonite shell of mature specimens of the bivalve mollusk Arctica islandica’, *Palaeogeography, Palaeoclimatology, Palaeoecology*, 302, pp. 21–30. doi: 10.1016/j.palaeo.2010.03.038.

Carpenter, S. J. and Lohmann, K. C. (1995) ‘d18O and d13C values of modern brachiopod shells’, *Geochimica et Cosmochimica Acta*, 59(18), pp. 3749–3764.

Carre, Matthieu, Bentaleb, Ilhem, Bruguier, Olivier, Ordinola, Elmer, Barrett, Nicholas T. and Fontugne, Michel (2006) ‘Calcification rate influence on trace element concentrations in aragonitic bivalve shells : Evidences and mechanisms’, *Geochemistry, Geophysics, Geosystems*, 70, pp. 4906–4920. doi: 10.1016/j.gca.2006.07.019.

Casella, L. A., Griesshaber, E., Simonet Roda, M., Ziegler, A., Mavromatis, V., Henkel, D., Laudien, J., Häussermann, V., Neuser, R. D., Angiolini, L., Dietzel, M., Eisenhauer, A., Immenhauser, A., Brand, U. and Schmahl, W. W. (2018) ‘Micro- and nanostructures reflect the degree of diagenetic alteration in modern and fossil brachiopod shell calcite : A multi-analytical screening approach (CL , FE-SEM , AFM , EBSD)’, *Palaeography, Palaeoclimatology, Palaeoecology*, 502, pp. 13–30. doi: 10.1016/j.palaeo.2018.03.011.

Casella, Laura A., Griesshaber, Erika, Yin, Xiaofei, Ziegler, Andreas, Mavromatis, Vasileios, Müller, Dirk, Ritter, Ann-christine, Hippler, Dorothee, Harper, Elizabeth M., Dietzel, Martin, Immenhauser, Adrian, Schöne, Bernd R., Angiolini, Lucia and Schmahl, Wolfgang W. (2017) ‘Experimental diagenesis : insights into aragonite to calcite transformation of Arctica islandica shells by hydrothermal treatment’, *Biogeosciences*, 14, pp. 1461–1492. doi: 10.5194/bg-14-1461-2017.

Chanda, Piyali, Gorski, Christopher A., Oakes, Rosie L. and Fantle, Matthew S. (2019) ‘Low temperature stable mineral recrystallization of foraminiferal tests and implications for the fidelity of geochemical proxies’, *Earth and Planetary Science Letters*, 506, pp. 428–440. doi: 10.1016/j.epsl.2018.11.011.

Checa, Antonio G., Bonarski, Jan T., Willinger, Marc G., Faryna, Marek, Berent, Katarzyna, Kania, Bogusz, Gonzalez-Segura, Alicia, Pina, Carlos M., Pospiech, Jan and Morawiec, Adam (2013) ‘Crystallographic orientation inhomogeneity and crystal splitting in biogenic calcite’, *Journal of the Royal Society Interface*, 10, pp. 1–10.

Checa, Antonio G., Macias-Sanchez, E., Harper, Elizabeth M. and Cartwright, Julyan H. E. (2016) ‘Organic membranes determine the pattern of the columnar prismatic layer of mollusc shells’, *Proceedings of the Royal Society B*, 283, pp. 1–8.

Checa, Antonio G., Rodrigeuez-Navarro, A. B. and Esteban-Delgado, Fransico J. (2005) 'The nature and formation of calcitic columnar prismatic shell layers in pteriomorphian bivalves', *Biomaterials*, 26, pp. 6404–6414. doi: 10.1016/j.biomaterials.2005.04.016.

Cisneros-Lazaro, D., Adams, A., Guo, Jinming, Bernard, Sylvain, Baumgartner, Lukas P., Daval, Damien, Baronnet, A., Grauby, O., Vennemann, T., Stolarski, Jarosław, Escrig, Stéphane and Meibom, Anders (2021) *Foraminifera Test Area and Diameter Analysis macro for ImageJ*, *Interdisciplinary Earth Data Alliance (IEDA)*. doi: https://doi.org/10.26022/IEDA/112180.

Cisneros-Lazaro, Deyanira, Adams, Arthur, Guo, Jinming, Bernard, Sylvain, Baumgartner, Lukas P., Daval, Damien, Baronnet, Alain, Grauby, Olivier, Vennemann, Torsten, Escrig, Stéphane and Meibom, Anders (2022) 'Fast and pervasive diagenetic isotope exchange in foraminifera tests is species-dependent', *Nature Communications*, 13(113), pp. 1–11. doi: 10.1038/s41467-021-27782-8.

Cramer, B. S., Toggweiler, J. R., Wright, J. D., Katz, M. E. and Miller, K. G. (2009) 'Ocean overturning since the Late Cretaceous: Inferences from a new benthic foraminiferal isotope compilation', *Paleoceanography*, 24, pp. 1–14.

Cuif, J. P., Dauphin, Y. and Sorauf, J. E. (2010a) *Biominerals and fossils through time*. Cambridge University Press.

Cuif, J. P., Dauphin, Y. and Sorauf, J. E. (2010b) 'Diversity of structural patterns and growth modes in skeletal Ca-carbonate of some plants and animals', in *Biominerals and Fossils Through TIme*, pp. 185–276.

Cuif, Jean-pierre, Belhadj, Oulfa, Borensztajn, Stephan, Marc, G., Prado, Patricia and Dauphin, Yannicke (2020) 'Prism substructures in the shell of Pinna nobilis (Linnaeus , 1758), Mollusca – Evidence for a three-dimensional pulsed-growth model', *Heliyon*, 6, pp. 2–12. doi: 10.1016/j.heliyon.2020.e04513.

Cuif, Jean-pierre, Burghammer, Manfred, Chamard, Virginie, Dauphin, Yannicke, Godard, Pierre, Moullac, Gilles Le, Nehrke, Gernot and Perez-huerta, Alberto (2014) 'Evidence of a Biological Control over Origin, Growth and End of the Calcite Prisms in the Shells of Pinctada margaritifera (Pelecypod, Pterioidea)', *Minerals*, 4, pp. 815–834. doi: 10.3390/min4040815.

Cuif, Jean-pierre, Dauphin, Yannicke, Nehrke, Gernot, Nouet, Julius and Perez-huerta, Alberto (2012) 'Layered Growth and Crystallization in Calcareous Biominerals: Impact of Structural and Chemical Evidence on Two Major Concepts in Invertebrate Biomineralization Studies', *Minerals*, 2, pp. 11–39. doi: 10.3390/min2010011.

Currey, J. D. (1977) 'Mechanical Properties of Mother of Pearl in Tension', *Proceedings of the Royal Society B*, 196, pp. 443–463. doi: 10.1098/rspb.1977.0050.

Currey, John D. (1989) 'Biomechanics of Mineralized Skeletons', in Carter, Joseph G. (ed.) *Short courses in Geology*. American Geophysical Union.

Curry, Gordon B. and Fallick, Anthony E. (2002) 'Use of stable oxygen isotope determinations from brachiopod shells in palaeoenvironmental reconstruction', *Palaeography, Palaeoclimatology, Palaeoecology*, 182, pp. 133–143.

Cusack, Maggie, Dauphin, Yannicke, Cuif, Jean-pierre, Salomé, Murielle, Freer, Andy and Yin, Huabing (2008a) 'Micro-XANES mapping of sulphur and its association with magnesium and phosphorus in the shell

of the brachiopod , Terebratulina retusa', 253, pp. 172–179. doi: 10.1016/j.chemgeo.2008.05.007.

Cusack, Maggie, England, J., Dalbeck, P., Tudhope, A. W., Fallick, A. E. and Allison, Nicola (2008b) 'Electron backscatter diffraction (EBSD) as a tool for detection of coral diagenesis', *Coral Reefs*, 27, pp. 905–911. doi: 10.1007/s00338-008-0414-3.

D'Hondt, Steven D. and Arthur, Michael A. (1996) 'Late Cretaceous Oceans and the Cool Tropic Paradox', *Science*, 271(5257), pp. 1838–1841.

Dalbeck, Paul, Cusack, Maggie, Dobson, Phillip S., Allison, Nicola, Fallick, Anthony E., Tudhope, Alexander W. and EIMF (2011) 'Identification and composition of secondary meniscus calcite in fossil coral and the effect on predicted sea surface temperature', *Chemical Geology*, 280, pp. 314–322. doi: 10.1016/j.chemgeo.2010.11.018.

Dauphin, Y., Cuif, J. P., Doucet, J., Salome, M., Susini, J. and Williams, C. T. (2003a) 'In situ mapping of growth lines in the calcitic prismatic layers of mollusc shells using X-ray absorption near-edge structure (XANES) spectroscopy at the sulphur K-edge', *Marine Biology*, 142, pp. 299–304. doi: 10.1007/s00227-002-0950-2.

Dauphin, Y., Zolotoyabko, E., Berner, A., Lakin, E., Rollion-bard, C., Cuif, J. P. and Fratzl, P. (2019) 'Breaking the long-standing morphological paradigm: Individual prisms in the pearl oyster shell grow perpendicular to the c-axis of calcite', *Journal of Structural Biology*, 205, pp. 121–132. doi: 10.1016/j.jsb.2019.01.004.

Dauphin, Yannicke (2003) 'Soluble Organic Matrices of the Calcitic Prismatic Shell Layers of Two Pteriomorphid Bivalves', *Journal of Biological Chemistry*, 278(17), pp. 15168–15177. doi: 10.1074/jbc.M204375200.

Dauphin, Yannicke (2005) 'Speciation and distribution of sulfur in a mollusk shell as revealed by in situ maps using X-ray absorption near-edge structure (XANES) spectroscopy at the S K-edge', *American Journal of Science*, 90, pp. 1748–1758. doi: 10.2138/am.2005.1640.

Dauphin, Yannicke, Ball, Alexander D., Castillo-Michel, Hiram, Chevallard, Corinne, Cuif, Jean-pierre, Farre, Bastien, Pouvreau, Stéphane and Salomé, Murielle (2013) 'In situ distribution and characterization of the organic content of the oyster shell Crassostrea gigas (Mollusca , Bivalvia)', *Micron*, 44, pp. 373–383.

Dauphin, Yannicke, Ball, Alexander D., Cotte, Marine, Cuif, Jean-pierre, Meibom, Anders, Salomé, Murielle, Susini, Jean and Williams, C. Terry (2008) 'Structure and composition of the nacre – prisms transition in the shell of Pinctada margaritifera (Mollusca , Bivalvia)', *Anal Bioanal Chem*, 390, pp. 1659–1669. doi: 10.1007/s00216-008-1860-z.

Dauphin, Yannicke, Brunelle, A., Cotte, Marine, Cuif, Jean-pierre, Farre, B., Laprévote, O., Meibom, Anders, Salomé, M. and Williams, C. T. (2010) 'A Layered Structure in the Organic Envelopes of the Prismatic Layer of the Shell of the Pearl Oyster Pinctada margaritifera (Mollusca , Bivalvia)', *Microscopy and Microanalysis*, 16, pp. 91–98.

Dauphin, Yannicke, Cuif, Jean-pierre, Doucet, Jean, Salom, Murielle, Susini, Jean and Willams, C. Terry (2003b) 'In situ chemical speciation of sulfur in calcitic biominerals and the simple prism concept', *Journal of Structural Biology*, 142, pp. 272–280. doi: 10.1016/S1047-8477(03)00054-6.

Debenay, Jean-pierre, Guillou, Jean-jacques, Geslin, Emmanuelle and Lesourd, Maurice (2000) 'Crystallization of Calcite in Foraminiferal Tests', *Micropaleontology*, 46, pp. 87–94.

Delaney, Margaret Lois (1983) *Foraminiferal trace elements: Uptake, diagenesis and 100 M.Y. paleochemical history.* Massachusetts Institute of Technology.

Demarchi, Beatrice *et al.* (2016) 'Protein sequences bound to mineral surfaces persist into deep time', *eLife*, 5, pp. 1–50. doi: 10.7554/eLife.17092.

Deng, Zhifei, Chen, Hongshun, Yang, Ting, Jia, Zian, Weaver, James C., Shevchenko, Pavel D., De Carlo, Francesco, Mirzaeifar, Reza and Li, Ling (2020) 'Strategies for simultaneous strengthening and toughening via nanoscopic intracrystalline defects in a biogenic ceramic', *Nature Communications*, 11, pp. 1–11. doi: 10.1038/s41467-020-19416-2.

Deng, Zhifei, Jia, Zian and Li, Ling (2022) 'Biomineralized Materials as Model Systems for Structural Composites : Intracrystalline Structural Features and Their Strengthening and Toughening Mechanisms', *Advanced Science*, 2103524, pp. 1–32. doi: 10.1002/advs.202103524.

van Dijk, I., de Nooijer, L. J., Boer, W. and Reichart, G. J. (2017) 'Sulfur in foraminiferal calcite as a potential proxy for seawater carbonate ion concentration', *Earth and Planetary Science Letters*, 470, pp. 64–72. doi: 10.1016/j.epsl.2017.04.031.

van Dijk, Inge, Mouret, Aurélia, Cotte, Marine, Le Houedec, Sandrine, Oron, S., Reichart, Gert-Jan, Reyes-Herrera, J., Filipsson, Helena L. and Barras, Christine (2019) 'Chemical Heterogeneity of Mg, Mn, Na, S and Sr in Benthic Foraminiferal Calcite', *Frontiers in Earth Science*, 7, pp. 1–23. doi: 10.3389/feart.2019.00281.

van Dijk, Inge, Raitzsch, Markus, Brummer, Geert-Jan A. and Bijma, Jelle (2020) 'Novel Method to Image and Quantify Cogwheel Structures in Foraminiferal Shells', *Frontiers in Ecology and Evolution*, 8, pp. 1–13. doi: 10.3389/fevo.2020.567231.

Drake, Jeana L., Whitelegge, Julian P. and Jacobs, David K. (2020) 'First sequencing of ancient coral skeletal proteins', *Scientific Reports*. Nature Publishing Group UK, 10(19407), pp. 1–11.

Dubicka, Zofia, Owocki, Krzysztof and Gloc, Michał (2018) 'Micro and Nanostructures of calcareous foraminiferal tests: Insight from representatives of Miliolida, Rotaliida and Lagenida', *Journal of Foraminiferal Research*, 48(2), pp. 142–155.

Dunca, Elena, Schöne, B., Hickson, Jon, Dunca, Elena and Dunca, Elena (2005) 'Mutvei's solution: An ideal agent for resolving microgrowth structures of biogenic carbonates', *Palaeogeography, Palaeoclimatology, Palaeoecology*, 228, pp. 149–166. doi: 10.1016/j.palaeo.2005.03.054.

Duplessy, J. C., Lalou, C. and Vinot, A. N. (1967) 'Differential Isotopic Fractionation in Benthic Formaninifera and Paleotemperatures Reassessed', *Science*, 168, pp. 250–251.

Edgar, Kirsty M., Anagnostou, Eleni, Pearson, Paul N. and Foster, Gavin L. (2015) 'Assessing the impact of diagenesis on δ11B, δ13C, δ18O, Sr/Ca and B/Ca values in fossil planktic foraminiferal calcite', *Geochimica et Cosmochimica Acta*, 166, pp. 189–209. doi: 10.1016/j.gca.2015.06.018.

Edgar, Kirsty M., Palike, H. and Wilson, Paul A. (2013) 'Testing the impact of diagenesis on the δ18O and δ13C of benthic foraminiferal calcite from a sediment burial depth transect in the equatorial Pacific',

American Geophysical Union, 28(3), pp. 468–480. doi: 10.1002/palo.20045.

Elorza, J. and Garcia-Garmilla (1998) 'Palaeoenvironmental implications and diagenesis of inoceramid shells (Bivalvia) in the mid-Maastrichtian beds of the Sopelana , Zumaya and Bidart sections (coast of the Bay of Biscay, Basque Country)', *Palaeogeography, Palaeoclimatology, Palaeoecology*, 141, pp. 303–328.

Elorza, Javier and Garcia-Garcia, F. (1996) 'Petrological and geochemical evidence for diagenesis of inoceramid bivalve shells in the Plentzia Formation (Upper Cretaceous , Basque- Cantabrian Region , northern Spain)', *Cretaceous Research*, 17, pp. 479–503.

Emiliani, Cesare (1955) 'Pleistocene Temperaturres', *The Journal of Geology*, 63(6), pp. 538–578.

Emiliani, Cesare (1958) 'Ancient Temperatures', *Scientific American*, 198(2), pp. 54–66.

Epstein, S., Buchsbaum, R., Lowenstam, H. A. and Urey, Harold C. (1953) 'Revised Carbonate-water Isotopic Temperature Scale', *Bullentin of the Geological Society of America*, 64, pp. 1315–1326.

Epstein, S., Buchsbaum, R., Lowenstam, H. and Urey, Harold C. (1951) 'Carbonate-water isotopic temperature scale', *Bulletin of the Geological Society of America*, 62(April), pp. 417–426.

Erez, J. (2003) 'The Source of Ions for Biomineralization in Foraminifera and Their Implications for Paleoceanographic Proxies', *Reviews in Mineralogy and Geochemistry*, 54(1), pp. 115–149. doi: 10.2113/0540115.

Evans, David, Mu, Wolfgang and Erez, Jonathan (2018) 'Assessing foraminifera biomineralisation models through trace element data of cultures under variable seawater chemistry', *Geochimica et Cosmochimica Acta*, 236, pp. 198–217. doi: 10.1016/j.gca.2018.02.048.

Farre, B. and Dauphin, Y. (2009) 'Lipids from the nacreous and prismatic layers of two Pteriomorpha Mollusc shells', *Comparative Biochemistry and Physiology, Part B*, 152(2), pp. 103–109. doi: 10.1016/j.cbpb.2008.10.003.

Farre, Bastien, Brunelle, Alain, Laprévote, Olivier, Cuif, Jean-pierre, Williams, C. Terry and Dauphin, Yannnicke (2011) 'Shell layers of the black-lip pearl oyster Pinctada margaritifera: Matching microstructure and composition', *Comparative Biochemistry and Physiology, Part B*, 159(3), pp. 131–139. doi: 10.1016/j.cbpb.2011.03.001.

Fehrenbacher, Jennifer and Martin, Pamela A. (2014) 'Exploring the dissolution effect on the intrashell Mg/Ca variability of the planktic foraminifer Globigerinoides ruber', *American Geophysical Union*, 29(9), pp. 825–892. doi: 10.1002/2013PA002571.

Fehrenbacher, Jennifer S., Russell, Ann D., Davis, Catherine V., Gagnon, Alexander C., Spero, Howard J., Cliff, John B., Zhu, Zihua and Martin, Pamela (2017) 'Link between light-triggered Mg-banding and chamber formation in the planktic foraminifera Neogloboquadrina dutertrei', *Nature Communications*. Nature Publishing Group, 8, pp. 1–10. doi: 10.1038/ncomms15441.

Fhlaithearta, Shauna Ní, Ernst, Sander R., Nierop, Klaas G. J., Lange, Gert J. De and Reichart, Gert-jan (2013) 'Molecular and isotopic composition of foraminiferal organic linings', *Marine Micropaleontology*, 102, pp. 69–78. doi: 10.1016/j.marmicro.2013.06.004.

Fichtner, Vanessa, Strauss, Harald, Mavromatis, Vasileios, Dietzel, Martin, Huthwelker, Thomas, Borca, Camelia N., Guagliardo, Paul, Kilburn, Matt R., Göttlicher, Jörg, Pederson, Chelsea L., Griesshaber, Erika, Schmahl, Wolfgang W. and Immenhauser, Adrian (2018) 'Incorporation and subsequent diagenetic alteration of sulfur in Arctica islandica', *Chemical Geology*, 482, pp. 72–90. doi: 10.1016/j.chemgeo.2018.01.035.

Flügel, E. (1982) 'Carbonate Diagenesis', in *Microfacies Analysis of Limestones*, pp. 62–104.

Forjanes, Pablo, Roda, María Simonet, Greiner, Martina, Griesshaber, Erika and Lagos, Nelson A. (2022) 'Experimental burial diagenesis of aragonitic biocarbonates : from organic matter loss to abiogenic calcite formation', *Biogeosciences*, 19, pp. 3791–3823.

Friedrich, Oliver, Norris, Richard D. and Erbacher, Jochen (2012) 'Evolution of middle to Late Cretaceous oceans — A 55 m.y. record of Earth's temperature and carbon cycle', *Geological Society Of America*, 40(2), pp. 107–110. doi: 10.1130/G32701.1.

Furuhashi, Takeshi F., Beran, Anton, Blazso, Marianne, Czegeny, Zsuzsanna, Shwarzinger, Clemens and Steiner, Gerhard (2009a) 'Pyrolysis GC / MS and IR Spectroscopy in Chitin Analysis of Molluscan Shells', *Bioscience, Biotechnology and Biochemistry*, 73, pp. 93–103. doi: 10.1271/bbb.80498.

Furuhashi, Takeshi, Schwarzinger, Clemes, Miksik, Ivan, Smrz, Miloslav and Beran, Anton (2009b) 'Molluscan shell evolution with review of shell calcification hypothesis', *Comparative Biochemistry and Physiology, Part B*, 154(3), pp. 351–371. doi: 10.1016/j.cbpb.2009.07.011.

Gaskell, Daniel E. and Hull, Pincelli M. (2023) 'Technical note : A new online tool for δ 18 O-temperature conversions', *Climate of the past Discussions*, 19(6), pp. 1–11.

Geerken, E., de Nooijer, L. J., Roepert, A., Polerecky, L., King, H. E. and Reichart, G. J. (2019) 'Element banding and organic linings within chamber walls of two benthic foraminifera', *Scientific Reports*. Springer US, 9(1), pp. 1–15. doi: 10.1038/s41598-019-40298-y.

Geerken, Esmee, de Nooijer, Lennart, Toyofuku, Takashi, Roepert, Anne, Middelburg, Jack J., Kienhuis, Michiel V. M., Nagai, Yukiko and Polerecky, Lubos (2022) 'High precipitation rates characterize biomineralization in the benthic foraminifer Ammonia beccarii', *Geochimica et Cosmochimica Acta*, 318, pp. 70–82. doi: 10.1016/j.gca.2021.11.026.

Géhin, A., Gilbert, B., Chakraborty, S., Stack, A. G., Allard, L. F., Robinet, J. C. and Charlet, L. (2021) 'Long Term 13C Uptake by 12C Enriched Calcite', *Earth and Space Chemistry*, 5, pp. 998–1005.

Gilbert, P. U. P. A., Young, Anthony and Coppersmith, Susan N. (2011) 'Measurement of c-axis angular orientation in calcite (CaCO3) nanocrystals using X-ray absorption spectroscopy', *PNAS*, 108(28), pp. 11350–11355. doi: 10.1073/pnas.1107917108.

Gilow, C., Zolotoyabko, Emil, Paris, Oskar, Fratzl, Peter and Aichmayer, Barbara (2011) 'Nanostructure of Biogenic Calcite Crystals : A View by Small-Angle X-Ray scatterring', *Crystal Growth and Design*, 11, pp. 2054–2058.

Gim, Jiseok, Schnitzer, Noah, Otter, Laura M., Cui, Yuchi, Motreuil, Sébastien, Marin, Frédéric, Wolf, Stephan E., Jacob, Dorrit E., Misra, Amit and Hovden, Robert (2019) 'Nanoscale deformatiom mechanics reveal resilience in nacre of Pinna nobilis shell', *Nature Communications*. Springer US, 10, pp. 1–8. doi: 10.1038/s41467-019-12743-z.

Giuffre, Anthony J., Hamm, Laura M., Han, Nizhou, Yoreo, James J. De and Dove, Patricia M. (2013) 'Polysaccharide chemistry regulates kinetics of calcite nucleation through competition of interfacial energies', *PNAS*, 110(23), pp. 9261–9266. doi: 10.1073/pnas.1222162110.

Glock, Nicolaas, Liebetrau, Volker, Vogts, Angela and Eisenhauer, Anton (2019) 'Organic Heterogeneities in Foraminiferal Calcite Traced Through the Distribution of N, S, and I Measured With NanoSIMS: A New Challenge for Element-Ratio-Based Paleoproxies?', *Frontiers in Earth Science*, 7(July), pp. 1–14. doi: 10.3389/feart.2019.00175.

Gomez-Alday, J. J. and Elorza, J. (2003) 'Diagenesis, regular growth and records of seasonality in inoceramid bivalve shells from mid-Maastrichtian hemipelagic beds of the Bay of Biscay', *Netherlands Journal of Geosciences*, 82(3), pp. 289–301.

Gorski, Christopher A. and Fantle, Matthew S. (2017) 'Stable mineral recrystallization in low temperature aqueous systems: A critical review', *Geochimica et Cosmochimica Acta*, 198, pp. 439–465. doi: 10.1016/j.gca.2016.11.013.

Grossman, Ethan L. (2012) 'Applying oxygen isotope paleothermometry in deep time', *The Paleontological Society Papers*, 18, pp. 39–68.

Grossman, Ethan L. and Joachimski, Michael M. (2022) 'Ocean temperatures through the Phanerozoic reassessed', *Scientific Reports*. Nature Publishing Group UK, pp. 1–13. doi: 10.1038/s41598-022-11493-1.

Gruszczynski, M., Halas, S., Hoffman, A. and Malkowski, K. (1989) 'A brachiopod calcite record of the oceanic carbon and oxygen isotope shifts at the Permian/Triassic transition', *Nature*, 337, pp. 64–67.

Harper, Elizabeth M. and Checa, Antonio (2017) 'Physiological versus Biological Control in Bivalve Calcite Prisms : Comparison of Euheterodonts and Pteriomorphs', *Biological Bulletin*, 232, pp. 19–29.

Harrison, Anna L., Heuser, Alexander, Liebetrau, Volker, Eisenhauer, Anton, Schott, Jacques and Mavromatis, Vasileios (2023) 'Equilibrium Ca isotope fractionation and the rates of isotope exchange in the calcite-fluid and aragonite-fluid systems at 25 ◦ C', *Earth and Planetary Science Letters*, 603, pp. 1–12. doi: 10.1016/j.epsl.2022.117985.

Harrison, Anna L., Schott, Jacques, Oelkers, Eric H., Maher, Katharine and Mavromatis, Vasileios (2022) 'Rates of carbon and oxygen isotope exchange between calcite and fluid at chemical equilibrium', *Geochimica et Cosmochimica Acta*, 335, pp. 369–382. doi: 10.1016/j.gca.2022.06.041.

Haynes, J. R. (1981) 'Test Morphology and Composition', in *Foraminifera*. London: Palgrave Macmillan, pp. 40–59.

Hays, J. D., Imbrie, John and Shackleton, N. J. (1976) 'Variations in the Earth's Orbit :Pacemaker of the Ice Ages', *Science*, 194(4270), pp. 1121–1132.

Hendry, James P., Ditchheld, Peter W. and Marshall, James D. (1995) 'Two-stage neomorphism of jurassic aragonitic bivalves: implications for early diagenesis', *Journal of Sedimentary Research*, (1), pp. 214–224.

Hoppe, Peter, Cohen, Stephanie and Meibom, Anders (2013) 'NanoSIMS: Technical Aspects and Applications in Cosmochemistry and Biological Geochemistry', *Geostandards and Geoanalytical Research*, 37(2), pp. 111–154. doi: 10.1111/j.1751-908X.2013.00239.x.

Huang, Jingliang, Liu, Yangjia, Liu, Chuang, Xie, Liping and Zhang, Rongqing (2021) 'Heterogeneous distribution of shell matrix proteins in the pearl oyster prismatic layer', *International Journal of Biological Macromolecules*, 189, pp. 641–648. doi: 10.1016/j.ijbiomac.2021.08.075.

Immel, Françoise, Broussard, Cédric, Catherinet, Bastien and Plasseraud, Laurent (2016) 'The Shell of the Invasive Bivalve Species Dreissena polymorpha : Biochemical , Elemental and Textural Investigations', *Plos One*, 11(5), pp. 1–28. doi: 10.1371/journal.pone.0154264.

Immenhauser, A., Schöne, B., Hoffman, R. and Niedermayr, A. (2016) 'Mollusc and brachiopod skeletal hard parts : Intricate archives of their marine environment', *Sedimentology*, 63, pp. 1–59. doi: 10.1111/sed.12231.

Immenhauser, Adrian, Thomas, F. N., Steuber, Thomas and Hippler, Dorothee (2005) 'A critical assessment of mollusk 18 O / 16 O , Mg / Ca , and 44 Ca / 40 Ca ratios as proxies for Cretaceous seawater temperature seasonality', *Palaeogeography, Palaeoclimatology, Palaeoecology*, 215, pp. 221–237. doi: 10.1016/j.palaeo.2004.09.005.

Ivany, L. C. and Runnegar, B. (2010) 'Early Permian seasonality from bivalve δ18O and implications for the oxygen isotopic composition of seawater', *Geological Society Of America*, (11), pp. 1027–1030. doi: 10.1130/G31330.1.

Jackson, A. P., Vincent, J. F. V and Turner, R. M. (1988) 'The mechanical design of nacre', *Proceedings of the Royal Society B*, 234, pp. 415–440.

Jacob, D. E., Wirth, R., Agbaje, O. B. A., Branson, O. and Eggins, S. M. (2017) 'Planktic foraminifera form their shells via metastable carbonate phases', *Nature Communications*. Springer US, 8(1265), pp. 1–9. doi: 10.1038/s41467-017-00955-0.

Katz, M. E., Cramer, B. S., Franzese, A., Honisch, B., Miller, K. G., Rosenthal, Yair and Wright, J. D. (2010) 'Traditional and emerging geochemical proxies in foraminifera', *Journal of Foraminiferal Research*, 40(2), pp. 165–192.

Kim, Yi-yeoun, Carloni, Joseph D., Demarchi, Beatrice, Sparks, David, Reid, David G., Kunitake, Miki E., Tang, Chiu C., Duer, Melinda J., Freeman, Colin L., Pokroy, Boaz, Penkman, Kirsty, Harding, John H., Estro, Lara A., Baker, She P. and Meldrum, Fiona C. (2016) 'Tuning hardness in calcite by incorporation of amino acids', *Naure Materials*, 15. doi: 10.1038/NMAT4631.

Kintsu, Hiroyuki, Okumura, Taiga, Negishi, Lumi, Ifuku, Shinsuke, Kogure, Toshihiro, Sakuda, Shohei and Suzuki, Michio (2017) 'Crystal defects induced by chitin and chitinolytic enzymes in the prismatic layer of Pinctada fucata', *Biochemical and Biophysical Research Communications*, 489, pp. 89–95. doi: 10.1016/j.bbrc.2017.05.088.

Knauth, L. P. and Epstein, S. (1976) 'Hydrogen and oxygen isotope ratios in nodular and bedded cherts', *Geochimica et Cosmochimica Acta*, 40, pp. 1095–1108.

Knight, Brenna M., Edgar, Kevin J., Yoreo, James J. De and Dove, Patricia M. (2023) 'Chitosan as a Canvas for Studies of Macromolecular Controls on CaCO 3 Biological Crystallization', *Biomacromolecules*, 24, pp. 1078–1102. doi: 10.1021/acs.biomac.2c01394.

Kobayashi, Iwao and Samata, Tetsuro (2006) 'Bivalve shell structure and organic matrix', *Material Science*

and Engineering, 26, pp. 692–698. doi: 10.1016/j.msec.2005.09.101.

Kontakiotis, George, Mortyn, Graham Peter, Antonarakou, Assimina and Drinia, Hara (2016) 'Assessing the reliability of foraminiferal Mg/Ca thermometry by comparing field-samples and culture experiments: A review', *Geological Quarterly*, 60(3), pp. 547–560. doi: 10.7306/gq.1272.

Korte, C., Hesselbo, Stephen P., Jenkyns, H., Rickaby, R. M. and Spötl, C. (2009) 'Palaeoenvironmental significance of carbon- and oxygen-isotope stratigraphy of marine Triassic – Jurassic boundary sections in SW Britain', *Journal of the Geological Society*, 166, pp. 431–445. doi: 10.1144/0016-76492007-177.Palaeoenvironmental.

Kozdon, R., Ushikubo, T., Kita, N. T., Spicuzza, M. and Valley, J. W. (2009) 'Intratest oxygen isotope variability in the planktonic foraminifer N. pachyderma: Real vs. apparent vital effects by ion microprobe', *Chemical Geology*, 258, pp. 327–337. doi: 10.1016/j.chemgeo.2008.10.032.

Kozdon, Reinhard, Kelly, D. C., Kitajima, K., Strickland, A., Fournelle, J. H. and Valley, J. W. (2013) 'In situ δ 18 O and Mg / Ca analyses of diagenetic and planktic foraminiferal calcite preserved in a deep-sea record of the Paleocene-Eocene thermal maximum', *Paleoceanography*, 28, pp. 517–528. doi: 10.1002/palo.20048.

Kozdon, Reinhard, Kelly, D. Clay, Kita, Noriko T., Fournelle, John H. and Valley, John W. (2011) 'Planktonic foraminiferal oxygen isotope analysis by ion microprobe technique suggests warm tropical sea surface temperatures during the Early Paleogene', *Paleoceanography*, 26, pp. 1–17. doi: 10.1029/2010PA002056.

Kroenke, L. W., Berger, W. H., Janecek, T. R. and Party, Shipboard Scientific (1991) *Proceedings of the Ocean Drilling Program, Initial Reports, Vol. 130, Site 807*.

Kunioka, Daisuke, Shirai, Kotaro, Takahata, Naoto, Sano, Yuji, Toyofuku, Takashi and Ujiie, Yurika (2006) 'Microdistribution of Mg/Ca, Sr/Ca, and Ba/Ca ratios in Pulleniatina obliquiloculata test by using a NanoSIMS: Implication for the vital effect mechanism', *Geochemistry, Geophysics, Geosystems*, 7(12). doi: 10.1029/2006GC001280.

Kunitake, Miki E., Mangano, Lauren M., Peloquin, John M., Baker, Shefford P. and Estroff, Lara A. (2013) 'Evaluation of strengthening mechanisms in calcite single crystals from mollusk shells', *Acta Biomaterialia*. Acta Materialia Inc., 9, pp. 5353–5359. doi: 10.1016/j.actbio.2012.09.030.

Land, Lynton S. (1995) 'Comment on " Oxygen and carbon isotopic composition of Ordovician brachiopods : Implications for coeval seawater " by H . Qing and J . Veizer', *Geochimica et Cosmochimica Acta*, 59(13), pp. 2843–2844.

Lang, Arad, Mijowska, Sylwia, Polishchuk, Iryna, Fermani, Simona and Falini, Giuseppe (2020) 'Acidic Monosaccharides become Incorporated into Calcite Single Crystals', *Chemistry- A European Journal*, 26, pp. 16860–16868. doi: 10.1002/chem.202003344.

Lange, Skadi M., Krause, Stefan and Ritter, Ann-christine (2018) 'Anaerobic microbial activity affects earliest diagenetic pathways of bivalve shells', *Sedimentology*, 65, pp. 1390–1411. doi: 10.1111/sed.12428.

Langer, Martin R. (1992) 'Biosynthesis of glycosaminoglycans in foraminifera : A review', *Marine Micropaleontology*, 19, pp. 245–255.

Lastam, J., Griesshaber, E., Yin, X., Rupp, U., Almazo, I. Sánchez, Heß, M., Walther, P., Checa, A. and Schmahl, W. W. (2023a) 'The unique fibrilar to platy nano - and microstructure of twinned rotaliid foraminiferal shell calcite', *Scientific Reports*, pp. 1–19. doi: 10.1038/s41598-022-25082-9.

Lastam, J., Griesshaber, E., Yin, X., Rupp, U., Sanchez-Almazo, I., Hess, M., Walther, P., Checa, A. and Schmahl, W. W. (2023b) 'Patterns of crystal organization and calcite twin formation in planktonic, rotaliid, foraminifera shells and spines', *Journal of Structural Biology*, 215(107898), pp. 1–26.

Lea, David W., Pak, Dorothy K. and Spero, Howard J. (2000) 'Climate Impact of Late Quaternary Equatorial Pacific Sea Surface Temperature Variations', *Science*, 289(2000). doi: 10.1126/science.289.5485.1719.

Levi, Adam, Müller, Wolfgang, Erez, Jonathan, Patrick, William and Iii, Gilhooly (2019) 'Intrashell Variability of Trace Elements in Benthic Foraminifera Grown Under High CO 2 Levels', *Frontiers in Earth Science*, 7(October), pp. 1–15. doi: 10.3389/feart.2019.00247.

Li, Hanying, Xin, Huolin L., Kunitake, Miki E., Keene, Ellen C., Muller, David A. and Estroff, Lara A. (2011) 'Calcite Prisms from Mollusk Shells (Atrina Rigida): Swiss cheese-like Organic – Inorganic Single-crystal Composites', *Advanced Functional Materials*, 21, pp. 2028–2034. doi: 10.1002/adfm.201002709.

Liang, S. M., Ji, H. M. and Li, X. W. (2023) 'The crucial role of platelet stacking mode in strength and toughness of nacre', *Materials & Design*, 230, pp. 1–13. doi: 10.1016/j.matdes.2023.111987.

Löffler, N., Fiebig, J., Mulch, A., Tütken, T., Schmidt, B. C., Bajnai, D., Conrad, A. C., Wacker, U. and Böttcher, Michael E. (2019) 'Refining the temperature dependence of the oxygen and clumped isotopic compositions of structurally bound carbonate in apatite', *Geochimica et Cosmochimica Acta*, 253, pp. 19–38. doi: 10.1016/j.gca.2019.03.002.

Lohmann, G. P. (1995) 'A model for variation in the chemistry of planktonic foraminifera due to secondary calcification and selective dissolution', *Paleoceanography*, 10(3), pp. 445–457.

Lorens, Robert B., Williams, Douglas F. and Bender, Michael L. (1977) 'The Early Nonstructural Chemical Diagenesis of Foraminiferal Calcite', *Journal of Sedimentary Petrology*, 47(4), pp. 1602–1609.

Lowenstam, H. A. and Weiner, Steve (1989) *On Biomineralization*. Oxford University Press.

Malinverno, Alberto and Martinez, Ernesto A. (2015) 'The effect of temperature on organic carbon degradation in marine sediments', *Scientific Reports*. Nature Publishing Group, 5, pp. 1–10. doi: 10.1038/srep17861.

Mancuso, Arianna, Yam, Ruth, Prada, Fiorella, Stagioni, Marco, Goffredo, Stefano and Shemesh, Aldo (2022) 'Oxygen and carbon isotope variations in Chamelea gallina shells : Environmental influences and vital effects', *Geobiology*, 21, pp. 119–132. doi: 10.1111/gbi.12526.

Marin, Frederic, Le Roy, Nathalie and Marie, Benjamin (2012) 'The formation and mineralization of mollusk shell', *Frontiers in Bioscience*, S4, pp. 1099–1125.

Mavromatis, Vasileios, Bundeleva, Irina A., Shirokova, Liudmila S., Millo, Christian, Pokrovsky, Oleg S., Bénézeth, Pascale, Ader, Magali and Oelkers, Eric H. (2015) 'The continuous re-equilibration of carbon isotope compositions of hydrous Mg carbonates in the presence of cyanobacteria', *Chemical Geology*, 404, pp. 41–51. doi: 10.1016/j.chemgeo.2015.03.016.

Mccorkle, Daniel C., Martin, Pamela A., Lea, David W. and Klinkhammer, Gary P. (1995) 'Evidence of a dissolution effect on benthic foraminiferal shell chemistry : δ13C , Cd/Ca, Ba/Ca , and Sr/Ca results from the Ontong Java Plateau', *Paleoceanography*, 10(4), pp. 699–714.

McCrea, J. M. (1950) 'On the Isotopic Chemistry of Carbonates and a Paleotemperature Scale', *The Journal of Chemical Physics*, 18(6), pp. 849–857. doi: 10.1063/1.1747785.

Mckinney, C. R., Mccrea, J. M., Epstein, S., Allen, H. A. and Urey, H. C. (1950) 'Improvements in Mass Spectrometers for the Measurement of Small Differences in Isotope Abundance Ratios', *Review of Scientic Instruments*, 724, pp. 724–730. doi: 10.1063/1.1745698.

Meibom, Anders, Yurimoto, Hiyayoshi, Cuif, Jean-pierre, Domart-coulon, Isabelle, Houlbreque, Fanny, Constantz, Brent, Dauphin, Yannicke, Tambutte, E., Allemand, Denis, Wooden, Joseph and Dunbar, Robert (2006) 'Vital effects in coral skeletal composition display strict three- dimensional control', *Geophysical Research Letters*, 33, pp. 1–4. doi: 10.1029/2006GL025968.

Metcalfe, Brett, Lougheed, Bryan C., Waelbroeck, Claire and Roche, Didier M. (2020) 'A proxy modelling approach to assess the potential of extracting ENSO signal from tropical Pacific planktonic foraminifera', *Climate of the Past*, 16, pp. 885–910.

Metzger, Till H., Politi, Yael, Carbone, Gerardina, Bayerlein, Bernd, Zlotnikov, Igor, Zolotoyabko, Emil and Fratzl, Peter (2014) 'Nanostructure of Biogenic Calcite and Its Modification under Annealing : Study by High-Resolution X-ray Diffraction and Nanoindentation', *Crystal Growth and Design*, 14, pp. 5275–5282.

Mitchell, Simon F., Ball, James D., Crowley, Stephen F., Marshall, Jim D., Paul, Christopher R. C., Veltkamp, Cornelis J. and Samir, Ashraf (1997) 'Isotope data from Cretaceous chalks and foraminifera : Environmental or diagenetic signals ?', *Geology*, (8), pp. 691–694.

Montañes, I. P. and Crossey, L. J. (2018) 'Diagenesis', in White, W. M. (ed.) *Encyclopedia of Geochemistry*. Springer, Cham, pp. 353–361.

Mutterlose, Jörg, Malkoc, Matthias, Schouten, Stefan, Sinninghe, Jaap S. and Forster, Astrid (2010) 'TEX 86 and stable δ18O paleothermometry of early Cretaceous sediments: Implications for belemnite ecology and paleotemperature proxy application', *Earth and Planetary Science Letters*, 298, pp. 286–298. doi: 10.1016/j.epsl.2010.07.043.

Nagai, Yukiko, Uematsu, Katsuyuki, Chen, Chong, Wani, Ryoji, Tyszka, Jarosław and Toyofuku, Takashi (2018a) 'Weaving of biomineralization framework in rotaliid foraminifera: implications for paleoceanographic proxies', *Biogeosciences*, 15, pp. 6773–6789.

Nagai, Yukiko, Uematsu, Katsuyuki, Wani, Ryoji and Toyofuku, Takashi (2018b) 'Reading the Fine Print : Ultra-Microstructures of Foraminiferal Calcification Revealed Using Focused Ion Beam Microscopy', *Frontiers in Marine Science*, 5, pp. 1–15. doi: 10.3389/fmars.2018.00067.

Nakahara, H. and Beve (1971) 'The Formation and Growth of the Prismatic Layer of Pinctada radiata', *Calcified Tissue Research*, 45, pp. 31–45.

Nakajima, Kimiko, Nagai, Yukiko, Suzuki, Monami, Oaki, Yuya, Naito, Kimiyoshi, Tanaka, Yoshihisa, Toyofuku, Takashi and Imai, Hiroaki (2016) 'Mesoscopic crystallographic textures on shells of a hyaline radial foraminifer Ammonia beccarii', *CrystEngComm*, 18, pp. 7135–7139. doi: 10.1039/C6CE01611A.

Nehrke, G., Keul, N., Langer, G., De Nooijer, L. J., Bijma, J. and Meibom, A. (2013) 'A new model for biomineralization and trace-element signatures of Foraminifera tests', *Biogeosciences*, 10(10), pp. 6759–6767. doi: 10.5194/bg-10-6759-2013.

de Nooijer, L. J., Hathorne, E. C., Reichart, G. J., Langer, G. and Bijma, J. (2014a) 'Variability in calcitic Mg / Ca and Sr / Ca ratios in clones of the benthic foraminifer Ammonia tepida', *Marine Micropaleontology*, 107, pp. 32–43. doi: 10.1016/j.marmicro.2014.02.002.

de Nooijer, L. J., Spero, H. J., Erez, J., Bijma, J. and Reichart, G. J. (2014b) 'Biomineralization in perforate foraminifera', *Earth Science Reviews*, 135, pp. 48–58. doi: 10.1016/j.earscirev.2014.03.013.

de Nooijer, Lennart Jan, Toyofuku, Takashi and Kitazato, Hiroshi (2009) 'Foraminifera promote calcification by elevating their intracellular pH', *PNAS*, 106(36), pp. 15374–15378.

Nudelman, Fabio, Chen, Hong H. and Goldberg, Harvey A. (2007) 'Lessons from biomineralization : comparing the growth strategies of mollusc shell prismatic and nacreous layers in Atrina rigida', *Faraday Discussions*, 136, pp. 9–25. doi: 10.1039/b704418f.

Nudelman, Fabio and Sommerdijk, Nico A. J. M. (2012) 'Biomineralization as an Inspiration for Materials Chemistry', *Angewandte Chemie International Edition*, 51, pp. 6582–6596. doi: 10.1002/anie.201106715.

Oelkers, Eric H., Berninger, Ulf-niklas, Peréz-Fernàndez, Andrea, Chmeleff, Jérôme and Mavromatis, Vasileios (2018) 'The temporal evolution of magnesium isotope fractionation during hydromagnesite dissolution, precipitation, and at equilibrium', *Geochimica et Cosmochimica Acta*, 226, pp. 36–49. doi: 10.1016/j.gca.2017.11.004.

Oelkers, Eric H., Pogge von Strandmann, P. A. E. and Mavromatis, Vasileios (2019) 'The rapid resetting of the Ca isotopic signatures of calcite at ambient temperature during its congruent dissolution precipitation, and at equilibrium', *Chemical Geology*, 512(November 2018), pp. 1–10. doi: 10.1016/j.chemgeo.2019.02.035.

Oerlemans, Johannes (2004) 'Correcting the Cenozoic d18O deep-sea temperature record for Antarctic ice volume', *Palaeography, Palaeoclimatology, Palaeoecology*, 208, pp. 195–205. doi: 10.1016/j.palaeo.2004.03.004.

Okumura, Taiga, Suzuki, Michio, Nagasawa, Hiromichi and Kogure, Toshihiro (2010) 'Characteristics of biogenic calcite in the prismatic layer of a pearl oyster, Pinctada fucata', *Micron*, 41, pp. 821–826. doi: 10.1016/j.micron.2010.05.004.

Okumura, Taiga, Suzuki, Michio, Nagasawa, Hiromichi and Kogure, Toshihiro (2012) 'Microstructural Variation of Biogenic Calcite with Intracrystalline Organic Macromolecules', *Crystal Growth and Design*, 12, pp. 224–230.

Okumura, Taiga, Suzuki, Michio, Nagasawa, Hiromichi and Kogure, Toshihiro (2013) 'Microstructural control of calcite via incorporation of intracrystalline organic molecules in shells', *Journal of Crystal Growth*, 381, pp. 114–120. doi: 10.1016/j.jcrysgro.2013.07.020.

Olson, Ian C., Metzler, Rebecca A., Tamura, Nobumichi, Kunz, Martin, Killian, Christopher E. and Gilbert, Pupa U. P. A. (2013) 'Crystal lattice tilting in prismatic calcite', *Journal of Structural Biology*, 183, pp. 180–190. doi: 10.1016/j.jsb.2013.06.006.

Otter, L. M., Eder, K., Kilburn, M. R., Yang, L., Reilly, P. O., Nowak, D. B., Cairney, J. M. and Jacob, D. E. (2023) 'Growth dynamics and amorphous-to- crystalline phase transformation in natural nacre', *Nature Communications*, 14, pp. 1–11. doi: 10.1038/s41467-023-37814-0.

Otter, Laura M., Förster, M. W., Belousova, Elena, O'Reilly, Padraic, Nowak, Derek, Park, Sung, Clark, Simon, Foley, Stephen F. and Jacob, Dorrit E. (2021) 'Chemical Imaging by Photo-Induced Force Microscopy : Technical Aspects and Application to the Geosciences', *Geostandards*, 45(1), pp. 5–27. doi: 10.1111/ggr.12373.

Oudot, Morgane, Neige, Pascal, Shir, Ira Ben, Schmidt, Asher, Strugnell, Jan M., Plasseraud, Laurent, Broussard, Cédric, Hoffmann, René, Lukeneder, Alexander and Marin, Frédéric (2020) 'The shell matrix and microstructure of the Ram ' s Horn squid : Molecular and structural characterization', *Journal of Structural Biology*, 211, pp. 1–20. doi: 10.1016/j.jsb.2020.107507.

Paris, G., Fehrenbacher, J., Sessions, A., Spero, H. and Adkins, J. (2014) 'Experimental determination of carbonate-associated sulfate δ34S in planktonic foraminifera shells', *Geochemistry, Geophysics, Geosystems*, 15, pp. 1452–1461. doi: 10.1002/2014GC005563.Received.

Pawlowski, Jan, Holzmann, Maria, Gooday, Andrew J., Cedhagen, Tomas, Habura, Andrea and Bowser, Samuel S. (2003) 'The evolution of early Foraminifera', *PNAS*, 100(20), pp. 11494–11498. doi: 10.1073/pnas.2035132100.

Pearson, Paul N. and Burgess, Catherine E. (2008) 'Foraminifer test preservation and diagenesis: comparison of high latitude Eocene sites', *Geological Society, London, Special Publications*, 303(1), pp. 59–72. doi: 10.1144/SP303.5.

Pearson, Paul N., Ditch, Peter W., Singano, Joyce, Harcourt-brown, Katherine G., Nicholas, Christopher J., Olsson, Richard K., Shackleton, Nicholas J. and Hall, Mike A. (2001) 'Warm tropical sea surface temperatures in the Late Cretaceous and Eocene epochs', *Nature*, pp. 481–488.

Pearson, Paul N., van Dongen, Bart E., Nicholas, Christopher J., Pancost, Richard D., Schouten, Stefan, Singano, Joyce M. and Wade, Bridget S. (2007) 'Stable warm tropical climate through the Eocene Epoch', *Geology*, 35(3), pp. 211–214. doi: 10.1130/G23175A.1.

Pearson, Paul Nicholas (2012) 'Oxygen isotopes in foraminifera: Overview and historical review', *Paleontological Society Papers*, 18, pp. 1–38. Available at: http://orca.cf.ac.uk/41988/.

Pearson, Paul Nicholas, Evans, Sam L. and Evans, James (2015) 'Effect of diagenetic recrystallization on the strength of planktonic foraminifer tests under compression', *Journal of Micropalaeontology*, 34, pp. 59–64.

Pederson, C. L., Mavromatis, V., Dietzel, M., Rollion-bard, C., Breitenbach, S. F. M., Yu, D., Nehrke, G. and Immenhauser, A. (2020) 'Variation in the diagenetic response of aragonite archives to hydrothermal alteration', *Sedimentary Geology*, 406, pp. 1–16. doi: 10.1016/j.sedgeo.2020.105716.

Pederson, C., Mavromatis, V., Dietzel, M., Rollion-Bard, C., Nehrke, G., Jöns, N., Jochum, K. P. and Immenhauser, A. (2019) 'Diagenesis of mollusc aragonite and the role of fluid reservoirs', *Earth and Planetary Science Letters*, 514, pp. 130–142. doi: 10.1016/j.epsl.2019.02.038.

Perez-Huerta, Alberto, Cusack, Maggie and England, Jennifer (2007) 'Crystallography and diagenesis in fossil craniid brachiopods', *Palaeontology*, 50, pp. 757–763.

Petersen, Jassin, Riedel, Bettina, Barras, Christine, Pays, Olivier, Guihéneuf, Anaïs, Mabilleau, Guillaume, Schweizer, Magali, Meysman, Filip J. R. and Jorissen, Frans J. (2016) 'Improved methodology for measuring pore patterns in the benthic foraminiferal genus Ammonia', *Marine Micropaleontology*, 128, pp. 1–13. doi: 10.1016/j.marmicro.2016.08.001.

Pokroy, Boaz, Fitch, Andrew N., Marin, Frederic, Kapon, Moshe, Adir, Noam and Zolotoyabko, E. (2006a) 'Anisotropic lattice distortions in biogenic calcite induced by intra-crystalline organic molecules', *Journal of Structural Biology*, 155, pp. 96–103. doi: 10.1016/j.jsb.2006.03.008.

Pokroy, Boaz, Fitch, Andy N. and Zolotoyabko, Emil (2006b) 'The Microstructure of Biogenic Calcite : AView by High-Resolution Synchrotron Powder Diffraction', *Advanced Materials*, 18, pp. 2363–2368. doi: 10.1002/adma.200600714.

Putnis, Andrew (2014) 'Why mineral interfaces matter', *Science*, 343(6178), pp. 1441–1442. doi: 10.1126/science.1250884.

Ravelo, Ana Christina and Hillaire-Marcel, Claude (2007) 'Chapter Eighteen The Use of Oxygen and Carbon Isotopes of Foraminifera in Paleoceanography', *Developments in Marine Geology*, 1(07), pp. 735–764. doi: 10.1016/S1572-5480(07)01023-8.

Regenberg, M., Nurnber, D., Steph, S., Groeneveld, J., Garbe-Schonberg, D., Tiedemann, R. and Dullo, W. C. (2006) 'Assessing the effect of dissolution on planktonic foraminiferal Mg/Ca ratios: Evidence from Caribbean core tops', *Geochemistry, Geophysics, Geosystems*, 7(7), pp. 1–23. doi: 10.1029/2005GC001019.

Reich, Elke, Schoeppler, Vanessa, Lemanis, Robert, Lakin, Evgeny, Zolotoyabko, Emil, Zöllner, Dana and Zlotnikov, Igor (2019) 'Morphological and textural evolution of the prismatic ultrastructure in mollusc shells: A comparative study of Pinnidae species', *Acta Biomaterialia*, 85, pp. 272–281. doi: 10.1016/j.actbio.2018.12.023.

Resplandy, R., Keeling, R. F., Eddebar, Y., Brooks, M., Wang, R., Bopp, L., Long, M. C., Dunne, J. P., Koeve, W. and Oschlies, A. (2019) 'Quantification of ocean heat uptake from changes in atmospheric O 2 and CO 2 composition', *Scientific Reports*, 9(20244), pp. 1–10. doi: 10.1038/s41598-019-56490-z.

Richirt, Julien, Schweizer, Magali, Bouchet, Vincent M. P., Mouret, Aurelia, Quinchard, Sophie and Jorissen, Frans J. (2019) 'Morphological distinction of three Ammonia phylotypes occuring along European coasts', *Journal of Foraminiferal Research*, 49(1), pp. 76–93.

Rodríguez-Navarro, Carlos, Ruiz-Agudo, Encarnación, Harris, Joe and Wolf, Stephan E. (2016) 'Nonclassical crystallization in vivo et in vitro (II): Nanogranular features in biomimetic minerals disclose a general colloid-mediated crystal growth mechanism', *Journal of Structural Biology*, 196, pp. 260–287. doi: 10.1016/j.jsb.2016.09.005.

Rögl, Fred, Ćorić, Stjepan, Harzhauser, Mathias, Jimenez-Moreno, Gonzalo, Kroh, Andreas, Schultz, Ortwin, Wessely, Godfrid and Zorn, Irene (2008) 'The Middle Miocene Badenian stratotype at Baden-Sooss (Lower Austria)', *Geologica Carpathica*, 59(5), pp. 367–374.

Rosenthal, Y., Lohmann, G. P., Lohmann, K. C. and Sherrell, R. M. (2000) 'Incorporation and preservation of Mg in Globigerinoides sacculifer : Implications for reconstructing the temperature and of seawater', *Paleoceanography*, 15(1), pp. 135–145.

Rosenthal, Yair and Lohmann, George P. (2002) 'Accurate estimation of sea surface temperatures using dissolution- corrected calibrations for Mg / Ca paleothermometry', *Paleoceanography*, 17(3), pp. 1–6. doi: 10.1029/2001PA000749.

Ross, James, Pirrie, Duncan, Marshall, James D., Pirrie, Duncan, Cross, High, Road, Madingley, Oet, Cambridge C. B. and Marshall, James D. (1990) 'Diagenesis of Inoceramus and Late Cretaceous Paleoenvironmental Geochemistry : A Case Study from James Ross Island , Antarctica', *Society for Sedimentary Geology*, 5(4), pp. 336–345.

Ruiz-Agudo, E., Putnis, C. V. and Putnis, A. (2014) 'Coupled dissolution and precipitation at mineral-fluid interfaces', *Chemical Geology*, 383, pp. 132–146. doi: 10.1016/j.chemgeo.2014.06.007.

Schenk, Anna S. and Kim, Yi-yeoun (2015) 'Unraveling the internal microstructure of biogenic and bioinspired calcite single crystals', *MRS Bulletin*, 40(6), pp. 499–508. doi: 10.1557/mrs.2015.100.

Schneider, Andrea, Crémière, Antoine, Panieri, Giuliana, Lepland, Aivo and Knies, Jochen (2017) 'Diagenetic alteration of benthic foraminifera from a methane seep site on Vestnesa Ridge (NW Svalbard)', *Deep-Sea Research 1*, 123, pp. 22–34. doi: 10.1016/j.dsr.2017.03.001.

Schone, B. R. and Surge, Donna (2012) 'Part N, Revised, Volume 1, Chapter 14: Bivalve sclerochronology and geochemistry. Treatise Online 46', in Seldon, P. and Hardesty, J. (eds) *Treatise of Invertebrate Paleontology*. Paleontological Institute, The University of Kansas, pp. 1–24.

Schöne, Bernd R. and Gillikin, David P. (2013) 'Unraveling environmental histories from skeletal diaries — Advances in sclerochronology', *Palaeogeography, Palaeoclimatology, Palaeoecology*, 373, pp. 1–5. doi: 10.1016/j.palaeo.2012.11.026.

Schöne, Bernd R., Zhang, Zengjie, Radermacher, Pascal, Thébault, Julien, Jacob, Dorrit E., Nunn, Elizabeth V and Maurer, Anne-france (2011) 'Sr/Ca and Mg/Ca ratios of ontogenetically old, long-lived bivalve shells (Arctica islandica) and their function as paleotemperature proxies', *Palaeogeography, Palaeoclimatology, Palaeoecology*, 302, pp. 52–64. doi: 10.1016/j.palaeo.2010.03.016.

Sexton, P. F. and Wilson, P. A. (2009) 'Preservation of benthic foraminifera and reliability of deep-sea temperature records : Importance of sedimentation rates , lithology , and the need to examine test wall structure', *Paleoceanography*, 24, pp. 1–14. doi: 10.1029/2008PA001650.

Sexton, P. F., Wilson, P. A. and Norris, R. D. (2006a) 'Testing the Cenozoic multisite composite δ18O and δ13C curves: New monospecific Eocene records from a single locality, Demerara Rise (Ocean Drilling Program Leg 207)', *Paleoceanography*, 21(PA2019), pp. 1–17. doi: 10.1029/2005PA001253.

Sexton, Philip F., Wilson, Paul A. and Pearson, Paul N. (2006b) 'Microstructural and geochemical perspectives on planktic foraminiferal preservation: "Glassy" versus "Frosty"', *Geochemistry, Geophysics, Geosystems*, 7(12), pp. 1–29. doi: 10.1029/2006GC001291.

Shackleton, Nicholas (1967) 'Oxygen Isotope Analyses and Pleistocene Temperatures Re-assessed', *Nature*, 215, pp. 15–17.

Shackleton, Nicholas J., Hall, Mike A. and Boersma, A. (1984) 'Oxygen and carbon isotope data from Leg 74 Foraminifers', *Initial report of the Deep Sea Drilling project*, 74, pp. 599–612.

Shackleton, Nicholas J. and Opdyke, N. D. (1973) 'Oxygen isotope and paleomagnetic stratigraphy of equatorial Pacific core V28-238: oxygen isotope temperature and ice volume on a 105 year and 106 year time scale.', *Quaternary Research*, 55, pp. 39–55.

Shieh, Ying-tzung, You, Chen-feng, Shea, Kai-shuan and Horng, Chorng-shern (2002) 'Identification of diagenetic artifacts in foraminiferal shells using carbon and oxygen isotopes', *Journal of Asian Earth Sciences*, 21, pp. 1–5.

Song, Haijun, Wignall, Paul B., Song, Huyue, Dai, Xu and Chu, Daoliang (2019) 'Seawater Temperature and Dissolved Oxygen over the Past 500 Million Years', *Journal of Earth Sciences*, 30(2), pp. 236–243.

Spero, H. J. (1988) 'Ultrastructural examination of chamber morphogenesis and biomineralization in the planktonic foraminifer Orbulina universa', *Marine Biology*, 99, pp. 9–20.

Spötl, C. and Vennemann, T. (2003) 'RCM Letter to the Editor', *Rapid Communications in Mass Spectrometry*, 17, pp. 1004–1006. doi: 10.1002/rcm.1010.

Stainbank, Stephanie, Spezzaferri, Silvia, Boever, Eva De, Bouvier, Anne-sophie, Chilcott, Colin, Leau, Erica S. De, Foubert, Anneleen, Kunkelova, Tereza, Pichevin, Laetitia, Raddatz, Jacek, Rüggeberg, Andres, Wright, James D., Yu, Siyao M., Zhang, Manlin and Kroon, Dick (2020) 'Assessing the impact of diagenesis on foraminiferal geochemistry from a low latitude, shallow-water drift deposit', *Earth and Planetary Science Letters*, 545, p. 116390. doi: 10.1016/j.epsl.2020.116390.

Stancliffe, Author R. P. W. (1989) 'Microforaminiferal Linings : Their Classification , Biostratigraphy and Paleoecology , with Special Reference to Specimens from British Oxfordian Sediments', *Micropaleontology*, 35(4), pp. 337–352.

Staudigel, Philip T., John, Eleanor H., Buse, Ben and Lear, Caroline H. (2022) 'Apparent preservation of primary foraminiferal Mg/Ca ratios and Mg-banding in recrystallized foraminifera', *Geology*, 50(7), pp. 1–5. doi: 10.1130/G49984.1/5586029/g49984.pdf.

Steuber, T. (1999) 'Isotopic and chemical intra-shell variations in low-Mg calcite of rudist bivalves (Mollusca-Hippuritacea): disequilibrium fractionations and late Cretaceous seasonality', *International Jourrnal of Earth Sciences*, 88, pp. 551–570.

Stolarski, Jarosla W. (1991) 'Miocene Scleractinia from the Holy Cross Mountains, Poland; Part 1 - Caryophylliidae, Flabellidae, Dendrophylliidae, and Micrabaciidae', *Acta Geologica Polonica*, 41, pp. 37–67.

Stolarski, Jarosław, Drake, Jeana, Coronado, Ismael, Vieira, Ana R., Radwańska, Urszula, Heath-Heckman, Elizabeth A. C., Mazur, Maciej, Guo, Jinming and Meibom, Anders (2023) 'First paleoproteome study of fossil fish otoliths and the pristine preservation of the biomineral crystal host', *Scientific Reports*, 13(3822), pp. 1–11.

Stolarski, Jarosław and Mazur, Maciej (2005) 'Nanostructure of biogenic versus abiogenic calcium carbonate crystals', *Acta Palaeontologica Polonica*, 50(4), pp. 847–865.

Stolarski, Jaroslaw, Meibom, Anders, Przeniosło, R. and Mazur, M. (2016) 'A Cretaceous Scleractinian Coral with a Calcitic Skeleton', *Science*, 318(92), pp. 92–94. doi: 10.1126/science.1149237.

Strag, Martyna, Bieda, Magdalena, Maj, Łukasz, Jarzebska, Anna, Berent, Katarzyna, Nalepka, K., Checa, Antonio G. and Sztwiertnia, K. (2019) 'Misorientation characteristics of interphase boundaries in Pinctada margaritifera shell', *Materials Letters*, 253, pp. 302–305. doi: 10.1016/j.matlet.2019.06.099.

Suzuki, Michio and Nagasawa, Hiromichi (2013) 'Mollusk shell structures and their formation mechanism', *NRC Research Press*, 91, pp. 349–366.

Suzuki, Michio, Sakuda, Shohei and Nagasawa, Hiromichi (2007) 'Identification of Chitin in the Prismatic Layer of the Shell and a Chitin Synthase Gene from the Japanese Pearl Oyster Pinctada fucata', *Bioscience, Biotechnology and Biochemistry*, 71(7), pp. 1735–1744. doi: 10.1271/bbb.70140.

Sykes, A., Collins, J. and Walton, I. (1995) 'The significance of a geochemically isolated intracrystalline organic fraction within biominerals', *Organic Geochemistry*, 23(I), pp. 1059–1065.

Tamenori, Yusuke, Yoshimura, Toshihiro, Trong, Nguyen, Hasegawa, Hiroshi, Suzuki, Atsushi, Kawahata, Hodaka and Iwasaki, Nozomu (2014) 'Identification of the chemical form of sulfur compounds in the Japanese pink coral (Corallium elatius) skeleton using u-XRF / XAS speciation mapping', *Journal of Structural Biology*, 186(2), pp. 214–223. doi: 10.1016/j.jsb.2014.04.001.

Towe, K. and Cifelli, R. (1967) 'Wall Ultrastructure in the Calcareous Foraminifera: Crystallographic Aspects and a Model for Calcification', *Journal of Paleontology*, 41(3), pp. 742–762.

Towe, K. and Hemleben, C. (1976) 'Diagenesis of magnesian calcite: Evidence from miliolacean foraminifera', *Geology*, 4.

Toyofuku, Takashi, Matsuo, Miki Y., Nooijer, Lennart Jan De, Nagai, Yukiko, Kawada, Sachiko, Fujita, Kazuhiko, Reichart, Gert-jan, Nomaki, Hidetaka, Tsuchiya, Masashi, Sakaguchi, Hide and Kitazato, Hiroshi (2017) 'Proton pumping accompanies calcification in foraminifera', *Nature Communications*. Nature Publishing Group, 8, pp. 6–11. doi: 10.1038/ncomms14145.

Tyszka, J., Bickmeyer, Ulf, Raitzsch, Markus, Bijma, Jelle, Kaczmarek, Karina and Mewes, Antje (2019) 'Form and function of F-actin during biomineralization revealed from live experiments on foraminifera', *PNAS*, 116(10), pp. 4111–4116. doi: 10.1073/pnas.1810394116.

Ullmann, Clem V and Korte, Christoph (2015) 'Diagenetic alteration in low-Mgcal cite from macrofossils: a review', *Geological Quarterly*, 59(1), pp. 3–20. doi: 10.7306/gq.1217.

Urey, Harold C. (1948) 'Oxygen Isotopes in Nature and in the Laboratory', *Science*, 108(2810), pp. 489–496.

Urey, Harold C., Lowenstam, S., Epstein, S. and McKinney, C. R. (1951) 'Measurement of paleotemperatures and temperatures of the Upper Createceous of England, Denmark and the southeastern United States', *Bulletin of the Geological Society of America*, 62, pp. 399–416.

Veizer, Jan, Ala, Davin, Azmy, Karem, Bruckschen, Peter, Buhl, Dieter, Bruhn, Frank, Carden, Giles A. F., Diener, Andreas, Ebneth, Stefan, Godderis, Yves, Jasper, Torsten, Korte, Christoph, Pawellek, Frank, Podlaha, Olaf G. and Strauss, Harald (1999) '87Sr/86Sr, d13 Cand d18O evolution of Phanerozoic seawater', *Chemical Geology*, 161, pp. 59–88. doi: 10.1016/S0009-2541(99)00081-9.

Veizer, Jan and Prokoph, Andreas (2015) 'Temperatures and oxygen isotopic composition of Phanerozoic

oceans', *Earth Science Reviews*, 146, pp. 92–104. doi: 10.1016/j.earscirev.2015.03.008.

Velde, B. (1996) 'Compaction trends of clay-rich deep sea sediments', *Marine Geology*, 133, pp. 193–201.

Vinther, Jakob (2015) 'The origin of Mollusks', *Palaeontology*, 58, pp. 19–34. doi: 10.1111/pala.12140.

Wacker, Ulrike, Rutz, Tanja, Löffler, Niklas, Conrad, Anika C., Tütken, Thomas, Böttcher, Michael E. and Fiebig, Jens (2016) 'Clumped isotope thermometry of carbonate-bearing apatite : Revised sample pre-treatment, acid digestion, and temperature calibration', *Chemical Geology*, 443, pp. 97–110. doi: 10.1016/j.chemgeo.2016.09.009.

Wallis, David, Harris, Joe, Bo, Corinna F., Wang, Di, Zavattieri, Pablo, Feldner, Patrick, Merle, Benoit, Pipich, Vitaliy, Hurle, Katrin, Leupold, Simon, Hansen, L. N., Marin, F. and Wolf, Stephan E. (2022) 'Progressive changes in crystallographic textures of biominerals generate functionally graded ceramics', *Material Advances*. Royal Society of Chemistry, 3(3), pp. 1527–1538. doi: 10.1039/d1ma01031j.

Walton, Derek (1998) 'Degradation of intracrystalline proteins and amino acids in fossil brachiopods', *Organic Geochemistry*, 28(6), pp. 389–410. doi: 10.1016/S0146-6380(97)90126-1.

Wan, Chao, Ma, Y. and Gorb, Stanislav N. (2019) 'Compromise between mechanical and chemical protection mechanisms in the system of the bivalve Mytilus edulis shell', *Journal of Experimental Biology*, 222(15). doi: 10.1242/jeb.201103.

Warinner, Christina, Richter, Kristine Korzow and Collins, Matthew J. (2022) 'Paleoproteomics', *Chemical Reviews*, 122, pp. 12401–13446. doi: 10.1021/acs.chemrev.1c00703.

Warter, Viola, Erez, Jonathan and Müller, Wolfgang (2018) 'Environmental and physiological controls on daily trace element incorporation in Tridacna crocea from combined laboratory culturing and ultra-high resolution LA-ICP-MS analysis', *Palaeogeography, Palaeoclimatology, Palaeoecology*, 496, pp. 32–47. doi: 10.1016/j.palaeo.2017.12.038.

van der Weijden, H. C. (1992) 'Chapter 2: Early Diagenesis and Marine Pore Water', *Developments in Sedimentology*, 47, pp. 13–134.

Weiner, Stephen and Erez, Jonathan (1984) 'Organic matrix of the shell of the foraminifer, Heterostegina depressa', *Journal of Foraminiferal Research*, 14(3), pp. 206–212.

Wendler, Jens E., Wendler, Ines, Rose, Timothy and Huber, Brian T. (2012) 'Using Cathodoluminescence Spectroscopy of Cretaceous Calcareous Microfossils to Distinguish Biogenic from Early-Diagenetic Calcite', *Microscopy and Microanalysis*, 18, pp. 1313–1321.

Wheeler, Lucy J., Penkman, Kirsty E. H. and Sejrup, H. P. (2021) 'Assessing the intra-crystalline approach to amino acid geochronology of Neogloboquadrina pachyderma (sinistral)', *Quaternary Geochronology*, 61, pp. 1–13. doi: 10.1016/j.quageo.2020.101131.

Williams, Mark, Haywood, Alan M., Taylor, Steve P., Valdes, Paul J., Sellwood, Bruce W. and Hillenbrand, Claus-dieter (2005) 'Evaluating the efficacy of planktonic foraminifer calcite d 18 O data for sea surface temperature reconstruction for the Late Miocene', *Geobios*, 38, pp. 843–863. doi: 10.1016/j.geobios.2004.12.001.

Wilson, Paul A., Norris, R. D. and Cooper, M. J. (2002) 'Testing the Cretaceous greenhouse hypothesis using glassy foraminiferal calcite from the core of the Turonian tropics on Demerara Rise', *Geology*, 30(7), pp. 607–610.

Wilson, Paul A. and Norris, Richard D. (2001) 'Warm tropical ocean surface and global anoxia during the mid-Cretaceous period', *Letters to Nature*, 412, pp. 425–429.

de Winter, N. J. and Claeys, Philippe (2016) 'Micro X-ray fluorescence (μXRF) line scanning on Cretaceous rudist bivalves: A new method for reproducible trace element profiles in bivalve calcite', *Sedimentology*, 64, pp. 231–251. doi: 10.1111/sed.12299.

de Winter, Niels J., Ullmann, Clemens V, Sørensen, Anne M., Thibault, Nicolas, Goderis, Steven, Malderen, Stijn J. M. Van, Snoeck, Christophe, Goolaerts, Stijn, Vanhaecke, Frank and Claeys, Philippe (2020) 'Shell chemistry of the boreal Campanian bivalve Rastellum diluvianum (Linnaeus , 1767) reveals temperature seasonality , growth rates and life cycle of an extinct Cretaceous oyster', *Biogeosciences*, 17, pp. 2897–2922.

Wolf, Stephan E., Böhm, Corinna F., Harris, Joe, Demmert, Benedikt, Jacob, Dorrit E., Mondeshki, Mihail, Ruiz-Agudo, Encarnación and Rodríguez-Navarro, Carlos (2016) 'Nonclassical crystallization in vivo et in vitro (I): Process-structure- property relationships of nanogranular biominerals', *Journal of Structural Biology*, 196(2), pp. 244–259. doi: 10.1016/j.jsb.2016.07.016.

Woo, Kyung-sik, Anderson, Thomas F. and Sandberg, Philip A. (1993) 'Diagenesis of Skeletal and Nonskeletal Components of Mid-cretaceous Limestones', *Journal of Sedimentary Petrology*, 63(1), pp. 18–32.

Yin, X., Griesshaber, E., Checa, A., Nindiyasari-Behal, F., Sanchez-Almazo, I., Ziegler, A. and Schmahl, W. W. (2021) 'Calcite crystal orientation patterns in the bilayers of laminated shells of benthic rotaliid foraminifera', *Journal of Structural Biology*, 213(1–22). doi: 10.1016/j.jsb.2021.107707.

Yin, X., Griesshaber, Erika, Fernandez-Diaz, L., Ziegler, Andreas, Garcia-Garcia, F. J. and Schmahl, Wolfgang W. (2019) 'In fluence of Gelatin−Agarose Composites and Mg on Hydrogel-Carbonate Aggregate Formation and Architecture', *Crystal Growth and Design*, 19, pp. 5696–5715. doi: 10.1021/acs.cgd.9b00679.

Yoshimura, Toshihiro, Tamenori, Yusuke, Suzuki, Atsushi, Nakashima, Rei and Iwasaki, Nozomu (2013) 'Element profile and chemical environment of sulfur in a giant clam shell: Insights from μ-XRF and X-ray absorption near-edge structure', *Chemical Geology*, 352, pp. 170–175. doi: 10.1016/j.chemgeo.2013.05.035.

Zachos, James C., Lowell, D. and Lohmann, Kyger C. (1994) 'Evolution of early Cenozoic marine temperatures', *Paleoceanography*, 9(2), pp. 353–387.

Zachos, James C., Pagani, Mark, Sloan, Lisa, Thomas, Ellen and Billups, Katharina (2001) 'Trends, Rhythms, and Aberrations in Global Climate 65 Ma to Present', *Science*, 292(5517), pp. 686–693. doi: 10.1126/science.1059412.

Zágoršek, K., Radwańska, Urszula and Radwański, A. (2012) 'Bryozoa from the Korytnica Basin (Middle Miocene; Holy Cross Mountains, Central Poland)', *Bulletin of Geosciences*, 87(2), pp. 201–218. doi: 10.3140/bull.geosci.1249.

Zolotoyabko, E., Caspi, E. N., Fieramosca, J. S., Dreele, R. B. Von, Marin, F., Mor, G., Addadi, Lia, Weiner,

Steve and Politi, Yael (2010) ‘Differences between Bond Lengths in Biogenic and Geological Calcite’, *Crystal Growth and Design*, 10(3), pp. 1207–1214. doi: 10.1021/cg901195t.

Zolotoyabko, Emil (2017) ‘Anisotropic Lattice Distortions in Biogenic Minerals Originated from Strong Atomic Interactions at Organic / Inorganic Interfaces’, *Advanced Matieral Interfaces*, 4(1600189). doi: 10.1002/admi.201600189.

8 *Curriculum Vitae*

Deyanira Graciela Cisneros Lazaro

ORCID :	0000-0001-8216-3716
Nationality :	Cuban
Birth date:	13th July 1994
Languages:	English and Spanish (native) French (fluent)

Education

2019–ongoing	**Ph.D.**, Laboratory for Biological Geochemistry, École Polytechnique Fédérale de Lausanne (EPFL); Lausanne, Switzerland *Diagenetic isotope exchange in biocalcites* Advisor: Prof. Anders Meibom
2017–2019	**M.Sc. in Geology (cum laude)**, Department of Earth Sciences, Stellenbosch University; Stellenbosch, South Africa *Role of Myrmekites and Associated Deformation Fabrics in Controlling Development of Granitic Mylonites in the Pofadder Shear Zone, Southern Namibia* Advisors: Prof. Jodie Miller, Prof. Lukas Baumgartner
2016	**B.Sc. (Hons) in Earth Sciences**, Department of Earth Sciences, Stellenbosch University; Stellenbosch, South Africa *Analysis of Textures in the Pofadder Shear Zone Associated with the Strain Shadow of the Tantalite Valley Complex* Advisor: Prof. Jodie Miller
2013–2015	**B.Sc., in Earth Sciences**, Department of Earth Sciences, Stellenbosch University; Stellenbosch, South Africa

Publications

2023	Rapid grain boundary diffusion in foraminifera tests biases paleotemperature records *Communications Earth and Environment*, **4**, 144 Adams, A., Daval, D., Baumgartner, L. P., Bernard, S., Vennemann, T., **Cisneros-Lazaro, D.,** Stolarski, J., Baronnet, A., Grauby, O., Guo, J., Meibom, A.

2022	Fast and pervasive diagenetic isotope exchange in foraminifera tests is species-dependent *Nature Communications*, **13**, 113 **Cisneros-Lazaro, D.**, Adams, A., Guo, J., Bernard, S., Baumgartner, L.P., Daval, D., Baronnet, A., Grauby, O., Vennemann, T., Stolarski, J., Escrig. S., Meibom, A.
2021	Species-specific foraminiferal ultrastructures modulate surfaces available for diagenesis *Microscopy and Microanalysis*, **27**, S1 **Cisneros-Lazaro, D.,** Adams, A., Guo, J., Bernard S., Daval, D., Baronnet, A., Grauby, O., Vennemann, T., Stolarski, J., Baumgartner, L. P., Meibom, A.
2019	Role of myrmekite and associated deformation fabrics in controlling development of granitic mylonites in the Pofadder Shear Zone of southern Namibia *Contributions to Mineralogy and Petrology*, **174,** 22 **Cisneros-Lazaro, D.,** Miller, J. A., Baumgartner, L. P.

Student Supervision

2020	Julie Reznicek, Master Semester project titled *Ocean paleotemperatures from foraminiferal tests oxygen isotopic composition: A brief history, and how current research questions long-held theories*, EPFL

Invited Talks

April, 2023	Marine biocalcites as seen with optical photothermal infrared spectroscopy (OPTIR). *University of Lausanne*, Lausanne, Switzerland.
March, 2023	The role of microstructure and organic matter in diagenetic isotope exchange in marine biocalcites as revealed by PiFM. *Australian National University,* Canberra, Australia.
January, 2023	Paleoclimate reconstruction from marine biocalcites: using NanoSIMS imaging to visualise diagenetic isotope exchange. *SwissSIMS winter school*, Lausanne, Switzerland.
August, 2021	Species-specific foraminiferal ultrastructures modulate surfaces available for diagenesis. *Microscopy and Microanalysis*, Virtual meeting.

First Author Conference Proceedings

September, 2023	Biomacromolecules increase diagenetic isotope exchange in biocalcites. *Bathurst Meeting, Naples, Italy (Oral)* **Cisneros-Lazaro, D**., Adams, A, Raut, H. K, Otter, L. M., Daval, D., Vennemann, T., Baumgartner, L. P., Stolarski, J., Bernard, S., Baronnet, A., Grauby, O., Meibom, A.
July, 2023	In-situ identification of the biomacromolecules relevant to diagenetic isotope exchange in biocalcites. *Goldschmidt2023, Lyon, France (Oral)* **Cisneros-Lazaro, D**., Otter, L. M., Adams, A., Daval, D., Vennemann, T., Baumgartner, L. P., Stolarski, J., Bernard, S., Baronnet, A., Grauby, O., Meibom, A.
June, 2022	Paleoclimate reconstruction from biocalcites: the key role of microstructure and organic matter in diagenetic isotope exchange. *Goldschmidt2022, Virtual. (Oral)* **Cisneros-Lazaro, D**., Adams, A., Raut, H. K., Bernard, S., Daval, D., Baronnet, A., Grauby, O., Vennemann, T., Stolarski, J., Escrig, S., Baumgartner, L. P., Meibom, A.
June, 2022	Cooking seashells: How isotopic tracers can help correct paleoclimate records. *IIE Green Days, Anzere, Switzerland. (Poster)* **Cisneros-Lazaro, D.**, Meibom, A.
April, 2022	^{18}O tracer shows diagenetic isotope exchange in biocalcites to be fast, pervasive and species-dependent. *EGU22, Vienna, Austria. (Oral)* **Cisneros-Lazaro, D.,** Adams, A., Guo, J., Bernard, S., Baumgartner, L. P., Daval, D., Baronnet, A., Grauby, O., Vennemann, T., Stolarski, J., Escrig, S., Meibom, A.
July, 2021	Direct imaging of diagenetic fluid penetration into benthic foraminifera tests. *Goldschmidt2021, Virtual. (Oral)* **Cisneros-Lazaro, D.,** Adams, A., Guo, J., Bernard, S., Daval, D., Baronnet, A., Grauby, O., Vennemann, T., Stolarski, J., Escrig, S., Baumgartner, L. P, Meibom, A.
July, 2020	Diagenesis of Benthic Foraminifera: Fluid Penetration and Isotopic Exchange Visualized with NanoSIMS. *Goldschmidt2020, Virtual. (Oral)*

Cisneros-Lazaro, D., Adams, A., Guo, J., Baumgartner, L. P., Bernard, S., Daval, D., Baronnet, A., Grauby, O., Vennemann, T., Stolarski, J., Meibom, A.

April, 2017 Lithological controls on microstructural development in the Pofadder Shear Zone and the role of fluids, rheology and metamorphic grade.
EGU2017, Vienna, Austria (Poster)

Cisneros-Lazaro, D., Miller, J., Rowe, C., Beach, A.

Co-Author Conference Proceedings

July, 2023 Measuring oxygen lattice diffusion in biominerals – Implications for paleotemperature reconstructions. (Oral)
Goldschmidt2023, Lyon, France

Adams, A., **Cisneros-Lazaro, D**., Daval, D., Vennemann, T., Baumgartner, L.P., Stolarski, J., Bernard, S., Baronnet, A., Grauby, O., Raut, H. K., Meibom, A.

June, 2023 Cogwheel structures in foraminifera shells and its implication for diagenesis. (Poster)
Forams2023, Perugia, Italy

van Dijk, I., **Cisneros-Lazaro, D**., Raitzsch, M., Moore, J., Meibom, A., Bijma, J.

November, 2021 Biogenic Carbonate Paleotemperature Records Biased by Grain Boundary Diffusion. (Oral)
19th Swiss Geoscience Meeting; Geneva, Switzerland

Adams, A., Baumgartner, L.P., Vennemann, T., Daval, D., Bernard, S., **Cisneros-Lazaro, D**., Baronnet, A., Grauby, O., Guo, J., Stolarski, J., Meibom, A.

July, 2021 Foraminifera Isotope Reequilibration Biases Paleotemperature Records. (Oral)
Goldschmidt2021, Lyon, France

Adams, A., Baumgartner, L.P., Vennemann, T., Daval, D., Bernard, S., **Cisneros-Lazaro, D**., Guo, J., Baronnet, A., Grauby, O., Stolarski, J., Meibom, A.

December, 2019 A reassessment of the geochemical and isotopic fidelity of biogenic carbonates. (Oral)
AGU 100, Fall Meeting; San Francisco, USA

Adams, A., Baumgartner, L.P., Vennemann, T., Daval, D., Bernard, S., **Cisneros-Lazaro, D.,** Baronnet, A., Grauby, O., Guo, J., Stolarski, J., Meibom, A.

September, 2019	SIMS investigations of recrystallisation of and diffusion in carbonate at low and high temperature. (Oral) The 2019 TIGer Conference; Perth, Australia. Baumgartner, L., Bégué, F., Adams, A., **Cisneros-Lazaro, D.**, Meibom A., Guo, J., Daval, D., Bernard, S., Baronnet, A., Grauby, O., Stolarski, J.

Academic Service

2023	Reviewer for *Frontiers in Marine Science*
2021	Reviewer for *American Mineralogist*

Relevant Experience

June 2015	Field assistant in Namibia for MSc and PhD projects with Prof. Christie Rowe
Nov. 2014 – Jan. 2015	Mining geologist assistant at Petra Diamonds with Wiehan Smit